

THE IMPACT OF SUBSTRATE CURVATURE ON THE SELF-ASSEMBLY OF LIQUID CRYSTALS

vorgelegt von

Master of Science (M. Sc.)

Sergej Püschel-Schlotthauer

geb. in Uralsk (Kasachstan)

von der Fakultät II – Mathematik und Naturwissenschaften

der Technischen Universität Berlin

zur Erlangung des akademischen Grades

Doktor der Naturwissenschaften

– Dr.-rer.-nat. –

GENEHMIGTE DISSERTATION

PROMOTIONS-AUSSCHUSS:

VORSITZENDER: Prof. Dr. Martin Oestreich

GUTACHTER: Prof. Dr. Martin Schoen

GUTACHTER: Prof. Dr. Keith E. Gubbins

TAG DER WISSENSCHAFTLICHEN AUSSPRACHE: 21. Juli 2017

BERLIN 2017

For my girls

DANKSAGUNG

An dieser Stelle möchte ich mich herzlich bei Prof. Dr. Martin Schoen für die Möglichkeit bedanken in seinem Arbeitskreis zu promovieren. Das Anfertigen der vorliegenden Arbeit wäre ohne seine hervorragende Betreuung undenkbar gewesen. Insbesondere das freie und selbständige Arbeiten sowie zahlreiche sehr produktive Diskussionen mit Ihm bereiteten mir viel Freude und trugen stets zur qualitativen Verbesserung meiner Arbeit bei. Ich möchte mich ebenfalls beim zweiten Gutachter Prof. Dr. Keith E. Gubbins für das Anfertigen des Gutachtens bedanken.

Ich bin dankbar für die finanzielle Unterstützung durch die Deutsche Forschungsgemeinschaft über das Internationale Graduiertenkolleg (IRTG) 1524, die es mir unter anderem einen sechsmonatigen Auslandsaufenthalt an der North Carolina State University (NCSU) ermöglichte. Für die angenehme Zeit an der NCSU möchte ich Prof. Dr. Carol K. Hall danken, die mich in Ihrem Arbeitskreis aufnahm und betreute. Ihre sehr interessanten Fragen brachten mich stets dazu meine Arbeit aus diversen Blickwinkeln zu betrachten.

Ich danke Dr. Marco Mazza und Dr. Michael Melle für das Korrekturlesen von Teilen dieser Arbeit und für die fruchtbare Zusammenarbeit. Dem gesamten Arbeitskreis Schoen, nämlich Dr. Tillmann Stieger, Robert Skutnik, Stefanie Wandrei, und Elsa Perrin, sowie Heidi Grauel und Nadine Rechenberg, danke ich für die schöne Zeit und angenehme Atmosphäre. Dabei gilt ein besonderer Dank Dr. Tillmann Stieger für die Unterstützung, anregende Diskussionen und eine tolle Zeit innerhalb sowie außerhalb des Arbeitskreises. Ebenso möchte ich mich bei Dr. Rohan Patil und Yeongun Ko bedanken, die durch Ihre offene und freundliche Art meinen Auslandsaufenthalt auch außerhalb des Universitätslebens außerordentlich machten.

Ein riesiger Dank geht an meine Frau Stefanie für die unglaubliche Unterstützung, sowie meine Töchter Julika und Elise, die für mich stets eine Motivation waren diese Arbeit fertig zu stellen. Als letztes danke ich meinen Eltern für Ihre jahrelange Unterstützung.

ABSTRACT

The interplay of anisotropic molecular interactions, nonlinearities of the orientational field, and long-range orientational correlations make the physics of liquid crystals both challenging and fascinating. Liquid crystals are known for their dual nature, i.e. a high degree of the orientational order combined with a certain degree of fluidity. The liquid-crystalline order can be enhanced, perturbed, or destroyed in the presence of external fields (i.e., magnetic, electric field), thermodynamic conditions (i.e., temperature, pressure gradient), or surface forces (i.e., colloidal particles, confinement). In this thesis, we investigate the impact of the surface curvature on the liquid-crystalline order.

In the simplest liquid-crystalline state, i.e., the nematic state, elongated liquid crystal molecules align their long axes with a global direction \hat{n}_0 . The presence of a spherical colloid gives rise to perturbations of the nematic phase. The global orientation along \hat{n}_0 is not compatible everywhere with the specific colloidal surface anchoring. Hence, because of competing alignments enforced by surface anchoring conditions and along \hat{n}_0 topological defects arise in the vicinity of the colloidal surface. These perturbations are the origin for effective anisotropic interactions driving colloidal self-assembly in a directed manner. More specifically, every molecular deviation from \hat{n}_0 causes a response force which reorients the molecule along \hat{n}_0 . However, local deviations from \hat{n}_0 may be stabilized by the colloidal surface such that the elastic energy is stored in the deformation of the director field $\hat{n}(\mathbf{r})$. If two or more colloids approach each other the stored elastic energy is released in a way that minimizes the stored energy. In order to study colloidal self-assembly we perform Monte Carlo simulations of a pair of colloids dispersed in a nematic host phase. We compute the director field $\hat{n}(\mathbf{r})$ for different colloidal configurations and derive a molecular interpretation of the well known Landau-de Gennes free energy in order to analyze $\hat{n}(\mathbf{r})$ and extract an effective pair potential. Furthermore, we test the coarse-grained potential by performing implicit-solvent simulations for low and high colloidal densities and compare the results with experimental findings.

Apparently, the effective interactions are mediated by the host phase. Hence, replacement of the nematic phase by a more complex liquid-crystalline phase would eventually lead to different effective inter-colloidal interactions and self-assembled structures. Recent experiments confirm this. Especially, colloidal inclusions in chiral phases have been studied in-depth and reveal fascinating aspects of colloidal self-assembly. On the other hand, non-chiral phases, e.g. the smectic A phase, have been considered as host fluid as well. Obviously, the perturbation of the liquid-crystalline order is key for understanding the self-assembly mechanism. Therefore, we develop a novel and simple model that exhibits a realistic phase behavior, dynamics, and elasticity. We perform Monte Carlo simulations and study perturbations of the host fluid

across the nematic-smectic A phase transition. In order to match perturbations observed in computer simulations and experiments, we vary the anchoring strength at the colloidal surface. Thereby, we observe the formation of an onion structure which has been observed, for example, in shear-strain experiments. However, to the best of our knowledge, the onion structure has never been reported for colloidal systems or has ever been seen in computer simulations so far.

Finally, we turn to a discussion of the order of liquid crystals that are confined within a mesoscopic channel. We consider a chiral model liquid crystal that exhibits a blue phase II in the bulk. Blue phases have attracted scientific attention because of their unique orientational structure, fast response time to external stimuli, and the capability to form regular networks of line defects. Because topological defects of the liquid-crystalline order attract molecules and colloids, blue phases are used as templates for regular polymer networks. Consequently, the manipulation of blue phases is of crucial importance for the design of polymer networks. In order to manipulate the liquid-crystalline order by confining a chiral liquid-crystal model to a mesoscopic channel. Performing Monte Carlo simulations in the grand canonical ensemble we determine the local order and $\hat{n}(\mathbf{r})$ to obtain a deeper insight into the structure of the defects. These defect structures depend on the shape, size, and anchoring conditions of the channel. Moreover, some of the defect structures presented here have been observed in experiments and have found independent configurations within the framework of a continuum theory.

ZUSAMMENFASSUNG

Aufgrund von anisotropen Wechselwirkungen, nicht linearen Orientierungsfeldern und langreichweitigen Korrelationen ist die Physik der Flüssigkristalle anspruchsvoll und faszinierend. Flüssigkristalle bilden ein hohes Maß an Orientierungsordnung aus und erhalten dabei die Viskosität einer Flüssigkeit. Aufgrund dieser dualen Natur sind Flüssigkristalle von hohem Interesse. Flüssigkristalline Ordnung kann verstärkt, gestört oder vernichtet werden, wenn der Flüssigkristall externen Feldern (z.B. elektrische oder magnetische) ausgesetzt ist, Änderung von thermodynamischen Bedingungen (z.B. Druck- oder Temperaturänderung) eintreten oder er sich in Gegenwart von Oberflächen (z.B. Kolloide oder begrenzende Wände) befindet. In der vorliegenden Arbeit untersuchen wir den Einfluss der Oberflächenkrümmung auf die flüssigkristalline Ordnung.

Die einfachste thermodynamische Phase, die Flüssigkristalle bilden können, ist die nematische Phase. In ihr richten sich die länglichen Moleküle entlang eines globalen Direktors \hat{n}_0 aus. In Gegenwart von kolloidalen Teilchen wird diese globale Ordnung gestört. Die spezifische Oberflächenverankerung der Flüssigkristallmoleküle auf dem Kolloid ist mit der globalen Ordnung entlang \hat{n}_0 nicht überall kompatibel. Aufgrund dieser widersprüchlichen Ausrichtungen der Flüssigkristallmoleküle entstehen lokale Defekte in der unmittelbaren Umgebung des Kolloids. Solche lokale Störungen des Direktorfeldes ist der Ursprung für effektive Wechselwirkungen zwischen kolloidalen Teilchen, welche sich durch diese Wechselwirkung zu hoch symmetrischen kolloidalen Kristallen aggregieren können. Die Selbstaggregation kolloidaler Teilchen in einer nematischen Phase lässt sich folgendermaßen erklären. Jegliche Abweichung der molekularen Orientierung von \hat{n}_0 ruft elastische Kräfte hervor, welche das Teilchen wieder entlang \hat{n}_0 orientieren. In Gegenwart eines Kolloids kann diese Abweichung der molekularen Orientierung von \hat{n}_0 durch Oberflächenverankerung kompensiert und stabilisiert werden. Damit bleibt eine gewisse Menge elastischer Energie als Deformation des lokalen Direktorfeldes $\hat{n}(\mathbf{r})$ gespeichert. Diese Energie wird teilweise freigesetzt, wenn sich zwei Kolloide annähern. In der vorliegenden Arbeit studieren wir die Selbstaggregation von zwei Kolloiden dispergiert in einer nematischen Phase, in der wir die Direktorfelder $\hat{n}(\mathbf{r})$ mithilfe von Monte Carlo Simulationen berechnen. Wir entwickeln eine molekulare Interpretation der bekannten Landau-de Gennes Theorie und nutzen diese um die freie Energie aus den Deformationen von $\hat{n}(\mathbf{r})$ zu extrahieren. Dieser Ansatz zur Berechnung eines effektiven Paarpotentials zwischen einem Kolloidpaar wird anschließend durch eine Simulation getestet, in der die Freiheitsgrade des Trägerfluids also der nematischen Phase aus den Wechselwirkungen ausintegriert wurden.

Die effektive Wechselwirkung zwischen zwei Kolloiden werden damit durch die Eigenschaften flüssigkristalliner Phasen bestimmt. Dies legt nahe, dass das Ersetzen

der nematischen Phase durch eine komplexere flüssigkristalline Phase zum neuen effektiven Wechselwirkungspotential and schließlich zu neuen kolloidalen Kristallen führen wird. Dies wird durch den aktuellen Forschungsstand belegt. Insbesondere rückten kolloidale Dispersionen in chiralen Phasen in den Fokus der Forschung. Aber auch achirale, smektische Phasen werden als Trägerfluid berücksichtigt. Der Schlüssel zum Verständnis der Selbstaggregation liegt in der Störung, welche von einzelnen Kolloiden ausgeht. Zur Aufklärung dieser führen wir Monte Carlo Simulation von einzelnen Kolloiden dispergiert in einer smektisch-A Phase durch. Wir modellieren die smektisch-A Phase mittels eines neuen Wechselwirkungspotentials, mithilfe dessen realistisches Phasenverhalten, Dynamik und Elastizität simuliert wird. Um experimentelle Befunde zu reproduzieren, untersuchen wir den Einfluss der Oberflächenverankerung auf die Defekte in der smektisch-A Phase. Neben der Reproduktion von experimentell beobachteten Defekten, prognostizieren wir die Existenz eines sogenannten Zwiebeldefektes. Solche Defekte sind von Scherexperimenten bekannt. Jedoch wurden sie bisher weder im Zusammenhang mit Kolloiden noch im Rahmen von Computersimulationen diskutiert.

Zum Schluss wenden wir uns chiralen Flüssigkristallen zu, welche durch einen mesoskopischen Kanal eingeschränkt sind. Unter den gewählten thermodynamischen Bedingungen bildet unser chirales Modell eine blaue Phase II aus. Blaue Phasen ziehen wegen ihrer exotischen und einzigartigen Orientierungsstruktur, ihrer schnellen Reaktionszeit auf externe Stimuli und ihrer Eigenschaft komplexe und reguläre Netzwerke aus Defektlinien zu formen die Aufmerksamkeit der Forscher auf sich. Solche Netzwerke aus Defektlinien werden als Template für Polymernetzwerke eingesetzt, da Defekte flüssigkristalliner Phasen dafür bekannt sind, Kolloide und Nanopartikel aber auch kleine Moleküle (z.B. Monomere) anzuziehen. Insbesondere die Manipulation der Netzwerkarchitektur ist von großer Bedeutung für das Design neuer Materialien. In der vorliegenden Arbeit führen wir großkanonische Monte Carlo Simulationen von chiralen Flüssigkristallen durch. Diese werden durch Substrate in zwei Dimensionen begrenzt, sodass ein Kanal von unterschiedlichen Geometrien simuliert werden kann. Durch das Berechnen der lokalen Ordnung und des Direktorfeldes erhalten wir Einblick in die Defektstruktur, welche von der Kanalgröße, Kanalform und der Oberflächenverankerung anhängig ist. Die von uns beobachteten Defektstrukturen wurden teilweise schon in früheren Experimenten und im Rahmen einer Kontinuums Theorie beobachtet.

LIST OF PUBLICATIONS

CONTRIBUTING PUBLICATIONS

1. S. Schlotthauer, R. A. Skutnik, S. Stieger and M. Schoen, *Defect topologies in chiral liquid crystals confined to mesoscopic channels*, J. Chem. Phys. **142**(19), 2015.
2. S. Püschel-Schlotthauer, T. Stieger, M. Melle, M. G. Mazza, and M. Schoen, *Coarse-grained treatment of the self-assembly of colloids suspended in a nematic host phase*, Soft Matter **12**(2), 2016.
3. S. Püschel-Schlotthauer, V. Meiwes Turrión, T. Stieger, R. Grotjahn, C. K. Hall, M. G. Mazza, and M. Schoen, *A novel model for smectic liquid crystals: elastic anisotropy and response to a steady-state flow*, J. Chem. Phys., **145**(16), 2016.
4. S. Püschel-Schlotthauer, V. Meiwes Turrión, C. K. Hall, M. G. Mazza, and M. Schoen, *The impact of colloidal surface anchoring on the smectic A phase*, Langmuir, **33**(9), 2017.

NON-CONTRIBUTING PUBLICATIONS

1. M. Melle, S. Giura, S. Schlotthauer, and M. Schoen, *Finite-size scaling analysis of isotropic–polar phase transitions in an amphiphilic fluid*, J. Phys.-Condens. Mat. **24**(20), 2012.
2. M. Melle, S. Giura, S. Schlotthauer, and M. Schoen, *Addendum to „Finite-size scaling analysis of isotropic–polar phase transitions in an amphiphilic fluid“*, J. Phys.-Condens. Mat. **24**(3), 2012.
3. M. Melle, S. Schlotthauer, M. G. Mazza, S. H. L. Klapp, and M. Schoen *Defect topologies in a nematic liquid crystal near a patchy colloid*, J. Chem. Phys. **136**(19), 2012.
4. M. Melle, S. Schlotthauer, C. K. Hall, E. Díaz-Herrera, and M. Schoen, *Disclination lines at homogeneous and heterogeneous colloids immersed in a chiral liquid crystal*, Soft Matter **10**(30), 2014.
5. T. Stieger, S. Püschel-Schlotthauer, M. Schoen, and M. G. Mazza, *Flow-induced deformation of closed disclination lines near a spherical colloid immersed in a nematic host phase*, Mol. Phys. **114**(2), 2016.

CONTENTS

I	INTRODUCTION	1	
1	LIQUID CRYSTALS	3	
1.1	Liquid-crystalline phases	4	
1.2	Liquid crystals under confinement	8	
1.3	Liquid-crystalline dispersion	10	
1.4	Goal of this thesis	12	
II	THEORY	15	
2	STATISTICAL PHYSICS	17	
2.1	Basic concepts	18	
2.2	Canonical ensemble	20	
2.3	Monte Carlo method	24	
2.3.1	Monte Carlo simulation	24	
2.3.2	Importance sampling	25	
2.3.3	Algorithm	26	
2.4	Isothermal-isobaric ensemble	28	
2.5	Grand canonical ensemble	30	
3	MODEL	33	
3.1	Non-chiral mesogen-mesogen interactions	33	
3.2	Mesogen-substrate interactions	38	
3.3	Mesogen-colloid interactions	39	
3.4	Chiral mesogen-mesogen interactions	40	
3.5	Mesogen-channel interactions	42	
4	CONTINUUM THEORY	47	
4.1	Order parameter	47	
4.2	Landau-de Gennes free energy	48	
4.3	Determination of the Landau-de Gennes parameters	51	
4.4	Frank free energy	53	
4.5	Determination of Frank's constants	55	
4.6	Topological defects	57	
III	RESULTS	61	
5	COLLOIDAL SELF-ASSEMBLY IN A NEMATIC HOST PHASE	63	
5.1	Technical details	64	
5.2	Nematic bulk phase	66	
5.3	Core region	69	
5.4	The effective interaction potential	71	
6	THE IMPACT OF COLLOIDAL ANCHORING ON THE SMECTIC A PHASE	77	
6.1	Bulk properties	78	

6.2	Colloid with homeotropic anchoring	85
6.3	Colloid with planar anchoring	90
7	CHIRAL LIQUID CRYSTALS CONFINED TO MESOSCOPIC CHANNELS	95
7.1	Technical details	96
7.2	Bulk blue phase II	98
7.3	Confinement effects	104
7.3.1	Homeotropic anchoring conditions	104
7.3.2	Circular planar anchoring conditions	112
7.3.3	Directional planar anchoring conditions	116
IV	CONCLUSIONS AND OUTLOOK	119
8	CONCLUSIONS AND OUTLOOK	121
8.1	Colloidal dispersion	121
8.2	Mesoscopic Channels	126
V	APPENDIX	129
	BIBLIOGRAPHY	131

Part I

INTRODUCTION

LIQUID CRYSTALS

Liquid crystals represent a class of complex soft matter systems that was discovered more than a hundred years ago.^{1,2} However, it took more than half a century to unravel their potential. After the development of the first *liquid crystal display* (LCD) in the late 1960's^{3,4} liquid crystals became part of everyday life. An LCD is based on the simple fact that the direction of polarized light traveling through a sample of the liquid crystal may be controlled by an electric field applied to this sample. The transmission/absorption of polarized light which is created behind the LCD is controlled by the strength of the applied electric field.^{3,4} Thus, the fascinating and active field of liquid crystals inspires scientists and engineers to this day. The easy response to electric and magnetic fields, surface forces, and the dual nature of liquid crystals provide as both ordered and disordered media innumerable applications. Beside the LCDs, liquid crystals are used nowadays as nonelectrical temperature sensors, in high-resolution display technology, electronic paper, optical computation, three-dimensional lasers, fibers with unique mechanical, optical, and/or electrical properties, and even in paintings.⁵

Liquid crystals are composed of organic molecules of anisotropic (i.e., prolate, oblate, or more complex) shape (see Fig. 1.1). Here, we explicitly focus on the discussion of prolate molecules. Because of this shape anisotropy, they are capable of forming ordered phases where the symmetry of their state is spontaneously broken. In the conventional high-temperature isotropic state orientational and positional correlations between liquid crystal molecules are short-ranged. As the temperature is decreased the liquid-crystal molecules form the nematic phase which is characterized by a long-range uniaxial orientational correlation, whereas the positional correlation remains short-ranged. Finally, as the temperature is decreased further, the mesogens may form smectic phases where long-range, one-dimensional positional order is exhibited in addition to the orientational nematic order.⁶ If chiral liquid crystals are considered, then, instead of the nematic state, one or more twisted (e.g., cholesteric or blue) phases occur where the left-right symmetry of the system is broken. Hence, liquid crystals combine optical properties of crystals with a certain amount of fluidity.

The focus of recent research is shifted to the perturbation of the liquid crystalline order. For example, perturbations arising in the vicinity of dispersed colloidal particles cause inter-colloidal elastic forces that lead to directed colloidal self-assembly into quasi-crystalline structures.^{9,10} These colloidal quasi-crystals are sensitive to external stimuli such as thermodynamic, electric, and magnetic fields.¹¹ Thus, liquid crystals provide a convenient route for a bottom-up synthesis of photonic crystals where their optical properties may be controlled by external fields.¹² Another exam-

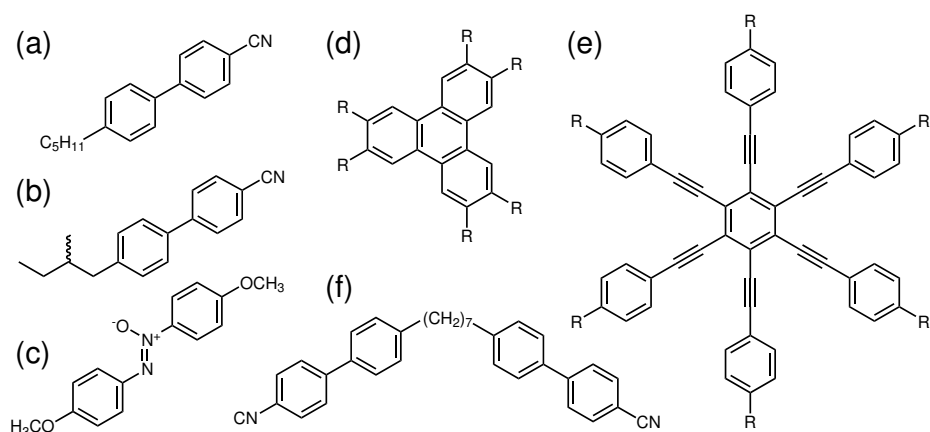


Figure 1.1. Chemical structures of liquid crystal molecules: (a) 4-Cyano-4'-pentylbiphenyl (5CB), (b) 4-Cyano-4'-(2R/S-methylbutyl)-biphenyl (15CB), and (c) *p*-Azoxyanisole (PAA) represent the class of prolate liquid crystals including (b) as the chiral derivative of (a). The class of oblate liquid crystal molecules is illustrated by (d) Hexa-*n*-alkoxytriphenylen and (e) Hexakis-((4-octylphenyl)-ethynyl)-benzene.⁷ (f) 1'',7''-bis(4-Cyanobiphenyl-4'-yl)heptane is a banana-shaped liquid crystal molecule.⁸

ple for the perturbation of liquid-crystalline order is visible when the liquid crystal is confined to certain geometries. For suitable choices of confinement (e.g., channel geometry), regions of undefined orientational order (i.e., defects) arise. These defects are known for attracting molecules and colloids,^{13–16} a property which is used in microfluidics to transport colloidal particles.¹⁷ Furthermore, monomers self-assembling at these defects may be polymerized by UV light. Particularly, blue phases are interesting in this context. Because of their inherent network of defect lines, blue phases are used as templates to achieve complex polymer networks.^{13,14} In both examples, liquid-crystalline order at curved surfaces (i.e., of a colloid or channel) has a crucial impact on the order/disorder of liquid crystals.

In order to investigate the impact of curved surfaces on the liquid-crystalline order, we introduce relevant liquid-crystalline phases and basic concepts of confined liquid crystals as well as colloidal inclusions in liquid-crystalline host phases in the present chapter. We recall some basic concepts of statistical mechanics in [Chapter 2](#), introduce our model system in [Chapter 3](#), and a continuum approach related to the problems studied in this work in [Chapter 4](#). Results presented in [Chapter 5–7](#) are summarized and discussed in [Chapter 8](#).

1.1 LIQUID-CRYSTALLINE PHASES

As already explained, liquid crystal molecules (mesogens) are capable of forming ordered phases. In general, these are classified as achiral and chiral phases. We begin with a discussion of achiral liquid crystals. Here, the simplest ordered state is the nematic one. In the nematic phase, the correlation of the mesogens' centers of

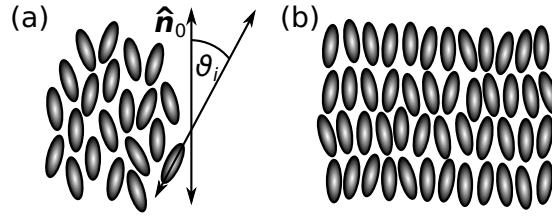


Figure 1.2. Schematic illustration of the (a) nematic and (b) smectic A phase. Double arrows indicate the head-tail symmetry of the mesogens which is also reflected in \hat{n}_0 .

mass is short-ranged as in the isotropic phase. However, the mesogens align their longer axes such that a global preferred direction exists described by the vector \hat{n}_0 to referred to the global director (see Fig. 1.2). Hence, the liquid crystal exhibits a long range orientational correlation.⁶ Notice, because of the head-tail symmetry of the mesogens, the global director \hat{n}_0 is equivalent to $-\hat{n}_0$. The quantification of the molecular alignment along \hat{n}_0 is determined by a nematic order parameter originally introduced by Maier and Saupe^{18,19}

$$S = \frac{1}{N} \sum_{i=1}^N \frac{1}{2} (3 \cos^2 \vartheta_i - 1) \quad (1.1)$$

where ϑ_i is the angle between the molecular axis of the mesogen i and \hat{n}_0 [see Fig. 1.2(a)]. Hence, $S = 0$ in the isotropic phase and $S = 1$ in the perfectly aligned nematic phase. As stated by Maier and Saupe^{18,19} the nematic phase is observed for $S \geq 0.4292$ which is slightly higher than the value $S = 1/3$ predicted by the phenomenological Landau-de Gennes theory.⁶ Clearly, experimentally such a unique value of S does not exist. However, it has been demonstrated for the homologous series of 4-cyano-4'-(n-alkyl)biphenyls that the nematic phase is exists over the range $0.33 \leq S \leq 0.45$.²⁰

If the temperature is lowered, the mesogens may undergo a nematic-smectic A phase transition. In the smectic A phase the mesogens exhibit layered structures such that this phase is characterized by long-range positional in addition to long-range orientational order. The layers occur in a direction parallel to \hat{n}_0 . The fluid-like, short-ranged positional order remains inside the layers (i.e., in directions perpendicular to \hat{n}_0). Because the nematic and smectic A phase have the same orientational symmetry, S is not suitable to distinguish between these two phases (see Fig. 1.2). The quantification of the layered character of a smectic A phase is given by the smectic order parameter

$$\Lambda = \frac{1}{N} \left| \sum_{j=1}^N \exp \left[\frac{2\pi i (\mathbf{r}_j \cdot \hat{n}_0)}{d} \right] \right| \quad (1.2)$$

which is the leading coefficient of the Fourier transform of the local density.²¹ Here, \mathbf{r}_j is the position of the mesogen j and d is the layer separation distance which is in the order of the length of a mesogen.

Considering chiral mesogens, it is helpful to clarify the difference between chiral and achiral liquid crystals. Because of the delocalized π -electrons of the achiral mesogens illustrated in Fig. 1.1(a) and (c), the π - π stacking promotes the side-side arrangement of the elongated molecules. In chiral liquid crystals [see Fig. 1.1(b)], this side-side interaction is sterically hindered by chiral head and/or tail groups. In fact, the molecules form a tilt angle between their molecular axes where the handedness as well as the magnitude of this angle is controlled by the chiral nature of the liquid crystal molecules. For this reason, chiral liquid crystals are known for forming twisted phases. In the cholesteric phase, which is the simplest chiral phase, the global director becomes local and rotates in a helical fashion along one arbitrary direction. Because properties of the cholesteric phase are invariant with respect to any rotation of the Cartesian axes we may assume without any loss of generality that the direction along which the cholesteric helix evolves is parallel to the y -direction. Hence, the cholesteric helix described by the local director

$$\hat{\mathbf{n}}(y) = \left(\cos(q_0 y + \gamma_0), 0, \sin(q_0 y + \gamma_0) \right)^T \quad (1.3)$$

is characterized via the wave number $q_0 = 2\pi/p$ where p is the pitch of the cholesteric helix, and γ_0 is the phase shift (T denotes the transpose of a vector). Because the cholesteric helix evolves along the y -direction, $\hat{\mathbf{n}}(y)$ is always parallel to the x - z plane [see Fig. 1.3(a)] where the particular orientation of $\hat{\mathbf{n}}(y)$ depends on y .⁶ Moreover, because of this constant in-plane orientation a cholesteric phase can be thought as a sequence of two-dimensional nematic planes where the in-plane director varies along the direction perpendicular to the plane.

It is immediately clear that the preferred tilted configuration of a pair of chiral mesogens is not realized inside the x - z plane where all the molecules align parallel. Hence, one could expect to find more twisted phases formed by chiral molecules. In fact, Reinitzer¹ observed the reflection of blue light within a small temperature range when a sample of cholesterol benzoate was cooled down from the *clear* (isotropic) phase to a *cloudy* (cholesteric) phase. About a century later, Armitage and Price²² measured discontinuous density changes as a function of temperature for different cholesterol derivatives and confirmed thereby the existence of at least one *blue* phase. Exactly 100 years after Reinitzer's observation, Thoen²³ studied the isotropic-cholesteric phase transition performing high-resolution heat-capacity measurements and observed a series of phase transition between the isotropic and the cholesteric phase within a temperature range of less than 1 K. This was the proof for the existence of three blue phases predicted by Yang and Crooker²⁴ from optical measurements one year before. Moreover, Yang and Crooker²⁴ studied liquid crystal mixtures of chiral/achiral components and observed the formation of blue phases only for systems of high chirality (i.e., high mole fraction of the chiral component) within a narrow temperature range of few Kelvin. Up to date new materials have been synthesized^{25,26} and different techniques have been developed¹³ to stabilize blue phases over a much broader temperature range, including room temperature,

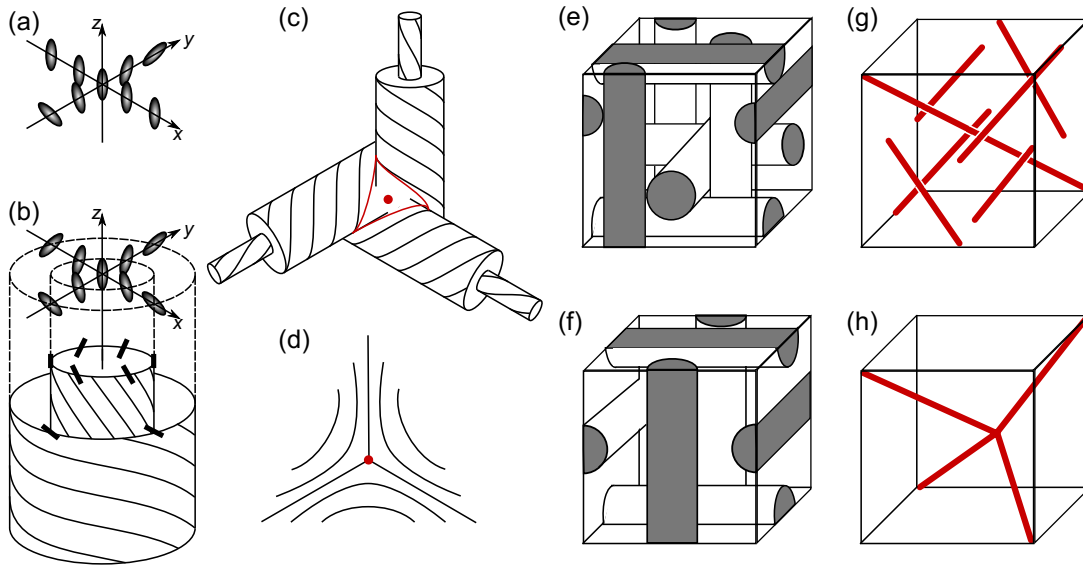


Figure 1.3. Schematic illustration of a (a) single twist helix, (b) double twist helix/cylinder, (c) orthogonal arrangement of three double twist cylinders, (d) topological defect, (e) face-centered cubic and (f) simple cubic arrangement of the double twist cylinders in a unit cell leading to the characteristic disclination lines in (g) and (h), respectively.

and provide thereby the practical applicability such as for fast light modulators or three-dimensional blue-phase lasers.²⁷

Using thermal^{22,23} or optical²⁴ techniques the presence of three different blue phases could be established. However, their molecular structure was still unclear. Theoretical studies based on Landau theory^{28–32} or lattice models^{33–37} predicted a cubic symmetry of the orientational order in blue phases. The lattice constant of the unit cell corresponds to the cholesteric pitch which is typical of the order of visible light. Hence, Bragg scattering of visible light is a useful experimental technique to identify the symmetry. Instead of reviewing a series of experiments which were performed to identify the structure of blue phases we refer the interested reader to the review by Crooker.³⁸

Experimentally, three blue phases with different symmetries have been found, i.e., face-centered cubic and simple cubic symmetry as well as an amorphous structure. Finally, the interplay between theory and experiment reveal that the molecular structure of blue phases. It can be explained by considering so-called *double-twist cylinders* as substructures of each blue phase.

Inside a double-twist cylinder, the molecules rotate in a helical fashion around a reference molecule in two directions instead of one as for the cholesteric helix. Hence, all molecules are tilted with respect to their neighbors [see Fig. 1.3(b)]. The spatial variation of the local director is given in cylindrical coordinates by

$$\hat{n}(\varrho) = -\sin(q_0\varrho)\hat{e}_\phi + \cos(q_0\varrho)\hat{e}_z \quad (1.4)$$

where ϱ is the radius of the cylinder and \hat{e}_ϕ and \hat{e}_z are basis vectors referring to the cylindrical coordinates ϕ and z , respectively. As illustrated in Fig. 1.3(b) the reference mesogen located at $\varrho = 0$ is pointing in the z -direction. However, the mesogens' orientation rotates as one increases ϱ [see also Eqn. (1.4)].

Because a double-twist cylinder cannot fill the entire space, a set of three cylinders orthogonal to each other is found in blue phases [see Fig. 1.3(c)]. However, this spatial arrangement of double-twist cylinders gives rise to the formation of singularities (i.e., defects) of the local director field $\hat{n}(\mathbf{r})$ [see Fig. 1.3(c) and (d)].^{6,39} If more than three double-twist cylinders are considered these point defects connect to a set and form defect lines, so-called *disclination* lines. These disclination lines extend over the entire volume forming a regular network. The periodicity of this disclination network gives rise to Bragg scattering. According to the specific stacking of double-twist cylinders, the disclination line-network changes. For example, in blue phase I the double-twist cylinders are stacked in a face-centered cubic fashion [see Fig. 1.3(e)] which gives rise to the formation of straight disclination lines that never intersect [see Fig. 1.3(g)]. In blue phase II, the tetrahedral conjunction of disclination lines [see Fig. 1.3(h)] is caused by a simple cubic stacking of the double twist cylinders [see Fig. 1.3(f)]. Finally, for the blue phase III it is assumed that the stacking of the double-twist cylinders is amorphous such that no regular network of disclination lines is formed.^{6,39} However, less is known about blue phase III compared with either blue phase I or II.

1.2 LIQUID CRYSTALS UNDER CONFINEMENT

Blue phases introduce one of the basic concepts in liquid crystal physics, i.e., the concept of topological defects and disclination lines. As already mentioned, defects are singularities of the local director field $\hat{n}(\mathbf{r})$. They are caused by the orientational frustration of the molecules which arise because of competing forces affecting the molecular orientation. These forces may arise because of the presence of two or more nematic domains with different directors which results in beautiful nematic textures (see Fig. 3.14 of Ref. 39), differently arranged double twist cylinders, external fields such as electric and magnetic fields, but also through surface forces. In fact, the interaction between liquid crystals and surfaces is of crucial importance. For example, planar, parallel aligned plates are used in the LCD to control the nematic order inside the LCD cell.

The key concept is the induction of liquid crystalline order locally in the vicinity of a surface. In ordered liquid crystals the order is caused by the long-range orientational correlation between molecules. Thus, locally induced order by a surface evolves through the entire system. In the vicinity of a surface, the alignment of the mesogens may or may not be controlled by the surface. If the mesogens are free to align, they form an angle between their longer axes and the surface. Faetti and Palleschi⁴⁰ investigated this angular dependence for the homologous series of 4-cyano-4'-(n-alkyl)biphenyl liquid crystals and concluded that with increasing aspect ratio the molecules align homeotropically (i.e. perpendicularly) whereas molecules

of smaller aspect ratio tend to align planar (i.e., parallel) to the surface. However, neither perfect homeotropic nor planar alignment was observed. In order to control the molecular orientation in the vicinity of a surface, plenty of chemical and mechanical techniques have been developed.⁴¹ Thus, surface anchoring is used to control, create, enhance, destroy, or manipulate liquid-crystalline order.

In particular, curved surfaces have fascinated researcher for decades.⁴² In order to study the effect of curvature on liquid-crystalline order, a nematic liquid crystal is confined to a cylindrical capillary.⁴² The symmetry of the cylindrical capillary is compatible with the global nematic director only for one specialized case, i.e., when the cylindrical axis is parallel to \hat{n}_0 . Except for this special case, a uniform alignment of mesogens cannot be achieved and topological defects occur. For homeotropic surface anchoring, four different structures are observed [see Fig. 1.4(a)-(d)].⁴²⁻⁴⁴ The stability of these defects depends on the size of the capillary, anchoring strength, and the elastic moduli of the liquid crystal. For small diameters of the capillary a radial-planar director field is observed. Here, the terminology *planar* refers to the two-dimensional nature of the local director. However, if the diameter of the capillary is increased then the radial-planar configuration becomes unstable and undergoes a transition to the preferred planar-polar configuration [see Fig. 1.4(b)]. For weaker surface anchoring the formation of escaped-radial configurations with and without defects is observed [see Fig. 1.4(c) and (d)] where the terminology *escape* refers to the directors escape to the third dimension.²¹ If the anchoring is planar-circular, then similar defect structures arise [see Fig. 1.4(e) and (g)].^{42,43} However, the configuration of the local director is different if the surface anchoring is planar-circular instead of homeotropic. Finally, planar-directional surface anchoring may be used to enhance nematic order [see Fig. 1.4(h)]. Because optical, electrical, and mechanical properties depend on the specific director field, quantities such as surface anchoring, anchoring strength, and the diameter of the capillary are utilized in order to tune these properties.

This example of nematic liquid crystals confined to a cylindrical geometry demonstrates the complexity and the broad variety of topologies which may occur. Of course, replacing the cylindrical capillary by more complex channels and/or introducing heterogeneous surface anchoring results in much more complex director fields and defects.¹⁷ However, these defects are either point defects or straight disclination lines aligned parallel to the capillary's axis. In order to create more complex networks made of disclination lines, one needs to replace the nematic liquid crystal by a liquid-crystalline phase with a more complex symmetry, e.g., blue phases. Fukuda and Žumer^{45,46} reported recently a host of novel defect structures which arise if a blue phase is placed between two plates. One of the central goals of this work is to investigate the influence of surface anchoring, channel size, and shape on the formation of defect structures in a blue phase confined to a mesoscopic channel.

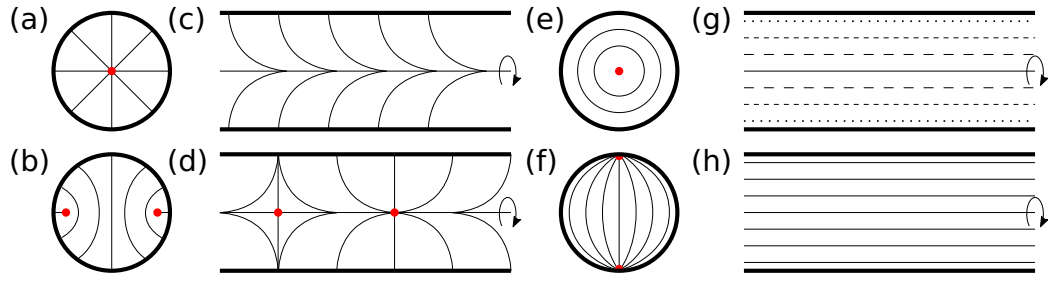


Figure 1.4. Configurations of the local director field which arise in a nematic liquid crystal confined to cylindrical capillary that anchors the mesogens in a homeotropic (a)-(d), circular planar (e)-(g), or directional planar (h) fashion: (a) planar-radial, (b) planar-polar, (c) escaped-radial, (d) escaped-radial with point defects, (e) planar-circular, (f) circular-bipolar, (g) escaped-twisted, and (h) directional-planar configuration.⁴²⁻⁴⁴ Director-field lines indicate the orientation of the mesogens and red dots mark topological defects. In (g), dotted director-field lines indicate a perpendicular alignment to the paper plane whereas dashed director-field lines indicate a certain angle closed between the local director and the paper plane.

1.3 LIQUID-CRYSTALLINE DISPERSION

Liquid-crystal interactions with curved surfaces play a crucial role in the process of colloidal self-assembly in liquid-crystalline host phases. This very active field of complex soft matter fascinates the scientific community for the last two decades.⁹ Colloids suspended in a nematic phase perturb the overall order locally in the vicinity of their surfaces such that defects arise.⁴⁷ These perturbations cause long-range inter-colloidal forces driving the colloidal self-assembly in a directed manner.⁴⁷ In fact, depending on the specific anchoring scenario colloids self-assemble in straight chains parallel to \hat{n}_0 ,^{10,48} in zig-zag chains perpendicular to \hat{n}_0 ,^{48,49} or into chains tilted with respect to \hat{n}_0 .^{10,50} Clearly, in order to study the self-assembly mechanism one needs to understand how the nematic order is perturbed by colloids with different surface anchoring.

The specific director field configuration which arises due to the presence of a spherical colloid depends on the nature of the colloidal surface anchoring.¹⁰ In fact, for a homogeneous surface anchoring, the global preferred orientation cannot be realized all across the colloidal surface. Hence, topological defects arise if the direction of the surface anchoring is locally perpendicular to \hat{n}_0 . For example, colloids which anchor the mesogens in a locally planar fashion cause the formation of two point defects at the colloidal surface located at the north and south pole characterized via $\hat{n}_0 \cdot \hat{s} = \pm 1$ (\hat{s} is the surface normal), respectively. The director-field configuration of such a point defect is termed Boojum defect, thus the colloid is known as Boojum colloid [see Fig. 1.5(a)].¹⁰ However, if the locally planar surface anchoring is replaced by weakly homeotropic anchoring then the formation of a ring defect is observed. This as surface-ring termed disclination loop is located at the colloidal surface and surrounds it around the equator ($\hat{n}_0 \cdot \hat{s} = 0$) [see Fig. 1.5(b)]. It can be rationalized

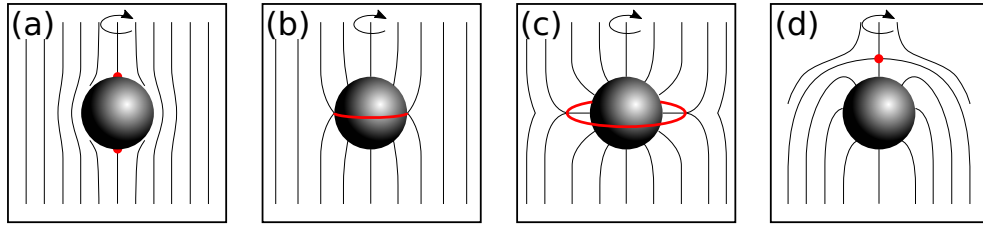


Figure 1.5. Director-field configuration of a nematic liquid crystal in the vicinity of spherical a colloid with (a) strong planar, (b) weak homeotropic, and (c)-(d) strong homeotropic surface anchoring.¹⁰ Topological defects and disclination lines are illustrated by red dots and red lines, respectively. We emphasize that although (b) and (c) seem to have similar director-field topologies, their defects differ in topological charges (i.e., $q = -\frac{1}{4}$ and $q = -\frac{1}{2}$, respectively) and physical nature (i.e., surface and bulk defect, respectively).

by searching for the maximum competition between \hat{n}_0 and the surface anchoring which is located at the equator in case of the considered homeotropic surface anchoring. With increasing anchoring strength the ring defect is pushed away from the colloidal surface and a disclination loop encircles the colloidal particle around its equator [see Fig. 1.5(c)]. Thus, these colloids are termed Saturn ring colloids.¹⁰ We emphasize that although the defect topology of the surface-ring and Saturn ring colloids are similar, their nature differs. The disclination loop around the Saturn ring colloid is classified as a “bulk” defect and arises because of two competing forces acting on liquid crystal molecules in the bulk. On the other hand, defects observed at the surface of the colloid, for example, the Boojum or surface-ring colloids indicate orientational frustration of the molecular alignment at a surface. In order to study such perturbations experimentally, colloidal inclusions are placed between two glass plates. Depending on the colloidal size, anchoring strength, but also the separation distance of the glass plates a second configuration of the director field may be observed for strong homeotropic anchoring, i.e., the hedgehog defect [see Fig. 1.5(d)].^{10,49}

To understand the colloidal self-assembly in a liquid-crystalline host phase it is important to realize that every local deviation of the mesogens’ orientations from \hat{n}_0 stores elastic energy of the nematic field which is stabilized by the colloidal particle. If two or more colloids are sufficiently close together this elastic energy may be released partially. Clearly, in the equilibrium configuration the colloids release the maximum amount of stored energy whereas other configurations are energetically unfavorable. This gives rise to effective interactions between a pair of colloids mediated by the perturbation of the overall order. In order to study and quantify the effective interactions we use the Landau-de Gennes free energy approach. In fact, the Landau-de Gennes free energy is a phenomenological and continuum description of liquid-crystalline phases. More specifically, it is used successfully as a free energy functional which is minimized numerically to obtain the director field and local nematic order parameter in the vicinity of colloids.^{48,49} Because the Landau-de Gennes theory lacks any molecular foundation a quantitative comparison with molecule-based simulations

turns out to be difficult. In this work we derive a molecule-based expression of the Landau-de Gennes free energy. In order to test our expression we perform Monte Carlo simulations to investigate and analyze the local perturbations which arise in the vicinity of a pair of Boojum colloids. Boojum colloids have been studied in experiments^{10,50} and within the framework of Landau-de Gennes calculations.⁵¹ Hence, Boojum colloids are a useful example to validate our molecular approach.

The effective inter-colloidal interactions are mediated by the liquid-crystalline host phase. Hence, the replacement of the nematic host phase (e.g., by a cholesteric phase) causes other effective interactions which eventually lead to novel structures.⁵²⁻⁵⁵ As already explained and for the sake of simplicity and efficiency the Landau-de Gennes theory is usually the method of choice to study such phenomena. However, it is not possible to describe all liquid crystalline phases within the framework of the Landau-de Gennes theory. The validity of the theory is limited to phases of homogeneous density. However, recent studies of Zuhail *et al.*⁵⁶⁻⁵⁸ on colloidal inclusions in smectic A phases reveal interesting features. Because of the additional degree of order (i.e., positional long-range order in one dimension) of the smectic A phase in contrast to the nematic phase, the separation distance and also the angle between the colloids' distance vector and \hat{n}_0 are different in the smectic A phase. In order to study the orientational but also positional perturbations caused by a spherical colloidal particle in a smectic A phase we develop a novel model potential. Despite the small aspect ratio (i.e., ≈ 2) our model is capable of forming the nematic and smectic A phase for a suitable choices of thermodynamic conditions and reproduce dynamic and elastic properties adequately. We perform Monte Carlo simulations to study the perturbations caused by a colloid across the nematic-smectic A phase transition.

1.4 GOAL OF THIS THESIS

In this work, we focus on the impact of curved surfaces on liquid-crystalline order. Liquid crystal molecules may align on the concave (e.g., inside a cylindrical capillary) and the convex side (e.g., at the spherical colloid) of a curved surface. In order to investigate both cases, we perform Monte Carlo simulations of colloidal dispersions in a liquid-crystalline host phase and of liquid crystals confined to a mesoscopic capillary.

The first part of this work is based on an earlier article⁵⁹ where a model system is introduced to investigate the perturbations of the liquid-crystalline order in the vicinity of a single colloid immersed in a nematic host phase. Subsequently, we extend the model system by including a second colloid to study the *effective* interactions which arise if the colloids approach each other. In order to quantify perturbations of liquid-crystalline order and derive an *effective* pair potential, we develop a novel method where we link the microscopic to the well known macroscopic/phenomenological treatment of the problem (see [Chapter 5](#)).

In the second part of this thesis, we replace the nematic phase by the smectic A phase modeled by a novel potential. The additional degree of order (i.e., the positional long-range order in one direction) is perturbed by the colloids as well. We compute local quantities such as density, order parameter, and director in the vicinity of a single colloid across the nematic-smectic A phase transition in order to get a deeper understanding of the problem. Because our model potential is sufficiently realistic we can compare our results with recently performed experiments^{57,58} (see [Chapter 6](#)).

Finally, in the third part of this thesis, we investigate the impact of mesoscopic channels on liquid-crystalline order. In order to do this, we vary the size, shape, and surface anchoring of the channel and study the local director field of the chiral liquid crystal. This is motivated by recent studies of Fukuda and Žumer.^{45,46} These authors demonstrated the broad variety of novel defect structures exhibited by chiral blue phases confined to a slit pore. For a blue phase confined to a mesoscopic channel, we observe a whole “zoo” of novel defect structures (see [Chapter 7](#)).

Part II

THEORY

Everyday phenomena such as the melting of ice, boiling water, mixing and decomposition of multicomponent liquids, or the propagation of heat are well understood and adequately described within the framework of thermodynamics. Thermodynamics is one of the five pillars of modern physics (others are classical mechanics, electrodynamics, the theory of relativity, and quantum mechanics). Based on fundamental postulates, the so-called laws of thermodynamics, it describes macroscopic systems via few macroscopic variables such as temperature, density, pressure, etc. The hallmark of thermodynamics is generality, first in the sense that it can be applied to all types of macroscopic systems, and second in the sense that numerical values for observables are not predictable within the theory. Instead, thermodynamics establish relations between apparently unrelated properties. The numerical determination of any observable requires a numerical input which can be obtained experimentally.

Because a big part of thermodynamics was developed in the 19th century, it contains no information about the composition of matter and treats it as a macroscopic and continuous object. This point of view changed in the second half of 19th century after the beginning and confirmation of atomistic theories. The main idea of these theories is that the continuous composition of matter and energy is an illusion. Instead of that, on a length scale of 10^{-7} cm the matter consists of a huge number of discrete particles, i.e., atoms.[‡]

The description of such a system involves dynamics of an N -body system. The evolution in time of each of the N particles is determined by quantum mechanical or classical equations of motions. In principle, the description of phenomena on a macroscopic and microscopic level is equivalent. However, the formalism of the laws derived for these two levels is so different that the relation between corresponding macroscopic and microscopic quantities is not obvious. The bridge between these different formalism is provided by statistical physics.

The state of a piece of matter is determined in terms of positions and momenta (as well as orientations and corresponding angular momenta in the case of anisotropic molecules). However, because of the enormous number of atoms/molecules (approximately 10^{23}) this description is on the one hand too detailed and on the other hand cannot be accomplished. Even if a supercomputer could determine and record positions and momenta of N particles as a function of time, the initial conditions are still unknown.

Fortunately, the knowledge of specific initial conditions is not necessarily required. A macroscopic experiment that is repeated many times reproduces the results per-

[‡] After the discovery of a tunnel effect microscope in 1980s, last doubts about the existence of atoms have been lifted. This technique allows not only the observation of atoms at a surface but also their manipulation. In fact, it was demonstrated that individual atoms can be picked up and displaced.⁶⁰

fectly with respect to a certain measuring inaccuracy. Although the initial conditions of each experiment are equal on the macroscopic level they differ microscopically. In fact, an enormous number of molecular configurations exists that correspond to macroscopic constraints at the beginning of the experiment. The experimental evidence shows that on the macroscopic level the system is insensitive to different microscopic initial conditions.

Hence, the idea is that all different microscopic configurations compatible with macroscopic constraints are realized with a certain probability. Mathematically, this can be realized by attaching a weighting to every microscopic state which we shall specify below. Thus, any mechanical macroscopic observable is understood as its corresponding microscopic quantity averaged over all microscopic states and weighted properly.

Finally, we arrive at a point where a many-body system can be described statistically in terms of distributions of microscopic states and their probabilities in order to determine macroscopic properties of that system. In this chapter, we focus on the formalism of statistical physics and introduce basic concepts, ensemble theory, and the Monte Carlo simulation used as a numerical method to solve multidimensional integrals.

2.1 BASIC CONCEPTS

The goal of this work is a description of systems composed of N liquid-crystal molecules (i.e., mesogens) within in the framework of statistical physics. As introduced in [Chapter 1](#), mesogens are particles of uniaxial (i.e., linear) symmetry. Hence, we consider two rotational and three translational degrees of freedom. The microscopic state of the system is defined by the set of generalized coordinates $\mathbf{r}^N = \{\mathbf{r}_1, \dots, \mathbf{r}_N\}$, corresponding momenta $\mathbf{p}^N = \{\mathbf{p}_1, \dots, \mathbf{p}_N\}$, Euler angles $\boldsymbol{\omega}^N = \{\boldsymbol{\omega}_1, \dots, \boldsymbol{\omega}_N\}$ describing orientations of the mesogens [$\boldsymbol{\omega}_i = (\phi_i, \theta_i)$ for uniaxial particles], and angular momenta $\mathbf{p}_\omega^N = \{\mathbf{p}_{\omega_1}, \dots, \mathbf{p}_{\omega_N}\}$ conjugate to $\boldsymbol{\omega}^N$. Hence, the phase vectors \mathbf{r}^N , \mathbf{p}^N , $\boldsymbol{\omega}^N$, and \mathbf{p}_ω^N span a 10^N -dimensional phase space where every point given by $\boldsymbol{\pi} \equiv \{\mathbf{r}^N, \mathbf{p}^N, \boldsymbol{\omega}^N, \mathbf{p}_\omega^N\}$ corresponds to one microscopic state.⁶¹

Clearly, the system changes its microscopic state with time. Hence, the evolution of the system in time is described by the phase space trajectory which is defined as the set of microscopic states $\boldsymbol{\pi}(t) \equiv \{\mathbf{r}^N(t), \mathbf{p}^N(t), \boldsymbol{\omega}^N(t), \mathbf{p}_\omega^N(t)\}$ the system assumes at time t . In fact, using Hamilton's equations of motion it is possible to compute every future microscopic state for given initial conditions $\boldsymbol{\pi}(0)$ and a given Hamiltonian $\mathcal{H} = \mathcal{H}(\boldsymbol{\pi}(t))$ which describes the total energy of the system. If every microscopic state is uniquely defined by $\boldsymbol{\pi}(t)$ then every observable \mathcal{A} may be written as a function of the phase-space trajectory $\mathcal{A} = \mathcal{A}(\boldsymbol{\pi}(t), t)$. However, because of the time dependence and the huge number of particles an exact computation of \mathcal{A} is not practicable. On the other hand, the determination of an exact solution is not ne-

cessary. Because properties measured in experiments are represented by averaged values we focus on the description of time averages

$$\langle \mathcal{A} \rangle_t = \lim_{\tau \rightarrow \infty} \frac{1}{\tau} \int_0^\tau dt \mathcal{A}(\boldsymbol{\pi}(t), t) \quad (2.1)$$

that are denoted by “ $\langle \cdot \rangle_t$ ”. In the limit of an infinite measuring time τ the dependence on initial conditions of $\langle \mathcal{A} \rangle_t$ vanishes. This is a fundamental postulate of statistical physics and is known as ergodic hypothesis. The ergodic hypothesis implies that every microscopic state of a system is realized over time.⁶¹

We divide the phase space into infinitesimal volume elements $d\boldsymbol{\pi} \equiv \{d\mathbf{r}^N, d\mathbf{p}^N, d\boldsymbol{\omega}^N, d\boldsymbol{p}_\omega^N\}$. Let $q_t(\boldsymbol{\pi}, \tau)$ be the unnormalized distribution function, then

$$q_t(\boldsymbol{\pi}, \tau) d\boldsymbol{\pi} \quad (2.2)$$

represents the number of states the system assumes in the volume element $d\boldsymbol{\pi}$ around a point $\boldsymbol{\pi}$ at time τ .⁶¹ However, as τ increases, the number of states increases as well such that q_t diverges for infinite observation time τ . Hence, it is convenient to introduce

$$\hat{q}_t(\boldsymbol{\pi}, \tau) = \frac{q_t(\boldsymbol{\pi}, \tau)}{\int d\boldsymbol{\pi} q_t(\boldsymbol{\pi}, \tau)} \quad (2.3)$$

which is normalized according to

$$1 = \int d\boldsymbol{\pi} \hat{q}_t(\boldsymbol{\pi}, \tau) \quad (2.4)$$

and can be interpreted as the probability to locate the system in the interval $[0, \tau]$ in the volume element $d\boldsymbol{\pi}$ around the point $\boldsymbol{\pi}$. For the determination of an averaged quantity, it is irrelevant when a certain value was assumed, such that we may write

$$\langle \mathcal{A} \rangle_t = \int d\boldsymbol{\pi} \hat{q}_t(\boldsymbol{\pi}, \tau) \mathcal{A}(\boldsymbol{\pi}) \quad (2.5)$$

where \mathcal{A} is not an implicit function of time anymore.⁶¹ In molecular dynamics simulations, where the equations of motions are integrated numerically for a sufficiently long observation time, Eqn. (2.5) provides a route to determine $\langle \mathcal{A} \rangle_t$.⁶²

An alternative way to compute averages without knowledge of the initial conditions is based on the concept of statistical ensembles. A statistical ensemble is a set of imaginary copies of a system. Each of these copies is subject to the same macroscopic conditions, i.e., temperature, pressure, etc. and represents one microscopic state of the system. The ergodic hypothesis says that a system realizes all of the microscopic states for a sufficiently long time such that an ensemble contains the entire time evolution of the system. Hence, we may replace the time average by the ensemble

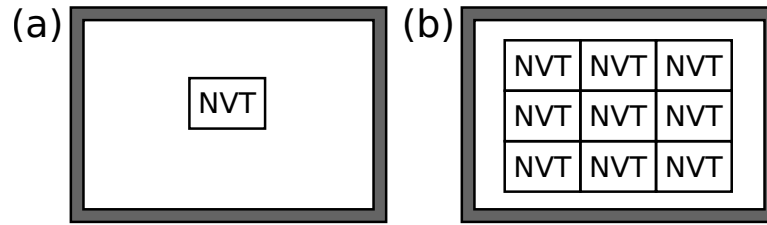


Figure 2.1. Scheme of (a) closed system at thermal equilibrium with a heat reservoir (see text) and (b) canonical ensemble of the closed system presented in (a). Isolating and heat conducting walls are marked by gray shapes and black lines, respectively.

average, $\langle \mathcal{A} \rangle_t = \langle \mathcal{A} \rangle$. We introduce the distribution function q_e and the probability density

$$\widehat{q}_e(\boldsymbol{\pi}, t) = \frac{1}{\mathcal{Q}} q_e(\boldsymbol{\pi}, t) \quad (2.6)$$

for an ensemble in a similar way as for their time analogs [see Eqn. (2.2) and Eqn. (2.3)]. Here,

$$\mathcal{Q} = \int d\boldsymbol{\pi} q_e(\boldsymbol{\pi}, t) \quad (2.7)$$

is the normalization factor representing the number of the imaginary copies of the system.⁶¹ The ensemble average denoted by “ $\langle \cdot \rangle$ ” of an observable \mathcal{A} is then given by

$$\langle \mathcal{A} \rangle = \int d\boldsymbol{\pi} \widehat{q}_e(\boldsymbol{\pi}, t) \mathcal{A}(\boldsymbol{\pi}). \quad (2.8)$$

We emphasize the equivalence of Eqn. (2.5) and Eqn. (2.8) which is explained by the ergodic hypothesis.⁶¹ Furthermore, we focus in this work on equilibrium states where $d\mathcal{A}/dt = 0$ such that the probability density loses its explicit time dependence, thus, $\widehat{q}_e(\boldsymbol{\pi}, t) \rightarrow \widehat{q}_e(\boldsymbol{\pi})$.

2.2 CANONICAL ENSEMBLE

As shown in the previous section the probability density $\widehat{q}_e(\boldsymbol{\pi})$ is of vital importance in determining the ensemble average of an observable \mathcal{A} . In this section we focus on the description of $\widehat{q}_e(\boldsymbol{\pi})$ as well as other quantities relevant for the determination of $\langle \mathcal{A} \rangle_e$. In fact, instead of giving a detailed derivation of $\widehat{q}_e(\boldsymbol{\pi})$ we outline important steps of that derivation and refer the interested reader to text books.^{61,63–65}

We consider a system where the number of mesogens N and its volume V is fixed. The system is closed in the thermodynamic sense such that heat transfer is possible across the heat conducting walls whereas any mass transport or volume change are impossible. Furthermore, we place the system to a heat bath [see Fig. 2.1(a)]. Hence, at equilibrium the system assumes the temperature T of the heat reservoir whose

size is supposed to be much larger than that of subsystem. Moreover, the heat bath is insulated against its surroundings such that its energy \mathcal{E} is fixed.

The macroscopic state of the subsystem is determined by N , V , and T . Microscopically, an overwhelmingly large number of states $\{\pi\}$ exists such that each of these states is compatible with macroscopic constraints. In order to consider all possible microscopic states $\{\pi\}$ we follow a *gedankenexperiment* originally introduced by Gibbs.⁶⁴

We consider a huge number of $Q - 1$ identical and virtual copies of our subsystem such that the original subsystem is surrounded by its copies [see Fig. 2.1(b)]. Moreover, all subsystems (i.e., the original and its copies) are in thermal contact and exchange heat among themselves. Hence, at equilibrium all subsystems have the same macroscopic state, i.e., fixed N , V , and T . Together the set of Q subsystems and the heat reservoir form the so-called *canonical*- or *NVT*-ensemble (other ensembles are specified by a different set of thermodynamic variables and are introduced in Sec. 2.4 and Sec. 2.5).

Although the entire ensemble is specified as one macroscopic state, its microscopic composition is not uniform. At equilibrium and for a given N , V , and T , the ensemble is distributed according to microscopic states $\{\pi\}$ the subsystems assume. At any instant, the point π of the phase space, that is occupied by one of the N -body subsystems, makes this particular system distinct and distinguishable from the others. Clearly, on the macroscopic scale we can not distinguish between states π_i and π_j . We discriminate the subsystems on their energetic level given by the Hamiltonian $\mathcal{H}(\pi)$ such that it is conceivable that one or more subsystems are characterized by the same energy. Hence, a distribution function $q_{NVT}(\pi)$ exists denoting the occupation number of systems at the energetic level. Any specific distribution $q_{NVT}(\pi)$ can be realized in^{63,64}

$$w(q_{NVT}) = \frac{Q!}{\prod_{\pi} q(\pi)!} \quad (2.9)$$

different ways where $q(\pi) \propto \mathcal{H}(\pi)$. Furthermore, the distribution function $q_{NVT}(\pi)$ is subjected to

$$Q = \int d\pi q_{NVT}(\pi) \quad (2.10)$$

and

$$\mathcal{E} = \int d\pi \mathcal{H}(\pi) q(\pi) \quad (2.11)$$

accounting for a constant number of ensemble members Q and constant total energy of the ensemble \mathcal{E} .

Because of the last constraint, we may understand the entire canonical ensemble consisting of Q independent systems as an isolated system. Consequently, applying the *principle of equal a priori probability* we expect that all possible distributions $\{q_{NVT}(\pi)\}$ are realized with equal probability. However, it can be demonstra-

ted^{61,63–65} that at equilibrium and for an arbitrary large Q (in fact, Q can be made infinite in our *gedankenexperiment*) a distribution $q_{NVT}^*(\boldsymbol{\pi})^\ddagger$ exists such that $w(q_{NVT}^*)$ overwhelms other values of $\{w(q_{NVT})\}_{q_{NVT} \neq q_{NVT}^*}$.

This particular, so-called most probable, distribution $q_{NVT}^*(\boldsymbol{\pi})$ maximizes the entropy.^{61,63} Hence, the determination of $q_{NVT}^*(\boldsymbol{\pi})$ requires a method that maximizes a function with many variables and two constraints, namely $Q = \text{const.}$ and $\mathcal{E} = \text{const.}$ This can be achieved by the method of Lagrange undefined multipliers. The determination of these multipliers is eventually obtained by the normalization of the distribution function and from the comparison with the phenomenological thermodynamics, more precisely, the entropy.^{61,63} In order to link microscopic (i.e., statistical) and macroscopic description of thermodynamics one needs to apply one of the fundamental postulates of statistical physics by Gibbs. It says that an ensemble average of any microscopic observable corresponds to its macroscopic observable.⁶³

Finally, one obtains the most probable distribution^{61,66}

$$q_{NVT}^*(\boldsymbol{\pi}) \propto \exp[-\beta_B \mathcal{H}(\boldsymbol{\pi})]. \quad (2.12)$$

and the probability density^{61,66}

$$\begin{aligned} \hat{q}_{NVT}(\boldsymbol{\pi}) &= \frac{\exp[-\beta_B \mathcal{H}(\boldsymbol{\pi})]}{1/h^{5N} N! \int d\boldsymbol{\pi} \exp[-\beta_B \mathcal{H}(\boldsymbol{\pi})]} \\ &= \frac{\exp[-\beta_B \mathcal{H}(\boldsymbol{\pi})]}{Q_{NVT}} \end{aligned} \quad (2.13)$$

of the NVT -ensemble for N identical and undistinguishable mesogens of uniaxial symmetry. Here h is Plank's constant introduced to keep the denominator dimensionless, $\beta_B = 1/k_B T$, and k_B is the Boltzmann constant.⁶¹ The factor $1/N!$ takes into account the mesogens' indistinguishability and the exponent $5N$ the 5 degrees of freedom (three translational and two rotational) of N uniaxial mesogens. The canonical partition function Q_{NVT} [see Eqn. (2.13)] contains the entire information of a system and is therefore the key quantity in statistical physics. If the partition function is known, the computation of the probability density and finally the ensemble average is straightforward.

The Hamiltonian [see Eqn. (2.13)] for a uniaxial mesogen is given by

$$\mathcal{H}(\boldsymbol{\pi}) = \sum_{i=1}^N \frac{\mathbf{p}_i^2}{2m} + \sum_{i=1}^N \sum_{\alpha=x,y} \frac{\mathcal{L}_{i,\alpha}^2}{2I} + U(\mathbf{r}^N, \boldsymbol{\omega}^N), \quad (2.14)$$

where the terms on the right-hand side describe translational and rotational kinetic and configurational contributions, respectively. Here, m is the mesogens' mass, I the scalar moment of inertia, and $\mathcal{L}_{i,\alpha}$ is the component of the angular momentum referring to the body-fixed axis α of the particle i . For particles with isotropic shape (i.e., spheres) momenta \mathbf{p}_i are independent of \mathbf{p}_j (for all $i \neq j$) and of \mathbf{r}^N such that the

‡ Here, a star is introduced to mark the most probable distribution and should not be confused with the notation used later for chirality.

division of the Hamiltonian immediately results in the factorization of the partition function \mathcal{Q}_{NVT} into a kinetic contribution and the configurational integral. However, as discussed by Gray and Gubbins⁶⁶ because $\mathcal{L}^N = \mathcal{L}^N(\omega^N, \mathbf{p}_\omega^N)$ a similar factorization of \mathcal{Q}_{NVT} is achieved after the transformation $\mathbf{p}_\omega^N \rightarrow \mathcal{L}^N$. Hence, we cast the partition function as

$$\mathcal{Q}_{NVT} = \frac{1}{h^{5N} N!} \int d\mathbf{r}^N d\mathbf{p}^N d\omega^N |J^{(N)}| d\mathcal{L}^N \exp \left[-\beta_B \mathcal{H}(\mathbf{r}^N, \mathbf{p}^N, \omega^N, \mathcal{L}^N) \right] \quad (2.15)$$

where $|J^{(N)}|$ is the magnitude of the Jacobian of this transformation. Because of the independence of \mathcal{L}_i on \mathbf{p}_{ω_j} , for all $i \neq j$, $J^{(N)} = J_1 J_2 \dots J_N$ with

$$J_i = \frac{\partial(p_{\phi_i} p_{\theta_i})}{\partial(\mathcal{L}_{x_i} \mathcal{L}_{y_i})} = \sin \theta_i. \quad (2.16)$$

Furthermore, we substitute

$$d\hat{\mathbf{u}}_i = \sin \theta_i d\theta_i d\phi_i \quad (2.17)$$

where

$$\hat{\mathbf{u}}_i = (\sin \theta_i \cos \phi_i, \sin \theta_i \sin \phi_i, \cos \theta_i)^T \quad (2.18)$$

is a unit vector specifying the orientation of the mesogen i . Thus, we factorize the partition function as

$$\mathcal{Q}_{NVT} = \mathcal{Q}_{\text{trans}} \mathcal{Q}_{\text{rot}} \mathcal{Q}'_{\text{config}} \quad (2.19)$$

where the translational contribution

$$\mathcal{Q}_{\text{trans}} = \frac{1}{\lambda^{3N}} \quad (2.20)$$

and the rotational contribution

$$\mathcal{Q}_{\text{rot}} = \frac{1}{\lambda^{2N}} \left(\frac{I}{m} \right)^N \quad (2.21)$$

are obtained analytically. Here, $\lambda = \sqrt{h^2/2\pi m k_B T}$ is the thermal de Broglie wave length. The configurational contribution is given by

$$\mathcal{Q}'_{\text{config}} = \frac{1}{N! 2^N} \iint d\mathbf{r}^N d\hat{\mathbf{u}}^N \exp \left[-\beta_B U(\mathbf{r}^N, \omega^N) \right] = \frac{1}{N! 2^N} \mathcal{Q}_{\text{config}} \quad (2.22)$$

where $\mathcal{Q}_{\text{config}}$ is the configurational integral and the factor 2^N corrects the double counting of equivalent orientations $\hat{\mathbf{u}}_i$ and $-\hat{\mathbf{u}}_i$ caused by the head-tail symmetry of the mesogens.⁶⁷ Hence, the canonical partition function is given by⁶⁶

$$\mathcal{Q}_{NVT} = \frac{1}{2^N N! \lambda^{5N}} \left(\frac{I}{m} \right)^N \mathcal{Q}_{\text{config}} \quad (2.23)$$

and the ensemble average of \mathcal{A} is obtained via

$$\langle \mathcal{A} \rangle = \frac{1}{\mathcal{Q}_{NVT}} \iint d\mathbf{r}^N d\hat{\mathbf{u}}^N \exp \left[-\beta_B U(\mathbf{r}^N, \hat{\mathbf{u}}^N) \right] \mathcal{A}(\mathbf{r}^N, \hat{\mathbf{u}}^N). \quad (2.24)$$

2.3 MONTE CARLO METHOD

The integration over the configurational space $\Omega \equiv \{\mathbf{r}^N, \hat{\mathbf{u}}^N\}$ of a multidimensional integral such as the one presented in Eqn. (2.24) is accomplishable only for few exceptional cases, e.g., for an ideal gas or two-dimensional Ising magnet.⁶⁸ Therefore, we have to solve this integral numerically. Conventional numerical methods such as Simpson's rule or trapezoidal integration become inefficient as the dimension of the integral increases. This is because the number of points at which the integrand has to be evaluated is equal $w^{\mathcal{D}}$ where w is the number of increments and \mathcal{D} denotes the dimension of the integral (i.e., $\mathcal{D} = 5N$).⁶⁹ Hence, the inefficiency of conventional methods can be demonstrated by a simple calculation. Let us consider a system composed of 100 particles. Taking $w = 5$, one would be confronted with the evaluation of the integrand at approximately 3.1×10^{349} points.

Moreover, the generation of Ω according to a regular grid is not advisable. It can be demonstrated that because of the high dimension of the configurational space an overwhelmingly large number of generated points are located at the surface of the configurational space.^{70,71} Hence, the sampling of the hyperspace is inadequate.

To tackle this problem different techniques such as polynomial based integration or Monte Carlo (MC) method have been developed.⁷² Here we focus on evaluating multidimensional integrals via the MC method, more precisely, the MC importance sampling algorithm introduced by Metropolis *et al.*⁷³

2.3.1 Monte Carlo simulation

Because the MC method is a numerical technique we discretize the multidimensional configurational integral in Eqn. (2.24) according to

$$\langle \mathcal{A} \rangle = \lim_{M \rightarrow \infty} \sum_{m=1}^M \mathcal{A}(\Omega_m) \hat{q}_{NVT}(\Omega_m) \quad (2.25)$$

where M is the number of configurations $\Omega_m = \{\mathbf{r}_{m_1}^N, \omega_{m_2}^N\}$ and subscripts m_1 and m_2 indicate that \mathbf{r}^N and ω^N are independent of each other. Hence, the idea behind the MC technique is to generate a set of configurations $\Omega = \{\Omega_m\}$ and estimate the ensemble average according to Eqn. (2.25).

Because a regular generation of Ω is inefficient, we focus on randomly generated configurations. This guarantees the sampling of the configurational space without any bias. In principle, one would generate a sufficient large number M of configurations Ω_m , compute $\mathcal{A}(\Omega_m)$, and average it according to its probability $\hat{q}_{NVT}(\Omega_m)$ in order to evaluate $\langle \mathcal{A} \rangle$.

This naive MC approach, however, has two problems. First, because of the infinite number of states, the system may assume, the configurational space is too large to be sampled completely. Additionally, most of these states are not representative and can be neglected because of a vanishing probability $\hat{q}_{NVT}(\Omega_m)$. Hence, M has to be huge to sample a representative set of states. Second and the most serious problem concern the application of Eqn. (2.25). It requires the knowledge of $\hat{q}_{NVT}(\Omega_m)$ which is not given *a priori*. More specifically, $\hat{q}_{NVT}(\Omega_m)$ depends on the partition function Q_{NVT} which involves a configurational integration as illustrated in Eqn. (2.36). Hence, because Q_{NVT} is unknown, $\hat{q}_{NVT}(\Omega_m)$ remains undetermined.

Alternatively, one could try to generate a set of representative configurations according to their probability $\hat{q}_{NVT}(\Omega_m)$. This would allow us to replace Eqn. (2.25) by an arithmetic average according to^{62,69-71}

$$\langle \mathcal{A} \rangle = \lim_{M \rightarrow \infty} \frac{1}{M} \sum_{m=1}^M \mathcal{A}(\Omega'_m) \quad (2.26)$$

where a prime was added to Ω_m to remind the reader that configurations $\Omega' = \{\Omega'_m\}$ were generated according to their probability. Of course, practically M cannot be infinite and therefore, we assume M is large enough.

The careful reader may now wonder about the advantage of the *importance sampling* method over the naive one presented in Eqn. (2.26) and Eqn. (2.25), respectively. On the one hand, the method of importance sampling allows the computation of $\langle \mathcal{A} \rangle$ as an arithmetic average. On the other hand, for the generation of neighboring configurations Ω'_m and Ω'_{m+1} absolute probabilities $\hat{q}_{NVT}(\Omega'_m)$ and $\hat{q}_{NVT}(\Omega'_{m+1})$, which are required for the naive MC but remain undetermined, are irrelevant in the importance sampling MC. As we shall demonstrate in the following section, relative probabilities are used to generate a new configuration Ω'_{m+1} from the old one Ω'_m . This is a direct consequence of the *principle of detailed balance* which we discuss in the following section.⁷⁰ Hence, in order to compute $\langle \mathcal{A} \rangle$ from Eqn. (2.26) we focus on the generation of a chain of representative configurations Ω' .

2.3.2 Importance sampling

Importance sampling is a technique which has its roots in statistics and describes the generation of representative states. Here, the term “representative state” refers to states of high probability $\hat{q}_{NVT}(\Omega'_m)$. More generally, importance sampling can be used to generate states distributed differently. In the MC simulation a Markov process realized by the Metropolis algorithm⁷³ generates a set of representative states according to the Boltzmann distribution. Hence, one generates a Markov chain $\Omega' = \{\Omega'_m\}$, for $m = 1, 2, \dots, M$ such that every new state is generated from the state before. The probability to create a new state depends on the energy difference of

these two states. The time evolution (referring to MC time τ_{MC}) of the Markov chain is given by the Chapman-Kolmogoroff master equation⁷¹

$$\frac{\partial \hat{q}_{NVT}(\mathbf{\Omega}_n, \tau_{\text{MC}})}{\partial \tau_{\text{MC}}} = - \sum_{n \neq m} [\hat{q}_{NVT}(\mathbf{\Omega}_n, \tau_{\text{MC}}) \mathcal{W}_{nm} - \hat{q}_{NVT}(\mathbf{\Omega}_m, \tau_{\text{MC}}) \mathcal{W}_{mn}] \quad (2.27)$$

where \mathcal{W}_{nm} is transition probability for state $n \rightarrow m$. Because at equilibrium

$$\frac{\partial \hat{q}_{NVT}(\mathbf{\Omega}_n, \tau_{\text{MC}})}{\partial \tau_{\text{MC}}} = 0, \quad (2.28)$$

the condition of detailed balance

$$\hat{q}_{NVT}(\mathbf{\Omega}_n, \tau_{\text{MC}}) \mathcal{W}_{nm} = \hat{q}_{NVT}(\mathbf{\Omega}_m, \tau_{\text{MC}}) \mathcal{W}_{mn} \quad (2.29)$$

is satisfied. According to Eqn. (2.13) the probability to observe the system in state n at time τ_{MC} is given by

$$\hat{q}_{NVT}(\mathbf{\Omega}_n, \tau_{\text{MC}}) = \frac{\exp[-\beta_B U(\mathbf{\Omega}_n)]}{Q_{NVT}} \quad (2.30)$$

where Q_{NVT} is the canonical partition function. In principle, the partition function is unknown and the computation of $\hat{q}_{NVT}(\mathbf{\Omega}_n, \tau_{\text{MC}})$ is impossible. To avoid the determination of Q_{NVT} , one considers the relative transition probability

$$\frac{\hat{q}(\mathbf{\Omega}_n, \tau_{\text{MC}})}{\hat{q}(\mathbf{\Omega}_m, \tau_{\text{MC}})} = \exp[-\beta_B \Delta U(\mathbf{\Omega})] \quad (2.31)$$

to generate new states based on the energy difference $\Delta U(\mathbf{\Omega}) = U(\mathbf{\Omega}_n) - U(\mathbf{\Omega}_m)$. In general, the acceptance criterion for the creation of a new state has no limitation, however, the transition probability

$$\mathcal{W}_{nm} = \begin{cases} 1, & \text{if } \Delta U(\mathbf{\Omega}) \leq 0 \\ \exp[-\beta_B \Delta U(\mathbf{\Omega})], & \text{if } \Delta U(\mathbf{\Omega}) > 0 \end{cases} \quad (2.32)$$

originally suggested by Metropolis *et al.*⁷³ is reasonable because every state of lower configurational energy is accepted. Furthermore, instead of an immediate rejection of the high energy state, the transition probability is given by the Boltzmann factor. Hence, also energetically unfavorable states are accepted to avoid a permanent stay in a local energy minimum.

2.3.3 Algorithm

The distribution of states in the canonical ensemble is given by the probability density \hat{q}_{NVT} [see Eqn. (2.30)]. After generating the initial conditions randomly or in a controlled manner (e.g., begin out of an ideal crystal), the sampling of the states can be achieved by following the simulation protocol:

1. Select a mesogen randomly or sequentially and calculate the energy of the state $U(\Omega_m)$.
2. Decide with equal probability whether to translate or to rotate the selected mesogen.
3. The translation of the selected mesogen is realized via

$$\mathbf{r}(n) = \mathbf{r}(m) + \delta_r \begin{pmatrix} \kappa_1 - 0.5 \\ \kappa_2 - 0.5 \\ \kappa_3 - 0.5 \end{pmatrix} \quad (2.33)$$

where κ_i denotes three independent random numbers in the interval $0 \leq \kappa \leq 1$, and δ_r is the maximum displacement. The rotation by an angle $\gamma = \delta_\gamma(2\kappa - 1)$ about one of the Cartesian axis $\alpha = x, y, z$ where the specific axis is chosen randomly with equal probability is given by

$$\hat{\mathbf{u}}(n) = \mathbf{R}_\alpha(\gamma)\hat{\mathbf{u}}(m). \quad (2.34)$$

Here, \mathbf{R}_α is the rotation matrix and δ_γ is the maximum angle of rotation. Notice that the optimal values of δ_r and δ_γ are unknown *a priori*. Are these parameters too small, one considers very small changes of the configuration affected by translations or rotations of the mesogens, thus, the majority of the moves get accepted. However, in this case the only a small part of the phase space could be sampled in a reasonable time. If δ_r and δ_γ are too large, then it is more likely that the translation and rotation of the mesogens cause an overlap such that the most of the trial moves get rejected based on the energy criterion in Eqn. (2.32). Hence, for both cases the system would stuck in the configurational space. In fact, in order to sample the configurational space adequately one has to adjust the values for δ_r and δ_γ during the simulation and keep the acceptance ratio between 40 and 60%.^{62,69} We emphasize that the choice of these acceptance ratios is somewhat arbitrary, however, based on the experience it turned out that keeping them between 40 and 60% provide an adequate sampling of the configurational space within a reasonable time.

4. The trial move of displacing or rotating a mesogen is accepted with a probability [see Eqn. (2.32)]

$$\text{acc} = \min \left(1, \exp\{-\beta_B[U(\Omega_n) - U(\Omega_m)]\} \right) \quad (2.35)$$

If the trial move is rejected the old configuration Ω_m is kept as initial configuration for the new trial move. In early 1950's, especially this step confused Kirkwood after his meeting with Rosenbluth, a co-author of Ref. 73 by Metropolis *et al.* In the correspondence between Kirkwood and Wood,⁷⁴ Kirkwood was convinced that the MC method introduced by Metropolis *et al.*⁷³ was wrong.

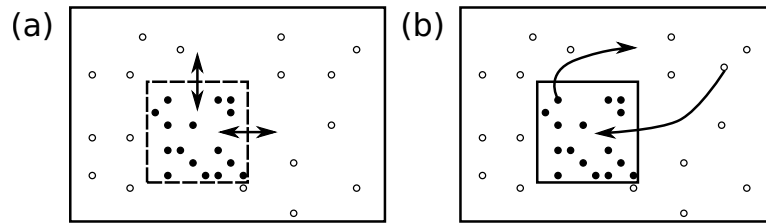


Figure 2.2. Scheme of (a) NPT and (b) μVT ensemble where the mesogens are represented by full dots and the ideal particles by circles.

Instead of that he suggested to repeat this step until the algorithm succeed to create a new configuration which gets accepted by the energy criterion. However, by comparing analytic results with Metropolis MC simulations of one-dimensional hard spheres (i.e., hard rods) Rosenbluth and Wood have shown independently from each other that Kirkwood's statement was wrong. Later, Kirkwood accepted this procedure.⁷⁴

As already explained, this scheme and in particular the acceptance rule, satisfy the detailed balance condition because the generation of a new configuration is independent of the actual configuration the transition probabilities \mathcal{W}_{nm} and \mathcal{W}_{mn} are equal.

2.4 ISOTHERMAL-ISOBARIC ENSEMBLE

In the previous section, we introduced a method providing the computation of macroscopic quantities as ensemble averages $\langle \mathcal{A} \rangle$. Therefore, configurations representing a microscopic state are generated within the framework of importance sampling MC method and every microscopic property \mathcal{A}_n associated with the n -th member of the ensemble is sampled for averaging. Each of these configurations is generated in the canonical ensemble at fixed temperature, volume, and number of mesogens. However, because most experiments are carried out at constant pressure rather than constant volume, a direct comparison between simulations in the canonical ensemble and experiments frequently turns out to be difficult. Hence, it is not surprising that the *isothermal-isobaric* ensemble is widely used for MC simulations. It provides the opportunity of computing ensemble averages at constant pressure P , constant number of particles N , and constant temperature T and therefore enables a direct comparison between simulation and experiment. The advantage over the canonical ensemble is the prevention of phase separations in the isothermal-isobaric or NPT ensemble. In this section we focus on the derivation of the isothermal-isobaric partition function and the probability density following Frenkel and Smit.⁶⁹

We consider a system composed of N mesogens in a cubic box with side length L . The coordinates \mathbf{r}_i of the i th mesogen are scalable relative to L via $\mathbf{r}_i = L\mathbf{s}_i$ where \mathbf{s}_i represents the rescaled coordinates. We place the center of this box at the origin of Cartesian coordinate system such that $-0.5 \leq s_{\alpha_i} \leq 0.5$ where $\mathbf{s}_i = (s_{x_i}, s_{y_i}, s_{z_i})^T$

and $\alpha = x, y, z$. Furthermore, by substituting $V = L^3$ we may rewrite the canonical partition function as

$$\mathcal{Q}_{NVT} = \frac{V^N}{2^N N! \lambda^{5N}} \left(\frac{I}{m} \right)^N \iint ds^N d\hat{u}^N \exp \left[-\beta_B U(s^N, L, \hat{u}^N) \right]. \quad (2.36)$$

Notice, that U is still a function of the real coordinates $r_i = Ls_i$, $i = 1, \dots, N$. We consider a reference system which is surrounded by a much bigger system of an ideal gas. Thus, the total volume V_{tot} and the total number of particles N_{tot} are constant. The volume of the ideal gas is given by $V_{\text{id}} = V_{\text{tot}} - V$ and the particle number by $N_{\text{id}} = N_{\text{tot}} - N$ [see Fig. 2.2(a)]. The partition function of the total system is a product of both subsystems and may be written as

$$\mathcal{Q}_{\text{tot}} = \frac{V^N V_{\text{id}}^{N_{\text{id}}}}{2^N N! N_{\text{id}}! \lambda^{2N} \lambda^{3N_{\text{tot}}}} \left(\frac{I}{m} \right)^N \int ds^{N_{\text{id}}} \iint ds^N d\hat{u}^N \exp \left[-\beta_B U(s^N, L, \hat{u}^N) \right] \quad (2.37)$$

where the integration over $s^{N_{\text{id}}}$ results in 1. Now we consider that the reference system is able to vary its side lengths L and therefore the volume V . We may expect V to fluctuate around a value which minimizes the thermodynamic potential. The probability to find a N -mesogen system at volume V is given by[‡]

$$\hat{q}_{\text{tot}}(V) = \frac{V^N (V_{\text{tot}} - V)^{N_{\text{id}}} \iint ds^N d\hat{u}^N \exp \left[-\beta_B U(s^N, L, \hat{u}^N) \right]}{\int_0^{V_{\text{tot}}} dV' V'^N (V_{\text{tot}} - V')^{N_{\text{id}}} \iint ds^N d\hat{u}^N \exp \left[-\beta_B U(s^N, L', \hat{u}^N) \right]}. \quad (2.38)$$

Assuming an infinite extent of the ideal system such that $N_{\text{tot}}, V_{\text{tot}} \rightarrow \infty$ and $N_{\text{id}}/V_{\text{tot}} = \rho$. Thus, the volume fluctuation of the subsystem has no impact on the pressure of the ideal gas. Furthermore, by using $V/V_{\text{tot}} \rightarrow 0$ and the equation of state $\rho = \beta_B P$ of an ideal gas we obtain (by expanding $\exp(V/V_{\text{tot}})$ in a Taylor series)⁶⁹

$$\begin{aligned} V_{\text{id}}^{N_{\text{id}}} &= (V_{\text{tot}} - V)^{N_{\text{id}}} = V_{\text{tot}}^{N_{\text{id}}} \left(1 - \frac{V}{V_{\text{tot}}} \right)^{N_{\text{id}}} \\ &\simeq V_{\text{tot}}^{N_{\text{id}}} \exp \left(-\frac{N_{\text{id}}}{V_{\text{tot}}} V \right) = V_{\text{tot}}^{N_{\text{id}}} \exp(-\beta_B P V) \end{aligned} \quad (2.39)$$

which we use to rewrite \mathcal{Q}_{tot} in the partition function

$$\mathcal{Q}_{NPT} = \frac{\beta_B P}{2^N N! \lambda^{5N}} \left(\frac{I}{m} \right)^N \int dV V^N \exp(-\beta_B P V) \iint ds^N d\hat{u}^N \exp \left[-\beta_B U(s^N, L, \hat{u}^N) \right] \quad (2.40)$$

‡ The justification of this step is hard because of the lack of natural “metric” for the volume integration. Compared with degeneracy of energy levels or number of mesogens the volume cannot be counted. For a detailed discussion of that problem we refer the interested reader to the book by Frenkel and Smit⁶⁹ and further reading listed there.

of the NPT ensemble where we included the factor $\beta_B P$ to keep the \mathcal{Q}_{NPT} dimensionless.⁶⁹ Hence, the probability to find N mesogens in a particular configuration specified by \mathbf{s}^N and $\hat{\mathbf{u}}^N$ in a volume V is given by

$$\hat{Q}_{NPT} = \frac{V^N \exp(-\beta_B P V) \iint d\mathbf{s}^N d\hat{\mathbf{u}}^N \exp[-\beta_B U(\mathbf{s}^N, L, \hat{\mathbf{u}}^N)]}{\int_0^{V_{\text{tot}}} dV' V'^N \exp(-\beta_B P V') \iint d\mathbf{s}^N d\hat{\mathbf{u}}^N \exp[-\beta_B U(\mathbf{s}^N, L, \hat{\mathbf{u}}^N)]}. \quad (2.41)$$

This is the starting point for the constant pressure MC simulation where $\hat{Q}_{NPT} \propto \exp\{-\beta_B U(\mathbf{s}^N, \hat{\mathbf{u}}^N, V) - \beta_B P V + N \ln(V)\}$.

In an MC simulation, the volume change of a system can be implemented in the same way as the translation and rotation of mesogens. Typically, after N attempts to displace or rotate the mesogens the algorithm attempts to change the volume V to

$$V' = V + \delta_V (\kappa - 0.5) = L^3 [1 + \delta_L^3 (\kappa - 0.5)] \quad (2.42)$$

where δ_V and δ_L denote the maximum change of the volume and the side length L of the cubic simulation box, respectively, and κ is again a random number in the interval of $0 \leq \kappa \leq 1$. As discussed for translational and rotational trial moves (see [Sec. 2.3](#)) δ_L has to be adjusted within the simulation run such that the acceptance ratio for the volume change is between 40 and 70% in order to guarantee an accurate sampling of the phase space. The acceptance criterion for the trial to change the volume

$$\text{acc} = \min \left(1, \exp\{-\beta_B [U(\mathbf{s}^N, \hat{\mathbf{u}}^N, V') - U(\mathbf{s}^N, \hat{\mathbf{u}}^N, V)] - \beta_B P (V' - V) + N \ln(V'/V)\} \right) \quad (2.43)$$

was originally introduced by McDonald⁷⁵ and Vorontsov-Veljaminov *et al.*⁷⁶ independent from each other.

2.5 GRAND CANONICAL ENSEMBLE

The ensembles we have considered so far are characterized by a constant number of particles. However, sometimes one is interested in the average number of particles as a function of the external field. For example, one could ask for the amount of adsorbed particles at a surface which is in contact with a gaseous bulk phase as a function of pressure or temperature. In fact, there are many examples of experimental systems under confinement (i.e., slit pores, channels, etc.) which are in contact with a bulk phase such that an exchange of particles between the confined and the bulk phase is allowed. From thermodynamics, it is known that at equilibrium the chemical potential of both, the confined and the bulk phase, is equal. Hence, by fixing the chemical potential one automatically permit the variation of the number of particles in the system. This is described in the grand canonical ensemble where the exchange of particles between the system and its environment is possible. On account of constant chemical potential, the number of particles fluctuates around a value which minimizes the grand canonical potential. In addition to the chemical potential μ , the

volume V , and the temperature T are kept constant in the so called μVT ensemble. We introduce the grand canonical partition function by following Frenkel and Smit.⁶⁹

As for \mathcal{Q}_{NPT} we consider a reference system which is surrounded by an ideal gas system of infinite extent. The total partition function is again given by Eqn. (2.36). Instead of volume fluctuation we consider the transport of particles from the volume V to the volume V_{id} and/or reversed [see Fig. 2.2(b)]. Moreover, we assume that particles in both volumes are identical, however, the interactions of the particles located in V_{id} are switched off. Such a particle transfer causes the change of the potential energy from $U(\mathbf{s}^N, L, \hat{\mathbf{u}}^N)$ to $U(\mathbf{s}^{N\pm 1}, L, \hat{\mathbf{u}}^{N\pm 1})$. Because each of these transfers is independent we may write the partition function of the grand canonical ensemble as a sum over all possible transfers. Furthermore, using $N_{\text{tot}}, V_{\text{tot}} \rightarrow \infty$, $N_{\text{id}}/V_{\text{tot}} = \rho$, and the chemical potential $\mu = \beta_{\text{B}}^{-1} \ln(\rho\lambda^3)$ of an ideal gas we obtain

$$\mathcal{Q}_{\mu VT} = \sum_{N=0}^{\infty} \frac{V^N \exp(\beta_{\text{B}}\mu N)}{2^N N! \lambda^{5N}} \left(\frac{I}{m}\right)^N \iint d\mathbf{s}^N d\hat{\mathbf{u}}^N \exp\left[-\beta_{\text{B}}U(\mathbf{s}^N, L, \hat{\mathbf{u}}^N)\right]. \quad (2.44)$$

as the grand canonical partition function.⁶⁹

The grand canonical MC simulation consists of two steps in order to sample states given by the probability density $\hat{q}_{\mu VT} \propto \exp\{-\beta_{\text{B}}[U(\mathbf{\Omega}) - N\mu] - \ln(N!) - N \ln(2m\lambda^5/VI)\}$. The first step is the conventional canonical step where the N mesogens are displaced or rotated (see Sec. 2.3). Subsequently, the fluctuation of the number of mesogens is realized by N attempts of creation or destruction of mesogens. For each attempt it is decided with equal probability whether to destroy a random mesogen or to create a new mesogen at a randomly chosen position and with a randomly chosen orientation. The acceptance criteria of the creation and destruction trial are given by

$$\text{acc} = \min\left(1, \frac{VI}{2m\lambda^5(N+1)} \exp\{\beta_{\text{B}}[\mu - U(\mathbf{s}^{N+1}, \hat{\mathbf{u}}^{N+1}) + U(\mathbf{s}^N, \hat{\mathbf{u}}^N)]\}\right) \quad (2.45)$$

and

$$\text{acc} = \min\left(1, \frac{2m\lambda^5 N}{VI} \exp\{-\beta_{\text{B}}[\mu + U(\mathbf{s}^{N-1}, \hat{\mathbf{u}}^{N-1}) - U(\mathbf{s}^N, \hat{\mathbf{u}}^N)]\}\right), \quad (2.46)$$

respectively.

MODEL

In the previous chapter, we introduced a method to describe macroscopic quantities as an ensemble average of microscopic quantities associated with a certain configuration. Moreover, we introduced a numerical method to generate these configurations in order to compute the ensemble average. In both, the description of ensemble averages as well as generation of configurations, the configurational energy $U(\mathbf{r}^N, \hat{\mathbf{u}}^N)$ is of vital importance and depends strongly on the specific system considered.

In the present work, we consider two different systems. The first system is composed of up between two colloidal particles surrounded by N non-chiral mesogens, and confined between two planar, structureless substrates. Hence, the total potential energy may be cast as

$$U(\mathbf{r}^N, \hat{\mathbf{u}}^N) = U_{\text{mm}}(\mathbf{r}^N, \hat{\mathbf{u}}^N) + U_{\text{ms}}(z^N, \hat{\mathbf{u}}^N) + U_{\text{mc}}(\mathbf{r}^N, \hat{\mathbf{u}}^N) \quad (3.1)$$

where U_{mm} , U_{ms} , and U_{mc} are configurational potential energies corresponding to the mesogen-mesogen (mm), mesogen-substrate (ms), and mesogen-colloid (mc) interactions, respectively, and $z^N = \{z_1, \dots, z_N\}$ is the set of the z -components of the positions of mesogens given by \mathbf{r}^N . Notice that because the colloidal motion takes place on a much larger time scale than the motion of the mesogens, we consider colloidal particles that are fixed in space. Hence, terms accounting for colloid-colloid or colloid-substrate interactions vanish.

The second system is composed of N chiral mesogens confined to a mesoscopic channel. Hence, in the absence of colloidal particles (i.e., for $U_{\text{mc}} = 0$) the total configurational energy is given by

$$U(\mathbf{r}^N, \hat{\mathbf{u}}^N) = U_{\text{mm}}^* + U_{\text{mch}}(\mathbf{r}^N, \hat{\mathbf{u}}^N). \quad (3.2)$$

where U_{mm}^* and U_{mch} are configurational potential energies corresponding to the chiral mesogen-mesogen (mm) and mesogen-channel (mch) interactions, respectively. Here, the star indicates the chiral nature of the interactions.

3.1 NON-CHIRAL MESOGEN-MESOGEN INTERACTIONS

Considering pairwise additive mesogen-mesogen interactions, U_{mm} can be written as

$$U_{\text{mm}}(\mathbf{r}^N, \boldsymbol{\omega}^N) = \sum_{i=1}^{N-1} \sum_{j>i}^N u_{\text{mm}}(\mathbf{r}_{ij}, \boldsymbol{\omega}_i, \boldsymbol{\omega}_j) \quad (3.3)$$

where $\mathbf{r}_{ij} = \mathbf{r}_i - \mathbf{r}_j$ is the distance vector connecting the centers of mass of mesogens i and j . For convenience we express the orientations of mesogens via Euler angles $\boldsymbol{\omega}_i$ and $\boldsymbol{\omega}_j$ [see Eqn. (2.18)] in a space-fixed frame of reference. Following Giura and Schoen⁷⁷ we split the pair potential u_{mm} into an isotropic and anisotropic contribution according to

$$u_{\text{mm}}(\mathbf{r}_{ij}, \boldsymbol{\omega}_i, \boldsymbol{\omega}_j) = u_{\text{iso}}(r_{ij}) + u_{\text{anis}}(\mathbf{r}_{ij}, \boldsymbol{\omega}_i, \boldsymbol{\omega}_j) \quad (3.4)$$

where $r_{ij} = |\mathbf{r}_{ij}|$ is the distance between two mesogens i and j .

For the description of isotropic interactions, we take the well known 12-6 Lennard-Jones potential

$$u_{\text{iso}}(r_{ij}) = u_{\text{iso}}^{\text{LJ}}(r_{ij}) = 4\epsilon_{\text{mm}} \left[\left(\frac{\sigma}{r_{ij}} \right)^{12} - \left(\frac{\sigma}{r_{ij}} \right)^6 \right] \equiv u_{\text{rep}}^{\text{LJ}} + u_{\text{att}}^{\text{LJ}} \quad (3.5)$$

where $u_{\text{rep}}^{\text{LJ}}$ and $u_{\text{att}}^{\text{LJ}}$ correspond to the repulsive and attractive Lennard-Jones contributions, respectively. Here, σ is the diameter of a spherical reference particle and ϵ_{mm} is the depth of the attractive well.

The anisotropic interactions

$$u_{\text{anis}}(\mathbf{r}_{ij}, \boldsymbol{\omega}_i, \boldsymbol{\omega}_j) = \sum_{l_i=0}^{\infty} \sum_{l_j=0}^{\infty} \sum_{l=0}^{\infty} \varphi_{l_i l_j l}(r_{ij}) \Phi_{l_i l_j l}(\boldsymbol{\omega}_i, \boldsymbol{\omega}_j, \boldsymbol{\omega}) \quad (3.6)$$

are expanded in terms of rotational invariants

$$\Phi_{l_i l_j l} = \sum_{m_i=-l_i}^{l_i} \sum_{m_j=-l_j}^{l_j} \sum_{m=-l}^l \mathcal{C}(l_i, l_j, l; m_i, m_j, m) Y_{l_i m_i}(\boldsymbol{\omega}_i) Y_{l_j m_j}(\boldsymbol{\omega}_j) Y_{lm}^*(\boldsymbol{\omega}) \quad (3.7)$$

where $\{\varphi_{l_i l_j l}\}$ is the set of expansion coefficients, \mathcal{C} is a Clebsch-Gordan coefficient, and Y_{lm} is a spherical harmonic (the asterisk denotes the complex conjugate). Here, $\boldsymbol{\omega}$ denotes the Euler angles related to the orientation of the distance vector specified by $\hat{\mathbf{r}}_{ij} = \mathbf{r}_{ij}/r_{ij}$ [see Eqn. (2.18)].^{66,77}

On account of symmetry considerations the expansion in Eqn. (3.6) may be restricted. In fact, in the absence of chirality, the interacting potential is invariant if mesogen i and j are exchanged.⁶⁶ This corresponds to the transformation $\boldsymbol{\omega} \rightarrow -\boldsymbol{\omega}$. Due to the parity relation of spherical harmonics

$$Y_{lm}(\boldsymbol{\omega}) = (-1)^l Y_{lm}(-\boldsymbol{\omega}) \quad (3.8)$$

the anisotropic contribution u_{anis} is unaffected by exchanging mesogen i and j only for even l and $l = 0$.^{66,77} Furthermore, because of the assumed head-tail symmetry of the mesogens, u_{anis} is invariant to the exchange of $\boldsymbol{\omega}_i$ and/or $\boldsymbol{\omega}_j$ by $-\boldsymbol{\omega}_i$ and/or $-\boldsymbol{\omega}_j$. Hence, the parity relation implies that l_i and l_j must be either even or zero as well.⁷⁷

In addition to the symmetry considerations, one may also make use of the vanishing nature of the Clebsch-Gordon coefficients if the triangular inequality⁶⁶

$$|l_i - l_j| \leq l \leq l_i + l_j \quad (3.9)$$

is not satisfied to restrict the expansion in Eqn. (3.6). However, despite the restrictions due to the symmetry and the selection rule for the Clebsch-Gordon coefficients the number of spherical invariants that has to be considered increases rapidly with increasing l_i , l_j , and l . Therefore, we truncate the expansion in Eqn. (3.6) after the first leading terms, i.e., for $l_i, l_j \leq 2$.⁷⁷ Hence, on account of Eqn. (3.9) six rotational invariants remain, namely Φ_{000} , Φ_{220} , Φ_{202} , Φ_{022} , Φ_{222} , and Φ_{224} .

The computation of the isotropic term Φ_{000} is straightforward. Because of $l_i = l_j = l = 0$ and thus $m_i = m_j = m = 0$ the triple sums in Eqn. (3.6) and Eqn. (3.7) vanish and we obtain $\Phi_{000} = (4\pi)^{-3/2}$ by applying $Y_{00} = (4\pi)^{-1/2}$. The determination of rotational invariants of higher order is algebraically straightforward, but tedious, and has been reported many times before.⁷⁷⁻⁸⁰ After substituting the angular representation of the orientations ω_i , ω_j , and ω by unit vectors $\hat{\mathbf{u}}_i$, $\hat{\mathbf{u}}_j$, and $\hat{\mathbf{r}}_{ij}$ [see Eqn. (2.18)], respectively, we obtain

$$\Phi_{220} \propto P_2(\hat{\mathbf{u}}_i \cdot \hat{\mathbf{u}}_j) \quad (3.10)$$

$$\Phi_{202} \propto P_2(\hat{\mathbf{u}}_i \cdot \hat{\mathbf{r}}_{ij}) \quad (3.11)$$

$$\Phi_{022} \propto P_2(\hat{\mathbf{u}}_j \cdot \hat{\mathbf{r}}_{ij}) \quad (3.12)$$

where $P_2(x) = \frac{1}{2}(3x^2 - 1)$ is again the second Lagrange polynomial. To reduce the complexity of the potential we assume that Φ_{220} , Φ_{202} , and Φ_{022} are sufficient to describe the liquid-crystalline behavior adequately. Therefore, we neglect Φ_{222} and Φ_{224} .

Finally, one needs to determine the set of expansion coefficients $\{\varphi_{l_i l_j l}\}$. Following the discussion of Giura and Schoen⁷⁷ we focus on dispersion interactions because the mesogens are uncharged and nonpolar, such that $\varphi_{l_i l_j l} \propto r_{ij}^{-6}$ irrespective of l_i , l_j , and l . As demonstrated by Gray and Gubbins⁶⁶ $\varphi_{000} = u_{\text{att}}^{\text{LJ}}$ where ϵ_{mm} depends on the static polarizability along and perpendicular to the principle axis of the mesogens. In a similar fashion, constants of proportionality of expressions shown in Eqn. (3.10)-(3.12) are proportional to various combinations of static polarizabilities. We combine these constants into two dimensionless parameters $\epsilon_1 \equiv \epsilon_{220}$ and $\epsilon_2 \equiv \epsilon_{202} = \epsilon_{022}$ such that $\epsilon_{\text{mm}}\epsilon_1$ and $\epsilon_{\text{mm}}\epsilon_2$ represent the strength of interactions associated with these polarizabilities. The determination of polarizabilities is of no concern in this work. Instead of that, we refer the interested reader to the book by Gray and Gubbins.⁶⁶ Hence, we finally obtain

$$u_{\text{anis}}(\mathbf{r}_{ij}, \hat{\mathbf{u}}_i, \hat{\mathbf{u}}_j) = u_{\text{att}}^{\text{LJ}}(r_{ij})\Psi(\hat{\mathbf{r}}_{ij}, \hat{\mathbf{u}}_i, \hat{\mathbf{u}}_j), \quad (3.13)$$

where

$$\Psi(\hat{\mathbf{r}}_{ij}, \hat{\mathbf{u}}_i, \hat{\mathbf{u}}_j) = \varepsilon_1 P_2(\hat{\mathbf{u}}_i \cdot \hat{\mathbf{u}}_j) + \varepsilon_2 [P_2(\hat{\mathbf{u}}_i \cdot \hat{\mathbf{r}}_{ij}) + P_2(\hat{\mathbf{u}}_j \cdot \hat{\mathbf{r}}_{ij})] \quad (3.14)$$

is the anisotropy function.

In Eqn. (3.14), the term proportional to ε_1 corresponds to the simplest liquid-crystalline interaction introduced by Maier and Saupe.^{18,19} Terms proportional to ε_2 are corrections to the Maier-Saupe interactions. They describe the anisotropic shape of the mesogens, i.e., oblate and prolate ellipsoids of revolution for $\varepsilon_2 > 0$ and $\varepsilon_2 < 0$, respectively [see Fig. 3.1(a) and (b)].⁸⁰ Hence, the parameter ε_2 can be understood as the ellipsoidal eccentricity of the mesogens shape. By substituting Eqn. (3.5) and Eqn. (3.13) in Eqn. (3.4) one obtains the full potential

$$u_{\text{mm}}^{\text{LJ}}(\mathbf{r}_{ij}, \hat{\mathbf{u}}_i, \hat{\mathbf{u}}_j) = 4\epsilon_{\text{mm}} \left[\left(\frac{\sigma}{r_{ij}} \right)^{12} - \left(\frac{\sigma}{r_{ij}} \right)^6 \left\{ 1 + \Psi(\hat{\mathbf{r}}_{ij}, \hat{\mathbf{u}}_i, \hat{\mathbf{u}}_j) \right\} \right] \quad (3.15)$$

which has been proposed by Hess and Su⁸⁰ for the first time.

The impact of Ψ on the interaction potential is shown in Fig. 3.1. For oblate mesogens [i.e., $2\varepsilon_1 = \varepsilon_2 = 0.4$, see also Fig. 3.1(a)] we observe strong attractive interactions if the mesogens are in the end-end configuration ($\hat{\mathbf{u}}_i \cdot \hat{\mathbf{u}}_j = \hat{\mathbf{u}}_i \cdot \hat{\mathbf{r}}_{ij} = \hat{\mathbf{u}}_j \cdot \hat{\mathbf{r}}_{ij} = \pm 1$) in contrast to the side-side configuration ($\hat{\mathbf{u}}_i \cdot \hat{\mathbf{u}}_j = \pm 1$ and $\hat{\mathbf{u}}_i \cdot \hat{\mathbf{r}}_{ij} = \hat{\mathbf{u}}_j \cdot \hat{\mathbf{r}}_{ij} = 0$). The longitudinal and transversal extension of the shape of the mesogens may be determined by the zeros of u_{mm} for a pair of mesogens in the end-end and side-side configuration, respectively. Hence, the ratio of these zeros may be understood as the aspect ratio which is approximately 0.86 for the oblate mesogens as illustrated in Fig. 3.1(a).

In this work, however, we focus on prolate mesogens, $\varepsilon_2 < 0$. The interaction potential for a pair of prolate (i.e., $2\varepsilon_1 = -\varepsilon_2 = 0.4$) mesogens of an aspect ratio approximately 1.26 is illustrated in Fig. 3.1(b). We emphasize that in our model the side-side configuration is favored by prolate mesogens in contrast to the end-end configuration. This is in perfect agreement with real liquid-crystal molecules where the π - π stacking is responsible for a parallel alignment of two molecules.

However, to reveal the full picture of the anisotropic interactions it is necessary to analyze the anisotropy function $\Psi(\hat{\mathbf{u}}_i, \hat{\mathbf{u}}_j, \hat{\mathbf{r}}_{ij})$. By fixing one of the three orientations (i.e., $\hat{\mathbf{u}}_i, \hat{\mathbf{u}}_j, \hat{\mathbf{r}}_{ij}$) in space, Ψ can be evaluated as a function of two angles with respect to the fixed direction. Therefore, we fix $r_{ij} = \sigma$ and $\hat{\mathbf{u}}_i = (1, 0, 0)^T$ and introduce the angles $\phi = \arccos(\hat{\mathbf{u}}_1 \cdot \hat{\mathbf{r}}_{12})$ and $\theta = \arccos(\hat{\mathbf{u}}_1 \cdot \hat{\mathbf{u}}_2)$. As illustrated by the plot of $\Psi(\phi, \theta)$ in Fig. 3.1(c) we identify four different configurations for a pair of mesogens where the side-side configuration is the most favorable. Moreover, evaluating the potential energy u_{mm} we find $u_{\text{mm}}(\text{ss}) < u_{\text{mm}}(\text{X}) < u_{\text{mm}}(\text{T}) < u_{\text{mm}}(\text{ee})$ where ss, X, T, and ee refer to side-side, cross, T, and end-end configurations, respectively [see Fig. 3.1(c)].

In particular, for $2\varepsilon_1 = -\varepsilon_2 = 0.4$ it has been shown that the mesogens undergo an isotropic-nematic phase transition which is weakly first order similar to experimental observations.^{6,81} Furthermore, results obtained from MC simulations of colloidal inclusions in a nematic host phase are in perfect agreement with those obtained

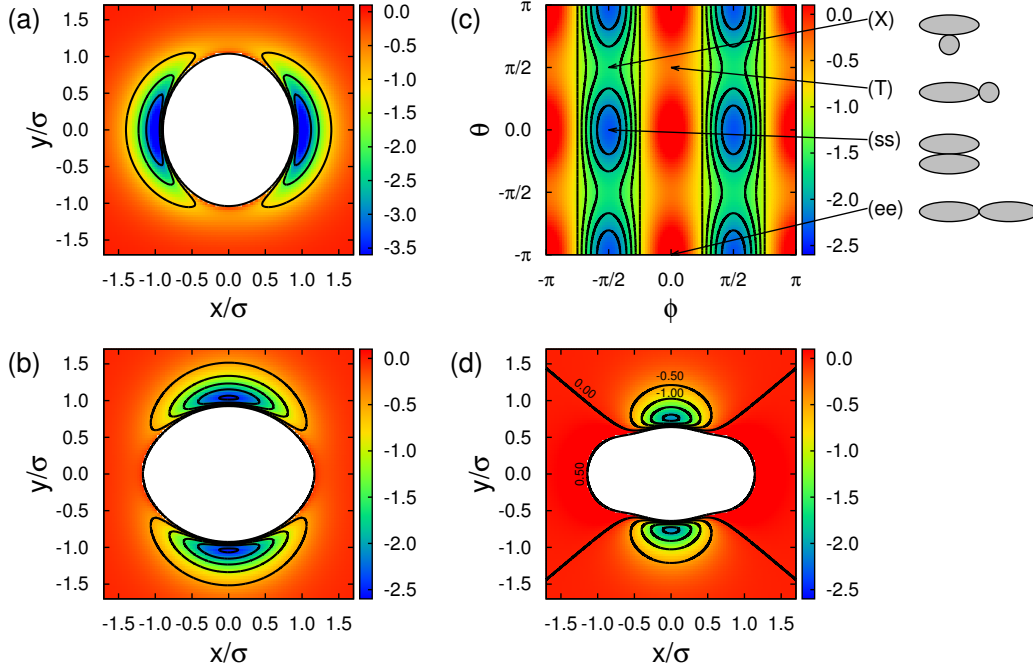


Figure 3.1. Contour plots of $u_{\text{mm}}(\mathbf{r}_{12}, \hat{\mathbf{u}}_1, \hat{\mathbf{u}}_2)$ for a pair of mesogens located in the x - y plane such that $\mathbf{r}_{12} = (x_{12}, y_{12}, 0)^T$. Both mesogens have the orientation $\hat{\mathbf{u}}_1 = \hat{\mathbf{u}}_2 = (1, 0, 0)^T$. The color code indicates the value of u_{mm} and the black lines are contour lines. (a) Contour plot for oblate mesogen as obtained for $u_{\text{mm}}^{\text{LJ}}$ [see Eqn. (3.15)] and $2\varepsilon_1 = \varepsilon_2 = 0.4$. (b) Same as (a) but for prolate mesogens, with $2\varepsilon_1 = -\varepsilon_2 = 0.4$. (c) Same as (b) but as function of $\phi = \arccos(\hat{\mathbf{u}}_1 \cdot \hat{\mathbf{r}}_{12})$ and $\theta = \arccos(\hat{\mathbf{u}}_1 \cdot \hat{\mathbf{u}}_2)$ at constant distance $r_{12} = \sigma$ such that $u_{\text{mm}}^{\text{LJ}}(\mathbf{r}_{12}, \hat{\mathbf{u}}_1, \hat{\mathbf{u}}_2) = -4\epsilon_{\text{mm}}\Psi(\phi, \theta)$ [see Eqn. (3.13)]. Cartoons on the right side visualize the spatial orientation of a pair of mesogens relative to each other. The cross (X), T- (T), end-end (ee), and side-side (ss) configurations are formed for $\{\phi = \frac{2k+1}{2}\pi, \theta = \frac{2k+1}{2}\pi\}$, $\{\phi = k\pi, \theta = \frac{2k+1}{2}\pi\}$, $\{\phi = \frac{2k+1}{2}\pi, \theta = k\pi\}$, and $\{\phi = k\pi, \theta = k\pi\}$, respectively ($k \in \mathbb{Z}$). (d) Contour plot is obtained for u_{mm}^{Y} [see Eqn. (3.19)] and $2\varepsilon_1 = -\varepsilon_2 = 4.0$.

experimentally.⁵⁹ The model potential also reproduces non-equilibrium properties adequately.⁸² Thus, we conclude that this potential captures the essential properties of the nematic phase. However, because of the rather small aspect ratio this model potential is not capable of forming a smectic phase.

In order to model the smectic A phase, we replace the isotropic contribution to u_{mm} by a Yukawa-like potential

$$\begin{aligned}
 u_{\text{iso}}(r_{ij}) &= u_{\text{iso}}^{\text{Y}}(r_{ij}) = \epsilon_{\text{mm}} \left[a_{\text{mm}} \left(\frac{\sigma}{r_{ij}} \right)^{10} - b_{\text{mm}} \frac{\exp(-\eta_{\text{mm}} r_{ij})}{r_{ij}} \right] \\
 &\equiv u_{\text{rep}}^{\text{Y}}(r_{ij}) + u_{\text{att}}^{\text{Y}}(r_{ij})
 \end{aligned} \tag{3.16}$$

where u_{att}^Y and u_{rep}^Y correspond to the attractive and repulsive contributions of the Yukawa-like potential, respectively. Here, η_{mm} is the inverse Debye screening length which we take as $\eta_{\text{mm}} = 3.0/\sigma$ throughout this work. Parameters

$$a_{\text{mm}} = \frac{1 + \sigma\eta_{\text{mm}}}{10(9 - \sigma\eta_{\text{mm}})} \quad (3.17)$$

and

$$b_{\text{mm}} = \frac{\sigma \exp(\sigma\eta_{\text{mm}})}{9 - \sigma\eta_{\text{mm}}} \quad (3.18)$$

are introduced to guarantee that the minimum of u_{iso}^Y is always located at $r_{\text{min}} = \sigma$ and $u_{\text{iso}}^Y(r_{\text{min}}) = -0.1\epsilon_{\text{mm}}$ irrespective of η_{mm} . Hence, the mesogens interact via

$$u_{\text{mm}}^Y(\mathbf{r}_{ij}, \hat{\mathbf{u}}_i, \hat{\mathbf{u}}_j) = \epsilon_{\text{mm}} \left[a_{\text{mm}} \left(\frac{\sigma}{r_{ij}} \right)^{10} - b_{\text{mm}} \frac{\exp(-\eta_{\text{mm}}r_{ij})}{r_{ij}} \left\{ 1 + \Psi(\hat{\mathbf{r}}_{ij}, \hat{\mathbf{u}}_i, \hat{\mathbf{u}}_j) \right\} \right]. \quad (3.19)$$

At this point, it is noteworthy that some attention has to be paid to the choice of η_{mm} . For $\eta_{\text{mm}} \rightarrow 0$ the attractive part of u_{mm}^Y [see Eqn. (3.16)] becomes a Coulomb potential. Because of its long-range nature one needs special techniques such as Ewald summation method to handle such long range interactions in computer simulations.^{62,69} On the other hand, for large η_{mm} a repulsive barrier arise in u_{mm}^Y [see Eqn. (3.16)].

By considering rather weak isotropic interactions [i.e., $u_{\text{iso}}^Y(r_{\text{min}}) = \epsilon_{\text{mm}}/10$] of short-ranged nature (i.e., $\eta_{\text{mm}} = 3.0/\sigma$) and at the same time increasing the anisotropic contributions (i.e., $2\epsilon_1 = -\epsilon_2 = 4.0$) one obtains the equipotential plot presented in Fig. 3.1(d). As one immediately realizes, in this version of u_{mm}^Y the pair of mesogens repel each other if they are in the end-end configuration. As we shall demonstrate below (see Chapter 6) mesogens interacting via u_{mm}^Y capture essential properties of a realistic liquid-crystal regarding their phase behavior, structure, dynamics, and elasticity. In fact, they are capable of forming the isotropic, nematic, and smectic A phases for a suitable choice of thermodynamic conditions.

3.2 MESOGEN-SUBSTRATE INTERACTIONS

A nematic phase is characterized by the global director $\hat{\mathbf{n}}_0$ which indicates the overall preferred molecular orientation. However, the prediction of $\hat{\mathbf{n}}_0$ in the nematic bulk phase or in the smectic bulk phase is impossible *a priori*. In fact, there is an infinite number of orientations $\hat{\mathbf{n}}_0$ may take on, resulting from a continuous symmetry breaking. In experiments, the liquid crystal is confined between planar substrates which can be chemically prepared to align the liquid crystal molecules in a degenerate planar fashion to the substrates surface, for example. Additionally, the substrates are mechanically prepared to align the liquid crystal molecules in a unidirectional fashion.⁵⁶⁻⁵⁸ Despite the short-range nature of the interaction potential

between liquid-crystal molecules, the orientational correlation is long-ranged. Hence, this local alignment at surfaces induce a global unidirectional alignment. In fact, many other ways to control the surface anchoring have been known for years.⁴¹

In order to control $\hat{\mathbf{n}}_0$ we confine our system between two planar, structureless substrates in the z -direction. Notice that we choose the substrates separation distance s_z sufficiently large, such that any colloid-substrate interactions are negligible. Hence, the configurational contribution of the mesogen-substrate interactions in Eqn. (3.1) can be written as

$$U_{\text{ms}}(z^N, \hat{\mathbf{u}}^N) = \sum_{k=1}^2 \sum_{i=1}^N u_{\text{ms}}^{[k]}(z_i, \hat{\mathbf{u}}_i) \quad (3.20)$$

where z_i is the position of mesogen i along the z -direction, and

$$u_{\text{ms}}^{[k]}(z_i, \hat{\mathbf{u}}_i) = \epsilon_{\text{ms}} \left[\frac{2}{5} \left(\frac{\sigma}{\Delta z_i} \right)^{10} - \left(\frac{\sigma}{\Delta z_i} \right)^4 g_x(\hat{\mathbf{u}}_i) \right] \quad (3.21)$$

is the interaction potential. Here, $\epsilon_{\text{ms}} = 5\epsilon_{\text{mm}}$ is the depth of the attractive well and $\Delta z_i = z_i \pm 0.5s_z$ is the distance between the mesogen and the lower ($k = 1$) or upper ($k = 2$) substrate located at $-0.5s_z$ and $+0.5s_z$, respectively.

In Eqn. (3.21), g_x is the anchoring function which we introduce to control the local orientation of the mesogens at the substrates. Depending on the orientation of the mesogens attractive mesogen-substrate interactions in u_{ms} are switched on or off continuously. Mesogens with an undesired orientation are energetically discriminated, such that $0 \leq g_x \leq 1$. In fact, g_x is the mathematical device to mimic experimental surface anchoring. We choose

$$g_x(\hat{\mathbf{u}}_i) = (\hat{\mathbf{u}}_i \cdot \hat{\mathbf{e}}_x)^2, \quad (3.22)$$

where $\hat{\mathbf{e}}_x$ is a unit vector pointing in the x -direction. From Eqn. (3.22) one realizes immediately that every orientation of the mesogens that is not parallel (or anti parallel) to $\hat{\mathbf{e}}_x$ reduces the attractive contribution to u_{ms} .

3.3 MESOGEN-COLLOID INTERACTIONS

Finally, we include into our system up to two spherical colloids of radius r_0 located in the x - y plane equidistantly from the substrates. Considering pairwise additive interactions, the contribution of the mesogen-colloid interactions to the total configurational energy in Eqn. (3.1) is given by

$$U_{\text{mc}}(\mathbf{r}^N, \hat{\mathbf{u}}^N) = \sum_{i=1}^{N_c} \sum_{j=1}^N u_{\text{mc}}(\mathbf{r}_{ij}, \hat{\mathbf{u}}_j) \quad (3.23)$$

Table 3.1. Model parameters used to realize specific defect topologies near a spherical colloid immersed in a liquid crystalline host phase.^{59,82,84}

Defect topology	Anchoring	η_{mc}	ϵ_{mc}
Boojum	planar	1.0	3.5
Saturn ring	homeotropic	0.5	1.0

where $N_c = 1$ or 2 is the number of colloidal particles and \mathbf{r}_{ij} is the distance vector between the centers of mass of colloid i and mesogen j . Following earlier works^{59,83,84} we cast the pair potential as

$$u_{mc}(\mathbf{r}_{ij}) = \epsilon_{mc} \left[a_{mc} \left(\frac{\sigma}{r_{ij} - r_0} \right)^{10} - b_{mc} \frac{\exp[-\eta_{mc}(r_{ij} - r_0)]}{r_{ij} - r_0} g_c(\hat{\mathbf{r}}_{ij}, \hat{\mathbf{u}}_j) \right], \quad (3.24)$$

where $r_{ij} - r_0$ denotes the distance between mesogen j and the surface of colloidal particle i . Parameters ϵ_{mc} , η_{mc} ,

$$a_{mc} = \frac{1 + \sigma\eta_{mc}}{9 - \sigma\eta_{mc}}, \quad (3.25)$$

and

$$b_{mc} = \frac{10\sigma \exp(\sigma\eta_{mc})}{9 - \sigma\eta_{mc}} \quad (3.26)$$

have the same meaning as a_{mm} and b_{mm} that are already introduced for u_{iso}^Y in Eqn. (3.16). However, their value may differ from those in Eqn. (3.16).

Again, g_c is the anchoring function which controls the desired orientation of the mesogens at the colloidal surface. Experimentally, colloidal particles and even nano particles may be functionalized to anchor liquid crystal molecules either in a planar or homeotropic fashion.^{56–58,85} To mimic this we choose

$$g_c(\hat{\mathbf{r}}_{ij}, \hat{\mathbf{u}}_j) = g_{\parallel}(\hat{\mathbf{r}}_{ij}, \hat{\mathbf{u}}_j) = (1 - |\hat{\mathbf{u}}_j \cdot \hat{\mathbf{r}}_{ij}|)^2 \quad (3.27)$$

for planar alignment^{59,84} of the mesogens at the colloidal surface and

$$g_c(\hat{\mathbf{r}}_{ij}, \hat{\mathbf{u}}_j) = g_{\perp}(\hat{\mathbf{r}}_{ij}, \hat{\mathbf{u}}_j) = (\hat{\mathbf{u}}_j \cdot \hat{\mathbf{r}}_{ij})^2 \quad (3.28)$$

for homeotropic alignment.^{59,82} Depending on the desired anchoring scenario different sets of model parameters are used to realize various defect topologies (see Tab. 3.1 and Fig. 1.5).

3.4 CHIRAL MESOGEN-MESOGEN INTERACTIONS

We now turn to a description of the second system [see Eqn. (3.2)], that is a chiral system confined to a mesoscopic channel. Chiral mesogen-mesogen interactions are

obtained in the same manner as the interactions of non-chiral mesogens in [Sec. 3.1](#). In fact, [Eqn. \(3.3\)](#)-[Eqn. \(3.7\)](#) remain the same. However, due to chirality the parity relation [see [Eqn. \(3.8\)](#)] is not satisfied for the transformation $\omega \rightarrow -\omega$. This gives rise to two additional spherical invariants, i.e., Φ_{221} and Φ_{223} , where we again neglect terms of higher order. Hence, we cast the chiral pair potential as

$$u_{\text{mm}}^*(\mathbf{r}_{ij}, \hat{\mathbf{u}}_i, \hat{\mathbf{u}}_j) = 4\epsilon_{\text{mm}} \left[\left(\frac{\sigma}{r_{ij}} \right)^{12} - \left(\frac{\sigma}{r_{ij}} \right)^6 \{1 + \Psi^*(\hat{\mathbf{r}}_{ij}, \hat{\mathbf{u}}_i, \hat{\mathbf{u}}_j)\} \right], \quad (3.29)$$

where

$$\Psi^*(\hat{\mathbf{r}}_{ij}, \hat{\mathbf{u}}_i, \hat{\mathbf{u}}_j) = \Psi(\hat{\mathbf{r}}_{ij}, \hat{\mathbf{u}}_i, \hat{\mathbf{u}}_j) + \epsilon_3 [(\hat{\mathbf{u}}_i \times \hat{\mathbf{u}}_j) \cdot \hat{\mathbf{r}}_{ij}] (\hat{\mathbf{u}}_i \cdot \hat{\mathbf{u}}_j) \quad (3.30)$$

is the chiral anisotropy function and Ψ is the non-chiral one [see [Eqn. \(3.14\)](#)]. The term proportional to ϵ_3 corresponds to Φ_{221} and has been introduced by Memmer *et al.*⁸⁶ to study the impact of chirality on Gay-Berne mesogens. Notice that the potential remains invariant under the exchange of $\hat{\mathbf{u}}_i$ and/or $\hat{\mathbf{u}}_j$ with $-\hat{\mathbf{u}}_i$ and/or $-\hat{\mathbf{u}}_j$, and maintains therefore the mesogens head-tail symmetry despite their chirality.

In [Eqn. \(3.30\)](#), ϵ_3 is the chirality coupling parameter quantifying the chiral contribution to u_{mm}^* . The impact of Ψ^* on the pair potential is illustrated by the contour plots in [Fig. 3.2](#). As illustrated by the plot of u_{mm}^* in [Fig. 3.2\(a\)](#) the potential is no longer invariant to the transformation $r_{ij} \rightarrow r_{ji}$. This is a direct consequence of the broken left-right symmetry introduced via Φ_{221} .

However, the plot presented in [Fig. 3.2\(a\)](#) visualizes one specific configuration between two mesogens as well as its distance-dependence corresponding to that configuration. In [Fig. 3.2\(b\)](#), we plot $\Psi^*(\phi, \theta)$ to illustrate the impact of chirality [see also [Fig. 3.1\(c\)](#)]. We notice that except for a parallel alignment (i.e., $\hat{\mathbf{u}}_i = \pm \hat{\mathbf{u}}_j$) the left-right symmetry of u_{mm}^* is broken for every other configuration $\hat{\mathbf{u}}_i$ and $\hat{\mathbf{u}}_j$ may assume. This is because $(\hat{\mathbf{u}}_i \times \hat{\mathbf{u}}_j) = (0, 0, 0)^T$ for a parallel alignment and thus, $\Psi^* = \Psi$ [see [Eqn. \(3.30\)](#)].

By comparison of Ψ with Ψ^* , plotted in [Fig. 3.1\(c\)](#) and [Fig. 3.2\(b\)](#), respectively, one first realizes that the minima of u_{mm} and u_{mm}^* are found for $\phi = \pm \frac{2k+1}{2}\pi$ but for different θ [see [Eqn. \(3.15\)](#) and [Eqn. \(3.29\)](#), respectively] which is rationalized as following. Starting in the side-side (ss) configuration (i.e., $\{\phi_{\text{ss}} = \frac{2k+1}{2}\pi, \theta_{\text{ss}} = k\pi\}$, $k \in \mathbb{Z}$) the minima of u_{mm}^* are found at $\theta_{\text{min}} = \theta_{\text{ss}} + \delta\theta$ and $\theta_{\text{min}} = \theta_{\text{ss}} - \delta\theta$ for negative and positive values of ϕ , respectively. Here, $\delta\theta$ represents the shift of the minima of u_{mm}^* with respect to u_{mm} caused by the chirality. Consequently, $\delta\theta = 0$ in the absence of chirality. The asymmetric shift of the minima of u_{mm}^* is a direct consequence of the broken left-right symmetry. The sign of the handedness is controlled by the sign of the chirality coupling parameter ϵ_3 whereas its magnitude controls the power of chirality.

As demonstrated elsewhere,^{84,87,88} mesogens interacting via u_{mm}^* are capable of forming a cholesteric phase for low values of $|\epsilon_3|$ but also blue phases I-III for higher values of $|\epsilon_3|$ and a suitable choice of thermodynamic conditions. The formation of

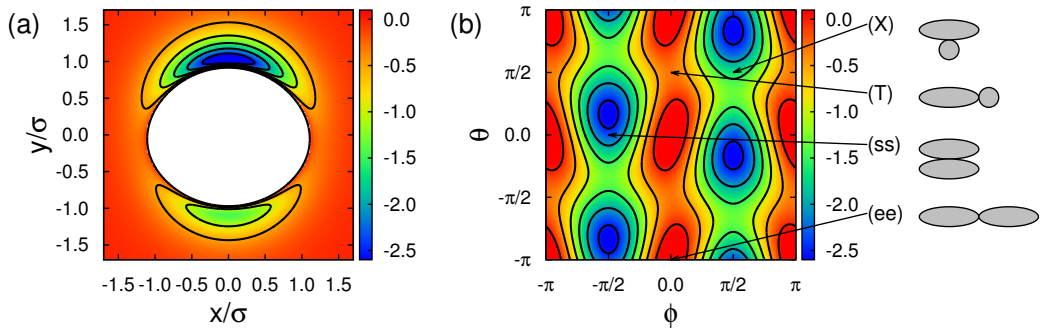


Figure 3.2. (a) Contour plot of $u_{\text{mmm}}^*(\mathbf{r}_{12}, \hat{\mathbf{u}}_1, \hat{\mathbf{u}}_2)$ for a pair of chiral mesogens located in the x - y plane such that $\mathbf{r}_{12} = (x_{12}, y_{12}, 0)^T$ with $\hat{\mathbf{u}}_1 = (1, 0, 0)^T$ and $\hat{\mathbf{u}}_2 = (\cos \theta, 0, \sin \theta)^T$ where $\theta = \pi/4$. The color bar indicates the value of u_{mmm}^* which is obtained for $\varepsilon_3 = 0.50$. (b) Same as Fig. 3.2(c) but for u_{mmm}^* .

chiral phases in our model system is in good qualitative agreement with experiments of Yang and Crooks²⁴ who report the formation of the cholesteric phase for low twist (i.e., large pitch) systems and the formation of blue phases for high twist (i.e., short pitch) systems. In fact, the magnitude of the chirality coupling parameter controls the tilt angle between two mesogens and therefore the pitch p via the simple relation $p \propto 1/|\varepsilon_3|$.⁶ From a macroscopic point of view, chiral phases are characterized by the pitch. Because the pitch is an intrinsic property of our model it depends on thermodynamic conditions such that it is not possible to derive its value from the potential. As discussed by Melle *et al.*⁸⁷ a determination of the pitch can be performed in a specific setup (see Chapter 7 where we discuss this setup in detail).

3.5 MESOGEN-CHANNEL INTERACTIONS

To study the impact of two-dimensional confinement on the order in a chiral liquid crystal we place the chiral mesogens in a mesoscopic channel. The axis of the channel is parallel to the x -axis such that the cross section of the channel is in the y - z plane. The channel is supposed to be of infinite extent in x -direction which is realized by applying periodic boundary conditions across the y - z plane located at $x = \pm s_x/2$. In y - and z -directions the mesogens are confined by the walls of the channel.

A mesogen interacts with different portions of the channel according to its location in the y - z plane. In order to model this we divide our system in three different zones (see Fig. 3.3) in which

1. the interaction with *both* top/bottom *and* left/right straight parts of the channel
2. the interaction with *either* top/bottom *or* left/right straight parts of the channel
3. the interaction with the curved corner of the channel

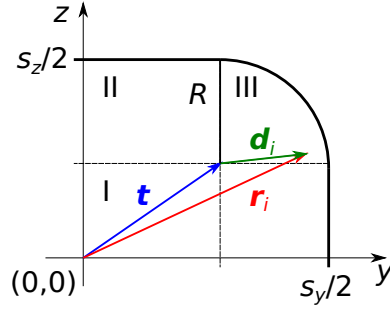


Figure 3.3. Schematic illustration of the channel's cross section in the y - z plane where the coordinate system has been chosen such that $-s_\alpha/2 \leq \alpha \leq s_\alpha/2$ ($\alpha = y, z$). For symmetry reasons only the upper right quadrant is shown. Generally, a mesogen located at \mathbf{r}_i (red arrow) interacts with different portions of a channel. In order to model these interaction we divide the system in three zones I-III separated by dashed lines (see text). Furthermore, R is the radius of the corners arc in zone III such that the shortest distance between a mesogen located in zone III and the channels surface is given by $\Delta d_i = R - |\mathbf{d}_i|$.

are considered. Hence, we cast the configurational contribution of the mesogen-channel interactions to the total configurational energy [see Eqn. (3.2)] as

$$U_{\text{mch}}(\mathbf{r}^N, \hat{\mathbf{u}}^N) = \sum_{i=1}^N [u_{\text{mch}}(\Delta y_i, \mathbf{r}_i, \hat{\mathbf{u}}_i) \Theta(\zeta_{i,y}) + u_{\text{mch}}(\Delta z_i, \mathbf{r}_i, \hat{\mathbf{u}}_i) \Theta(\zeta_{i,z}) + u_{\text{mch}}(\Delta d_i, \mathbf{r}_i, \hat{\mathbf{u}}_i) \Theta(-\zeta_{i,y}) \Theta(-\zeta_{i,z})] \quad (3.31)$$

where Θ is the Heaviside step function, $\zeta_{i,\alpha} \equiv |\alpha_i| - s_\alpha/2 + R$, $\Delta\alpha_i = \alpha_i - \text{sgn}(\alpha) s_\alpha/2$ ($\alpha = x, y$) is the mesogen-channel separation distance in α -direction,

$$\text{sgn}(x) = \begin{cases} -1, & x < 0 \\ 0, & x = 0 \\ +1, & x > 0 \end{cases} \quad (3.32)$$

is the signum function, and R is the radius of the channels curved corner (see Fig. 3.3). Furthermore, we use $2R \geq \min(s_y, s_z)$ such that the channel becomes a cylinder for $2R = s_y = s_z$, and rectangular in shape in the y - z plane for $R = 0$. In Eqn. (3.31), $\Delta d_i = R - |\mathbf{d}_i|$ is the shortest distance between a mesogen located in zone III and the channels arc and $\mathbf{d}_i = \mathbf{r}_i - \mathbf{t}$ (see Fig. 3.3). In Eqn. (3.31), the interaction potential

$$u_{\text{mch}}(\delta_i, \mathbf{r}_i, \hat{\mathbf{u}}_i) = \epsilon_{\text{mch}} \left[\frac{2}{5} \left(\frac{\sigma}{\delta_i} \right)^{10} - \left(\frac{\sigma}{\delta_i} \right)^4 g(\mathbf{r}_i, \hat{\mathbf{u}}_i) \right] \quad (3.33)$$

between a mesogen and the wall of the channel is introduced similarly to Eqn. (3.21). Here, $\delta_i = \Delta y_i, \Delta z_i, \Delta d_i$ is the distance between the mesogen's center of mass and a portion of the channel in y - or z -direction, or of the channels corner, respectively, and $\epsilon_{\text{mch}} = 2\epsilon_{\text{mm}}$ is the potential depth. Notice that the potential depth of the channel

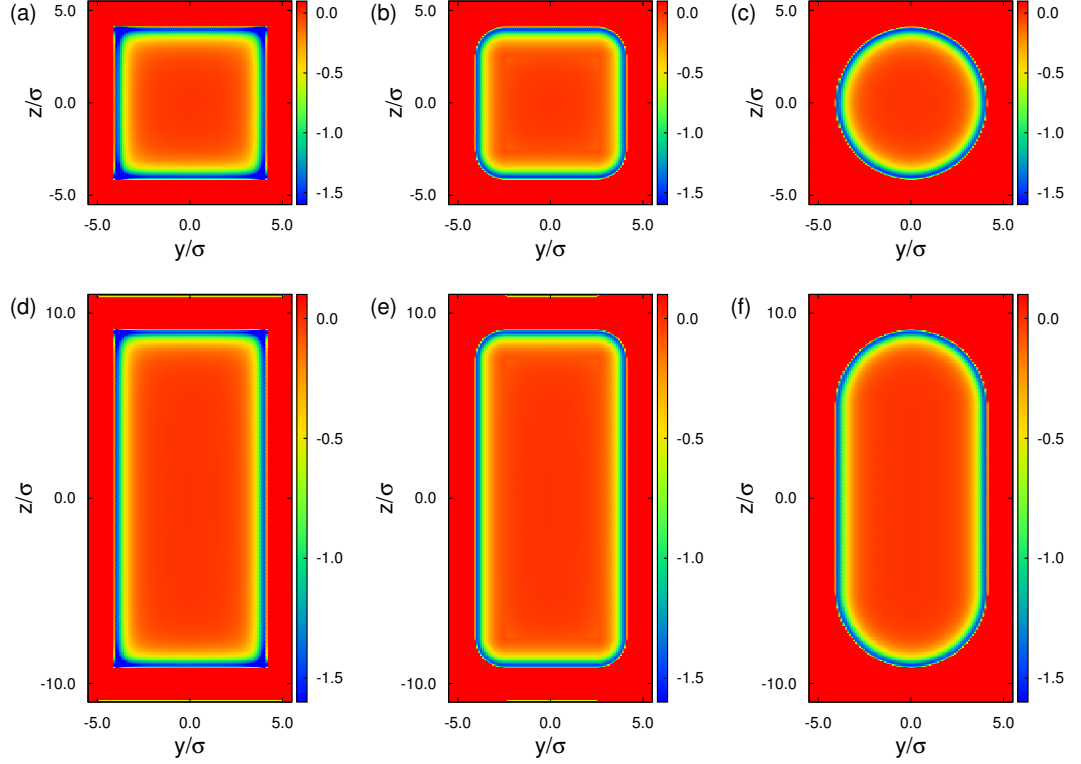


Figure 3.4. Contour plots of u_{mch} for (a)-(c) $s_y = s_z = 10\sigma$ and (d)-(f) $2s_y = s_z = 20\sigma$, $g(\mathbf{r}, \hat{\mathbf{u}}) = 1$, and (a),(d) $R/s_y = 0$, (b),(e) $R/s_y = 0.25$, and (c),(f) $R/s_y = 0.5$. The attached color bar indicates the local value of u_{mch} .

is smaller than the potential depth of the flat substrates introduced in Sec. 3.3 [see Eqn. (3.21)], i.e., $\epsilon_{\text{mw}}/\epsilon_{\text{mch}} = 5/2$. We reduce the strength of the interaction to prevent the confined liquid crystal from freezing in the corners where the attraction is strongest.

Hence, the variation of the shape of the channel via R , s_y , or s_z provides the investigation six different geometry types of the channel (see Fig. 3.4). Furthermore, we also investigate the impact of the surface anchoring. More specifically, we introduce three different anchoring scenarios, namely homeotropic, circular and directional planar anchoring. We use

$$g(\mathbf{r}_i, \hat{\mathbf{u}}_i) = g_{\perp}(\mathbf{r}_i, \hat{\mathbf{u}}_i) = [\hat{\mathbf{u}}_i \cdot \hat{\mathbf{s}}(\mathbf{r}_i)]^2 \quad (3.34)$$

to mimic local homeotropic surface anchoring. Here, $\hat{\mathbf{s}}(\mathbf{r}_i)$ is the local surface normal. The circular planar anchoring is realized via

$$g(\mathbf{r}_i, \hat{\mathbf{u}}_i) = g_{\parallel}(\mathbf{r}_i, \hat{\mathbf{u}}_i) = [1 - |\hat{\mathbf{u}}_i \cdot \hat{\mathbf{s}}(\mathbf{r}_i)|]^2 [(\hat{\mathbf{u}}_i \cdot \hat{\mathbf{e}}_y)^2 + (\hat{\mathbf{u}}_i \cdot \hat{\mathbf{e}}_z)^2] \quad (3.35)$$

where the second term on the far right-hand side of the equation controls the alignment parallel to the surface and the second term controls the mesogens' alignment

perpendicular to the channels axis, i.e., \hat{e}_x . Hence, the *circular* parallel alignment forces the mesogens' orientation to be parallel to the channel's wall as well as in the y - z plane. The other case of planar anchoring is the *directional* anchoring which is realized via

$$g(\mathbf{r}_i, \hat{\mathbf{u}}_i) = g_{\parallel}(\mathbf{r}_i, \hat{\mathbf{u}}_i) = [1 - |\hat{\mathbf{u}}_i \cdot \hat{\mathbf{s}}(\mathbf{r}_i)|]^2 (\hat{\mathbf{u}}_i \cdot \hat{e}_x)^2. \quad (3.36)$$

For this case, the second term on the right-hand side of Eqn. (3.36) controls the alignment of the mesogens along the channels axis \hat{e}_x in addition to the parallel alignment to the surface which is described by the first term on the right-hand side of Eqn. (3.36) in the same manner as for the circular planar anchoring [see Eqn. (3.35)].

CONTINUUM THEORY

Based on the principles of statistical physics we introduced a general method to compute observable properties of many-particle systems (see [Chapter 2](#)). Furthermore, we focus on the description of specific model systems of liquid crystals (see [Chapter 3](#)). Because the field of liquid crystals is very active and of recent interest, many experimental data are available that are described and analyzed within the framework of a Landau-type continuum theory.

Originally, Landau theory^{65,89} was developed to describe second order phase transitions by expanding the free energy in a Taylor series in terms of a suitable order parameter. Later, Ginzburg and Landau⁶⁵ modified the free energy expansion by a term describing the divergence of the order parameter. Thus, Landau's theory is based on three essential steps: (i) find a suitable order parameter, (ii) expand the free energy, and (iii) find the minima of the free energy.

Later, de Gennes⁹⁰ utilized Ginzburg and Landau's theory. He introduced an order parameter (see [Sec. 4.1](#), below) and expand the free energy in terms of this order parameter (see [Sec. 4.2](#), below) in order to describe the isotropic-nematic phase transition which is of weak first order.⁶ Nowadays, the so-called Landau-de Gennes theory succeeds in describing various problems in the field of liquid crystals such as confinement effects, colloidal dispersions, electric/magnetic fields, etc.^{45,46,48,91-93}

The essential quantity of the Landau-de Gennes theory is the free energy which is expanded in a Taylor series in terms of a suitable order parameter. Expansion coefficients of that free energy are observable in experiments.^{6,90} Hence, these phenomenological coefficients are the link between experimental and theoretical observations. As already mentioned, most of the results on liquid crystals are explained and analyzed within the framework of Landau-de Gennes theory, i.e., in terms of few phenomenological constants. Consequently, a quantitative comparison between our results obtained from MC simulations and those obtained experimentally or from Landau-de Gennes theory can be achieved by the calculation of these constants for our model system.

4.1 ORDER PARAMETER

We begin the presentation of the Landau-de Gennes theory by introducing the tensor order parameter

$$Q_{\alpha\beta} = \frac{1}{2}S \left(3n_{\alpha}^{(0)}n_{\beta}^{(0)} - \delta_{\alpha\beta} \right) + \zeta \left(n_{\alpha}^{(1)}n_{\beta}^{(1)} - n_{\alpha}^{(2)}n_{\beta}^{(2)} \right) \quad (4.1)$$

contains all the symmetries required to describe the isotropic-nematic phase transition.³⁹ In Eqn. (4.1), S is the Mayer-Saupe nematic order parameter [see Eqn. (1.1)], ζ is the biaxiality order parameter, $\delta_{\alpha\beta}$ is the Kronecker delta ($\alpha, \beta = x, y, z$), and $n_\alpha^{(k)}$ are components of the set of basis vectors \hat{n}_k ($k = 0, 1, 2$) of the Cartesian coordinate system, respectively, where \hat{n}_0 represents the global director. Because \mathbf{Q} is invariant with respect to any rotation of the Cartesian axes we can assume without any loss of generality that the global director points in the z -direction [i.e., $\hat{n}_0 = (0, 0, 1)^T$] such that the tensor order parameter is simplified to

$$\mathbf{Q} = \begin{pmatrix} -\frac{1}{2}S - \zeta & 0 & 0 \\ 0 & -\frac{1}{2}S + \zeta & 0 \\ 0 & 0 & S \end{pmatrix}. \quad (4.2)$$

Hence, \mathbf{Q} is a real, symmetric, and traceless second-rank tensor.

The molecular interpretation of \mathbf{Q} was given by Eppenga and Frekel⁹⁴ via

$$Q_{\alpha\beta} = \frac{1}{N} \left\langle \sum_{i=1}^N \frac{1}{2} (3u_{i,\alpha}u_{i,\beta} - \delta_{\alpha\beta}) \right\rangle, \quad (4.3)$$

where $u_{i,\alpha}$ is the α -component of the orientation \hat{u}_i of i -th mesogen. We compute S , ζ , and \hat{n}_k by solving the eigenvalue equation

$$\mathbf{Q} \cdot \hat{n}_k = s_k \hat{n}_k, \quad (k = 0, 1, 2) \quad (4.4)$$

where $s_0 \geq s_1 \geq s_2$ are eigenvalues associated with the eigenvectors \hat{n}_k . Following Eppenga and Frenkel,⁹⁴ we take the largest eigenvalue as the nematic order parameter $S = s_0$ and the corresponding eigenvector as the global director \hat{n}_0 . The eigenvalues $s_1 = \zeta - S/2$ and $s_2 = -\zeta - S/2$ associated with eigenvectors \hat{n}_1 and \hat{n}_2 , respectively, are used to compute the biaxiality order parameter [see Eqn. (4.2)] via

$$\zeta = \frac{s_1 - s_2}{2}. \quad (4.5)$$

4.2 LANDAU-DE GENNES FREE ENERGY

After choosing a proper order parameter we follow de Gennes^{6,90} and expand the free-energy density in terms of $Q_{\alpha\beta}$ according to

$$\begin{aligned} f(T) = & f_0 + \frac{1}{2}A(T)Q_{\alpha\beta}Q_{\beta\alpha} - \frac{1}{3}B(T)Q_{\alpha\beta}Q_{\beta\gamma}Q_{\gamma\alpha} + \frac{1}{4}C(T)(Q_{\alpha\beta}Q_{\beta\alpha})^2 \\ & + \frac{1}{2}L_1(\partial_\gamma Q_{\alpha\beta})(\partial_\gamma Q_{\beta\alpha}) + \frac{1}{2}L_2(\partial_\alpha Q_{\gamma\alpha})(\partial_\beta Q_{\gamma\beta}) \end{aligned} \quad (4.6)$$

where Einstein's summation convention is used. Here, f_0 is the free-energy density of the isotropic phase, A , B , and C are phenomenological expansion coefficients, and L_1 and L_2 are elastic constants referring to characteristic modes ($\partial_\alpha = \partial/\partial x_\alpha$ where

$\alpha = x, y, z$). We emphasize that in general f depends on any thermodynamic variable (e.g., temperature, pressure, density) driving the phase transition.

At this point some comments on the expansion coefficient are necessary. Because \mathbf{Q} is traceless the linear term in $Q_{\alpha\beta}$ vanishes in the expansion of the free-energy density. The expansion coefficient $A(T)$ is positive in the isotropic phase, it vanishes at the temperature T^* which indicates the limit of the metastability of the isotropic state, and it is negative in the nematic phase. The simplest way to realize these conditions is a linear combination in temperature, $a(T - T^*)$ where a is a temperature independent material constant.

Surprisingly, we notice the presence of a cubic term in the expansion of the free-energy density [see Eqn. (4.6)] which is forbidden in Landau's theory for ferromagnets. Ferromagnetic states characterized by the magnetization order parameter $|\mathbf{M}|$ and $-|\mathbf{M}|$ are equivalent such that the transformation of $|\mathbf{M}| \rightarrow -|\mathbf{M}|$ is allowed without changing the free energy of the system. Consequently, because the cubic term is odd in $|\mathbf{M}|$ it has to vanish in Landau's free energy expansion, i.e., $B = 0$. The nematic state, however, is not invariant under the transformation $Q_{\alpha\beta} \rightarrow -Q_{\alpha\beta}$ (or $S \rightarrow -S$), hence, $B \neq 0$. Because of the non-vanishing cubic term in $Q_{\alpha\beta}$ the isotropic-nematic phase transition is discontinuous according to Landau's theory in good agreement with experimental observations.^{6,39} However, it is noteworthy that discontinuities which have been observed experimentally in density, heat capacity, etc. are small.^{6,39} This is also reflected by the small value of B which has been measured experimentally for many real liquid crystals. Thus, B can be understood as a measure of the strength of the phase transition, i.e., $B \neq 0$ and $B = 0$ for a first and second order phase transition, respectively.³⁹ For further considerations one typically assumes, B and C to be constant and independent of temperature or other thermodynamic quantities. This assumption is made on the one hand to simplify the theory, on the other hand because neither a microscopic nor a macroscopic knowledge of B or C exists. In Sec. 4.3 we demonstrate that both B and C depend linearly on the temperature. However, because Landau-de Gennes theory is valid for temperatures in the vicinity of the isotropic-nematic phase transition, the assumption of constant B and C holds in that region.

Now we are in a position to determine the isotropic-nematic phase transition temperature. Therefore, we take the expression of the free-energy density in Eqn. (4.2) but for a uniaxial (i.e., $\xi = 0$) and uniformly aligned (i.e., $\partial_\alpha Q_{\beta\gamma} = 0$) nematic phase and rewrite it according to

$$\Delta f(T) = \frac{3}{4}a(T - T^*)S^2 - \frac{1}{4}BS^3 + \frac{9}{16}CS^4 \quad (4.7)$$

where $\Delta f(T) = f(T) - f_0$. At the phase transition temperature T_{IN} the isotropic and the nematic phases coexist such that the condition of two equivalent free energy

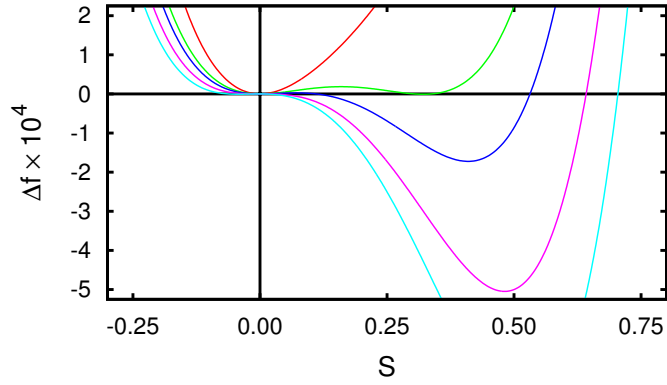


Figure 4.1. Plots of Δf [see Eqn. (4.7)] in arbitrary units as a function of the nematic order parameter for $T > T_{\text{IN}}$ (—), $T = T_{\text{IN}}$ (—), $T_{\text{IN}} > T > T^*$ (—), $T = T^*$ (—), and $T < T^*$ (—). Plots are generated for $a = 0.00552$, $B = 0.0724$, $C = 0.05013$, and $T^* = 318.3$.³⁹

densities $\Delta f(S = 0) = \Delta f(S \neq 0) = 0$ and the stability condition $\partial \Delta f / \partial S = 0$ have to be satisfied. We obtain

$$T_{\text{IN}} = T^* + \frac{B^2}{27aC} \quad (4.8)$$

by satisfying the above conditions analytically. Moreover, this simple theory predicts a universal value of the order parameter at the isotropic-nematic phase transition, i.e., $S(T = T_{\text{IN}}) = 1/3$ which is valid for our systems as we shall demonstrate later. The plot of the free-energy density as a function of the nematic order parameter (see Fig. 4.1) illustrates its dependence on temperature.

Hence, we place emphasis on the determination of the expansion coefficients. In principle, it is possible to measure the free energy in computer simulation because the probability to observe a certain value of S is given by

$$\mathcal{P}(S) = \mathcal{P}_0 \exp[-\beta F(S)]. \quad (4.9)$$

which can be sampled for different configurations as a histogram. In principle, the evaluation of the constants A , B , and C is then obtained by fitting a polynomial to $\ln \mathcal{P}(S)$. However, as discussed by Eppenga and Frenkel⁹⁴ for a system of discotic particles and later verified by Greschek and Schoen⁸¹ for the model potential used also in this thesis, the determination of B and C is almost impossible with sufficient statistical accuracy from $\mathcal{P}(S)$.

More recently, Gupta and Ilg⁹⁵ used the thermodynamic integration to measure the free energy of the isotropic state of Gay-Berne mesogens at different temperatures and extrapolated the free energy into the nematic phase in order to determine B and C . Again, this procedure turned out to be inaccurate for our model.

4.3 DETERMINATION OF THE LANDAU-DE GENNES PARAMETERS

For the determination of Landau-de Gennes parameters, we follow previous work on classical density functional theory for anisotropic particles by Range and Klapp⁹⁶ and later Giura and Schoen⁷⁷ and cast the free energy density as

$$f = f_{\text{hs}} + f_{\text{id}} + \Delta f_{\text{ex,iso}} + \Delta f_{\text{ex,anis}} \quad (4.10)$$

where terms on the right-hand side denote the free energy densities of a hard-sphere (hs) reference system, ideal gas (id), and the excess (ex) free-energy density split according to its isotropic (iso) and an anisotropic (anis) contributions, respectively. Similarly one may separate the ideal gas contribution

$$f_{\text{id}} = \underbrace{k_B T \rho \left[\ln \left(\frac{\rho \lambda^5 m}{I} \right) - 1 \right]}_{f_{\text{id,iso}}} + \underbrace{k_B T \rho \int_{-1}^{+1} dx \mathcal{P}_\theta(x) \ln[2\mathcal{P}_\theta(x)]}_{f_{\text{id,anis}}} \quad (4.11)$$

into an isotropic and anisotropic part. Again, λ is the thermal de Broglie wavelength, the exponent 5 accounts for three translational and two rotational degrees of freedom, m is the mass of the mesogens, I denotes the moment of inertia (see Sec. 2.2), $\mathcal{P}_\theta(x)$ is the orientation distribution function and $x \equiv \cos \theta$ where θ is the azimuthal angle between \hat{n}_0 and \hat{e}_z .

Finally, we are in a position to define the free energy difference between the anisotropic and isotropic phase as

$$\Delta f \equiv f - f_{\text{hs}} - f_{\text{id,iso}} - \Delta f_{\text{ex,iso}} = f_{\text{id,anis}} + \Delta f_{\text{ex,anis}} \quad (4.12)$$

$$= k_B T \rho \int_{-1}^{+1} dx \mathcal{P}_\theta(x) \ln[2\mathcal{P}_\theta(x)] + \rho^2 \sum_{\substack{l=2 \\ \text{even}}} a_l^2 u_l \quad (4.13)$$

where $\{a_l\}$ is a set of order parameters associated with the set of anisotropic contributions $\{u_l\}$ to the mesogen-mesogen interactions. In Eqn. (4.12), $f_{\text{id,anis}}$ represents the loss of orientational entropy the mesogens suffer upon entering the nematic phase.

As one eventually has realized both the free-energy density in Eqn. (4.13) and the Landau-de Gennes free-energy density in Eqn. (4.7) describe the energy difference with respect to the isotropic phase. Thus, the idea is to transform Eqn. (4.13) into Eqn. (4.7) in order to determine the expansion coefficients A , B , and C .

The orientation distribution function $\mathcal{P}_\theta(x)$ [see Eqn. (4.13)] is normalized according to

$$\int_{-1}^{+1} dx \mathcal{P}_\theta(x) = 1 \quad (4.14)$$

and depends only on θ because the uniaxiality of the nematic phase. We expand the orientation distribution function in terms of Legendre polynomials via

$$\mathcal{P}_\theta(x) = \frac{1}{2} + \sum_{\substack{l=2 \\ \text{even}}}^{\infty} \frac{2l+1}{l} a_l P_l(x) \equiv \frac{1}{2} + \mathcal{P}'_\theta(x) \quad (4.15)$$

such that $\mathcal{P}_\theta(x) = 1/2$ in the isotropic phase. Notice that in principle one would perform this expansion in terms of spherical harmonics. However, because the nematic phase is uniaxial, the orientational distribution is specified by the azimuthal angle solely such that we may expand $\mathcal{P}_\theta(x)$ in terms of Legendre polynomials.

We substitute Eqn. (4.15) into $f_{\text{id,anis}}$ [see Eqn. (4.13)] and expand the integrand in a Taylor series according to

$$\left(\frac{1}{2} + x\right) \ln(1 + 2x) = x + x^2 - \frac{2}{3}x^3 + \frac{2}{3}x^4 \mp \mathcal{O}(x^5) \quad (4.16)$$

such that

$$\begin{aligned} \int_{-1}^{+1} dx \left[\frac{1}{2} + \mathcal{P}_\theta(x) \right] \ln[1 + 2\mathcal{P}_\theta(x)] &= \int_{-1}^{+1} dx \left\{ \mathcal{P}'_\theta(x) + [\mathcal{P}'_\theta(x)]^2 - \frac{2}{3}[\mathcal{P}'_\theta(x)]^3 \right. \\ &\quad \left. + \frac{2}{3}[\mathcal{P}'_\theta(x)]^4 + \mathcal{O}(\mathcal{P}'_\theta)^5 \right\} \\ &\simeq \frac{2}{5}a_2^2 - \frac{8}{105}a_2^3 + \frac{4}{35}a_2^4 \end{aligned} \quad (4.17)$$

where we truncated the Taylor series after the term of 4th order and we also focused only on $l = 2$ in Eqn. (4.15). Because a_2 is associated with $P_2(\theta) = \frac{1}{2}(3\cos^2\theta - 1)$ and because θ is the angle between longer axes of the mesogens and \hat{n}_0 , a_2 is identified as the nematic order parameter S [see Eqn. (1.1)]. Hence, substituting Eqn. (4.17) into Eqn. (4.13) results in

$$\Delta f = \underbrace{\frac{2k_B\rho}{5}}_{\frac{3}{4}a} \left(T - \underbrace{\frac{5}{2}\rho Tu_2}_{T^*} \right) S^2 - \underbrace{\frac{8k_B T\rho}{105}}_{\frac{1}{4}B} S^3 + \underbrace{\frac{4k_B T\rho}{35}}_{\frac{9}{16}C} S^4 \quad (4.18)$$

where the expansion coefficients from the Landau-de Gennes free energy may easily be obtained. The determination of T^* via u_2 within the framework of classical density functional theory is inaccurate.⁷⁷ This is because in the present version density functional theory the pair correlation function is not available and needs to be estimated. For the mean-field approach of the density functional theory one neglects all correlation. This approach is exact for ideal gases. In order to improve the mean-field approach one expands the correlation function in terms of density and truncate the expansion after the leading term.^{63,77} This so-called modified-mean-field approach is exact in the limit of vanishing densities. However, for densities considered in this work this approach is inaccurate because packing effect are neglected.

However, the determination of T^* via u_2 within the framework of density functional theory is not necessary. Using Eqn. (4.8) it is possible to compute T^* if the exact phase transition temperature T_{IN} is known. As we shall discuss later, finite-size scaling theory is very convenient and accurate to measure the phase transition temperature. Hence, we obtain a simple approach for the free energy of our system.

4.4 FRANK FREE ENERGY

In previous sections, we considered a liquid crystal where the averaged molecular orientation is homogeneous in space. Consequently, we neglect the contribution of the spatial variation of the director given by

$$f_{\text{el}} = \frac{1}{2}L_1(\partial_\gamma Q_{\alpha\beta})(\partial_\gamma Q_{\beta\alpha}) + \frac{1}{2}L_2(\partial_\alpha Q_{\gamma\alpha})(\partial_\beta Q_{\gamma\beta}) \quad (4.19)$$

which is termed elastic or distortion free energy. However, under confinement, in presence of colloidal particle, and/or external fields the local director $\hat{\mathbf{n}}(\mathbf{r})$ may be deformed locally as illustrated in Fig. 4.2. In fact, a simple setup composed of two planar parallel substrates with antithetic surface anchoring causes a smooth variation of the local director $\hat{\mathbf{n}}(\mathbf{r})$. The variation of $\hat{\mathbf{n}}(\mathbf{r})$ occurs to fit the antithetic alignment directly at the substrates. Because of the rather slow spatial variation of $\hat{\mathbf{n}}(\mathbf{r})$ the local nematic order parameter remains constant. Hence, the change of the free energy between an unperturbed and a perturbed system is not captured by Eqn. (4.7) such that a discussion of the elastic free energy f_{el} is required.

To study f_{el} of a nematic liquid crystal we consider perturbations of the local director $\hat{\mathbf{n}}(\mathbf{r}) = \hat{\mathbf{n}}_0 + \delta\mathbf{n}$ on a scale larger than the molecular one. The perturbation appears perpendicular to $\hat{\mathbf{n}}_0$ such that $\hat{\mathbf{n}}_0 \cdot \delta\mathbf{n} = 0$ whereas $|\hat{\mathbf{n}}(\mathbf{r})| = 1$ is constant. Notice that perturbations along $\hat{\mathbf{n}}_0$ would enhance the nematic order rather than perturb it. Experimentally, a perpendicular perturbation of a nematic phase can be realized by confining the liquid crystal between two parallel and planar substrates with the same surface anchoring. In such a setup the nematic order is slightly enhanced by the anchoring of the substrates which control the molecular orientation. In the literature one finds the term *para*-nematic to indicate this enhanced nematic order.⁶ In fact, the surface anchoring induces a uniform alignment of the liquid crystal molecules. The uniformly aligned system can be perturbed by applying an external field, for instance an electric field E , perpendicular to $\hat{\mathbf{n}}_0$. In general, liquid crystal molecules are sensitive to electric and magnetic fields and align with this field.^{6,39} Hence, liquid crystal molecules try to fit both, the orientation parallel to E and the one parallel to the surface anchoring. We consider a rather weak electric field such that the orientation at the substrates is controlled by the surface anchoring and the orientation between the substrates is controlled by E . Thus, the molecules vary their orientation continuously to fit these competing conditions.

The application of an electric field perpendicular to $\hat{\mathbf{n}}_0$ can be realized in three diverse ways in order to deform $\hat{\mathbf{n}}(\mathbf{r})$ differently. These three basic deformations of a

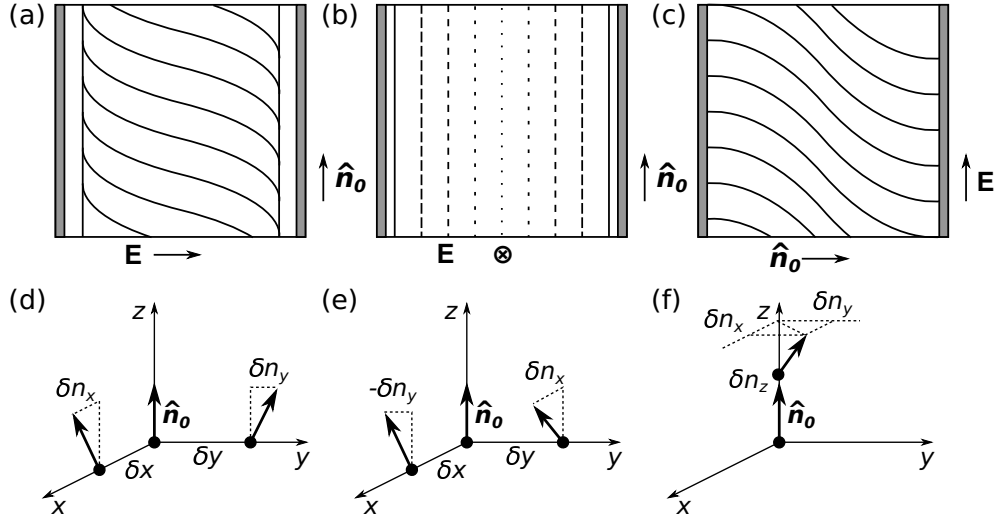


Figure 4.2. Schematic presentation of three basic deformations types: (a) splay, (b) twist, and (c) bend deformation of the nematic director field $\hat{\mathbf{n}}(\mathbf{r})$.

nematic liquid crystal are splay, twist, and bend distortions of the director field (see Fig. Fig. 4.2). Hence, a linear combination of the spatial variations of two modes δn_x and δn_y [see Fig. 4.2(d)-(f)] can be used to describe the elastic deformation via

$$f_{\text{el}} = \frac{1}{2}K_1(\partial_x n_x + \partial_y n_y)^2 + \frac{1}{2}K_2(\partial_y n_x - \partial_x n_y)^2 + \frac{1}{2}K_3(\partial_z n_x - \partial_z n_y)^2, \quad (4.20)$$

where we still assume, that $\hat{\mathbf{n}}_0$ is pointing in the z -direction. A coordinate-independent version is given by

$$f_{\text{el}} = \frac{1}{2}K_1[\nabla \cdot \hat{\mathbf{n}}(\mathbf{r})]^2 + \frac{1}{2}K_2[\hat{\mathbf{n}}(\mathbf{r}) \cdot \nabla \times \hat{\mathbf{n}}(\mathbf{r})]^2 + \frac{1}{2}K_3[\hat{\mathbf{n}}(\mathbf{r}) \times \nabla \times \hat{\mathbf{n}}(\mathbf{r})]^2 \quad (4.21)$$

and was originally derived by Frank.⁹⁷ Here, K_1 , K_2 , and K_3 are material constants referring to splay, twist, and bend deformations, respectively. More specifically, because K_i has the dimension of a force it corresponds to the response force which arises if the local orientation of the molecules deviates from $\hat{\mathbf{n}}_0$. We emphasize that in principle the full description of the elastic deformations contains also mixed terms, i.e., bend-splay and bend-twist as well as terms to describe helical twists of chiral phases.⁹⁷ However, for the sake of simplicity we focus on basic deformations only.

Notice also that de Gennes' tensorial version given in Eqn. (4.19) is equivalent to the description given by Frank in Eqn. (4.21). For example, one may follow the very detailed and straightforward transformation given in Appendix A of Ref. 98 to obtain

$$f_{\text{el}} = \frac{1}{27S^2}(K_3 - K_1 + 3K_2)(\partial_\gamma Q_{\alpha\beta})(\partial_\gamma Q_{\beta\alpha}) + \frac{2}{9S^2}(K_1 - K_2)(\partial_\alpha Q_{\gamma\alpha})(\partial_\beta Q_{\gamma\beta}) \quad (4.22)$$

as a link between Eqn. (4.19) and Eqn. (4.21). Using Eqn. (4.1) leads to Frank's vector representation of the free energy. Hence, the Landau-de Gennes expansion in Eqn. (4.6) is the general theory including Frank's theory as a special case.

4.5 DETERMINATION OF FRANK'S CONSTANTS

The measurement of the elastic Frank constants may be achieved in computer simulations as pointed out by Allen and Frenkel.^{99,100} In an unperturbed bulk liquid crystal, the local director fluctuates because of the thermal energy stored in the system. Because these fluctuations are rather small it is convenient to analyze them in Fourier space. For the sake of convenience, we present the derivation of one of these three constants, namely K_1 . The free energy [see Eqn. (4.20)] for a pure splay deformation reduces to

$$F_{\text{splay}} = \frac{1}{2} K_1 \int d\mathbf{r} (\partial_x n_x + \partial_y n_y)^2. \quad (4.23)$$

The Fourier transform (indicated by the tilde) of the components of the local director $\hat{\mathbf{n}}(\mathbf{r})$ is given by

$$\tilde{n}_\alpha(\mathbf{k}) = \int d\mathbf{r} n_\alpha(\mathbf{r}) \exp(-i\mathbf{k} \cdot \mathbf{r}) \quad (4.24)$$

where \mathbf{k} is the wave vector and $\alpha = x, y, z$. Consequently, the inverse transformation is obtained via

$$n_\alpha(\mathbf{r}) = \frac{1}{(2\pi)^3} \int d\mathbf{k} \tilde{n}_\alpha(\mathbf{k}) \exp(i\mathbf{k} \cdot \mathbf{r}) \quad (4.25)$$

which we substitute in Eqn. (4.23) leading to

$$F_{\text{splay}} = \frac{1}{2(2\pi)^6} K_1 \iiint d\mathbf{r} d\mathbf{k} d\mathbf{k}' [-\tilde{n}_x(\mathbf{k})k_1\tilde{n}_x(\mathbf{k}')k'_1 + 2\tilde{n}_x(\mathbf{k})k_1\tilde{n}_y(\mathbf{k}')k_2 - \tilde{n}_y(\mathbf{k})k_2\tilde{n}_y(\mathbf{k}')k'_2] \exp [i(\mathbf{k} + \mathbf{k}') \cdot \mathbf{r}]. \quad (4.26)$$

This expression for F_{splay} can be easily simplified by the application of the well known relations^{101,102}

$$\int d\mathbf{r} \exp [i(\mathbf{k} + \mathbf{k}') \cdot \mathbf{r}] = (2\pi)^3 \delta(\mathbf{k} + \mathbf{k}') \quad (4.27)$$

where δ is the Dirac- δ distribution and

$$\int d\mathbf{k}' f(\mathbf{k}') \delta(\mathbf{k} + \mathbf{k}') = f(-\mathbf{k}) \quad (4.28)$$

such that

$$F_{\text{splay}} = \frac{1}{2(2\pi)^3} K_1 \int d\mathbf{k} [\tilde{n}_x(\mathbf{k})\tilde{n}_x(-\mathbf{k})k_1^2 + 2\tilde{n}_x(\mathbf{k})k_1\tilde{n}_y(\mathbf{k})k_2 + \tilde{n}_y(\mathbf{k})\tilde{n}_y(-\mathbf{k})k_2^2]. \quad (4.29)$$

Furthermore, using $\tilde{n}_\alpha(-\mathbf{k}) = \tilde{n}_\alpha^*(\mathbf{k})$ and $\tilde{n}_\alpha(\mathbf{k})\tilde{n}_\alpha^*(\mathbf{k}) = |\tilde{n}_\alpha(\mathbf{k})|^2$, and replacing the integral by a sum over wave vectors we cast the final result as

$$F_{\text{splay}} = \frac{1}{2V} K_1 \sum_{\mathbf{k}} [|\tilde{n}_x(\mathbf{k})|k_1 + |\tilde{n}_y(\mathbf{k})|k_2]. \quad (4.30)$$

In the same manner, we obtain

$$F_{\text{twist}} = \frac{1}{2V} K_2 \sum_{\mathbf{k}} [|\tilde{n}_x(\mathbf{k})|k_2 - |\tilde{n}_y(\mathbf{k})|k_1] \quad (4.31)$$

and

$$F_{\text{bend}} = \frac{1}{2V} K_3 \sum_{\mathbf{k}} [|\tilde{n}_x(\mathbf{k})|^2 - |\tilde{n}_y(\mathbf{k})|^2] k_3 \quad (4.32)$$

for the free energy of the twist and bend deformations, respectively. Now we define a coordinate system **1,2,3** where the global director is pointing in z -direction and the wave vector is chosen to be in the 1-3 plane, such that $\mathbf{k} = (k_1, 0, k_3)^T$. Furthermore, we take the unit vector $\hat{\mathbf{e}}_1$ to be parallel to the plane spanned by \mathbf{k} and $\hat{\mathbf{n}}_0$. Hence, $\hat{\mathbf{e}}_2$ is perpendicular to that plane. Furthermore, $\mathbf{k} = k_1 \hat{\mathbf{e}}_1 + k_3 \hat{\mathbf{n}}_0$ is used to rewrite and summarize Eqn. (4.30), Eqn. (4.31), and Eqn. (4.32) to obtain

$$F_{\text{el}} = \frac{1}{2V} \sum_{\mathbf{k}} \sum_{\alpha=1}^2 |\tilde{n}_\alpha(\mathbf{k})|^2 (K_3 k_3^2 + K_\alpha k_1^2). \quad (4.33)$$

It is helpful to remember that $\tilde{n}_\alpha(\mathbf{k})$ is the Fourier transform of the components of $\hat{\mathbf{n}}(\mathbf{r})$ which describes local fluctuations of the director field. The fluctuations of the director field occur on account of molecular rotation. Because all three rotational degrees of freedom are decoupled we use the equipartition theorem to compute them separately as ensemble averages via

$$\langle |\tilde{n}_1(\mathbf{k})|^2 \rangle = \frac{V k_B T}{K_3 k_3^2 + K_1 k_1^2} \quad (4.34)$$

$$\langle |\tilde{n}_2(\mathbf{k})|^2 \rangle = \frac{V k_B T}{K_3 k_3^2 + K_2 k_1^2} \quad (4.35)$$

by analogy with Allen and Frenkel^{99,100} who used the tensorial version for their derivation. In order to rewrite expressions presented in Eqn. (4.34) and Eqn. (4.35) by their tensorial analogs we remember that $\hat{\mathbf{n}}_0$ points in the z -direction and that $\delta \hat{\mathbf{n}}$ is perpendicular to $\hat{\mathbf{n}}_0$ such that the local director corresponds to $\hat{\mathbf{n}}(\mathbf{r}) = (\delta n_1, \delta n_2, 1)^T$. Substituting $\hat{\mathbf{n}}(\mathbf{r})$ in Eqn. (4.1) results in $Q_{13}(\mathbf{r}) = \frac{3}{2} S \delta n_1$ and $Q_{23}(\mathbf{r}) = \frac{3}{2} S \delta n_2$ where the computation of δn_1 and δn_2 is performed in Fourier space via Eqn. (4.34) and Eqn. (4.35). Using this proportionality one can immediately rewrite Eqn. (4.34) and Eqn. (4.35) to obtain

$$\langle |\tilde{Q}_{13}(\mathbf{k})|^2 \rangle = \frac{9}{4} \frac{S^2 V k_B T}{K_3 k_3^2 + K_1 k_1^2}, \quad (4.36)$$

$$\langle |\tilde{Q}_{23}(\mathbf{k})|^2 \rangle = \frac{9}{4} \frac{S^2 V k_B T}{K_3 k_3^2 + K_2 k_1^2}, \quad (4.37)$$

where

$$\tilde{Q}_{\alpha\beta}(\mathbf{k}) = \int d\mathbf{r} Q_{\alpha\beta}(\mathbf{r}) \exp(-i\mathbf{k} \cdot \mathbf{r}) \quad (4.38)$$

is the Fourier transform of the instantaneous local alignment tensor

$$Q_{\alpha\beta}(\mathbf{r}) = \frac{1}{\rho} \sum_{i=1}^N \frac{1}{2} (3u_{i,\alpha}u_{i,\beta} - \delta_{\alpha\beta}) \delta(\mathbf{r} - \mathbf{r}_i) \quad (4.39)$$

which is defined in a similar manner as its global analog in Eqn. (4.3).

To extract Frank's constants from computer simulation we use the linearity of the rewritten Eqn. (4.36) and Eqn. (4.37)

$$E_{13}(k_1, k_3) \equiv \frac{9}{4} \frac{S^2 V k_B T}{\langle |\tilde{Q}_{13}(\mathbf{k})|^2 \rangle} \stackrel{k_1, k_3 \rightarrow 0}{\equiv} K_3 k_3^2 + K_1 k_1^2 \quad (4.40)$$

$$E_{23}(k_1, k_3) \equiv \frac{9}{4} \frac{S^2 V k_B T}{\langle |\tilde{Q}_{23}(\mathbf{k})|^2 \rangle} \stackrel{k_1, k_3 \rightarrow 0}{\equiv} K_3 k_3^2 + K_2 k_1^2 \quad (4.41)$$

in k_1^2 and k_3^2 in the limit of low k which is valid because of long wavelength fluctuations of the local director. Notice that because $E_{13}, E_{23} \rightarrow 0$ as $|\mathbf{k}_1|, |\mathbf{k}_3| \rightarrow 0$ the values $E_{13}(0,0) = 0$ and $E_{23}(0,0) = 0$ should be set manually. Frank's constants may be obtained from the slope of a linear fit to Eqn. (4.40) and Eqn. (4.41).

At this point, one eventually wonders why this continuum theoretical approach works in computer simulations at the molecular level. Elastic properties manifest themselves in computer simulations through fluctuations of the local director over a length scale larger than molecular correlation lengths which are typical of the molecular order. Allen *et al.*¹⁰³ demonstrated for different parameters of the Gay-Berne model potential that E_{13} and E_{23} are linear in k_1^2 and k_3^2 for $k^2 \sigma^2 < 2$ which corresponds approximately to 5σ . In fact, it has been reported repeatedly from computer simulations that the region of linearity is satisfied for length scales of about an order of magnitude larger than the molecular one.^{82,99,100,103,104} As we shall demonstrate below (see Fig. 6.5) this is also valid for the model system used in this work.

4.6 TOPOLOGICAL DEFECTS

So far we have discussed the free-energy change of an unperturbed liquid crystal across the isotropic-nematic phase transition as well as the free energy change which arises because of a smooth and *continuous* variation of the local director $\hat{\mathbf{n}}(\mathbf{r})$ caused by an external field. However, as already discussed in previous sections (see Sec. 1.2 and Sec. 1.3) the spatial variation of $\hat{\mathbf{n}}(\mathbf{r})$ may be large on a molecular scale and even *discontinuous* (see Fig. 4.3). More specifically, discontinuities and singularities of $\hat{\mathbf{n}}(\mathbf{r})$ termed *topological defects* may arise, for instance, due to the presence of competing external fields.

Topological defects are key entities in the physics of liquid crystals. In fact, as explained in Sec. 1.3 topological defects around a spherical colloid in the nematic phase drive colloidal self-assembly. More specifically, the colloidal surface may be treated to anchor the liquid crystal molecules in different ways. Consequently, the

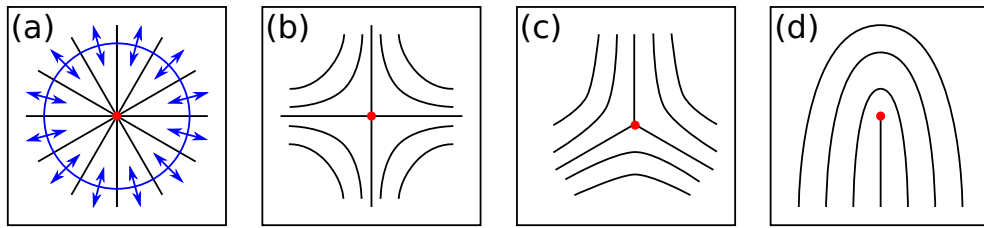


Figure 4.3. Director field configurations (black lines) in the vicinity of topological defects (red dots) of topological charge (a) $+1$, (b) -1 , (c) $-\frac{1}{2}$, and (d) $+\frac{1}{2}$ formed in the nematic phase.⁶ In (a), blue double arrows visualize the variation of the local director along of an arbitrary closed path (blue circle) encircling the defect.²¹

nematic phase is perturbed in different ways and forms different topological defects (see Fig. 1.5). This gives rise to different and rather complex anisotropic colloidal interactions.^{10,50,92} Furthermore, topological defects, especially line defects, are used to attract small particles and transport them.¹⁷ They may also be employed for the creation of complex polymer networks.¹³ Even in cosmology, liquid-crystalline defects are used as a model system to study cosmological defects.¹⁰⁵

Hence, understanding the physics of topological defects is of crucial importance. However, conventional experimental setups (i.e., microscopy techniques) do not provide any deeper insight. Therefore, theoretical approaches such as Frank's theory on the deformation of the local director⁹⁷ or Landau-de Gennes theory⁹⁰ were developed to understand topological defects. Later, model potentials (e.g., Gay-Bern potential) have been used to study defects in molecular simulation.¹⁰⁶ Recently, Wang *et al.*^{15,16} studied the self-assembly of lyotropic molecules in the core of a topological defect and revealed the nature of topological defects experimentally.

On a molecular scale, topological defects are exhibited between two (or more) competing forces trying to align the liquid crystal molecules in a different fashion. These forces are mediated by electric/magnetic fields, surface forces of confinements or colloids, as well as by a liquid-crystalline host phase (i.e., elastic forces discussed in Sec. 4.4). At a point, more precisely, within a region of a certain extent, where magnitudes of two forces are equal but in competition, the molecular orientation is undefined and molecules rotate freely.

Using Eqn. (4.3) to investigate the averaged nematic order at a topological defect, one satisfies himself that the nematic order parameter S decreases in the vicinity of a defect, before eventually vanishes at the defect core. This reflects the orientational frustration of the molecules within a defect. Because of a vanishing S no local director can be found. For this reason topological defects are associated with singularities of the director field $\hat{n}(\mathbf{r})$.

However, the notation as a *singularity* is somewhat misleading in this context. One immediately realizes from Eqn. (4.2) that for $S = 0$ the eigenvalues $s_1 = \zeta$ and $s_2 = -\zeta$ are finite and non-zero. More specifically, the biaxiality order parameter ζ increases as S declines in order to preserve the properties of \mathbf{Q} in the nematic phase (i.e., symmetric, traceless, real, and non-zero). We emphasize that for $S = \zeta = 0$, \mathbf{Q} is

given by a zero matrix and describes an isotropic phases. However, because the liquid crystal is not “melted” locally at the defect, ζ has to raise such that the biaxial nature of a topological defect manifests as we shall demonstrate later.^{6,39,107} Hence, despite $S = 0$ the local director is uniquely defined by $\hat{\mathbf{n}}(\mathbf{r}) = \hat{\mathbf{n}}_1(\mathbf{r}) \times \hat{\mathbf{n}}_2(\mathbf{r})$ where again $\hat{\mathbf{n}}_1$ and $\hat{\mathbf{n}}_2$ are eigenvectors associated with s_1 and s_2 , respectively [see Eqn. (4.4)].

As illustrated in Fig. 4.3 various director fields may include defects that are characterized via their topological charge in the same fashion as defects of vector fields.²¹ In order to determine the topological charge, we consider an arbitrary and closed surface Σ encircling the defect. The magnitude and the sign of the charge correspond to the number of rotations which $\hat{\mathbf{n}}(\mathbf{r})$ undergoes along this surface and the direction of the rotation, respectively [see Fig. 4.3(a)].²¹ Hence, following Trebin¹⁰⁸ the topological charge is given by

$$q = \frac{1}{8\pi} \int d\Sigma_\alpha \epsilon_{\alpha\beta\gamma} \hat{\mathbf{n}} \cdot (\partial_\beta \hat{\mathbf{n}} \times \partial_\gamma \hat{\mathbf{n}}) \quad (4.42)$$

where $\epsilon_{\alpha\beta\gamma}$ is the Levi-Civita totally asymmetric tensor ($\alpha, \beta, \gamma = x, y, z$). Notice that because of the head-tail symmetry of the director field, half-integer charges are possible unlike the case of vector fields where topological charges are given by integers solely. Moreover, positively and negatively charged defects are topologically equivalent and can be transformed into one another via a continuous rotation of $\hat{\mathbf{n}}(\mathbf{r})$. Again, this is a consequence of the head-tail symmetry.^{21,109} However, we emphasize that despite topological equivalence the free energies of positively and negatively charged defects may vary.

Furthermore, defects may be classified as point, line, or surface defects.³⁹ Point defects are known as hedgehog defects for obvious reasons, see Fig. 4.3(a)-(b) where director field configurations for the radial ($q = +1$) and hyperbolic hedgehog ($q = -1$) defect are illustrated, respectively. Line defects, also referred to as disclinations, have usually a half-integer charge [see Fig. 4.3(c)-(d)]. However, for a suitable choice of confinement (e.g., capillary or droplet, see also Fig. 1.4) a disclination line of integer charge may also be found. Surface defects are located at surfaces, for example on colloids or inside of droplets and are known as Boojums¹¹⁰ [see Boojum colloid in Fig. 1.5(a)]. Because of the excluded volume of the surface, the defects may be thought as truncated hedgehog defects or disclinations.

The study of topological defects is in principle not possible within the framework of Frank’s theory of elastic deformations of $\hat{\mathbf{n}}(\mathbf{r})$ [see Eqn. (4.21)] because it does not provide a correct *quantitative* description for rapid variations of $\hat{\mathbf{n}}(\mathbf{r})$. However, an approximation of the core energy may be obtained analytically.

For example, the radial-hedgehog is given by a director field $\hat{\mathbf{n}}(\mathbf{r}) = (x, y, z)^T / r$ ($r = \sqrt{x^2 + y^2 + z^2}$) [see Fig. 4.3(a)]. Evaluating this director field within the frame-

work of Frank's theory one immediately realizes that twist and bend contributions to f_{el} [see Eqn. (4.21)] vanish because

$$\nabla \times \hat{\mathbf{n}}(\mathbf{r}) = \begin{pmatrix} \partial_y n_z - \partial_z n_y \\ \partial_z n_x - \partial_x n_z \\ \partial_x n_y - \partial_y n_x \end{pmatrix} = \begin{pmatrix} -\frac{1}{r^3}(yz - zy) \\ -\frac{1}{r^3}(zx - xz) \\ -\frac{1}{r^3}(xy - yx) \end{pmatrix} = \mathbf{0} \quad (4.43)$$

where we used $\partial_\alpha n_\beta = -(\alpha n_\beta)/r^2$. Hence, f_{el} diverges with r^{-2} at the defect core because

$$f_{\text{el}} = \frac{1}{2}K_1 [\nabla \cdot \hat{\mathbf{n}}(\mathbf{r})]^2 = \frac{1}{2}K_1 \left(\frac{\partial x}{\partial x r} + \frac{\partial y}{\partial y r} + \frac{\partial z}{\partial z r} \right)^2 = \frac{2K_1}{r^2} \quad (4.44)$$

where $\partial_\alpha n_\alpha = (n_\beta^2 + n_\gamma^2)/r$ ($\alpha, \beta, \gamma = x, y, z$). However, the core energy is constant. Hence, integrating the free-energy density in a sphere of radius R_{core} , which includes the defect in the origin ($r = 0$), results in

$$F_{\text{radial}} = \int_0^{2\pi} \int_0^\pi \int_0^{R_{\text{core}}} dr d\phi d\theta r^2 \sin \theta \frac{2K_1}{r^2} = 8\pi K_1 R_{\text{core}}. \quad (4.45)$$

Following this scheme one may compute the core energies of the other point defects as well.^{39,109} Notice that if surface defects are considered the volume integration is limited to the volume which is occupied by the liquid crystal. In the case of disclinations, the integration in cylindrical coordinates yields an energy per unit length.

Hence, it is possible to describe the deformation outside the defects via Eqn. (4.21) and separately approximate the energy of the defects in order to obtain a full theoretical description of the nematic order. However, this method is rather inconvenient as an analysis of simulation data because the location of the defect core, its nature and size are not necessarily known.

For this reason, a different model has been developed to describe topological defects. It is based on the biaxial symmetry of topological defects.^{107,111} In fact, the uniaxial treatment of the defect core assumes an isotropic core because of the drop of the nematic order parameter S . However, considering a model that allows for order of biaxial symmetry one immediately realizes from Eqn. (4.2) that the biaxiality order parameter ζ has to rise as S drops in order to preserve a non-vanishing and traceless $Q_{\alpha\beta}$. Hence, the formation of true singularities is prevented. In this approach the computation of the free energy via Eqn. (4.19) is very convenient because it requires solely knowledge of the local alignment tensor $Q_{\alpha\beta}(\mathbf{r})$ [see Eqn. (4.39)].

In computer simulations $Q_{\alpha\beta}(\mathbf{r})$ can be computed as an ensemble average and therefore utilized to quantify the elastic deformation of the nematic liquid crystal irrespective of defects. However, as we shall demonstrate later (see Chapter 5) using the biaxial model for the computation of the free energy involves technical problems. Hence, regardless of the obvious advantage of the biaxial approach over the uniaxial one, approximations made above for the uniaxial case are valid and can be used if the biaxial approach fails for some reason.

Part III

RESULTS

We begin the presentation of the results by considering a system composed of a spherical colloid dispersed in a nematic host fluid. Depending on the anchoring scenario different defect topologies arise (see [Sec. 1.3](#)). In our previous work,⁵⁹ we have investigated defects of the local director field caused by a spherical colloid. More specifically, for planar surface anchoring, we observe the formation of two Boojum defects located at the surface of the north and south pole of the colloid [see [Fig. 5.1\(a\)](#)]. However, if the surface anchoring is homeotropic, a Saturn ring defect appears around the colloid's equator [see [Fig. 5.1\(b\)](#)]. The results for both anchoring conditions are in perfect agreement with experimental observations.¹⁰ We emphasize that irrespective of the surface anchoring, the local director field is perturbed in the vicinity of the colloidal surface. Hence, elastic forces, which would in principle arise to reorient the mesogens along \hat{n}_0 , are balanced by the colloidal surface anchoring such that the elastic energy is stored in local perturbations of $\hat{n}(\mathbf{r})$.

If a pair of colloids is sufficiently close together they exhibit effective anisotropic interactions. More specifically, depending on the colloidal configuration (i.e., the distance between the colloidal centers of mass as well as the angle between the distance vector and \hat{n}_0) the amount of local perturbation may increase or decrease and mediate thereby effective repulsive and attractive interactions, respectively.^{9,10,50,92} Apparently, the colloidal configuration at equilibrium corresponds to the maximum release of stored elastic energy. It was shown experimentally⁵⁰ that a pair of Boojum colloids (i.e., colloids with planar surface anchoring) forms an angle tilted by 30° with respect to \hat{n}_0 . This was recently confirmed by Eskandari *et al.*⁵¹ by minimizing the Landau-de Gennes free energy functional $\mathcal{F}_{\text{LdG}}[\mathbf{Q}] = \int_V dV f[\mathbf{Q}]$ [see [Eqn. \(4.6\)](#)] around a pair of Boojum colloids. However, a consistent way to extract information from microscopic, molecular scale up to meso- and macroscopic scale is still missing.

In this section, we bridge the gap between the microscopic and macroscopic treatment of the colloidal self-assembly in a nematic host phase. In fact, we perform extensive MC simulations to compute local director fields as ensemble averages around a pair of colloids that anchor the mesogens in a planar fashion locally. We take a microscopic version of the well known Landau-de Gennes free energy to analyze $\mathbf{Q}(\mathbf{r})$ which was derived in [Chapter 4](#). The evaluation of the tensor field configurations results in a free energy landscape which we use as a coarse-grained potential in a two-dimensional MC simulation to investigate the colloidal structure of several colloids. Finally, we compare the free energy landscape as well as colloidal structures with experimental^{10,50} and theoretical⁵¹ works.

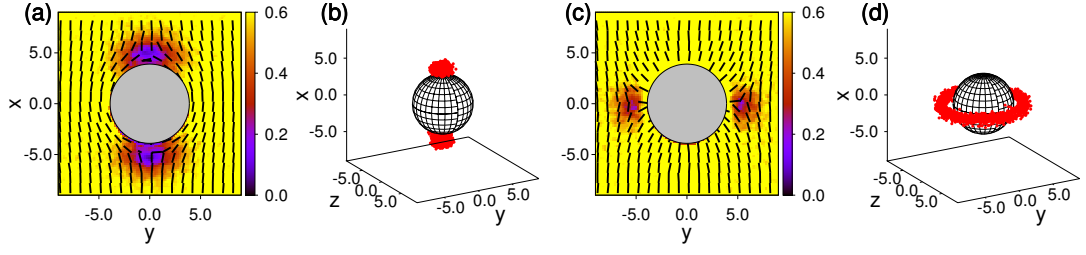


Figure 5.1. Plots of the local nematic order parameter $S(\mathbf{r})$ (see attached color bar) and the local director which is indicated by the dashes. Data are obtained for a colloidal particle that anchors the mesogens in a planar (a) and homeotropic (c) fashion. Plots in (b) and (d) are three-dimensional illustrations of defect topologies for colloids presented in (a) and (c), respectively. The black sphere represents the colloidal particle whereas red dots marks regions where the local nematic order is decreased, i.e., $S(\mathbf{r}) \leq S_{\text{IN}}$. Data are obtained in the same fashion as introduced in Ref. 59.

5.1 TECHNICAL DETAILS

Results presented here are based on MC simulations carried out in a specialized *isothermal-isobaric* ensemble. As discussed elsewhere,⁵⁹ the thermodynamic state is then given by the number of mesogens N , temperature T , substrates separation distance s_z , the ratio s_x/s_y (s_α is the length of the cubic simulation cell in α -direction) and the tangential pressure $P_{\parallel} = (P_{xx} + P_{yy})/2$ where $P_{\alpha\beta}$ are components of the pressure tensor

$$\mathbf{P} = \rho k_B T \mathbf{I} + \mathbf{P}_{\text{mm}} + \mathbf{P}_{\text{mc}} + P_{\text{ms}} \hat{\mathbf{e}}_z \otimes \hat{\mathbf{e}}_z. \quad (5.1)$$

The first term on the right-hand side of this expression is the ideal gas contribution,

$$\mathbf{P}_{\text{mm}} = \left\langle \frac{1}{V} \sum_{i=1}^{N-1} \sum_{j>i}^N \mathbf{r}_{ij} \otimes \mathbf{F}_{ij}^{\text{mm}} \right\rangle \quad (5.2)$$

accounts for mesogen-mesogen interactions,

$$\mathbf{P}_{\text{mc}} = \left\langle \frac{1}{V} \sum_{i=1}^N \sum_{k=1}^{N_c} \mathbf{r}_i \otimes \mathbf{F}_{ik}^{\text{mc}} \right\rangle \quad (5.3)$$

for mesogen-colloid interactions, and

$$P_{\text{ms}} = \left\langle \frac{1}{V} \sum_{k=1}^2 \sum_{i=1}^N F_{z,i}^{[k]} \left(z_i \pm \frac{s_z}{2} \right) \right\rangle \quad (5.4)$$

for mesogen-substrate interactions acting only in the z -direction because the solid substrates are assumed to be perfectly smooth on a molecular length scale [see Eqn. (3.21)].⁷⁰ Here, $\mathbf{F}_{ij}^{\text{mm}}$ and $\mathbf{F}_{ik}^{\text{mc}}$ are forces acting between mesogens i and j and mesogen i and a colloidal particle k , respectively, and $F_{z,i}^{[k]}$ is the force acting between

mesogen i and substrate k in the z -direction. According to earlier work,¹¹² we compute the forces via $F_{ij}^{\text{mm}} = -\nabla u_{\text{mm}}$, $F_{ik}^{\text{mc}} = -\nabla u_{\text{mc}}$, and $F_{z,i}^{[k]} = -\partial u_{\text{ms}}^{[k]} / \partial z_i$ where $\nabla \equiv \partial / \partial r_{ij}$. Note that the isotropy of the pressure tensor is satisfied in the bulk phase only, as discussed by Diestler *et al.*¹¹³ Furthermore, non-diagonal components of \mathbf{P} vanish because our system is not exposed to any shear strain.

For a given set of thermodynamic variables, we generate the configurational distribution in a $5N$ -dimensional space. This space is spanned by $3N$ Cartesian coordinates describing the position of N centers of mass and $2N$ Euler angles specifying the orientation of N mesogens of uniaxial symmetry. The distribution function is proportional to $\exp\{-\beta_{\text{B}}[U(\mathbf{r}^N, \hat{\mathbf{u}}^N) + P_{\parallel} A s_z - N\beta_{\text{B}}^{-1} \ln(A)]\}$ ^{59,113} where $A = s_x s_y$ is the area of the substrates. The generation of these distributions is achieved numerically by applying a conventional Metropolis algorithm^{62,73} adapted to the specialized isothermal-isobaric ensemble. The algorithm consists of two steps. Initially, one of the N mesogens is selected sequentially and then it is decided randomly with equal probability whether to displace the mesogen or to rotate it around one of the three Cartesian axis. The axis is picked randomly with equal probability. After all of the N mesogens are either displaced or rotated the algorithm attempts to change the side lengths of the box. Note that the side length s_z , denoting the substrates separation distance, is kept constant. The series of N attempts to displace/rotate a mesogen and one attempt to change the volume of the system represents one MC step.

For the sake of convenience quantities presented below are given in dimensionless so-called reduced units.⁶² For example, length is given in units of σ and energy in units of ϵ_{mm} . Other quantities may be expressed as a combination of σ and ϵ_{mm} . For instance, pressure, temperature, and density are given in units of $\epsilon_{\text{mm}} / \sigma^3$, $\epsilon_{\text{mm}} / k_{\text{B}}$, and σ^{-3} , respectively.

We follow our previous work⁵⁹ and adopt a model system which reproduces essential properties of colloidal inclusions adequately. However, instead of a single colloid, we include a pair of colloids fixed in the x - y plane at $z = 0$, i.e., equidistantly between two substrates located at $\pm s_z / 2$ where $s_z = 24$ is the distance between them. Inspired by the experimental setup we introduce the substrates to fix $\hat{\mathbf{n}}_0$ in space. We model the mesogen-mesogen, mesogen-substrate, and mesogen-colloid via U_{mm} , U_{ms} , and U_{mc} , respectively (see [Chapter 3](#)).

Results presented in this chapter are obtained for a thermodynamic state which is characterized by $N = 2.4 \times 10^4$, $T = 0.95$, and $P_{\parallel} = 1.80$ which corresponds to $\rho = 0.92$. At these conditions, the host phase is deep in the nematic state indicated by a bulk order parameter $S \simeq 0.7$. The results are based on the following simulation protocol. Typically, we equilibrate our system for 1.5×10^5 MC steps and compute the ensemble averages during the next 10^6 MC steps. The computation of local quantities is realized by dividing the simulation cell into a three-dimensional grid. To guarantee a statistically significant representation of the local ensemble averages we make sure that every volume element has at least 10^3 entries. To save computer time and because of the fast decay of $u_{\text{mm}}^{\text{LJ}}$ [see [Eqn. \(3.15\)](#)] and u_{mc} [see [Eqn. \(3.24\)](#)] we introduce cut-off radii and truncate these potentials at $r_{\text{mm}}^{\text{cut}} = 3.0$ and $r_{\text{mc}}^{\text{cut}} = r_0 + 5.0 = 8.0$ ($r_0 = 3.0$),

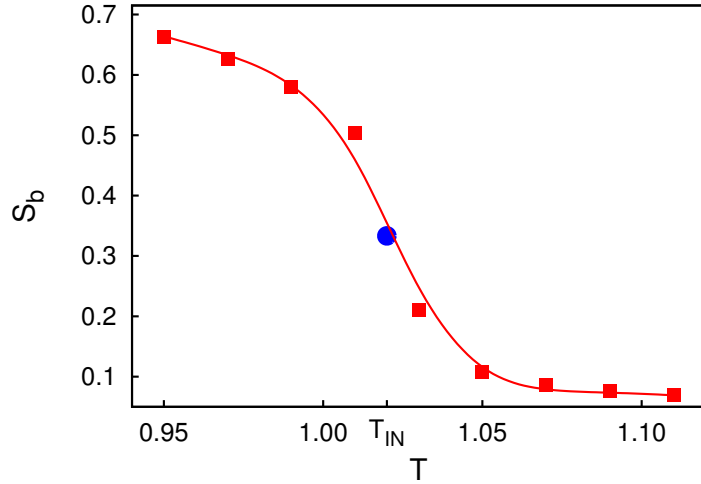


Figure 5.2. Plot of the nematic order parameter S as a function of temperature T (■). Data are shown for $N = 1000$ mesogens. The IN phase transition occurs at T_{IN} and is obtained from an analysis of the second-order cumulant (see text). The full line represents a spline fitted to the discrete data points and intended to guide the eye. Also shown is $S_{IN} = \frac{1}{3}$ at T_{IN} predicted by LdG theory (●) (see text).

respectively. Furthermore, we apply a combination of a linked-cell technique and a conventional Verlet neighbor-list technique⁶² to track the nearest neighbors of all particles. This implies that each of the N mesogens interact only with its nearest neighbors located in a sphere of the radius $r_N = 3.5$ around the reference mesogen.

5.2 NEMATIC BULK PHASE

We begin the discussion by presenting of bulk properties of the host fluid which are obtained in the absence of colloidal particles as well as walls. For chosen thermodynamic conditions the host fluid is deep in the nematic phase as illustrated by the plot of S as a function of temperature in Fig. 5.2. In principle, the isotropic-nematic phase transition is weakly discontinuous. However, because of the relatively small system size the phase transition appears rounded and continuous. Another well-known finite size effect is illustrated by a non-vanishing value of S in the isotropic phase, i.e., for $T > T_{IN}$. This is rationalized by the formation of molecular-size domains which exhibit a preferred orientation because of the form of the interaction potential u_{mm}^{LJ} [see Eqn. (3.15)]. In the isotropic phase these domains are not correlated. However, their number is finite such that the average of S over the domains yields a non-vanishing value of S . We emphasize, the finite size of the system affects S in the isotropic phases as well as in the vicinity of the isotropic-nematic phase transition whereas S is unaffected by the system size deep in the nematic phase as discussed by Greschek and Schoen⁸¹ and later by Giura and Schoen⁷⁷ for the a model system used for this work. Because for chosen thermodynamic condition the fluid is deep in the nematic phase system size effects are not expected for the bulk phase. In the

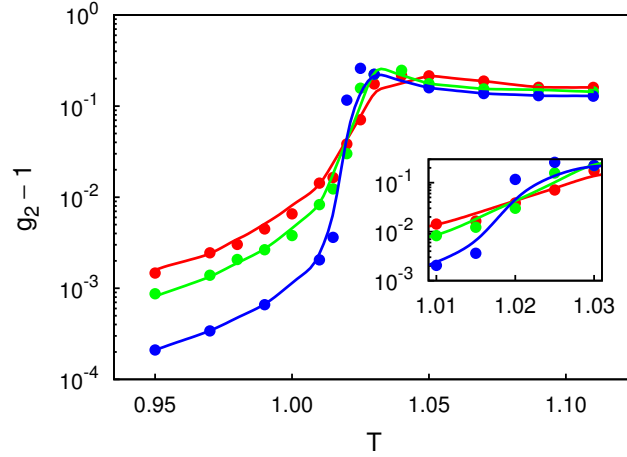


Figure 5.3. Plots of second-order cumulants g_2 as functions of temperature T for $N = 500$ (\bullet), $N = 1000$ (\bullet), and $N = 5000$ (\bullet).

vicinity of the colloidal surface we observe the formation of topological defects indicated by a drastic decrease of the local order parameter $S(\mathbf{r})$ upon a non-vanishing value as for the isotropic phase. However, the size and shape of these defects are determined by the colloidal surface anchoring. Moreover, as we shall demonstrate later the biaxiality in this regions rises as the nematic order drops which is not the case in the isotropic phase.⁸¹ Hence, we conclude that essential properties of topological defects are reproduced by our model adequately and should not be confused with the finite-size effect in the isotropic phase.

Our model system captures another interesting feature. The value of $S(T = T_{\text{IN}}) \equiv S_{\text{IN}} = 1/3$ predicted by the Landau-de Gennes theory (see Sec. 4.2) agrees with our MC data remarkably well where we obtain $S_{\text{IN}} \simeq 0.36$ from finite-size scaling theory (see below). A similar value is also found in the Maier-Saupe theory.^{18,19} In both mean-field approaches the estimated value of S_{IN} is universal in that it neither depends on temperature nor density. However, recent calculations (i.e., classical density functional theory) reveal an explicit temperature dependence of S_{IN} .⁷⁷

In order to localize the exact phase transition temperature T_{IN} (and therefore S_{IN}) we introduce finite-size scaling theory where we explicitly use the fact that in computer simulations one is always confronted with systems of finite size. The key quantity of finite-size scaling theory are cumulants. Here, we focus on the second-order cumulant defined as

$$g_2 = \frac{\langle S^2 \rangle}{\langle S \rangle^2} \quad (5.5)$$

where

$$\langle S^n \rangle = \int_0^1 dS' S'^n \mathcal{P}(S') \quad (5.6)$$

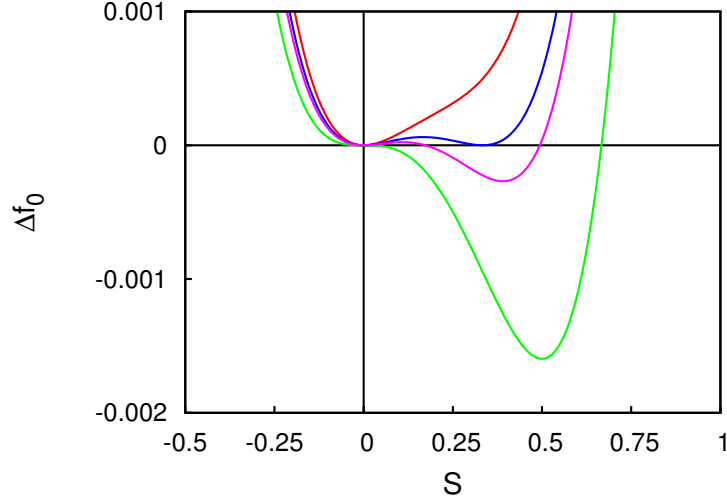


Figure 5.4. Plots of Δf_0 as a function of S for $T > T_{\text{IN}}$ (—), $T = T_{\text{IN}}$ (—), $T_{\text{IN}} > T > T^*$ (—), and $T = T^*$ (—).

is the n -th moment of the order parameter distribution function $\mathcal{P}(S)$.^{77,81} As discussed elsewhere,^{114,115} g_2 is different for different system sizes. However, at the phase transition g_2 turns out to be independent of system size such that cumulants for different system sizes intersect a unique point. As illustrated in Fig. 5.3, g_2 is almost independent of system size deep in the isotropic phase. As one approaches T_{IN} from above g_2 passes (for large systems) through a small maximum and decreases rapidly with decreasing temperature. Moreover, all of the three curves passes through a common intersection at $T_{\text{IN}} \simeq 1.02$ (see Fig. 5.3).

Having knowledge of the exact phase transition temperature we estimate $T^* \simeq 0.99$ from Eqn. (4.8). Moreover for our model system we obtain $T^*/T_{\text{IN}} \simeq 0.97^\ddagger$ which is in good agreement with experimental systems, e.g., for MBBA $T^*/T_{\text{IN}} \simeq 0.90$.¹¹⁶ Hence, we conclude that our model provides a realistic description of the nematic host phase. In fact, taking the expressions $a = 8\rho/15$, $B = 32T\rho/105$, and $C = 64T\rho/315$ [see (Eqn. (4.18))] together with $T^* \simeq 0.99$ and $\rho = 0.92$ we cast the Landau-de Gennes free energy density (with respect to the isotropic phase) of the bulk fluid as

$$\Delta f_0 = \frac{2}{5}\rho (T - T^*) S^2 - \frac{8}{105}T\rho S^3 + \frac{4}{35}T\rho S^4. \quad (5.7)$$

Plots of Δf_0 as a function of S illustrate the stability of the isotropic and nematic phases at various temperatures (see Fig. 5.4). More specifically, at $T > T_{\text{IN}}$, Δf_0 has a single minimum at $S = 0$ indicating the stability of the isotropic phase. At $T = T_{\text{IN}}$ the coexistence of the nematic and isotropic phases is illustrated by the double minimum at $S = 0$ and $S = 1/3$. As long as the temperature is in the range of $T_{\text{IN}} > T > T^*$ the isotropic state is metastable. Finally, $T = T^*$ marks the limit of the stability of the isotropic phase such that only the nematic state is stable for $T < T^*$.

[‡] Notice that in Ref. 84 $T^*/T_{\text{IN}} \simeq 0.746$ and is slightly different from the value given above. This is simply a mistake in Ref. 84.

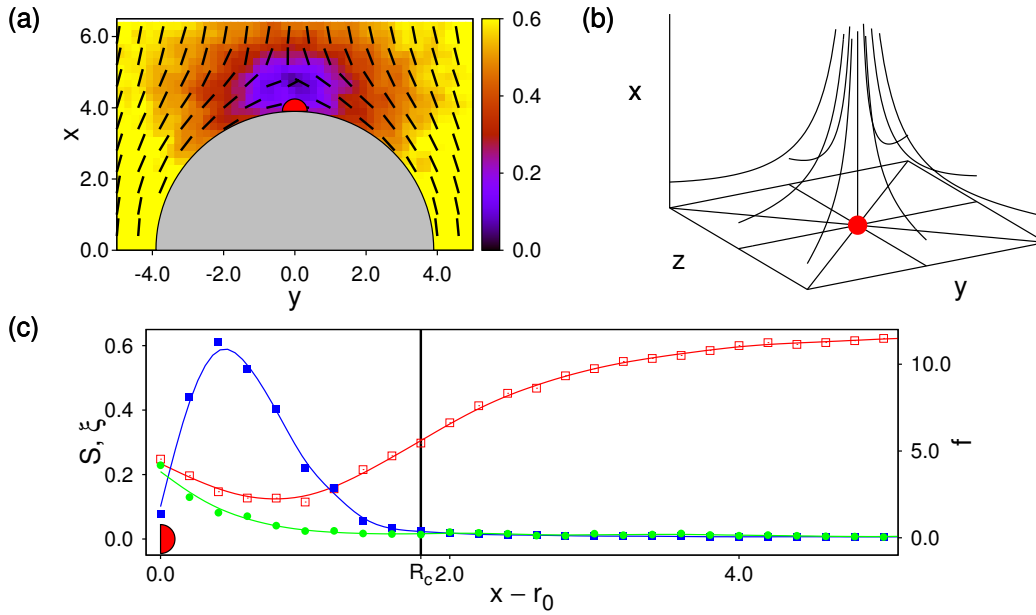


Figure 5.5. (a) Director field $\hat{n}(\mathbf{r})$ (dashes) and local nematic order parameter $S(\mathbf{r})$ (see attached color bar) projected onto the x - y plane. The gray semicircle marks the upper hemisphere of a colloidal particle with part of a Boojum defect topology centered on its north pole. (b) Three-dimensional plot of the variation of $\hat{n}(\mathbf{r}) = (x, y, -z)^T$ for a hyperbolic hedgehog defect topology. (c) Variation of $S(\mathbf{r})$ (left ordinate, \square), the contribution of the Frank free energy $f_{el}(\mathbf{r})$ [right ordinate, \blacksquare , see Eqn. (4.21)], and the local biaxiality order parameter $\zeta(\mathbf{r})$ (left ordinate, \bullet) as functions of $x - r_0$ and $z = 0$ cutting through the defect core. Notice that the data plotted have been averaged over a strip of width $\delta y = 1.2$ centered on $y = 0$ to get a reasonably smooth variation of all three quantities shown. The vertical solid line marks the radius R_{core} of the circular defect core. Red marks have been added to all three parts of the figure to assist the reader in relating them.

5.3 CORE REGION

We consider now a single colloid immersed in a nematic host phase. Plots of the local nematic order parameter $S(\mathbf{r})$ and the local director $\hat{n}(\mathbf{r})$ [see Fig. 5.5(a)] reveal the formation of a topological defect which is indicated by a rapid decrease of $S(\mathbf{r})$. As expected and already discussed for colloids with planar surface anchoring we observe two Boojum defects at the north and south pole of the colloid. More specifically, the sharp decline of $S(\mathbf{r})$ defines the shape of the defect visibly.

As already mentioned in Chapter 4 the energetic contribution of the defect core to the free energy Δf is somewhat special and has to be treated separately. In the core of the defect the structure of $\hat{n}(\mathbf{r})$ is similar to the hyperbolic hedgehog defect given by $\hat{n}(\mathbf{r}) = (x, y, -z)^T$ [see Fig. 5.5(a) and (b)]. Moreover, outside of the defect core the variation of $S(\mathbf{r})$ is rather small such that $\nabla S(\mathbf{r}) \approx 0$. Hence, the spatial variation of $\hat{n}(\mathbf{r})$ takes place on a larger length scale than the molecular scale. Con-

sequently, the elastic deformation of $\hat{\mathbf{n}}(\mathbf{r})$ can be described by the Frank free energy [see Eqn. (4.21)] which vanishes sufficiently far away from the colloidal surface [see Fig. 5.5(c)]. However, as illustrated in Fig. 5.5(c), $S(\mathbf{r})$ suddenly declines as one approaches the colloidal surface. Additionally, the Frank free energy passes through a sharp maximum inside the defect core. The drop of $S(\mathbf{r})$ indicates a large variation of $\hat{\mathbf{n}}(\mathbf{r})$ on a molecular scale such that the Frank free energy does not provide a quantitative description of the free energy anymore.

To account for the energetic contribution of the defect core we follow Lubensky *et al.*¹⁰⁹ who derived analytic expressions for the core energy considering analytic expressions for the director field, e.g., the hyperbolic hedgehog presented in Fig. 5.5(b). Because Boojum defects are surface defects we have to take into account the excluded volume of the colloid. In order to do that we integrate the director field over a hemisphere of the volume $\frac{2}{3}\pi R_{\text{core}}^3$ and obtain the free energy density of the defect core $f_{\text{core}} = K/R_{\text{core}}^2$ where R_{core} is the radius of the defect core and $K = K_1 = K_2 = K_3$. In this so-called one-constant approximation it is assumed that all three deformations (i.e., splay, twist, and bend) contribute equally to f_{el} . In fact, as discussed elsewhere⁸² this approximation is well satisfied for our model liquid crystal, such that $K = 1.66$. We determine R_{core} by cutting through the center of the defect core [i.e., along the x -direction for $y = z = 0$, see Fig. 5.5(c)] and taking R_{core} as that distance from the colloidal surface at which $S(\mathbf{r})$ drops below S_{IN} for the very first time. For $R_{\text{core}} \simeq 1.8$ we obtain $f_{\text{core}} \approx \frac{1}{2}k_B T$. This is in good agreement with the free energy values obtained from density functional theory.¹¹⁷

As we shall demonstrate later, defects of a pair of colloids at sufficient small distance interact and form thereby more complex defect topologies. We assume a constant free energy density f_{core} to approximate the defect core contribution to the free energy. Thus, we neglect the defect topology, particularly, the director field configuration inside the core. The assumption of a constant free-energy density inside the defect core is justified because f_{core} is of the same order of magnitude for different defect topologies.^{109,117} Hence, the free energy of the defect core is given by

$$F_{\text{core}} = f_{\text{core}} \int_{V_{\text{core}}} d\mathbf{r} = f_{\text{core}} V_{\text{core}} \quad (5.8)$$

where $V_{\text{core}} = \{\mathbf{r} | S(\mathbf{r}) \leq S_{\text{IN}}\}$ is the volume of the defect core. In practice, we determine V_{core} by dividing our system into a three-dimensional grid such that each cubic element of side length of 0.2 is used to sample and average local properties [e.g., $S(\mathbf{r})$, $\hat{\mathbf{n}}(\mathbf{r})$, $\mathbf{Q}(\mathbf{r})$, etc.] of the system. The volume of the cubes where $S(\mathbf{r}) \leq S_{\text{IN}}$ is equal to V_{core} . Furthermore, we compute the total local free-energy density

$$\Delta f(\mathbf{r}) = \Delta f_{\text{bulk}}(\mathbf{r}) + f_{\text{el}}(\mathbf{r}) + f_{\text{core}} \quad (5.9)$$

where

$$\Delta f_{\text{bulk}}(\mathbf{r}) = \frac{2}{5}\rho(T - T^*)S^2(\mathbf{r}) - \frac{8}{105}T\rho S^3(\mathbf{r}) + \frac{4}{35}T\rho S^4(\mathbf{r}) \quad (5.10)$$

accounts for the decrease of the local nematic order and

$$\begin{aligned} f_{\text{el}}(\mathbf{r}) &= \frac{1}{2}K_1[\nabla \cdot \hat{\mathbf{n}}(\mathbf{r})]^2 + \frac{1}{2}K_2[\hat{\mathbf{n}}(\mathbf{r}) \cdot \nabla \times \hat{\mathbf{n}}(\mathbf{r})]^2 + \frac{1}{2}K_3[\hat{\mathbf{n}}(\mathbf{r}) \times \nabla \times \hat{\mathbf{n}}(\mathbf{r})]^2 \\ &= \frac{1}{2}K \left\{ [\nabla \cdot \hat{\mathbf{n}}(\mathbf{r})]^2 + [\nabla \times \hat{\mathbf{n}}(\mathbf{r})]^2 \right\} \end{aligned} \quad (5.11)$$

for the elastic deformation of $\hat{\mathbf{n}}(\mathbf{r})$ in the one constant approximation. We obtain the free energy ΔF after the integration of $\Delta f(\mathbf{r})$ along x -, y -, and z -direction using trapezoidal rule.

5.4 THE EFFECTIVE INTERACTION POTENTIAL

Based on considerations presented in [Sec. 5.2](#) and [Sec. 5.3](#) we focus on the description of the effective interactions between a pair of Boojum colloids mediated by the nematic host phase. At sufficient small distances ($r_{12} = |\mathbf{r}_{12}|$) between the colloidal centers of mass, the defects interact with each other. In [Fig. 5.6\(a\)-\(c\)](#) we illustrate defect topologies for some representative colloidal configurations. More specifically, for $\theta = 0^\circ$ ($\cos \theta = \hat{\mathbf{n}}_0 \cdot \hat{\mathbf{r}}_{12}$) we observe a torus between the colloids. As θ increases the toroidal defect structure undergoes a transition and two isolated points are exhibited at the surfaces, e.g., for $\theta = 30^\circ$. Finally, for $\theta = 90^\circ$ we observe the formation of two line defects of finite length connecting the colloidal poles.

Plots presented in [Fig. 5.6\(d\)-\(f\)](#) and [Fig. 5.6\(g\)-\(i\)](#) are projections of $\hat{\mathbf{n}}(\mathbf{r})$, $S(\mathbf{r})$, and $\zeta(\mathbf{r})$ onto the x - y plane for same colloidal configuration as given in [Fig. 5.6\(a\)-\(c\)](#). Using these plots we notice that $\hat{\mathbf{n}}(\mathbf{r}) = \hat{\mathbf{n}}_0$ at sufficient large distances from the colloidal surface. However, in the vicinity of the colloidal surface $\hat{\mathbf{n}}(\mathbf{r})$ deviates from $\hat{\mathbf{n}}_0$. Moreover, as expected from previous theoretical considerations we observe an increase of the local biaxiality order parameter $\zeta(\mathbf{r})$ [see [Eqn. \(4.1\)](#)] as the nematic order parameter declines. Using the highest value of $\zeta(\mathbf{r})$ we can locate the center of the defect. A careful analysis of $\zeta(\mathbf{r})$ reveals that all of the defects presented in [Fig. 5.6](#) are surface defects. However, at sufficient small separations cores of these defects which are defined by $S(\mathbf{r}) \leq S_{\text{IN}}$ may overlap and form complex structures presented in [Fig. 5.6\(a\)-\(c\)](#).

The presence of biaxiality provides an alternative route for computing f_{el} namely by means of $\mathbf{Q}(\mathbf{r})$. As introduced in [Chapter 4](#) one would differentiate $\mathbf{Q}(\mathbf{r})$ via [Eqn. \(4.19\)](#) in order to determine f_{el} . Because the core of the defect is biaxial and not isotropic the tensor field $\mathbf{Q}(\mathbf{r})$ is free of singularities. Hence, f_{el} would also provide a correct description inside the defect core. Thus, the treatment of the defect core separately becomes redundant. Unfortunately, in practice we found, that our data are too noisy (especially inside the defect core) to follow this route. Moreover, because of the large spatial variation of $\hat{\mathbf{n}}(\mathbf{r})$ inside the defect core we would need a much finer discretization of our system. However, this would increase the number of MC cycles which are needed to sample statistically significant averages of local quantities. A further substantial increase of the number of MC cycles is therefore impossible

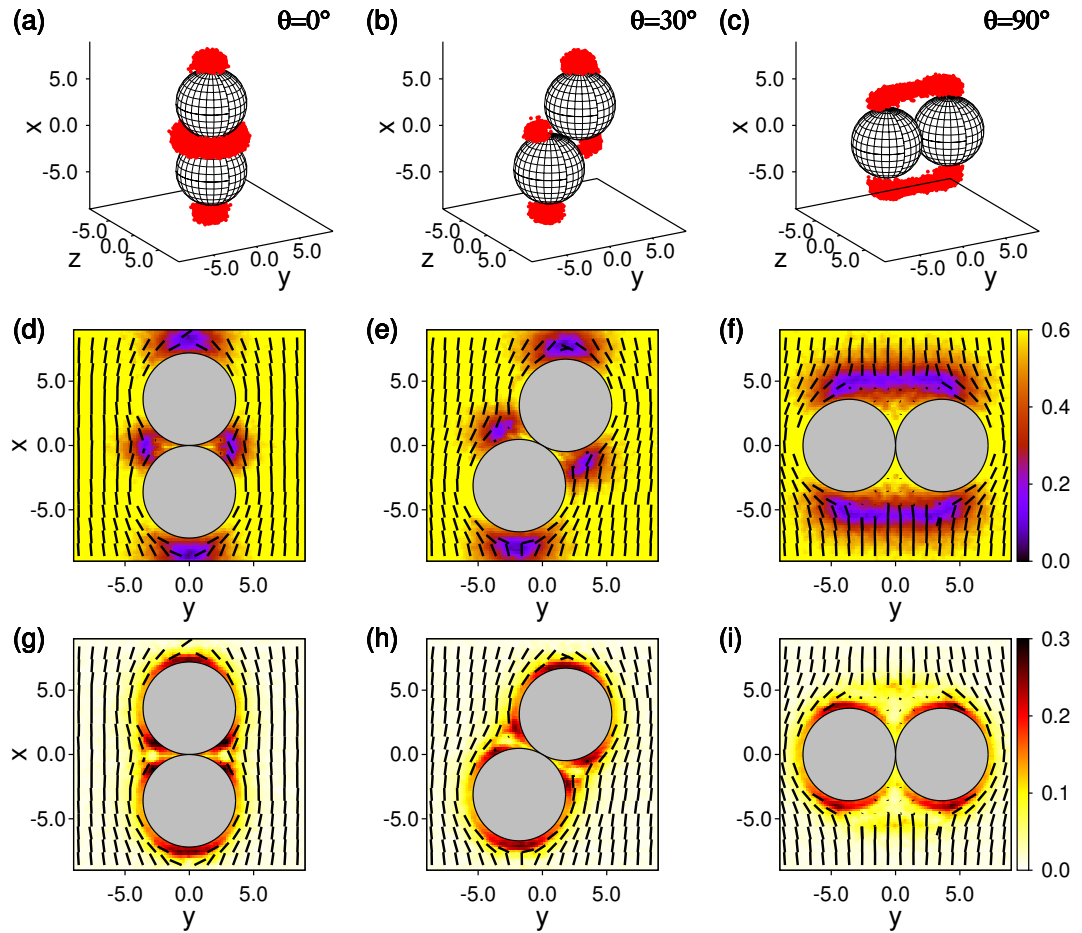


Figure 5.6. (a)-(c) show plots of the three-dimensional defect topologies of a pair of colloids (gray spheres) immersed in a nematic host fluid for various angles θ between the center-of-mass distance vector \mathbf{r}_{12} and the far-field nematic director $\hat{\mathbf{n}}_0$ given in the plots. Defect regions are colored in red subject to the condition $S(\mathbf{r}) \leq \frac{1}{3}$. Plots (d)-(f) show the corresponding local director field (dashes) and the local nematic order parameter (see attached color bar) projected onto the x - y plane where gray circles are similar two-dimensional projections of the colloids. Plots of the local biaxiality order parameter are shown in (g)-(i). In all cases $\hat{\mathbf{n}}_0 \cdot \hat{\mathbf{e}}_x = 1$.

presently for practical reasons. Hence, the *ansatz* presented in Sec. 5.3 is the best possible approximation we can use. We emphasize that data presented in Fig. 5.5(c) appear to be rather smooth because we averaged them over a certain region.

As illustrated by the plots in Fig. 5.6, $S(\mathbf{r})$, $\hat{\mathbf{n}}(\mathbf{r})$, and V_{core} vary with θ . Therefore, it seems intuitive to introduce the free energy difference as

$$\Delta F = \int d\mathbf{r} \Delta f_{\text{bulk}}(\mathbf{r}) + f_{\text{el}}(\mathbf{r}) + f_{\text{core}} \quad (5.12)$$

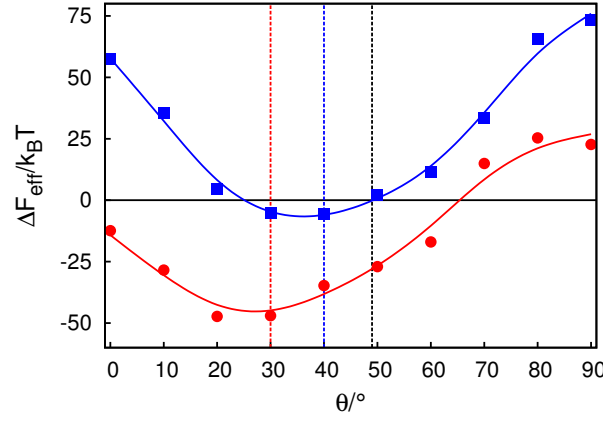


Figure 5.7. The effective free energy ΔF_{eff} in units of the change in free energy associated with an isolated Boojum colloid ΔF_{B} . Vertical dashed lines mark minima in the curves plotted; the limiting value $\theta \approx 49^\circ$ is also indicated (see text); $r_{12} = 7.2$ (\bullet), $r_{12} = 8.0$ (\blacksquare).

where it turns out that all three contributions are of the same order of magnitude. Instead of analyzing the free energy difference with respect to the unperturbed nematic phase we turn in the discussion of the effective free energy difference

$$\Delta F_{\text{eff}} = \Delta F - 2\Delta F_{\text{B}} \quad (5.13)$$

between a pair of Boojum colloids at sufficient small distance and two isolated Boojum colloids. Here, ΔF_{B} is the free energy associated with the perturbation of the nematic phase due to the presence of an isolated Boojum colloid.

Plots of ΔF_{eff} as functions of θ reveals some interesting aspects (see Fig. 5.7). First, ΔF_{eff} is either positive or negative with respect to θ indicating storage and release of free energy, respectively. The change in free energy with respect to two isolated colloids drives the colloidal self-assembly. Hence, any increase and decrease of ΔF_{eff} can be understood as repulsive and attractive interactions mediated by perturbations of the nematic host phase. Second, the minimum of ΔF_{eff} shifts to larger θ_{min} as the distance r_{12} is increased which agrees perfectly with experimental⁵⁰ and theoretical^{51,118} observations. Moreover, as discussed elsewhere¹¹⁸ θ_{min} increases monotonically up to a limit. One finds this limit by considering a pair of isolated Boojum colloids. The spatial variation of $\hat{n}(\mathbf{r})$ is similar to that of an electric field between two interacting quadrupoles. The angle dependence of the associated electrostatic energy is then given by

$$U \propto 9 - 90 \cos^2 \theta + 105 \cos^4 \theta \quad (5.14)$$

where $\theta_{\text{min}} = 49^\circ$ follows without further ado. For the smallest distance, $\theta_{\text{min}} \simeq 30^\circ$ in perfect agreement with experiment and theory.^{10,50,51}

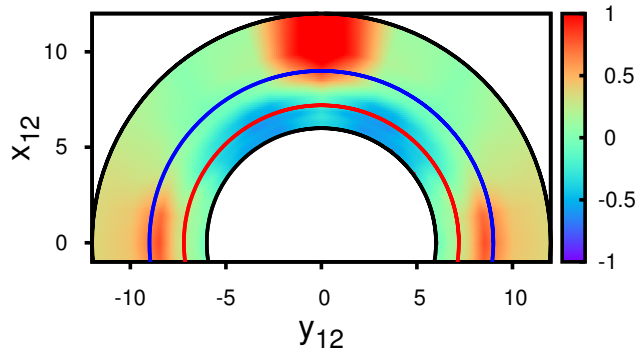


Figure 5.8. Contour plot of $\Delta F_{\text{eff}}/\Delta F_{\text{B}}$ (see attached color bar) as a function of $\mathbf{r}_{12}^{\text{T}} = (x_{12}, y_{12}, 0)^{\text{T}}$. Curves plotted in Fig. 5.7 correspond to $r_{12} = 7.2$ (—) and to $r_{12} = 8.0$ (—), respectively.

Moreover, from Fig. 5.7 we also notice a distance dependence of ΔF_{eff} . In fact, for the larger separation ΔF_{eff} is shifted upwards and indicates the presence of a larger repulsive regions. We investigate the distance dependence of ΔF_{eff} further and present a detailed illustration of the free-energy landscape where ΔF_{eff} is plotted as a function of the polar vector \mathbf{r}_{12} (see Fig. 5.8). Here, we find the global minimum of ΔF_{eff} at $r_{12} = 7.2$ and $\theta \simeq 30^\circ$, again in perfect agreement with theory and experiment.^{10,50,51} Data shown in Fig. 5.8 correspond to an effective coarse-grained potential where the interactions of the colloids and the nematic host phase are implicit. Hence, we are now in the position to perform simulations with several colloidal particles to check the validity of our assumptions.

For reasons of convenience we mimic the pseudo-two-dimensional experimental setup and perform two-dimensional coarse-grained MC simulations where the interactions between colloids and host phase are implied in ΔF_{eff} . We generate representative set of colloidal configurations in the canonical ensemble by employing a

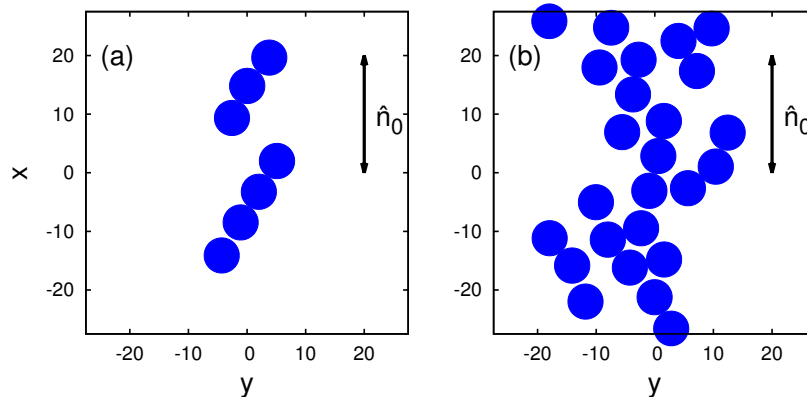


Figure 5.9. “Snapshots” from canonical-ensemble MC simulations of colloidal disks immersed in a nematic host phase taken into account implicitly via the effective interaction potential ΔF_{eff} shown in Fig. 5.8. (a) $\phi = 0.065$, (b) $\phi = 0.234$ ($s_x = s_y = 50$ and $\hat{\mathbf{n}}_0 \cdot \hat{\mathbf{e}}_x = 1$). The direction of the far-field director $\hat{\mathbf{n}}_0$ is indicated in the figure.

conventional Metropolis algorithm⁷³ such that the probability density is proportional to $\exp(-\Delta F_{\text{eff}}/\Delta F_{\text{B}})$. The pairwise interactions are treated as follows. We store ΔF_{eff} on a two-dimensional grid with a spacing of 0.2 and interpolate ΔF_{eff} in a bilinear fashion between the four nearest nodes if the distance vector between two colloidal centers of mass does not point directly on one of these nodes.

In Fig. 5.9, we illustrate characteristic “snapshots” of colloidal structures at thermodynamic equilibrium. We display those for different packing fractions $\phi = N_c \pi r_0^2 / s_x s_y$ where s_α is the dimension of the simulation cell in α -direction ($\alpha = x, y$). For small packing fractions the colloids form straight chains which are tilted with respect to \hat{n}_0 [see Fig. 5.9(a)]. The angle which is enclosed between the chain and \hat{n}_0 is approximately 30° . For large packing fractions we observe the formation of a more extended colloidal network [see Fig. 5.9(b)]. Both illustrations in Fig. 5.9 reveal a remarkable resemblance of colloidal structures with experimental systems shown in 1(b) and (c) of the work by Smalyukh *et al.*⁵⁰

THE IMPACT OF COLLOIDAL ANCHORING ON THE SMECTIC A PHASE

In the previous chapter, we showed that spherical colloids exhibit anisotropic interactions if they are dispersed in an ordered phase, such as the nematic phase. The origin of these effective interactions is found in local perturbations of the nematic order parameter and director field. We quantify these perturbations in order to extract an effective potential. Moreover, by using this effective potential in coarse-grained simulations we reproduce typical colloidal structures observed in experiments thus validating our treatment.

Hence, the mismatch of the orientational symmetry of the nematic phase and the colloidal anchoring conditions gives rise to perturbations of the director field that drive the colloidal self-assembly. Replacing the nematic host phase by a phase exhibiting an orientational symmetry different from the nematic one gives rise for other perturbations and defects which consequently affects the colloidal self-assembly. For example, colloids dispersed in a cholesteric phase (i.e., the chiral counterpart of the nematic phase) exhibit ring and line disclinations encircling the colloid in a twisted fashion.^{52–54,119} As reported by Jampani *et al.*⁵⁵ these colloids exhibit very complex quadrupole-like interactions where the assumption of pairwise additivity is not satisfied anymore.

In all of these phases (i.e., nematic, cholesteric, and blue phases) positional order is short-ranged like in an isotropic fluid. However, recent experimental works^{56–58} consider liquid crystalline phases with the one-dimensional positional order in addition to the orientational order, i.e., the smectic A phase. More specifically, it is shown that colloidal self-assemblies undergo a discontinuous and reversible transition as the nematic host fluid passes the nematic-smectic A phase transition. In order to study this phenomenon we derive a novel potential u_{mm}^{Y} [see Eqn. (3.19)] which exhibits realistic phase behavior, elasticity and dynamics as we shall demonstrate later. Interactions between the mesogens and a colloid of radius $r_0 = 6$ as well as mesogens and substrates separated by $s_z = 38$ are modeled in the same fashion as described in Chapter 5, namely via u_{mc} [see Eqn. (3.13)] and u_{ms} [see Eqn. (3.21)], respectively. We investigate the impact of colloidal surface anchoring on the perturbations of the liquid crystalline phases across the nematic-smectic A phase transition. Therefore, we follow considerations introduced in Chapter 5 and Ref. 59 and compute ensemble averages in the isothermal-isobaric ensemble for fixed $4 \times 10^4 \leq N \leq 7 \times 10^4$ and $P_{\parallel} = 1.0$ while studying the temperature dependence in the range of $0.7 \leq T \leq 0.9$.

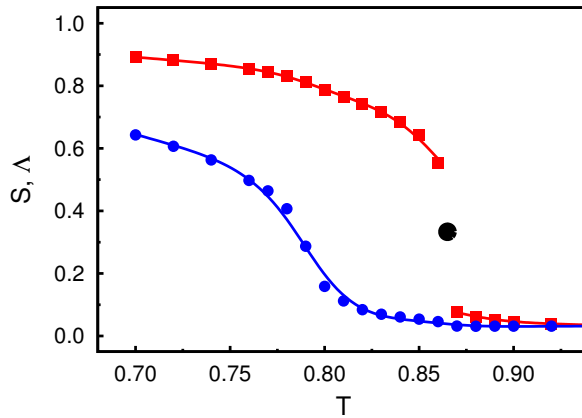


Figure 6.1. Plots of S (■) and Λ (●) as functions of temperature T for $N = 5000$. (●) marks $S_{\text{IN}} = \frac{1}{3}$ at the isotropic-nematic phase transition (see text). Lines are fits intended to guide the eye.

6.1 BULK PROPERTIES

As in the previous chapter, we begin the presentation of our results with a discussion of bulk properties of the host fluid. We characterize the phases via the nematic S and the smectic A order parameter Λ [see Eqn. (1.2)]. The temperature dependence of S and Λ across the isotropic-nematic and nematic-smectic A phase transition is illustrated in Fig. 6.1. At high temperature both S and Λ are small indicating a thermodynamically stable isotropic phase. Because of the finite size of the system neither S nor Λ vanish completely in the isotropic phase. Finite-size effects of this sort have been discussed in depth in the previous chapter (see Sec. 5.2) as far S is considered. Similar finite size effects observed for Λ are rationalized as following. Λ is a measure of density oscillation with a wave length d (i.e., layer separation). Hence, Λ increases if the location of the centers of mass of the mesogens are arranged periodically along \hat{n}_0 . However, also in phases without any positional long-range order (e.g., isotropic and nematic) configurations consisting of a few particles can be found where the centers of mass of the particles are separated by a particular but nonuniform d . In a system of infinite extent all possible values for d are realized equally such that all spurious effects of periodicity averages out. In a system of finite extent this gives rise for a small but non vanishing value of Λ .

As the temperature is decreased, we observe the isotropic-nematic phase transition indicated by a sudden increase of the nematic order parameter whereas the smectic A order parameter remains unchanged and relatively small. The nematic-smectic A phase transition occurs as the temperature is lowered further. The formation of smectic layers is illustrated by an increase of Λ (see Fig. 6.1). Again, we

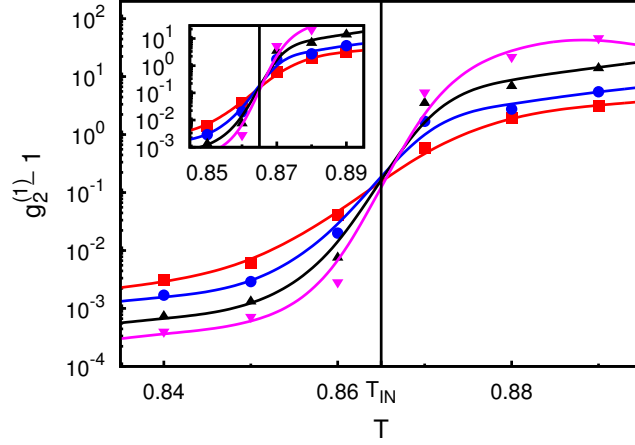


Figure 6.2. Plots of $g_2^{(1)} - 1$ as a function of temperature T and for various system sizes; $N = 500$ (■), $N = 1000$ (●), $N = 2500$ (▲), $N = 5000$ (▼). The horizontal line at the intersection of the curves marks the temperature $T_{\text{IN}} \simeq 0.87$ at the isotropic-nematic phase transition. Inset is an enlargement in the vicinity of T_{IN} and lines are fits intended to guide the eye.

determine T_{IN} via finite-size scaling theory. Therefore, we follow the considerations introduced in Sec. 5.2 and compute the second order cumulant

$$g_2^{(1)} = \frac{\langle s_1^2 \rangle}{\langle s_1 \rangle^2} \quad (6.1)$$

where $s_1 = -\frac{1}{2}S + \zeta$ is the middle eigenvalue of Q [see Eqn. (4.4)]. Notice, the usage of the middle eigenvalue of Q as opposed to the largest one as discussed in Sec. 5.2 is also suitable to locate T_{IN} as demonstrated by Greschek and Schoen.⁸¹ These authors also confirmed scaling laws

$$\langle S^n \rangle \propto N^{-n/2}, \quad n > 0 \quad (6.2)$$

$$\langle s_1 \rangle \propto N^{-1} \quad (6.3)$$

$$\langle s_1^n \rangle \propto N^{-n/2}, \quad n \geq 2 \quad (6.4)$$

in the isotropic phase. Hence, $g_2 = \langle S^2 \rangle / \langle S \rangle^2$ [see Eqn. (5.5)] is independent of system size and $g_2^{(0)} \propto N$ deep in the isotropic phase. Both expectations are confirmed by Fig. 5.4 and Fig. 6.1.

In addition to the different scaling behavior, g_2 exhibits a maximum in the isotropic close to T_{IN} . This behavior of g_2 makes the determination of T_{IN} difficult (see Fig. 5.3). On the other hand, $g_2^{(1)}$ does not exhibit any local extrema as illustrated in Fig. 6.1. Hence, practically it turned out to be more accurate to determine T_{IN} via $g_2^{(1)}$ rather than g_2 . Plots of $g_2^{(1)} - 1$ as a function of temperature for different system sizes reveal a common intersection of the curves at $T_{\text{IN}} \simeq 0.87$ (see Fig. 6.2). Moreover, $S_{\text{IN}} \simeq 0.35$

in our system and therefore it is in perfect agreement with the predicted value of $S_{\text{IN}} = \frac{1}{3}$ by the Landau-de Gennes theory (see [Sec. 4.2](#)).

Finite-size effects concerning the isotropic-nematic phase transition are found for $500 \leq N \leq 5000$. As illustrated in [Fig. 6.1](#), for a system composed of 5000 mesogens the system is large enough such that the isotropic-nematic phase transition appears almost discontinuous indicating the disappearance of finite-size effects. Unfortunately, a similar analysis cannot be performed for the nematic-smectic A phase transition. Because the smectic A order parameter Λ quantifies the periodicity of smectic layers one needs to analyze its dependence on the number of this layers that are composed of a host of mesogens. Hence, to study finite-size effects of Λ a much larger range of N has to be considered than for the isotropic-nematic phase transition. However, the consideration of such huge systems increase the CPU time and is simply not practical presently. Therefore we locate the nematic-smectic A phase transition by determining the point of inflection of $\Lambda(T)$. From this approach of Λ (see [Fig. 6.1](#)) we obtain $T_{\text{NSmA}} \simeq 0.78$.

After characterizing structural properties of our model we turn into a discussion of its dynamics. Therefore, we investigate self-diffusion along and perpendicular to the longer axes of the mesogens. We define $\mathbf{r}_i^{\parallel} \equiv (\mathbf{r}_i \cdot \hat{\mathbf{u}}_i)\hat{\mathbf{u}}_i$ and $\mathbf{r}_i^{\perp} \equiv \mathbf{r}_i - \mathbf{r}_i^{\parallel}$ and introduce the mean-square displacement

$$\Delta r_{\parallel,\perp}^2(t) = \frac{1}{N} \sum_{i=1}^N \left\langle [\mathbf{r}_i^{\parallel,\perp}(t+t_0) - \mathbf{r}_i^{\parallel,\perp}(t_0)]^2 \right\rangle_{t_0} \quad (6.5)$$

where $\langle \dots \rangle_{t_0}$ indicates an average over a set of different initial times $\{t_0\}$ due to stationary of the self-diffusion process.¹²⁰ Hence, we introduce the anisotropic diffusion coefficients

$$D_{\parallel} = \lim_{t \rightarrow \infty} \frac{\Delta r_{\parallel}^2(t)}{2t} \quad (6.6)$$

and

$$D_{\perp} = \lim_{t \rightarrow \infty} \frac{\Delta r_{\perp}^2(t)}{4t} \quad (6.7)$$

as a quantitative measure for the self-diffusion parallel and perpendicular to the mesogens' axes, respectively, at thermodynamic equilibrium. Data for $\Delta r_{\parallel,\perp}^2(t)$ and $D_{\parallel,\perp}$ presented here are obtained from molecular dynamic simulation in the isothermal-isobaric ensemble as described elsewhere.¹⁰⁴

Irrespective of the nature of the phase, Δr_{\perp}^2 exhibit two different regimes [see [Fig. 6.3\(a\)](#)]. At short time scales all three phases exhibit ballistic motion, such that $\Delta r_{\perp}^2 \propto t^2$. Ballistic motion arises as long as molecular interactions do not matter such that the motion of the mesogens is dominated by the free volume. Consequently, Δr_{\perp}^2 can be represented by a master curve for all three phases and for $t < 0.1$. The time interval of the ballistic motion depends on the density and kinetic energy. Hence, in the range $0.1 \leq t \leq 1.0$ molecular interactions become important and the motion of the

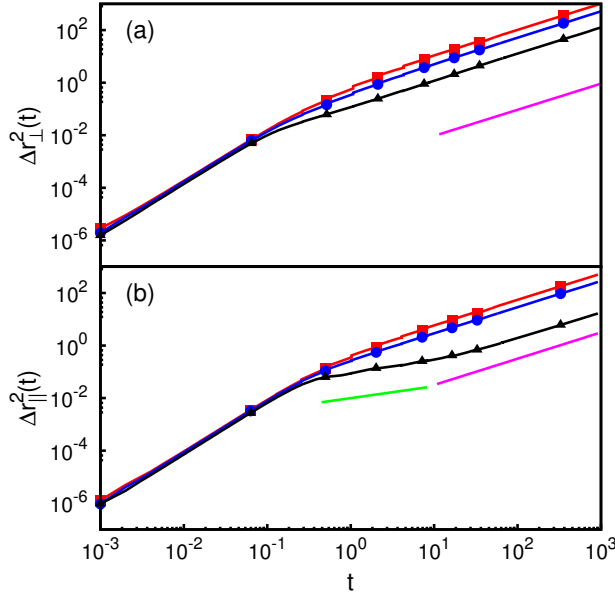


Figure 6.3. (a) Double-logarithmic plots of the mean square displacements $\Delta r_{\parallel}^2(t)$ as functions of time t . (b) as (a), but for $\Delta r_{\perp}^2(t)$. In both parts of the figure (■) $T = 0.90$ (isotropic), (●) $T = 0.84$ (nematic), (▲) $T = 0.70$ (smectic A) (see also Fig. 6.1). (—) and (—) indicate slopes proportional to t and t^{μ} ($\mu = 0.45$), respectively. Data are obtained from molecular dynamics simulations in an isobaric-isothermal ensemble (see Ref. 104 for more details).

mesogens changes from ballistic to diffusive such that $\Delta r_{\perp}^2 \propto t$ for $t \rightarrow \infty$. We identify ballistic and diffusive regimes of Δr_{\parallel}^2 for short and long time scales, respectively [see Fig. 6.3(b)]. Moreover, curves of Δr_{\parallel}^2 and Δr_{\perp}^2 are similar for the isotropic and nematic phase. However, in the smectic A phase the ballistic motion changes to subdiffusive motion where $\Delta r_{\parallel}^2 \propto t^{\mu}$ ($\mu < 1$) before becoming diffusive at long time scales. The subdiffusive regime at intermediate times reflects the one-dimensional positional ordering. In fact, diffusion along the global director, i.e., the diffusion from one layer to another is inhibited because of close and regular packing of layers. However, because the structure *within* the layer remains fluidic, diffusive behavior sets in but for longer times compared with the nematic or isotropic phase.

Because all mean-square displacements exhibit diffusive behavior at sufficiently long times (see Fig. 6.3), we compute D_{\parallel} and D_{\perp} via Eqn. (6.6) and Eqn. (6.7), respectively. Plots presented in Fig. 6.4(a) illustrate that $D_{\parallel, \perp}$ decrease monotonically as the temperature is lowered. In the isotropic phase $D_{\parallel} \approx D_{\perp}$ which makes sense because no spatial direction is distinguished. However, as one enters the nematic phase one sees from Fig. 6.4(b) that diffusional isotropy is abrogated. More specifically, diffusion along the mesogens' axes is larger than perpendicular to it such that $D_{\parallel} > D_{\perp}$ as also found in experiments.¹²¹ As one approaches the nematic-smectic A phase transition $D_{\parallel} \approx D_{\perp}$ [see Fig. 6.4(b)] because the diffusion along the mesogens' axes is inhibited. This effect is more pronounced deep in the smectic A phase

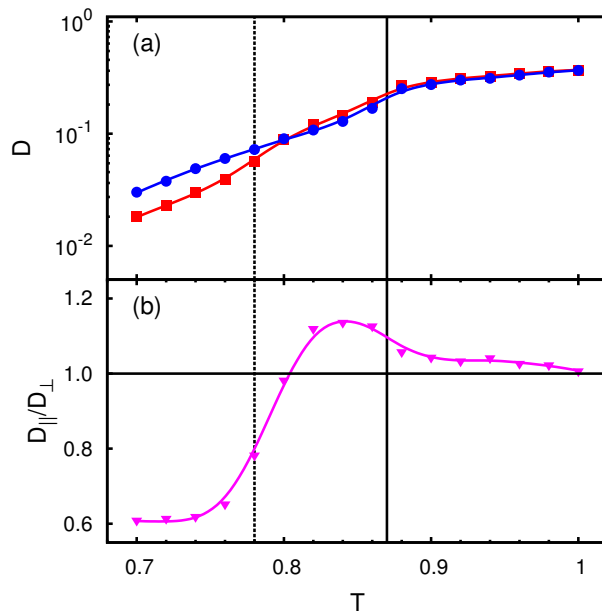


Figure 6.4. (a) Semi-logarithmic plots of diffusion coefficients D_{\parallel} (■) and D_{\perp} (●) as functions of temperature T . (b) Plots of the ratio D_{\parallel}/D_{\perp} (▼) as a function of T . Vertical lines (—) and (---) mark the isotropic-nematic and nematic-smectic A phase transitions, respectively (see Fig. 6.1).

at lower temperature, such that $D_{\parallel} < D_{\perp}$ which is again in good agreement with experimental observation.¹²¹

In summary, as the temperature is lowered the density increases and the diffusion becomes small. At low temperature, smectic layers are robust such that the diffusion between the layers almost vanishes. However, diffusion perpendicular to the longer axes of the mesogens remains relatively large reflecting the fluidic structure within the layers. We emphasize that Fig. 6.1 and Fig. 6.4 are fully consistent with each other and reflect the complete picture of the phase behavior. In comparison with the corresponding isotropic-nematic phase transition, the nematic-smectic A phase transition appears rounded (see Fig. 6.1) indicating the formation of smectic layers the vicinity of the phase transition. However, these layers are neither planar in shape nor are they regularly stacked. Because of the finite size of the system the formation of these irregular layers does not average out and results in a non-vanishing value of Λ as already discussed before. In the thermodynamic limit, this effect vanishes. Therefore, the transition from $D_{\parallel} > D_{\perp}$ to $D_{\parallel} < D_{\perp}$ appears right before the nematic-smectic A phase transition whereas in experiments this transition occurs right after that transition.

Before closing the presentation of bulk properties, we finally investigate elastic properties of our model. We follow earlier considerations given in Sec. 4.5 where we introduce a method to compute the Frank elastic constants directly in molecular simulations. Data of E_{12} and E_{23} computed via Eqn. (4.40) and Eqn. (4.41), respectively, exhibit the expected linear behavior in terms of k_1^2 and k_2^2 for sufficient small wave numbers (see Sec. 4.5). However, as the temperature decreases towards the nematic-

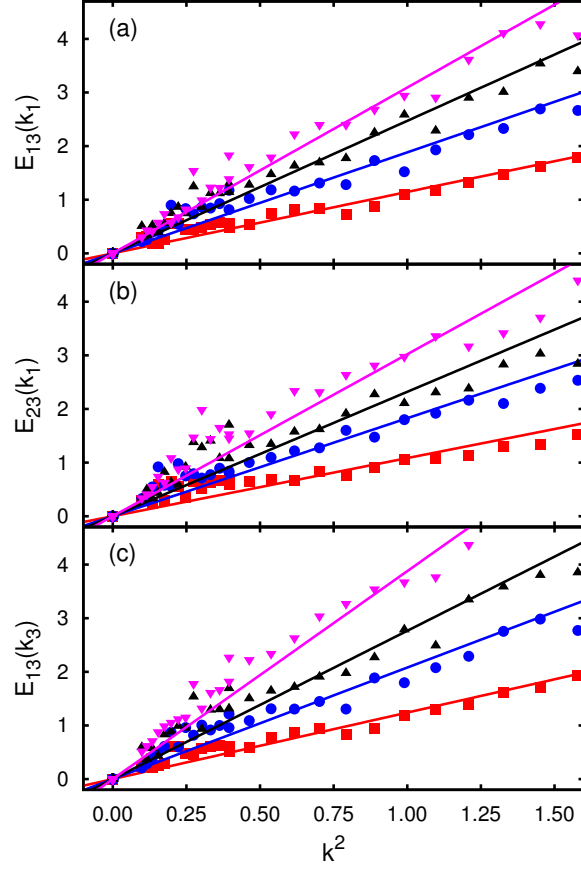


Figure 6.5. Plots of (a) $E_{13}(k_1)$, (b) $E_{23}(k_1)$, and (c) $E_{13}(k_3)$ as functions of the wave-numbers k_1^2 or k_3^2 and for temperatures $T = 0.86$ (■), $T = 0.84$ (●), $T = 0.82$ (▲), and $T = 0.80$ (▼), all of which are above the nematic-smectic A phase transition. Lines represent linear fits to the discrete simulation data.

smectic A phase transition the data presented in Fig. 6.5 become scattered. This is because fluctuations of the Fourier components $\tilde{Q}_{\alpha\beta} \propto \tilde{n}_{\alpha,\beta}$ decrease as the temperature is lowered.

From the slopes which we obtain from linear fits to the data presented in Fig. 6.5 we determine the elastic constants K_1 , K_2 , and K_3 and plot them as a function of temperature in Fig. 6.6(a). The so-called one-constant approximation, frequently used in theory and numerical calculations, is well satisfied for $T \geq 0.82$. Below this temperature, the elasticity becomes anisotropic reflected by different values of all three constants. More specifically, the elastic constant K_1 associated with the splay deformation increases monotonically and remains finite all the way down to the nematic-smectic A transition. On the other hand, K_2 and K_3 associated with twist and bend deformation, respectively, diverge as the temperature is decreased towards the nematic-smectic A phase transition. Furthermore, we observe a positive elastic anisotropy, i.e., $\Delta K = K_3 - K_1 > 0$ which increases with decreasing temperature. In fact, this is in good qualitative agreement with a real liquid crystal, e.g., 4'-n-octyloxy-

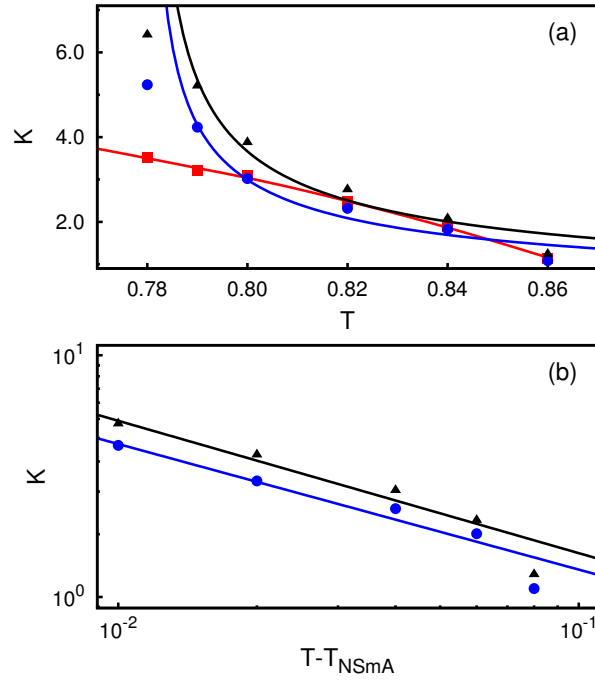


Figure 6.6. (a) Plots of the Frank elastic constants K_1 (■), K_2 (●), and K_3 (▲) as functions of temperature T . (b) Same as in (a), here (—) and (—) are fits of $K(T) = a(T - T_{\text{NSmA}})^\nu$ to the twist and bend elastic constants, respectively (see text).

4-cyanobiphenyl (8CB). For 8CB the elastic anisotropy ($K_3/K_1 = 8$)²⁰ is higher than in our model ($K_3/K_1 = 2$) at the nematic-smectic A phase transition. This can be rationalized by different aspect ratios of the mesogens in the experimental and in the model system. Compared with the model (aspect ratio of 2.2) the 8CB molecule is more elongated and has an aspect ratio of approximately 4.6.¹²² Hence, bend deformation of the 8CB liquid crystal is energetically more expensive than in our model which is reflected by the higher K_3 and thus by a higher elastic anisotropy.

Moreover, the temperature dependence of the twist and bend elastic constants follows an exponential law, i.e., $K_2, K_3 \propto (T - T_{\text{NSmA}})^{-\nu}$ as predicted by de Gennes¹²³ theoretically and confirmed in three independent experiments.^{124–126} The exponent ν describing the critical behavior of the elastic constants is $\frac{1}{2}$ at mean-field level whereas 0.66 is observed for experimental systems. Fitting the power law to our data [see figure Fig. 6.6(b)], we obtain $\nu = 0.55$ which is in between the mean-field value and that found experimentally. The anomaly of K_2 and K_3 in the nematic phase is rationalized by the formation of cybotactic clusters. Cybotactic clusters reported by de Vries¹²⁷ are smectic droplets arising in the vicinity of the nematic-smectic A phase transition because of fluctuations in local density.¹²³ The qualitative dependence of the Frank elastic constants on temperature as well as their critical behavior lends additional credibility to our model system.

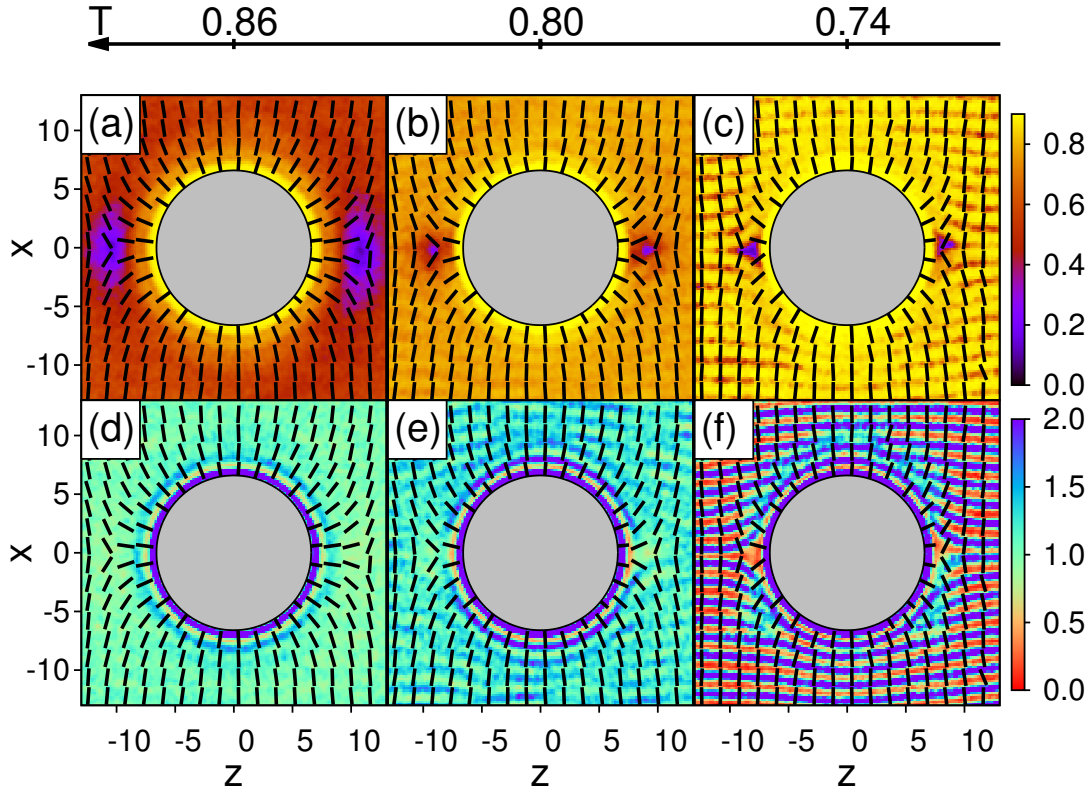


Figure 6.7. Plots of (a)-(c) local nematic order parameter $S(r)$ and (d)-(f) local density in the x - z plane, respectively (see attached color bars). The local director field is represented by dashes and the colloid by the gray circle. As indicated by the arrow above, the data in each column are obtained for the nematic phase at $T = 0.86$, in the nematic phase right before the nematic-smectic A phase transition at $T = 0.80$, and in the smectic A phase at $T = 0.74$, respectively.

6.2 COLLOID WITH HOMEOTROPIC ANCHORING

We now consider a system composed of a spherical colloid that is dispersed in a liquid-crystalline phase. Furthermore, we begin by focusing on a colloid with locally homeotropic surface anchoring. In comparison with previous works^{59,106,128} and in perfect agreement with experiments,^{10,58} we observe the formation of two regions where the nematic order is perturbed in the vicinity of the colloid's equator in the x - z plane [see Fig. 6.7(a)]. The formation of these defects can be rationalized as follows. At the colloidal surface the mesogens align homeotropically which is, however, not compatible with the global director \hat{n}_0 everywhere. As one moves away from the surface the impact of the colloidal surface anchoring decreases such that at a certain distance the influence of surface anchoring and that of \hat{n}_0 are equal. If both quantities compete with each other a topological defect arises because of the orientational

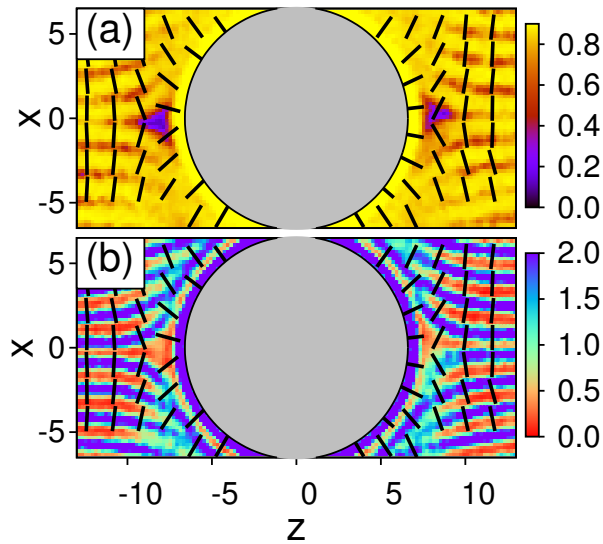


Figure 6.8. Enlargements of Fig. 6.7(c) and (f).

frustration of the mesogens. For a colloid with homeotropic surface anchoring the maximum mismatch between the mesogens' orientation at the colloidal surface and \hat{n}_0 is at the colloid's equator. Because of rotational symmetry, this orientational frustration arises around the colloid and therefore gives rise to a ring defect encircling the colloid which is consequently termed "Saturn ring".¹⁰

As the temperature is lowered nematic order increases. Hence, the perturbation of $\hat{n}(\mathbf{r})$ through the competing surface anchoring is energetically limited. This results in a contraction of the defect [see Fig. 6.7(b)]. In fact, not only the size of the ring defect but also its thickness decreases as the temperature is lowered which is in good agreement with experimental observations.⁵⁸ Furthermore, it has been shown in the experiments that a wider ring defect is transformed into a smaller one in the vicinity of the nematic-smectic A phase transition and finally disappears deep in the smectic A phase.⁵⁸ In our model, however, such a transformation is missing because of a stable monolayer of the mesogens at the colloidal surface. As discussed by Andrienko *et al.*¹⁰⁶ (in the same context) strong surface anchoring in addition to the mesogen-mesogen interactions in the favored side-side configuration stabilize the monolayer. This is illustrated by oscillations of the local density in the vicinity of the colloidal surface which is typical for a liquid-substrate interface [see Fig. 6.7(d) and (e)]. Furthermore, as expected the density is nearly homogeneous in the nematic phase sufficiently far from the colloidal surface [see Fig. 6.7(d) and (e)].

In the smectic A phase the ring defect does not vanish as predicted by experiments.⁵⁸ Instead, we observe a triangular shape of the defect [see Fig. 6.7(c) and Fig. 6.8(a)] corresponding to a low-density region [see Fig. 6.7(f) and Fig. 6.8(b)] around the colloid's equator. In these regions orientation of the mesogens is dominated neither by the strong surface anchoring nor by the orientation inside a smectic layer. Moreover, because of the relatively low density, the mesogens rotate more or

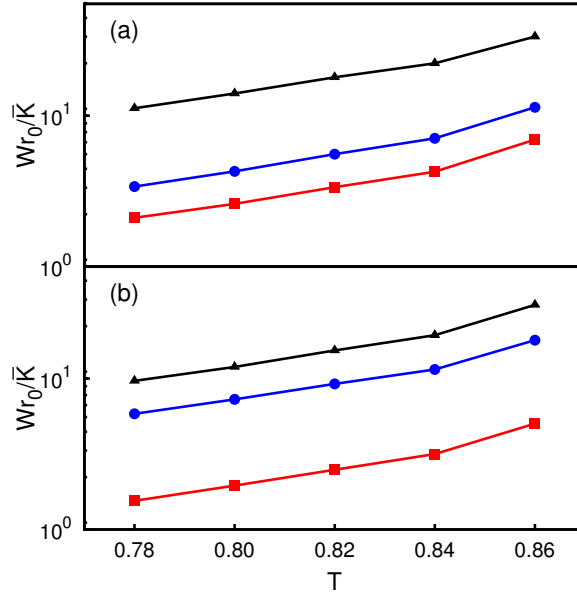


Figure 6.9. Semi-logarithmic plots of the relative anchoring strength Wr_0/\bar{K} as a function of temperature (in the range $T_{\text{NSmA}} \simeq 0.78 \leq T \leq T_{\text{IN}} \simeq 0.87$) for colloidal particles that anchor the mesogens in a planar (a) or homeotropic (b) fashion. Data in (a) are obtained for $\eta_{\text{mc}} = 2.5$ (■), $\eta_{\text{mc}} = 0.5$ (●), and $\eta_{\text{mc}} = 0.05$ (▲) and in (b) for $\eta_{\text{mc}} = 5.0$ (■), $\eta_{\text{mc}} = 1.0$ (●), and $\eta_{\text{mc}} = 0.1$ (▲).

less freely which causes the formation of a topological defect. This is only possible if surface anchoring is strong enough to compete with \hat{n}_0 and the bending of the layer.

We quantify this competition via the relative anchoring strength Wr_0/\bar{K} where $W = -\langle U_{\text{mc}} \rangle / 4\pi r_0^2$ the average mesogen-colloid potential energy per surface area of the colloid and $\bar{K} = (K_1 + K_2 + K_3)/3$ is a measure of the capability of the director field to be deformed. Strong and weak anchoring is characterized by the inequalities $Wr_0/\bar{K} \gg 1$ and $Wr_0/\bar{K} \ll 1$, respectively. This implies that three possible parameters exist that permit to tune the anchoring strength, namely W , r_0 , and \bar{K} . Because \bar{K} is a model-specific material constant, its variation is not possible unless one wants to change the model potential. For example, one can change K by using either the conventional Gay-Berne potential¹²⁹ for ellipsoids of revolutions or the Kihara potential for spherocylinders¹³⁰. Furthermore, the elastic anisotropy may be controlled via the aspect ratio of the mesogens because the bend elastic constant increases for increasing aspect ratios. The second useful parameter to manipulate the strength of surface anchoring is the colloidal radius r_0 . However, we emphasize that computer simulations with larger colloids automatically impose a larger number of mesogens which are needed to guarantee that the host phase is unaffected by the colloid at the periodic boundaries of the simulation cell. To perform the simulations in a reasonable time we fix $r_0 = 6$ such that $N \leq 7 \times 10^4$. Finally, as discussed elsewhere,¹²⁸ the variation of the inverse Debye screening length η_{mc} is a suitable tool to tune the anchoring strength [see Eqn. (3.24)].

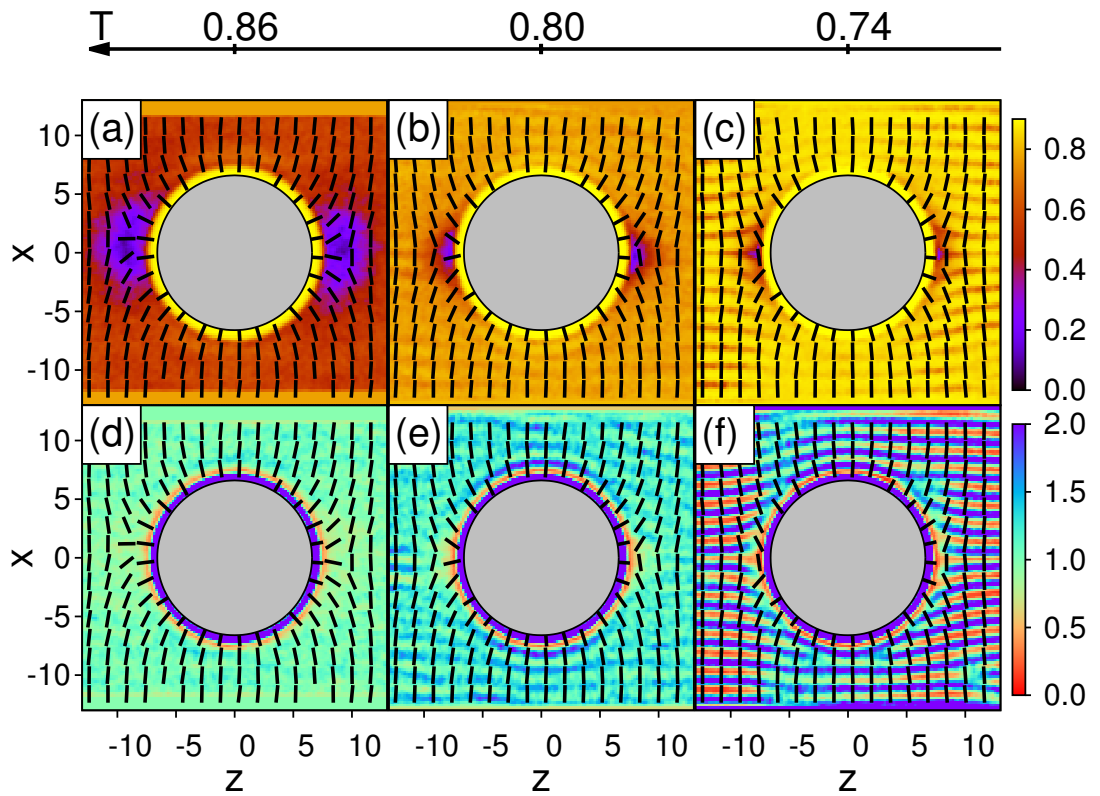


Figure 6.10. As Fig. 6.7 but for $\eta_{mc} = 5.0$.

As shown in Fig. 6.9(a) the anchoring strength decays monotonically as the temperature is lowered. At the nematic-smectic A phase transition (i.e., $T = 0.78$) the anchoring strength is neither strong nor weak [see Fig. 6.9(a)]. However, it is strong enough so that the surface of the colloid is able to impose its desired orientation and the smectic layers can form as clearly illustrated by the plot of $\rho(\mathbf{r})$ in Fig. 6.8(b). If one slightly reduces the anchoring strength (i.e., by setting $\eta_{mc} = 5.0$ and thereby reduces the range of u_{mc} [see Eqn. (3.24)], surface anchoring is still strong in the nematic phase. Thus, topological defects arising in the vicinity of the colloid in the nematic phase [see Fig. 6.10(a)-(b)] and also the local density profiles [see Fig. 6.10(d)-(e)] are similar to those obtained for a colloid with stronger surface anchoring (see Fig. 6.7). However, in the case of weaker surface anchoring the colloid cannot bend the smectic layers around its equator [see Fig. 6.10(f)] and therefore no low-density region occurs. Consequently, the smectic layers remain almost equidistant in the vicinity of the colloid as assumed by Zuhail *et al.*⁵⁸ For this reason the orientational frustration of the mesogens vanishes and no topological defect forms. Indeed, as illustrated by the plot of the local nematic order parameter [see Fig. 6.10(c)], local order is nearly homogeneous (apart from its wavy structure due to the layers) and almost

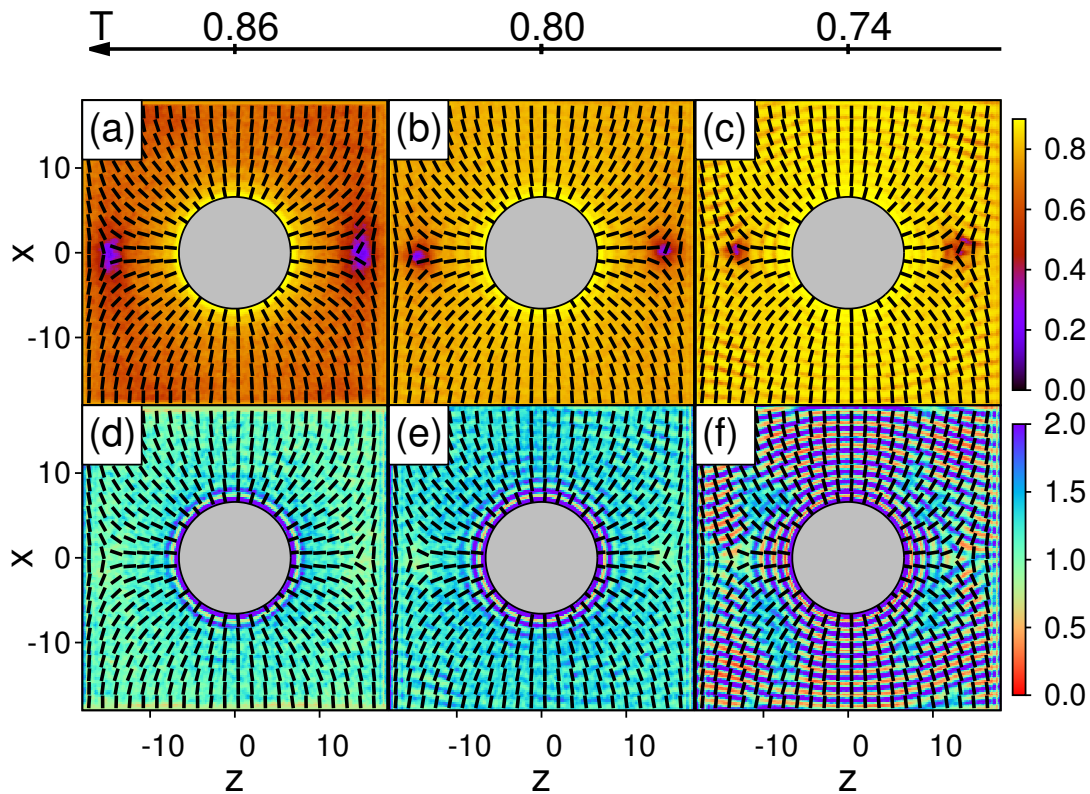


Figure 6.11. As Fig. 6.7 but for $\eta_{mc} = 0.05$.

unperturbed at the equator of the colloid. This is in perfect qualitative agreement with experiments.⁵⁸

Finally, we turn to a discussion of very strong surface anchoring. In order to realize that, we increase the range of u_{mc} by setting $\eta_{mc} = 0.05$. This has a crucial impact on the size of the ring defect. As discussed elsewhere¹²⁸ the length of the ring defect is proportional to η_{mc}^{-1} such that a much larger ring defect is stabilized by very strong surface anchoring (i.e., as η_{mc} decreases) even in the vicinity of the nematic-smectic A phase transition [see Fig. 6.11(a)-(b)]. On the other hand, $\rho(r)$ remains almost unaffected by the increased anchoring strength as illustrated in Fig. 6.11(d)-(e). However, in the smectic A phase the increase of the anchoring strength has a crucial impact on the local nematic order parameter as well as on the local density. As clearly depicted by the plot of $S(r)$ in Fig. 6.11(c), a non-vanishing defect remains in the smectic A phase which indicates a non-uniform layer spacing as discussed earlier in this section. However, now the defect is located at a much larger distance compared with, for instance, the situation depicted in Fig. 6.7(c). This is rationalized in terms of multiple layers formed around the colloid and stabilized by the surface anchoring over a large distance [see Fig. 6.11(f)]. This structure of concentric layers is known as *onion* structure in lyotropic liquid crystals and occurs if the lyotropic lamellar phase (an analog

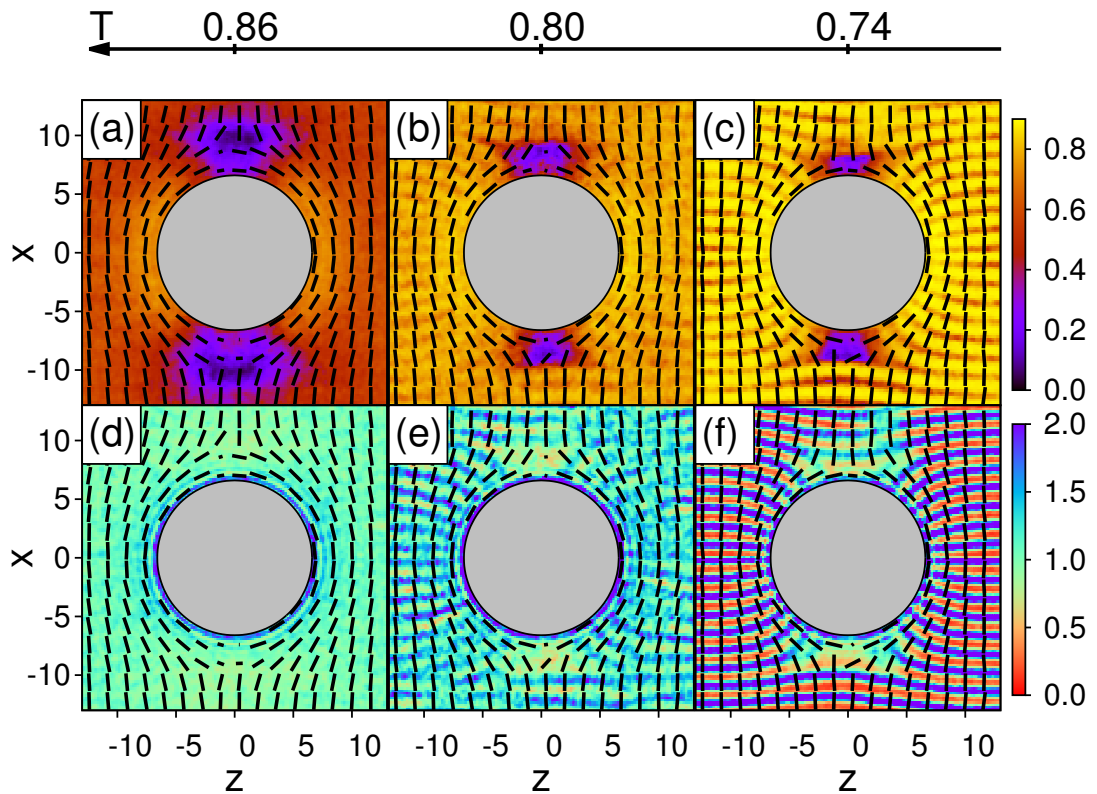


Figure 6.12. As Fig. 6.7 but for a colloid that anchors the mesogens in a planar fashion.

of a smectic phase) is exposed to a shear flow above a critical shear rate.^{131,132} Onion structures formed by thermotropic liquid crystals (e.g., 8CB) have been observed in micro-channels.¹³³ However, to the best of our knowledge the onion structure has never been reported for colloidal inclusions or observed in computer simulations before.

6.3 COLLOID WITH PLANAR ANCHORING

We now consider a colloid that anchors the mesogens in a locally planar fashion. Again, in perfect agreement with earlier works^{59,84} and experiments,^{10,57} we observe the formation of two Boojum defects in the nematic phase. This is indicated by a substantial decrease of $S(\mathbf{r})$ at the north ($\hat{\mathbf{r}}_i \cdot \hat{\mathbf{e}}_x = 1$) and south pole ($\hat{\mathbf{r}}_i \cdot \hat{\mathbf{e}}_x = -1$) of the colloid [see Fig. 6.12(a)]. The formation of these defects is explained by the competition between planar surface anchoring and the global director $\hat{\mathbf{n}}_0$.⁵⁹

As the temperature is lowered the defect region contracts because of the increasing global nematic order [see Fig. 6.12(b)]. Plots of the local density reveal that $\rho(\mathbf{r})$ is approximately constant sufficiently far away from the colloidal surface [see

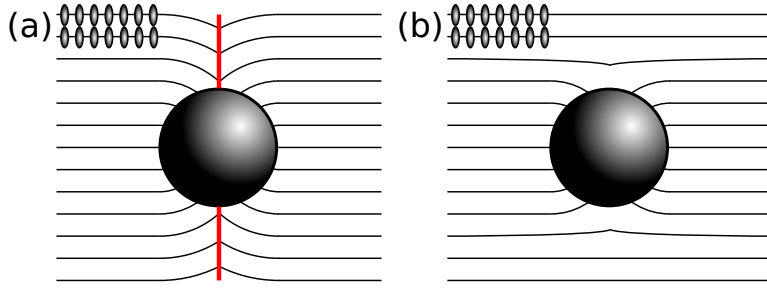


Figure 6.13. Schematic representation of bending of smectic layers caused by a spherical colloid with (a) strong and (b) weak planar surface anchoring. Red lines in (a) illustrate the discontinuous change of the smectic layer normal, so-called focal lines.

Fig. 6.12(d)-(e)]. After the fluid passes the nematic-smectic A phase transition (i.e., for $T < 0.78$), the size of the defects remains constant [see Fig. 6.12(c)] which is, however, in disagreement with experimental results.⁵⁷ From experiments, it is known that micro-spheres (i.e., colloidal particles of μm size) with strong planar surface anchoring and suspended in an 8CB liquid crystal exhibit an elongated defect line, the so-called focal line, parallel to \hat{n}_0 at the poles of the colloid when approaching the nematic-smectic A phase transition [see Fig. 1(a)-(c) of Ref. 57]. This is ascribed to the relatively large elastic anisotropy of 8CB, i.e., $K_3 = 8K_1$ at $T \gtrsim T_{\text{NSmA}}$. Because of this large elastic anisotropy, bend (and twist) deformations become energetically unstable and vanish at the phase transition. Hence, to satisfy the desired orientation at the colloidal surface and inside the smectic layers while keeping the layer separation constant, the layers have to bend. This bending is described by the stable splay deformation of $\hat{n}(\mathbf{r})$. Consequently, the focal line indicated by a low local order parameter arises [see Fig. 6.13(a)].

To clarify the discrepancy between the experimental observations⁵⁷ and the results presented here it is necessary to understand that there are two effects driving the formation of focal lines. These are, on the one hand strong surface anchoring responsible for the deformation of the smectic layers and layer compression, on the other hand, which is necessary to maintain an equal spacing between the layers everywhere. Because bend deformations are impossible to realize without varying the separation of the layers, their compression is reflected by a divergence of K_3 at the nematic-smectic A phase transition. In other words, the bend deformation is energetically inhibited in order to preserve equidistant layering. Hence, the bending of the smectic A layers is described by the splay deformation of $\hat{n}(\mathbf{r})$ only.^{6,21} In the vicinity of the colloidal particle the layers are bent strongly. To preserve the equidistant character of the smectic layers it is necessary to induce their deformation on a large length scale which finally results in the formation of a focal line [see Fig. 6.13(a)].

This formation depends crucially on the anchoring strength. As illustrated in Fig. 6.9(b), the anchoring strength decreases monotonically as the temperature is lowered and remains strong at the nematic-smectic A phase transition. Consequently, we assume the strong surface anchoring assumption to be valid in the smectic phase.

On the other hand, the compressibility of the smectic layers is rather weak in our model because of the repulsive nature of the mesogens in the end-end configuration.

As illustrated by the plot of $\rho(r)$ in Fig. 6.12(f) the smectic layers are bent strongly in the vicinity of the colloidal surface. However, it is not only the layers, which are destroyed by the colloidal particle that are affected. On account of the strong surface anchoring a few layers near the north and south pole which would not be interrupted by the mere presence of the colloid are, in fact, bent towards the colloidal surface such that they are “ripped apart” [see Fig. 6.12(f)]. To obtain a focal line, layers at sufficiently larger distances from the colloidal surface have to follow the strong deformation of the “ripped” layer to preserve equidistance. However, as shown by the plot of $\rho(r)$ in Fig. 6.12(f) and by the sketch in Fig. 6.13(b) this is not the case in our model. Instead, we observe slightly bent layers above and below the colloid towards the colloidal surface. Moreover, on account of this, the equidistant nature of the smectic layers is perturbed at the north and south pole of the colloid. This then gives rise to the formation of a low-density region where the local density corresponds to the density of a nematic phase at higher temperatures. Hence, we observe the formation of two point-like defects.

To increase layer compression we decrease the temperature to $T = 0.7$, close to the liquid-solid phase transition. Quenching the system affects the strength of surface anchoring as well. Hence, we observe a small shrinkage of the defect size at the poles of the colloid [see Fig. 6.14(a)] in accord with the decrease in the region of lowered density as shown in Fig. 6.14(b). However, the surface anchoring is not strong enough to bend layers at larger distances. As clearly illustrated by the plots of the local biaxial order parameter $\zeta(r)$ (see Fig. 6.12), which we use to locate the core of a topological defect, the defect remains at the colloidal surface.

As discussed in the previous section we may tune the strength of the anchoring function by a variation of the inverse screening length η_{mc} [see Eqn. (3.24)]. However, because ε_{mc} is much larger for planar as compare to homeotropic anchoring (see Tab. 3.1) the range of the interaction cannot be varied as strongly in the latter case. If η_{mc}^{-1} is too large one observes layering already in the nematic phase. Of course, this increases the computational cost of the simulations considerably. To obtain results in a reasonable time we choose $\eta_{\text{mc}} = 0.1$ as the minimum value. We emphasize that a further decrease of η_{mc} may also lead to the formation of a crystal-like layer around the colloid even in the nematic phase.

By setting $\eta_{\text{mc}} = 0.1$ we increase the strength of surface anchoring [see Fig. 6.9(b)]. As clearly depicted by the plot of $S(r)$ and confirmed by the plot of $\zeta(r)$ in Fig. 6.14(d) and (f), the defects are not point-like anymore as in Fig. 6.14(a) and (c). In fact, these defects are spread over a larger region. However, even if these defects look similar to focal lines observed in experiments, their origin is different. Focal lines arise because of the discontinuous change of the orientations of the mesogens inside the equidistantly packed layers.^{57,134} In our model system, however, defects are formed because of extended low-density regions [see Fig. 6.14(e)]. Additionally, in the vicinity of the defects the layers are not equidistant because of the strong bending of smectic lay-

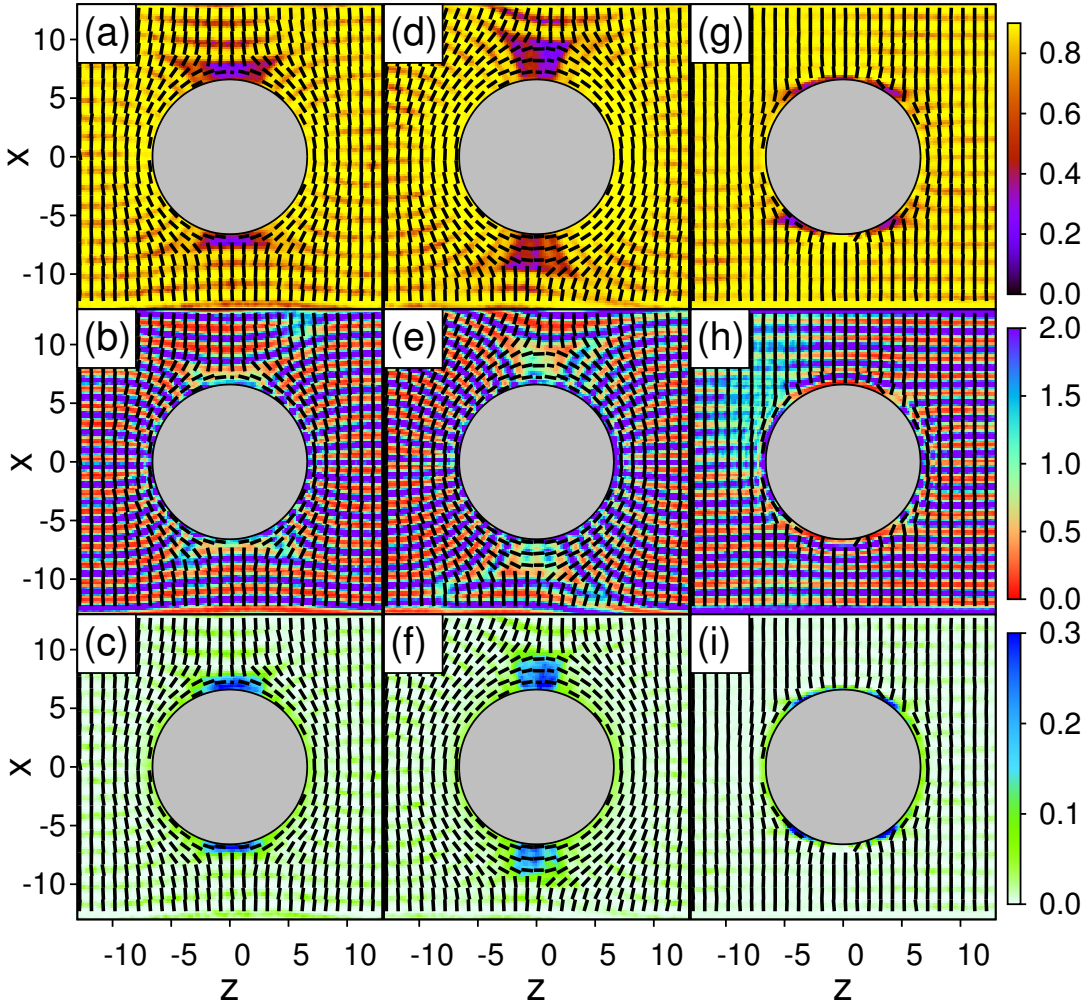


Figure 6.14. Plots of $S(\mathbf{r})$, $\rho(\mathbf{r})$, and $\zeta(\mathbf{r})$ are presented in the upper, middle, and lower panel, respectively. Data are obtained for $T = 0.7$ and for (a)-(c) $\eta_{\text{mc}} = 1.0$, (d)-(f) $\eta_{\text{mc}} = 0.5$, and (g)-(h) $\eta_{\text{mc}} = 5.0$.

ers. We assume that colloidal size, more specifically, the curvature of the surface is essential for the bending of smectic layers and thus the formation of focal lines. However, any further increase of the colloidal size is presently impossible for practical reasons. As already discussed, any enhancement of colloidal size implies a much larger number of mesogens which automatically raises the equilibration time. Hence, an efficient simulation cannot be performed in reasonable time because of this much larger equilibration time and also because of the larger number of interactions to be computed during each MC cycle.

Finally, we turn to a discussion of the impact of a colloid with weak planar surface anchoring [see Fig. 6.9(b)] on smectic A layers. Therefore, we decrease the range of u_{mc} by setting $\eta_{\text{mc}} = 5.0$. Deep in the smectic A phase, topological defects vanish at north and south pole of the colloid in favor of very high nematic order (i.e., $S \simeq 0.8$). However, nematic order is not uniform as illustrated by the plot of $S(\mathbf{r})$ in Fig. 6.14(g). At $\gamma_+ = 30^\circ$ and $\gamma_- = 150^\circ$ [$\cos \gamma_\pm = \pm \hat{\mathbf{n}}_0 \cdot \hat{\mathbf{s}}$, where $\hat{\mathbf{s}}$ denotes the surface normal of the colloidal surface] we observe the formation of two weak surface rings. This is

confirmed by the plots of $\zeta(\mathbf{r})$ which clearly verify the presence of surface defects. Additionally, a slight deviation from the equidistant layer spacing is observed in the same regions. Obviously, surface anchoring is not strong enough to overcome the strong nematic order and to flip the director by 90° as it would be the case at the north or south pole [see plots of $\hat{\mathbf{n}}(\mathbf{r})$ in Fig. 6.14(c), (f), and (i)]. Hence, the *effective* orientation of the mesogens at the north and south pole is homeotropic to the colloidal surface and thereby in contrast with the *intrinsic* planar surface anchoring. At the equator, however, surface anchoring is in good agreement with $\hat{\mathbf{n}}_0$ and the mesogens orient their longer axes parallel to the surface. Hence, a transition from *effective* homeotropic to *intrinsic* planar alignment has to occur between these antithetic anchoring conditions. At the transition point on the colloidal surface (i.e., at γ_+ or γ_-) both the *effective* homeotropic and *intrinsic* planar anchoring are of the same magnitude and cause orientational frustration which is ultimately responsible for the formation of a defect. This is analogous to the formation of a ring defect around a Janus colloid (i.e., a colloidal particle that anchors the mesogens in an antithetic fashion at different portions of its surface) which occurs due to the transition from planar to homeotropic anchoring.^{59,135} We emphasize that to the best of our knowledge neither a colloidal particle with weak planar surface anchoring nor colloids with two ring defects have been reported so far.

CHIRAL LIQUID CRYSTALS CONFINED TO MESOSCOPIC CHANNELS

In [Chapter 5](#) we demonstrated that the self-assembly of two colloidal particles included in a nematic liquid crystal is driven by orientational perturbations and defects of the host phase. Such perturbations and defects arise because the symmetry of the colloid and the nematic phase is incompatible. In [Chapter 6](#) we showed that the nature of the defect topology is controlled by the surface anchoring which describes the preferred orientation of the mesogens at the liquid-solid interface.

In [Chapter 5](#) and [Chapter 6](#) we focused on the liquid-crystalline order in the vicinity of convex interfaces. However, concave interfaces have been considered as well to perturb the order of a liquid crystal.^{39,42} For example, concave interfaces can be realized inside of liquid-crystalline droplets that are spontaneously formed as an apolar liquid crystal is placed in a polar solvent (i.e., water or aqueous polymer solution).³⁹ In this context not only the nematic phase¹³⁶ has been studied but also various smectic,¹³⁷ cholesteric,¹³⁸ as well as various blue phases.¹³⁹ Thus, a broad variety of topological defect structures and fascinating optical properties have been reported for such systems.

However, not only spherical interfaces are used to manipulate liquid-crystalline order. Crawford *et al.*¹⁴⁰ investigated the impact of cylindrical capillaries on a nematic phase experimentally and within the framework of Frank's elasticity theory (see [Sec. 4.4](#)). These authors reported that the director field of a liquid crystal depends on the surface curvature, anchoring conditions but also on the elastic properties of the liquid crystal (see [Fig. 1.4](#)). Based on Frank's elasticity theory Burylov⁴³ derived a phase diagram illustrating different director fields formed in a cylindrical capillary as a function of Frank's elastic constants, surface anchoring energy, and cylindrical radius.

Typically, the diameter of the capillary is of few microns. However, recently nanochannels have been considered to study the liquid-crystalline order of achiral¹⁴¹ and chiral¹⁴² liquid crystals. The consideration of nanochannels, however, involves some difficulties. (i) In fact, a porous material consisting of an array of parallel channels can be synthesized for different channel sizes with high precision.^{141,142} However, it is impossible to obtain data for a single channel. All quantities measured experimentally represent an average over the entire array of channels. (ii) Even if it is possible to synthesize or to measure a single channel, the local structure would remain unclear because of the insufficient optical resolution.¹⁴³ (iii) Continuum approaches such as Frank's elasticity theory or Landau-de Gennes theory fail on the nanometer scale.⁶

Fortunately, none of these problems are relevant for computer simulations. Hence, we perform MC simulations and study the impact of curved surfaces of a mesoscopic

channel (e.g., nanochannel) on the liquid-crystalline structure. However, instead of an achiral (i.e., nematic or smectic A) phase, we focus on chiral blue phases.

By considering chiral blue phases one is immediately confronted with periodic networks formed by defect lines on a supramolecular length scale.^{6,39} These defect lines attract small molecules, macromolecules as well as colloidal particles.^{13,15,16,144} This property provides a very convenient route for the bottom-up synthesis of regular networks where the blue phase serves as a template. In fact, monomers self-assembled at defect lines of a blue phase can be polymerized by UV light in order to obtain a polymer network which remains stable even after the liquid crystal is removed.^{13,14} Hence, manipulation and control of defect topologies in a chiral liquid crystal are key concepts for designing of new materials.

Chiral liquid crystals can be manipulated in the same way as their non-chiral counterparts. In fact, the thermodynamic state of chiral liquid crystals is determined by thermodynamic conditions²³ (i.e., temperature, pressure, density), electric and/or magnetic fields,¹⁴⁵ the presence of non-chiral liquid crystals,²⁴ colloidal particles,¹⁴⁴ polymer matrices,¹⁴ microfluidic flow^{146,147} as well as confinements.^{45,46} Recent works by Fukuda and Žumer^{45,46} reveal the broad variety of novel defect structures which arise if a blue phase is confined to a slit pore. Previous experimental,^{148,149} as well as theoretical studies,^{150,151} illustrate confinement-induced effects on chiral phases in a mesoscopic channel. However, due to the complexity of blue phases, a systematic analysis cannot be achieved experimentally. Hence, to the best of our knowledge, a systematic study of the problem is lacking. To close this gap we investigate the impact of the shape of the channel as well its surface anchoring on the defect structure of a chiral liquid-crystal model where the mesogens interact via u_{mm}^* [see Eqn. (3.29)]. As introduced in Sec. 3.5 the mesogen-channel interactions are modeled via u_{mch} [see Eqn. (3.33)] where the shape of the channel is determined by the radius R of the channel's corner and the ratio s_y/s_z (see Fig. 3.4).

7.1 TECHNICAL DETAILS

Results presented in this section are based on MC simulations carried out in the grand canonical and canonical ensembles. In both ensembles, the volume is kept constant by fixing the dimensions s_x , s_y , and s_z of the cuboid simulation cell in the x -, y -, and z -directions, respectively. However, because blue phases exhibit periodic structures one has to guarantee that dimensions of the simulation cell correspond to the multiple of the unit cell of a blue phase, similar as for crystals.

In principle, the formation of supramolecular and periodic structures poses a problem in computer simulations where periodic boundary conditions are applied to reduce surface effects. Let \hat{e}_α ($\alpha = x, y, z$) be a unit vector parallel to the direction in which the helical rotation evolves. Because of the head-tail symmetry of the mesogens, the helix can evolve along \hat{e}_α perfectly if $2s_\alpha/p = k$ ($k \in \mathbb{N}$). For non-integer values of k the helix is exposed to spurious tension and its free energy increase as demonstrated by Fukuda and Žumer.⁴⁶

The characteristic length describing the periodicity in a chiral liquid crystal is the pitch p . Because the pitch is an inherent property of the model it depends on the thermodynamic conditions and cannot be extracted from the interaction potential. For the model system employed here Melle *et al.*⁸⁷ measured the pitch as a function of the chirality coupling constant $|\varepsilon_3|$ at fixed $T = 0.95$ and $P = 1.81$ which corresponds to $\rho \simeq 0.92$. We emphasize that $\rho \simeq 0.92$ is valid for $|\varepsilon_3| = 0.25$ whereas the density increases/decreases for higher/lower values of $|\varepsilon_3|$ due to the stronger/weaker mesogen-mesogen interactions, respectively. As we shall demonstrate later we use the data collected by Melle *et al.*⁸⁷ to determine an empirical expression for $p(|\varepsilon_3|)$.

Hence, we are now in a position to determine the dimensions of the simulation cell and the number of mesogens N which the simulation cell should accommodate for any given $|\varepsilon_3|$. It has been shown that this model is capable of forming a cholesteric phase and blue phases I-III for $|\varepsilon_3| < 0.10$, $|\varepsilon_3| = 0.10$, $|\varepsilon_3| = 0.25$, and $|\varepsilon_3| = 0.90$, respectively.^{87,88} In the following we focus on blue phase II. Therefore, we take $|\varepsilon_3| = 0.25$ and consequently $p = 23.8$ throughout this chapter. For the given $N = V\rho$ where $V = s_x s_y s_z$ ($s_\alpha = p$, $\alpha = x, y, z$), T and P we perform a MC simulation in the isothermal-isobaric ensemble of a bulk fluid (i.e., in the absence of any walls or channels). We determine the chemical potential $\langle \mu \rangle_{NPT} \simeq -11.88$ via an adjusted version of Widom's test particle method. In this version volume fluctuations are included in the Boltzmann factor of the test particle's configurational potential energy.¹⁵² Moreover, the average side length $\langle s_\alpha \rangle_{NPT}$ ($\alpha = x, y, z$) agrees with p within few percent. To test the validity of $\langle \mu \rangle_{NPT}$ obtained from isothermal-isobaric simulation we perform a MC simulation in the grand canonical simulation with fixed μ , T , and V with $s_x = s_y = s_z = p$ to obtain the mean density and pressure which agree within few percent with the input values of the isothermal-isobaric MC simulation. Based on the acceptance ratio for creation/destruction of a mesogen, which always exceeded 5×10^{-4} , results of the grand canonical simulations are reliable and the two sets of simulations are consistent mutually.

Finally, having knowledge of μ , T , and p we are in a position to design a system composed of a mesoscopic channel which is in thermodynamic contact with a reservoir of mesogens. Therefore, we adjust the linear dimensions of the simulation cell s_y and s_z such that $2s_\alpha/p = k$ ($\alpha = y, z$ and $k = 1, 2, 3$) and $s_z \geq s_y$. Interactions between a mesogen and the wall of the channel are modeled via u_{mch} [see Eqn. (3.33)] consisting of an attractive and repulsive contribution. Because the repulsive part wins over the attractive one for $\delta_i \lesssim 0.86$, the mesogens can not stay directly at the wall (i.e., $\delta_i = 0$) where δ_i denotes the minimum separation between the wall and the mesogen i . Instead of that, it is more likely to find a mesogen at the minimum of u_{mch} (i.e., $\delta_i = 1$). This gives rise to excluded volume at the wall. On account of this excluded volume, we add a value of 2 to s_y and s_z to guarantee that a helix of pitch p may evolve parallel to \hat{e}_y and/or \hat{e}_z without any spurious stress. Furthermore, we take $2s_x/p = k$ ($k \in \mathbb{N}$), where k is chosen to limit the number of mesogens to the range $1.0 \times 10^4 \leq N \leq 1.5 \times 10^4$ and therefore the CPU time needed. Channels con-

sidered here are supposed to be infinitely long in the x -direction. This is realized by applying periodic boundary conditions across the y - z plane at $\pm s_x/2$. The volume of the channel is then given by

$$V = 4s_x \left[\frac{s_y s_z}{4} + R^2 \left(\frac{\pi}{4} - 1 \right) \right] \quad (7.1)$$

(see Fig. 3.3 and Fig. 3.4).

For a given μ and T we study the impact of the channel's surface anchoring as well as its shape on the local order of a blue phase II in the grand canonical ensemble. Therefore, we equilibrate the system for 2×10^4 grand canonical MC steps and monitor the fluctuation of the mean number of mesogens for another 1.0×10^5 steps. Each MC step in the grand canonical ensemble consists of two essential steps allow one to generate a Markov chain of configurations numerically. In the first event each of the N mesogens presently in the system is selected sequentially. Then it is decided randomly with equal probability whether to displace the center of mass of this mesogen or to rotate it around one of the three Cartesian axis where the specific axis is picked randomly with equal probability. Subsequently, based on the energy criterion [see Eqn. (2.32)] it is decided whether to accept or to reject this trial.

In the second step, it is decided with equal probability whether to destroy a randomly chosen mesogen of the system or to create a new mesogen at a randomly chosen position with random orientation. Again, an energy criterion [see Eqn. (2.45) and Eqn. (2.46)] is applied to decide whether the creation/destruction trial is accepted or rejected. The second step is repeated N' times where N' is the number of mesogens presently in the system at the beginning of the second step. Hence, one MC step in the grand canonical ensemble consists $N + N'$ attempts to generate a new configuration. In the canonical ensemble, one MC step consists of N attempts to displace/rotate a mesogen.

After the grand canonical simulation is accomplished, we take the mean number of mesogens as input for a corresponding MC simulation in the canonical ensemble where we compute the ensemble average of $Q(\mathbf{r})$ within of 5.0×10^5 MC steps. We switch the ensembles from grand canonical to canonical to avoid the computational demanding step of creation/destruction of a mesogen and save CPU time.

7.2 BULK BLUE PHASE II

As in the chapters before, we begin the presentation of results by discussing properties of the bulk. For $\varepsilon_3 \neq 0$ the left-right symmetry of the interaction potential u_{mm}^* [see Eqn. (3.29)] is broken, thus, u_{mm}^* becomes chiral. Phases formed by chiral mesogens are dominated by spatial helical rotation of the mesogens such as in the cholesteric or various blue phases. Hence, this helical structures are characterized by the local director $\hat{\mathbf{n}}(\mathbf{r})$, the local nematic order parameter $S(\mathbf{r})$, and the pitch p describing the periodicity of the helical structure.

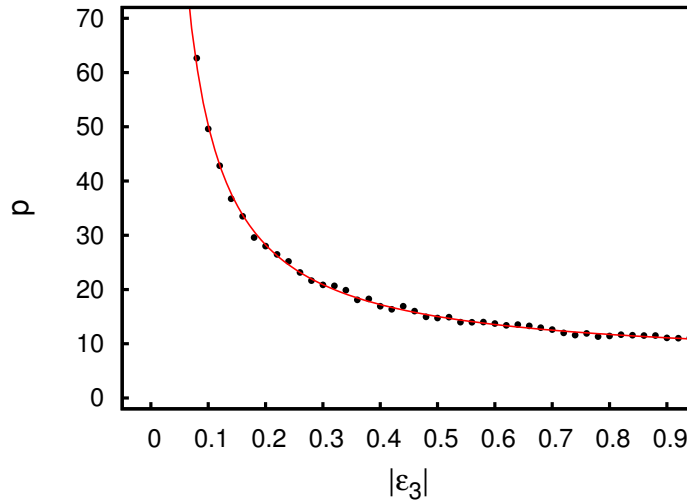


Figure 7.1. Plot of the pitch p as a function of the chiral coupling constant $|\varepsilon_3|$ (\bullet) obtained in MC simulations⁸⁷ together with a fit of $p = a/|\varepsilon_3| + b$ (—) (see text) where $a \simeq 4.41$ and $b \simeq 6.20$ have been obtained from a least squares fit to the simulation data.

As discussed in the previous section, the size of the simulation box is crucial for periodic structures. It should be large enough to accommodate at least a unit cell of the periodic structure which is not necessarily described by $p/2$. In fact, the unit cell of a blue phase II corresponds to a cube with a side length of $p/2$. The unit cell of a blue phase I, however, is represented by a cube with a side length of p . If dimensions of the simulation box do not match the size the unit cell then the direction along which the helical structure evolves changes to an *a priori* unknown direction in order to prevent its spurious tension and is no longer orthogonal to any of the faces of the cuboid simulation cell. In other words, a convenient choice of the side lengths of the simulation box simplifies the analysis of the problem.

In order to determine the pitch, we use data obtained by Melle *et al.*⁸⁷ for the pitch as a function of the chirality coupling constant $|\varepsilon_3|$ at $T = 0.95$ and $P = 1.80$ (see Fig. 7.1). For $|\varepsilon_3| \rightarrow 0$ the mesogens exhibit a nematic phase where $p \rightarrow \infty$. For $|\varepsilon_3| \neq 0$, however, chiral phases are exhibited and the pitch declines to a threshold value for increasing $|\varepsilon_3|$. Having knowledge of the function $p(|\varepsilon_3|)$ one could adjust the pitch of the system. Similarly, in experimental systems the pitch is adjusted by doping a non-chiral, nematic liquid crystal with a chiral component.²⁴

It has been demonstrated many times that $p \propto c^{-1}$ where chirality of the system is determined by the concentration c of the chiral component.^{148,153,154} Later it was shown by Wilson and Earl¹⁵⁵ that c is proportional to the change of the free energy due to the change of the effective interactions between the components of the binary mixture. In such mixtures, the concentration of the chiral component controls the amount of chirality the system possess. In our one-component system, the chirality is distributed equally over all mesogens and its amount is given by $|\varepsilon_3|$. Hence, we

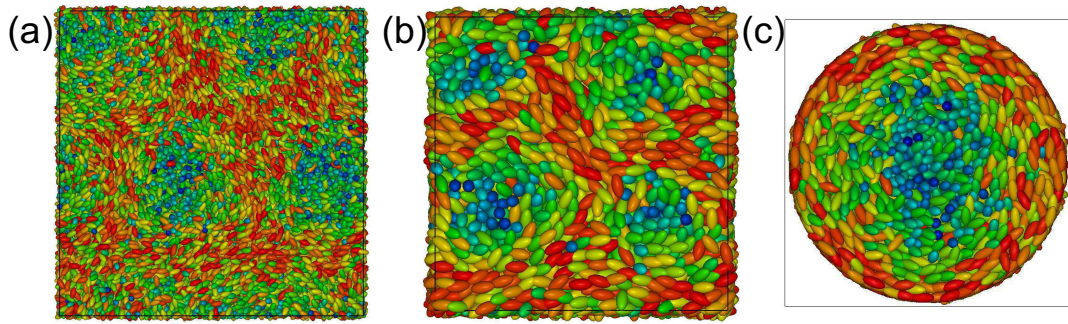


Figure 7.2. “Snapshots” of a configuration generated for (a) $|\varepsilon_3| = 0.10$ ($p = 50.4$) and (b) $|\varepsilon_3| = 0.25$ ($p = 23.8$, see Fig. 7.1). The aspect ratio of mesogens is greatly enlarged to enhance the visibility. The mesogens are colored in blue/red if their longer axes are perpendicular/parallel to the paper plane; other colors refer to orientations intermediate to a perfect parallel or perpendicular alignment. (c) Isolated double-twist cylinder [see Fig. 1.3(b)] configuration generated in a MC simulations where the mesogens are confined to a cylindrical capillary with suitable anchoring conditions. Data for (a) and (c) are taken from Ref. 88.

anticipate for our one-component system $p \propto |\varepsilon_3|^{-1}$. This expectation is confirmed by Fig. 7.1 where an analytic expression is fitted to data collected from Ref. 87.

Based on these considerations, we chose the lengths of our simulation box to be equal to p . Hence, we anticipate the evolution of helical structures orthogonal to the faces of the cuboid simulation box. This expectation is confirmed by “snapshots” illustrated in Fig. 7.2(a) and (b) for a blue phase I and II, respectively. Although we focus here on blue phase II, it might be interesting to compare the results to those obtained for blue phase I, which was observed by Skutnik⁸⁸ for the very first time in computer simulations for $|\varepsilon_3| = 0.10$. In both blue phases we observe the formation of double-twist cylinders as their substructure. As illustrated in Fig. 7.2(c), an isolated double-twist cylinder can be observed if a blue phase is confined to a cylindrical capillary of diameter $p/2$ and for a suitable choice of anchoring conditions (see Ref. 88).

However, in bulk, these double-twist cylinders can arrange spatially in different ways. More specifically, in blue phase I the double-twist cylinders are arranged in a face-centered cubic fashion whereas the simple cubic arrangement indicates the presence of blue phase II [see Fig. 7.2(a) and (b) and cf. Fig. 1.3(e) and (f)]. We emphasize that the formation of blue phases I and II at low and high chirality, respectively, are fully consistent with experimental observations.²⁴ Moreover, as demonstrated by Melle *et al.*⁸⁷ this model system forms a blue phase III for very large $|\varepsilon_3|$ where the arrangement of the double-twist cylinders is amorphous.

The high symmetry of blue phase II [see Fig. 7.2(b)] can be analyzed more quantitatively in terms of $\hat{n}(\mathbf{r})$ and $S(\mathbf{r})$. As illustrated in Fig. 7.3(a)-(c), the component of $\hat{n}(r_\beta)$ which is parallel to the line of vision $r_\beta = \mathbf{r} \cdot \hat{\mathbf{e}}_\beta$ ($\beta = x, y, z$) always vanishes whereas the other two reveal a regular sinusoidal variation. Here, the overbar deno-

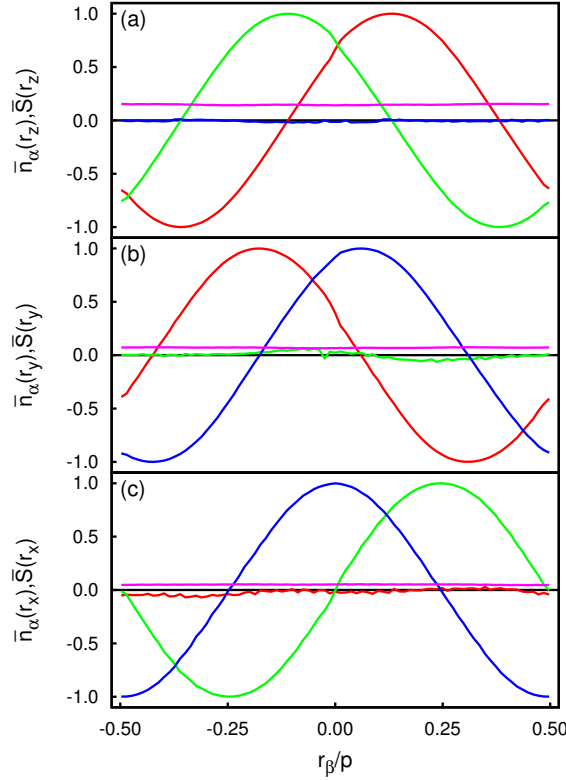


Figure 7.3. Plots of components of the nematic director $\bar{n}_\alpha(r_\beta)$ and the local nematic order parameter $S(r_\beta)$ (—) as functions of specific lines of vision $r_\beta = \mathbf{r} \cdot \hat{\mathbf{e}}_\beta$ where $\alpha = x$ (—), $\alpha = y$ (—), and $\alpha = z$ (—); (a) $\beta = z$, (b) $\beta = y$, and (c) $\beta = x$.

tes an average taken over the plane perpendicular to $\hat{\mathbf{e}}_\beta$. The shift of the sinusoidal curves is approximately $\pi/2$ and indicates a helical rotation of the local director in all three spatial directions as it is expected for blue phase II. Because blue phase I consists of double-twist cylinders as well, one observes a similar spatial rotation of $\hat{\mathbf{n}}(\mathbf{r})$.⁸⁸ Despite this high degree of symmetry the in-plane nematic order parameter $\bar{S}(r_\beta)$ remains small. This is consistent with “snapshots” shown in Fig. 7.2(a)-(b) where it is illustrated that no uniform order is exhibited in the plane which consequently results in a vanishing $\bar{S}(r_\beta)$.

Also characteristic for blue phases are their inherent networks of disclinations. As discussed in Sec. 1.1 different spatial arrangements of double-twist cylinders give rise to unequal networks (see Fig. 1.3). As already discussed in previous sections, the computation of defect structures from computer simulation is straightforward. Therefore, we define a disclination line as

$$\ell \equiv \{\mathbf{r} = (x, y, z)^T | S(\mathbf{r}) \leq \delta_S\} \quad (7.2)$$

where $\delta_S = 0.20$ is an arbitrary threshold value for $S(\mathbf{r})$ adjusted to maximize the visibility of ℓ . Moreover, because of rather complex defect structures of blue phases

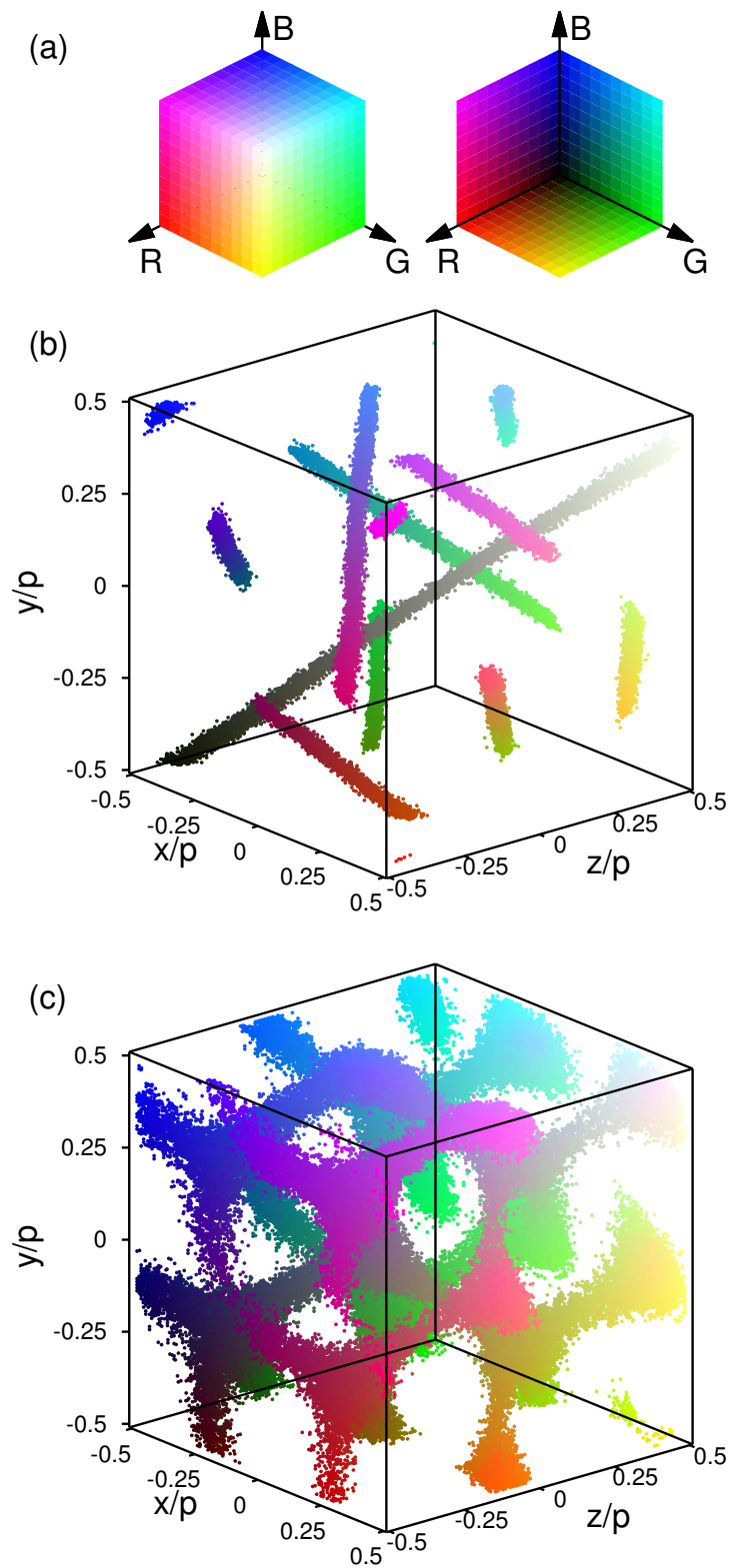


Figure 7.4. (a) Color cube to illustrate the spatial variation of color where $\hat{e}_R \cdot \hat{e}_x = \hat{e}_B \cdot \hat{e}_y = \hat{e}_G \cdot \hat{e}_z = 1$ where \hat{e}_R , \hat{e}_B and \hat{e}_G are unit vectors defining the axes used for the color cubes. Characteristic disclination lines ℓ are shown for (b) blue phase I and (c) blue phase II. Again, data for (b) are taken from Ref. 88.

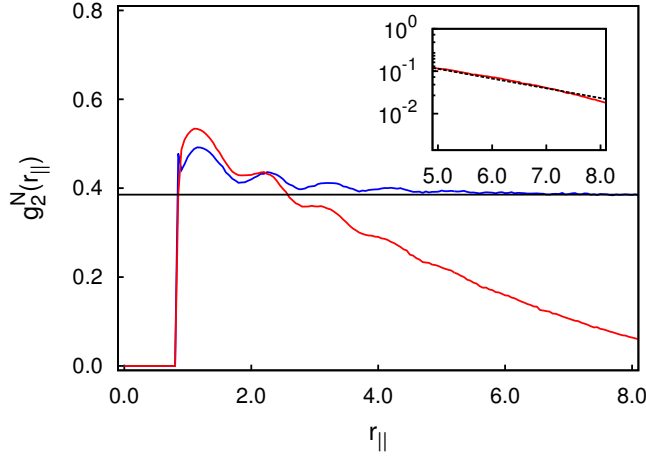


Figure 7.5. Plots of the nematic correlation function $g_2^N(r_{\parallel})$ defined in Eqn. (7.3) where $\varepsilon_3 = 0.00$ (—) and $|\varepsilon_3| = 0.25$ (—). The horizontal line (—) corresponds to S^2 . The inset is an enlargement of the plot for $|\varepsilon_3| = 0.25$ where we also show the function $a \exp(-r_{\parallel}/\zeta)$ (---) fitted to the simulation data and taking a and the nematic correlation length ζ as fit parameters (see text).

we develop a color code [see Fig. 7.4(a)] where a different color is assigned according to the specific point on ℓ . Plots of ℓ for blue phases I and II in Fig. 7.4(a) and (b), respectively, show different defect structures. In blue phase I, ℓ forms a network of straight lines which never intersect whereas a tetrahedrally linked network of ℓ is found in blue phase II. Both observations are in perfect agreement with previous numerical calculations.¹⁴⁴

Finally, to demonstrate that these structures are truly supramolecular and do not occur due to any artificial effects we introduce the nematic correlation function

$$g_2^N(r_{\parallel}) \equiv \left\langle \frac{1}{N(r_{\parallel})} \sum_{i=1}^N \sum_{j=1, j \neq i}^N P_2(\hat{\mathbf{u}}_i \cdot \hat{\mathbf{u}}_j) \delta(r_{\parallel} - r_{ij}^{\parallel}) \right\rangle \quad (7.3)$$

where P_2 is again the second Legendre polynomial, $r_{ij}^{\parallel} = |\mathbf{r}_i^{\parallel} - \mathbf{r}_j^{\parallel}|$, $\mathbf{r}_i^{\parallel} = (\mathbf{r}_i \cdot \hat{\mathbf{u}}_i) \hat{\mathbf{u}}_i$, and $N(r_{\parallel})$ is the number of particles located in a cylindrical shell of radius 0.5 and height of $\Delta r_{\parallel} = 0.05$. In a blue phase the mesogens are ordered locally but disordered globally. Hence, one anticipates this local nematic order to decay monotonically between two ordered regions.

In the limit of vanishing chirality and under the present thermodynamic conditions, the mesogen exhibit a nematic phase which is characterized by a global nematic order parameter $S = 0.62$. For a nematic phase it is therefore expected from Eqn. (7.3) that $\lim_{r_{\parallel} \rightarrow \infty} g_2^N(r_{\parallel}) = S^2$. For both cases (i.e., chiral and non-chiral), the expectations are confirmed by the plots of g_2^N (see Fig. 7.5).

Moreover, both curves in Fig. 7.5 reveal weak oscillations for $1.0 \leq r_{\parallel} \leq 5.0$ reflecting spatial correlations superimposed to the orientational ones. As these spatial

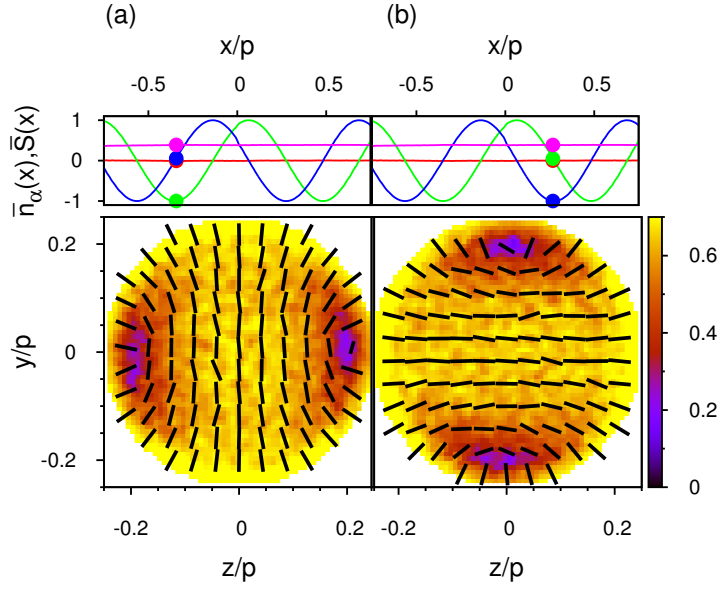


Figure 7.6. (Upper panels) Variation of components of the local director field $\bar{n}_\alpha(x)$ along the x -axis of a mesoscopic channel for $R/s_y = 0.50$; $\alpha = x$ (—), $\alpha = y$ (—), and $\alpha = z$ (—). Also shown is the local nematic order parameter $\bar{S}(x)$ (—). Dots, colored the same way as the above lines, indicate the actual position along the line of vision. (Lower panels) Plots of $\hat{n}(\mathbf{r}')$ (dashes) for given x in the upper panel. Values of $S(\mathbf{r}')$ correspond to the attached color bar.

correlations vanish, one may assume an exponential decay of $g_2^N - S^2$ proportional to $\exp(-r_{\parallel}/\zeta)$ where ζ is the nematic correlation length. For the nematic phase ζ is infinite whereas for the blue phase II the nematic short range correlations are indicated by $\zeta \simeq 2.70$. Taking ζ as a characteristic length scale of our model we immediately conclude that structures shown in Fig. 7.2 and Fig. 7.4 are truly supramolecular compared with the range of the nematic correlation.

7.3 CONFINEMENT EFFECTS

After validating that our bulk fluid exhibit a blue phase II at given thermodynamic conditions and for $|\varepsilon_3| = 0.25$, we focus on blue phase II and confine it to a mesoscopic channel. We refer the interested reader to Ref. 88 where the author investigate a blue phase I confined to a mesoscopic channel under the same conditions as discussed in the following. Throughout the present chapter we fix the line of vision along \hat{e}_x and analyze $\hat{n}(x)$ and $\bar{S}(x)$. Furthermore, we discuss the local director field $\hat{n}(\mathbf{r}')$ and local order $S(\mathbf{r}')$ for a cross section in the $y-z$ plane at a given $x = x'$. Here, \mathbf{r}' is a two-dimensional vector. Finally, we analyze ℓ in the same fashion as in Fig. 7.4.

7.3.1 Homeotropic anchoring conditions

SMALL CYLINDRICAL CHANNEL. We begin the presentation of our results by considering homeotropic anchoring conditions at the walls of our channel. The shape of this channel is controlled by s_y , s_z and R . For $s_y/p = s_z/p = 0.5$ and $R/s_y = 0.5$ the cross section of the channel is circular and the channel is cylindrical. Plots of components of $\bar{\mathbf{n}}(x)$ reveal its helical rotation along \hat{e}_x (see upper panels of Fig. 7.6). This is because $\bar{n}_y(x)$ and $\bar{n}_z(x)$ can be represented by sine functions shifted by $\pi/2$ with respect to each other whereas $\bar{n}_x(x) \simeq 0$.

The plot of $\bar{S}(x)$ reveal a relatively large nematic order parameter of $\bar{S}(x) \simeq 0.5$ in each plane orthogonal to \hat{e}_x (see upper panels of Fig. 7.6). Moreover, this relatively high degree of order indicate a uniform in-plane direction and eliminate thereby a possible rotation of $\hat{\mathbf{n}}(\mathbf{r})$ along other directions. From the helical rotation of $\bar{\mathbf{n}}(x)$ along a single axis and the constant, non-vanishing value for $\bar{S}(x)$ we conclude that the phase which has formed in the mesoscopic channel is quasi-cholesteric. Here, the term “quasi-cholesteric” is chosen to remind the reader that the cholesteric phase is formed because of the confinement whereas a blue phase would be formed in bulk.

The uniform in-plane orientation of $\bar{\mathbf{n}}(x)$ is not compatible with the homeotropic anchoring conditions everywhere at the wall of the channel. As illustrated in the lower panel of Fig. 7.6, $\hat{\mathbf{n}}(\mathbf{r}')$ is almost uniform at the center of the channel. However, in the vicinity of the wall two extreme cases are observed. If the surface anchoring agrees with $\hat{\mathbf{n}}(\mathbf{r}')$ the local nematic order is enhanced whereas the competition of these quantities causes the formation of a topological defect which is indicated by the relatively abrupt drop of $S(\mathbf{r}')$ (see lower panel of Fig. 7.6). In the vicinity of the topological defect $\hat{\mathbf{n}}(\mathbf{r}')$ is bent strongly and relaxes as one moves towards the center of the channel.

These director field configurations have been reported for an achiral liquid crystal in the nematic phase where the in-plane orientation $\bar{\mathbf{n}}(x)$ is constant along the x -direction.^{42,43} However, for chiral liquid crystals $\bar{\mathbf{n}}(x)$ rotates in a helical fashion along the cylindrical symmetry axis as observed experimentally¹⁴⁸ and confirmed later within the framework of a continuum theory of elastic director-field deformations¹⁵¹ (see upper panels of Fig. 7.6). Therefore, regions of enhanced or decreased nematic order follow the helical rotation of $\bar{\mathbf{n}}(x)$ along the x -direction. Hence, disclination lines ℓ which are visualized as regions of low $S(\mathbf{r})$ exhibit a double helix evolving along the x -directions as illustrated in Fig. 7.7(a). In particular, this disclination-line topology has been already reported experimentally by Cladis *et al.*¹⁴⁸ and within the framework of a continuum-theory by Besić and Žumer.¹⁵¹

SMALL CUBOID CHANNEL. Now we consider a channel with a rectangular cross-section by setting $R/s_y = 0.0$ while maintaining $s_y/p = s_z/p = 0.5$. Plots of $\bar{\mathbf{n}}(x)$ and $\bar{S}(x)$ in the upper panels of Fig. 7.8 reveal a helical rotation of the in-plane (i.e., in the y - z plane) director along the channel's axis and a relatively high nematic in-plane order of $\bar{S}(x) \simeq 0.5$. Hence, in agreement with the local structure discussed for a [small cylindrical channel](#) in Fig. 7.6, we conclude that the mesogens form a quasi-cholesteric phase in the present case as well. Lower panels of Fig. 7.8 illustrate the

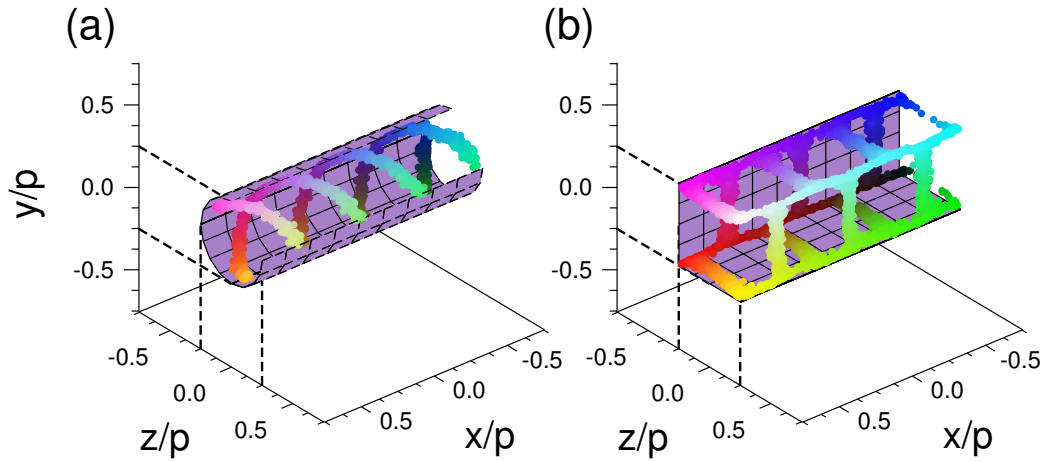


Figure 7.7. Three-dimensional representation of disclination lines ℓ . To enhance the visibility the lines have been colored according to the color cube shown in Fig. 7.4(a). The mesoscopic channels have been cut open so that one can look inside. Note that this does not eliminate part of from the plot. Data are obtained for (a) **small cylindrical channel** where $R/s_y = 0.5$ and $s_y/p = s_z/p = 0.5$, and (b) **small cuboid channel** where $R/s_y = 0.0$ and $s_y/p = s_z/p = 0.5$.

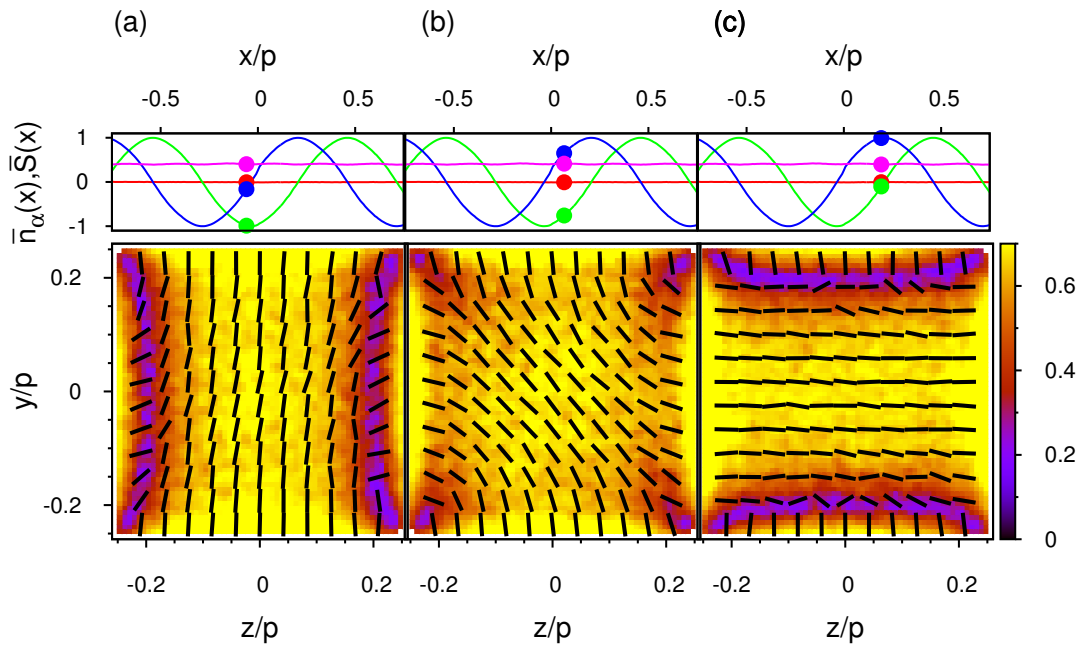


Figure 7.8. As Fig. 7.6, but for a 7.3.1 characterized via $s_y/p = s_z/p = 0.5$ and $R/s_y = 0.00$.

local director $\hat{n}(r')$ and the local nematic order parameter $S(r')$ at different positions x along the line of vision and thus demonstrate the helical rotation of $\bar{\hat{n}}(x)$.

More specifically, we observe three different states of the in-plane orientation. First, $\bar{\hat{n}}(x)$ is approximately parallel to \hat{e}_y and thus in perfect agreement with homeotropic

anchoring at the top and bottom wall along the y -axis [see Fig. 7.8(a)]. However, at the left and right wall separated in the z -direction surface anchoring is in competition with $\bar{\mathbf{n}}(x)$. Therefore, defect lines are formed parallel to \hat{e}_y at the left and right wall.

Second, as one travels along the channel's symmetry axis, $\bar{\mathbf{n}}(x)$ rotates and defects shown in Fig. 7.8(a) vanish. Instead of that the director field is bent toward the walls to match the local homeotropic anchoring conditions [see Fig. 7.8(b)]. This is valid as long as the in-plane orientation is not in direct competition with the local orientation at the surface of the channel which is imposed by the top/bottom or left/right part of the channel separated in y - and z -direction, respectively.

However, in the corners of the channel, we notice relatively small regions where $S(\mathbf{r}')$ is decreased with respect to $\bar{S}(x)$. These defects arise due to competing surface anchoring at the top/bottom and left/right walls. At small distances between two walls orthogonal to each other (i.e., in the corners) the mesogens cannot fulfill such a strong bending to fit both anchoring conditions and thus, this molecular frustration results in the formation of a defect.

As one travels further along the channel's symmetry axis one finally reaches the third state which is very similar to the first one shown in Fig. 7.8(a). However, as displayed in Fig. 7.8(c) now the in-plane orientation points along the z -direction. Therefore, we observe the formation of defect lines at the top and bottom walls. Because of the helical nature of $\bar{\mathbf{n}}(x)$ these vertical and horizontal defect lines occur periodically along the x -axis separated by a distance of $p/4$. Moreover, these periodic defects are linked through four defect lines in the corners of the channel along the x -direction. This results in the defect structure shown in Fig. 7.7(b).

LARGE CYLINDRICAL CHANNEL. As displayed in Fig. 7.9, if one increases the diameter of the cylindrical channel (i.e., for $s_y/p = s_z/p = 1.0$ and $R/s_y = 0.5$) the local structure changes dramatically from the one discussed for a **small cylindrical channel** in Fig. 7.6 and Fig. 7.7(a). Again, the spatial rotation of $\bar{\mathbf{n}}(x)$ along the line of vision indicates a helical structure (see upper panel of Fig. 7.9). However, the relatively small value of $\bar{S}(x) \simeq 0.2$ indicates that no uniform in-plane orientation is exhibited. Indeed, plots of $\hat{\mathbf{n}}(\mathbf{r}')$ and $S(\mathbf{r}')$ in the lower panels of Fig. 7.9 reveal the presence of four double-twist cylinders partially or fully accommodated. For the convenience of the reader and to improve the visualization of Fig. 7.9, we present a sketch in Fig. 7.10(a) where all four double-twist cylinders are illustrated by blue circles.

More specifically, in Fig. 7.9 we observe three regions of decreased nematic order along the curved wall. Each of these defects corresponds to a center of a double-twist cylinder partially located in the channel [see Fig. 7.10(a)]. At the center of each double-twist cylinder, the orientation of the mesogens is parallel to \hat{e}_x and thus perpendicular to the favored orientation at the wall of the channel. Because of this mismatch three topological defect occur along the wall of the channel.

A fourth, fully accommodated double-twist cylinder is located in the center of the channel. Because there is no external perturbation the mesogens rotate out of the y - z

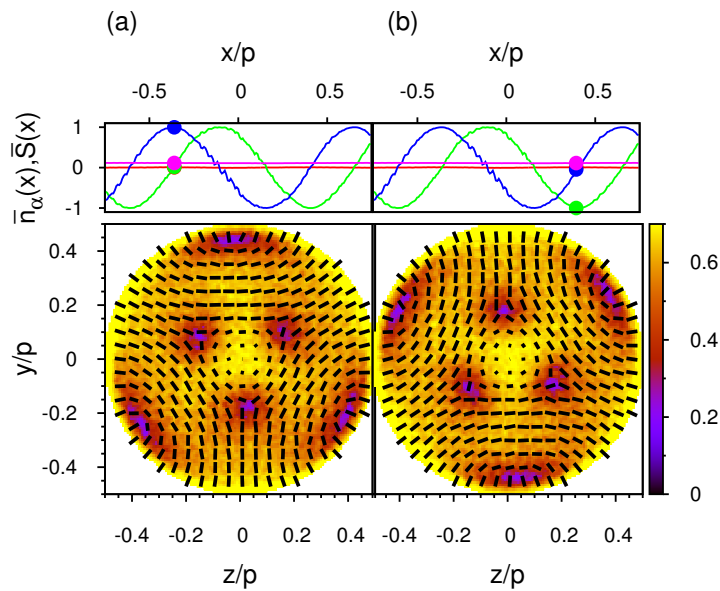


Figure 7.9. As Fig. 7.6, but for a large cylindrical channel characterized by $s_y/p = s_z/p = 1.00$ and $R/s_y = 0.5$.

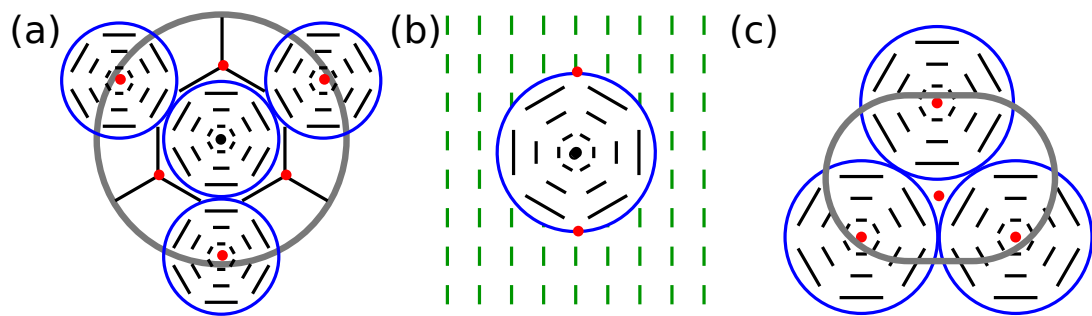


Figure 7.10. (a)-(c) Schematic representations of the liquid-crystalline order shown in Fig. 7.9(b), Fig. 7.12(a), and Fig. 7.13(a), respectively. Gray shapes in (a) and (c) represent the wall of the channel. Double-twist cylinders are encircled by a blue line to increase the visualization, red dots mark topological defect, and the local director is illustrated by black dashes and lines. Here, the contraction of the dashes indicates the rotation of the local director out of the paper plane whereas black dots mark a perpendicularly aligned director with respect to the paper plane.

plane and align along the x -direction indicated by a black dot in the corresponding sketch in Fig. 7.10(a). Thus, the director “escapes” into the third dimension to avoid the formation of an ordinary defect at $y = z = 0.0$. Instead, an *umbilic* defect is formed at the same position. Such umbilic defects have a topological charge although the director field is continuous at the core, whereas ordinary defects (see Sec. 4.6) are discontinuous at their core.¹⁵⁶ They are well known in the field of chiral liquid crystals.

Furthermore, we observe three regions, where the local orientation is not uniformly defined, indicated by $S(\mathbf{r}') \leq 0.2$, between two of the partially accommodated double-twist cylinders and the central one. Those are illustrated by red dots in Fig. 7.10(a)

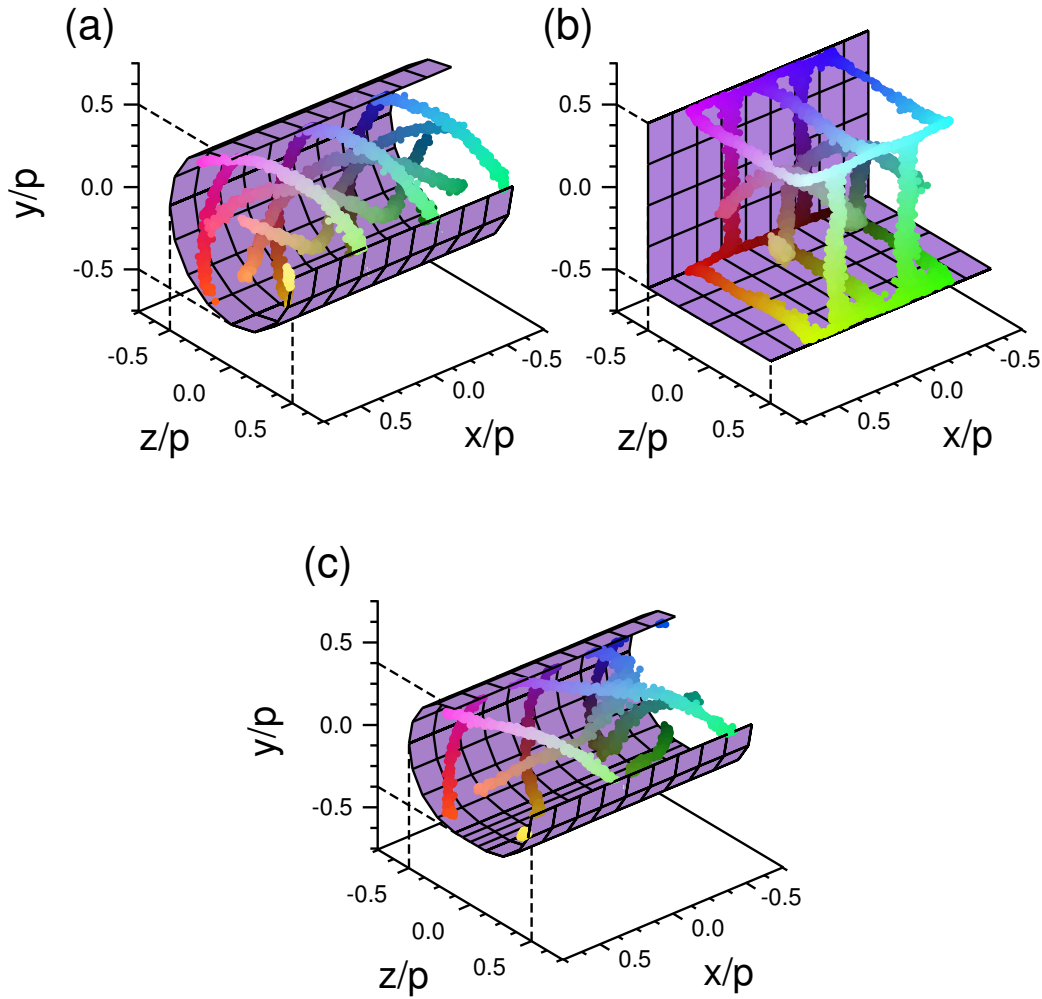


Figure 7.11. As Fig. 7.7, but for (a) **large cylindrical channel** ($R/s_y = 0.50$, $s_y/p = s_z/p = 1.00$), (b) **large cuboid channel** ($R/s_y = 0.00$, $s_y/p = s_z/p = 1.00$), and (c) **irregular cuboid channel with rounded corners** ($R/s_y = 0.50$, $s_y/p = 0.75$, $s_z/p = 1.00$).

located not directly at the walls but in the vicinity of the central double-twist cylinder. These six regions of lower nematic order follow the rotation of $\bar{\mathbf{n}}(x)$ and rotate counter-clockwise along the x -direction. The defect structure of six disclination lines entangling each other in a helical fashion is illustrated by the plot of ℓ in Fig. 7.11(a).

LARGE CUBOID CHANNEL. Now we consider a cuboid channel of the same size as a **large cylindrical channel** by keeping $s_y/p = s_z/p = 1.0$ and setting $R/s_y = 0.0$. In principle, it is possible to accommodate four double-twist cylinders next to each other as shown for the bulk (see Fig. 7.2). Plots of $\bar{\mathbf{n}}(x)$ in the upper panels of Fig. 7.12 reveal the helical rotation of the local director along the line of vision as discussed for the bulk in Fig. 7.3.

However, as displayed by upper panels of Fig. 7.12, under confinement the local in-plane order $\bar{S}(x) \simeq 0.4$ is higher than in the bulk. This relatively high degree

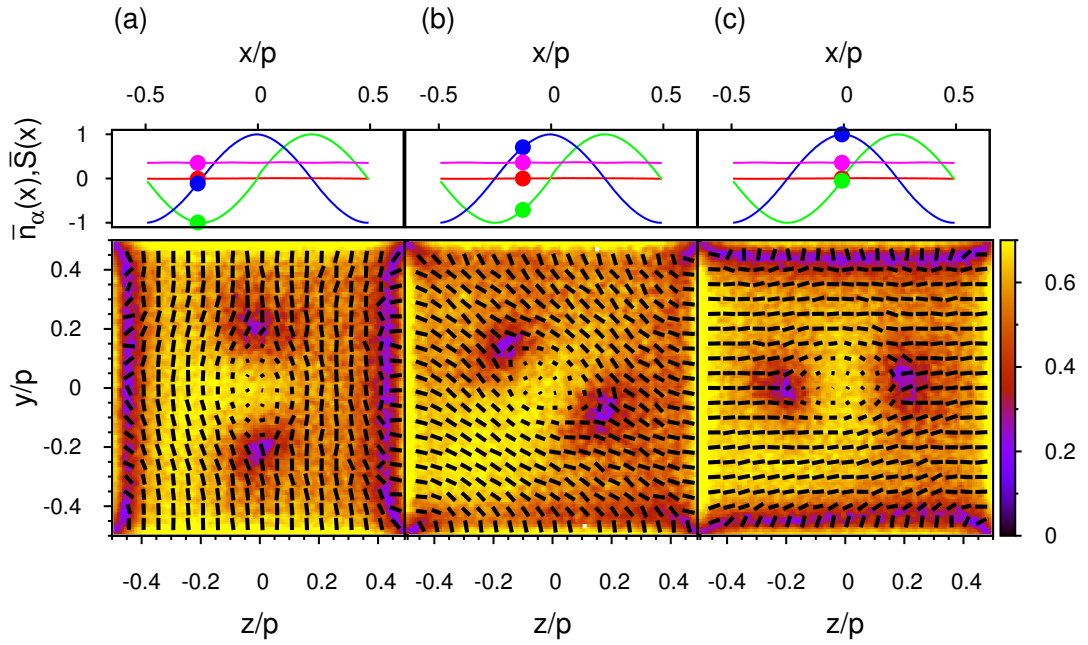


Figure 7.12. As Fig. 7.8, but for a large cuboid channel characterized via $R/s_y = 0.00$ and $s_z/p = s_y/p = 1.00$.

of nematic, in-plane order indicates a more or less pronounced in-plane orientation which is lacking in the bulk. In fact, as illustrated by the plots of $\hat{n}(\mathbf{r}')$ and $S(\mathbf{r}')$ in Fig. 7.12, a single double-twist cylinder is located at the center of the channel. Again, at $y = z = 0.0$ the local director escapes into the third dimension to avoid the formation of an ordinary defect in favor of an umbilic defect. Again, to simplify Fig. 7.12 we present sketch where the double-twist cylinder is encircled by a blue line [see Fig. 7.10(b)].

Outside the double-twist cylinder, the local director is parallel to the y - z plane and rotates along the x -direction. To define the scope of the double-twist cylinder we present director field in different colors in Fig. 7.10(b), i.e., black if the director belongs to the double-twist cylinder and green otherwise. This in-plane orientation outside the double-twist cylinder (i.e., parallel to the y - z plane) is consistent with the quasi-cholesteric phase discussed for the small cuboid channel in Fig. 7.8. Therefore, in the vicinity of the channel walls, we observe the same periodic defect structure along the channel's axis as presented in Fig. 7.7(b).

However, in the present case, the in-plane orientation is not homogeneous. The presence of the double-twist helix gives rise to additional defects that are marked by red dots in Fig. 7.10(b). At the circumference of the double-twist cylinder, all mesogens align parallel with the y - z plane in a circular fashion around its symmetry axis that is marked by a black dot in Fig. 7.10(b). This orientation inside the double-twist cylinder is not everywhere compatible with the homogeneous in-plane orientation formed outside the double-twist cylinder and gives rise to topological defect. Because outside of the double-twist cylinder $\hat{n}(x)$ rotates, these defects follow the rotation and entangle the double-twist cylinder in a helical fashion. Hence, combining the defect

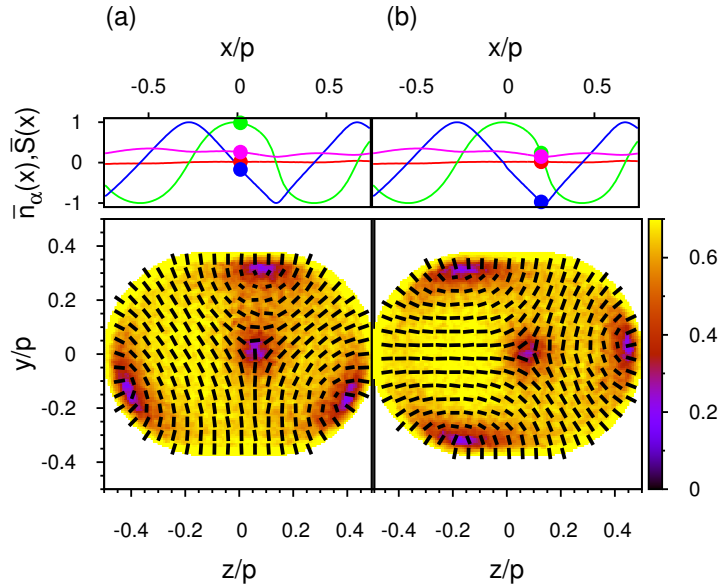


Figure 7.13. As Fig. 7.6, but for an **irregular cuboid channel with rounded corners** characterized via $s_y/p = 0.75$, $s_z/p = 1.00$, and $R/s_y = 0.50$.

structure in the vicinity of the walls, which has been explained for the **small cuboid channel** in Fig. 7.6 and Fig. 7.7(b), and the two disclination lines winding along the center of the channel we obtain the full picture of ℓ [see Fig. 7.11(b)].

IRREGULAR CUBOID CHANNEL WITH ROUNDED CORNERS. So far we considered channels characterized by cross-sections of equal size in the y - and z -directions. Plots in Fig. 7.13 illustrate the structure of a liquid crystal confined to a mesoscopic channel of a cross-section given by $s_y/p = 0.75$, $s_z/p = 1.0$, and $R/s_y = 0.5$. Because the ratio $s_y/s_z \neq 1$ the periodic rotation of the in-plane orientation cannot be described in terms of simple trigonometric functions. Despite similar geometry, the nematic in-plane order $\bar{S}(x) \simeq 0.35$ is higher in the **irregular cuboid channel with rounded corners** than in the **large cylindrical channel** discussed in Fig. 7.9. However, as plots of $\hat{n}(r')$ and $S(r')$ in the lower panels of Fig. 7.13 reveal, the orientational order is similar in both channels.

As discussed for the structure, which is exhibited within the **large cylindrical channel** and illustrated in Fig. 7.9 and Fig. 7.10(a), three defects occur in the vicinity of the walls. The origin of these defects is the same as discussed for the **large cylindrical channel**. In fact, as indicated by red dots in Fig. 7.10(c), defects arise because mesogens attempt to match surface anchoring conditions (i.e., parallel to the y - z plane) as well as the orientation at the center of the double-twist cylinder (i.e., orthogonal to the y - z plane). These defect regions rotate in an anti-clockwise fashion along the channel's axis.

Because the **irregular cuboid channel with rounded corners** is smaller in the y -direction than the **large cylindrical channel** (i.e., $s_y/p = 0.75$ and $s_y = 1.00$, respectively), a fourth double-twist cylinder cannot be accommodated in the present

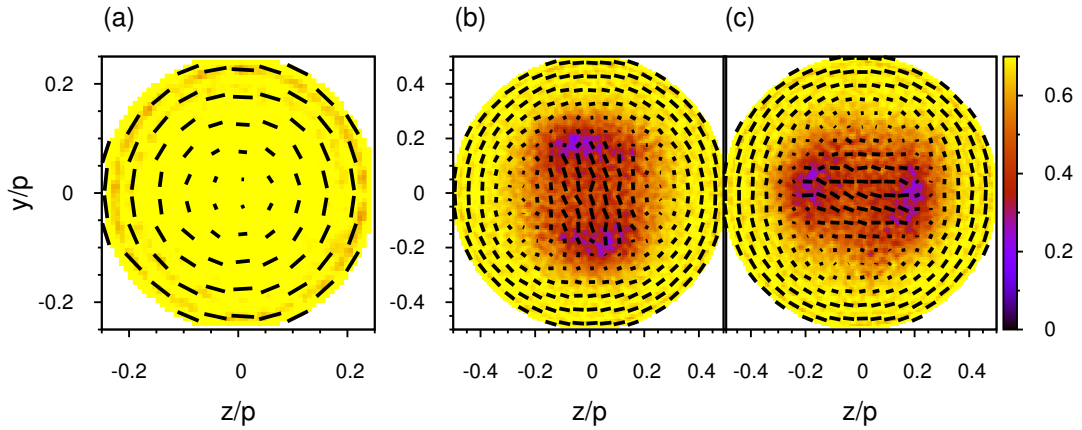


Figure 7.14. (a) as the [small cylindrical channel](#) and (b)-(c) as the [large cylindrical channel](#) presented in [Fig. 7.6](#) and [Fig. 7.9](#), respectively, but for locally circular planar anchoring of mesogens at the walls of the mesoscopic channel.

case. Hence, we do not observe three additional disclination lines inside the channel. Instead and because of orientational frustration of mesogens situated between the three double-twist cylinders, we observe a single disclination line located in the center of the channel. This is indicated by the central red dot in [Fig. 7.10\(c\)](#). Hence, the defect structure consists of a straight disclination line parallel to the x -direction which is entangled by three additional disclination lines rotating in a helical fashion [see [Fig. 7.11\(c\)](#)].

7.3.2 Circular planar anchoring conditions

Now we consider the case of locally monostable circular planar surface anchoring for which the mesogens in the vicinity of the channel walls are anchored parallel. As one realizes from [Eqn. \(3.35\)](#), any other in a local fashion alignment is energetically less favorable. Compared with the case of homeotropic surface anchoring one could expect that defect structures for locally circular planar anchoring are less spectacular. This is an immediate consequence of the compatibility of the surface anchoring and the molecular orientation at the circumference of a double-twist cylinder [see [Fig. 1.3\(b\)](#)].

SMALL CYLINDRICAL CHANNEL. For example, in [Fig. 7.14\(a\)](#) we consider a cylindrical channel of a diameter equal to half a pitch (i.e., for $s_y/p = s_z/p = 0.5$ and $R/s_y = 0.5$) where because of the circular, planar anchoring conditions the mesogens orientations are parallel to the y - z plane. As one moves from the wall towards the center of the channel, $\hat{n}(\mathbf{r}')$ rotates out of the y - z plane, which is indicated by the contraction of the dashes representing $\hat{n}(\mathbf{r}')$, and become finally orthogonal to it at the center of the channel. Hence, an unperturbed double-twist helix can evolve, indicated by the absence of any defects [see [Fig. 7.14\(a\)](#)]. Because there is no discrepancy

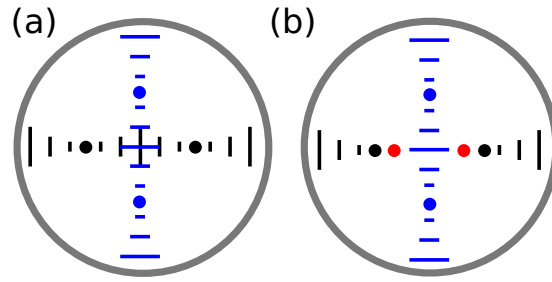


Figure 7.15. Schematic representation of the [large cylindrical channel](#) shown in [Fig. 7.14\(b\)](#) and (c). Blue and black dashes and dots represent the local director where the contraction reflects their rotation out of the paper plane such that the dots mark an orthogonal alignment to the paper plane. Topological defects are marked by red dots. (a) illustrates two different ways how a helical twist can match the anchoring conditions at the walls (see text) whereas (b) explains the defect structure shown in [Fig. 7.14\(c\)](#).

between the orientation of the mesogens and the local anchoring conditions at the walls, the double-twist cylinder is stabilized by the presence of the walls rather than perturbed. From another point of view this can be explained by the symmetries of the channel and the double-twist cylinder that are in perfect agreement.

LARGE CYLINDRICAL CHANNEL. As one doubles the radius of the cylindrical channel by setting $s_y/p = s_z/p = 1.0$ and $R/s_y = 0.5$, more than one double-twist cylinder can be accommodated. Moreover, as indicated by plots of $\hat{n}(r')$ and $S(r')$ in [Fig. 7.14\(b\)](#) and (c) the local orientation is not defined everywhere and topological defects arise which can be rationalized as follows.

Let us assume we follow the spatial variation of $\hat{n}(r')$ at fixed x along the y -direction that is presented in blue in [Fig. 7.15\(a\)](#). At the walls (i.e., at $y = \pm 0.5s_y$) the orientation of the mesogens is controlled by the surface anchoring such that $\hat{n}(r')$ is parallel to the y - z plane. In particular, $\hat{n}(r')$ points along the z -axis. As one moves along the y -direction $\hat{n}(r')$ rotates out of the y - z plane indicated by the contraction of the dashes in [Fig. 7.15\(a\)](#), is parallel to \hat{e}_x at a distance of $p/4$ from the wall, and eventually parallel to \hat{e}_z at the center of the channel (i.e., at distance of half a pitch).

If we repeat this *Gedankenexperiment* but now follow the spatial rotation of $\hat{n}(r')$ along the z -axis [i.e., black colored dashes in [Fig. 7.15\(a\)](#)] we obtain $\hat{n}(r')$ which is now aligned with the y -direction at the center of the channel. Apparently, two competing orientations cannot be realized locally. Therefore, one of these orientations wins over the other one [see [Fig. 7.15\(b\)](#)] and causes the formation of two defect regions [indicated by red dots in [Fig. 7.15\(b\)](#)] because of the orientational mismatch with the other orientation [see [Fig. 7.14\(b\)](#) and (c)].

Furthermore, both orientations rotate along the channels axis. Hence, the defects follow this in-plane rotation and form two disclination lines entangling each other in a helical fashion along the line of vision [see [Fig. 7.16\(a\)](#)]. A similar defect structure has been presented for the [small cylindrical channel](#) with homeotropic anchoring

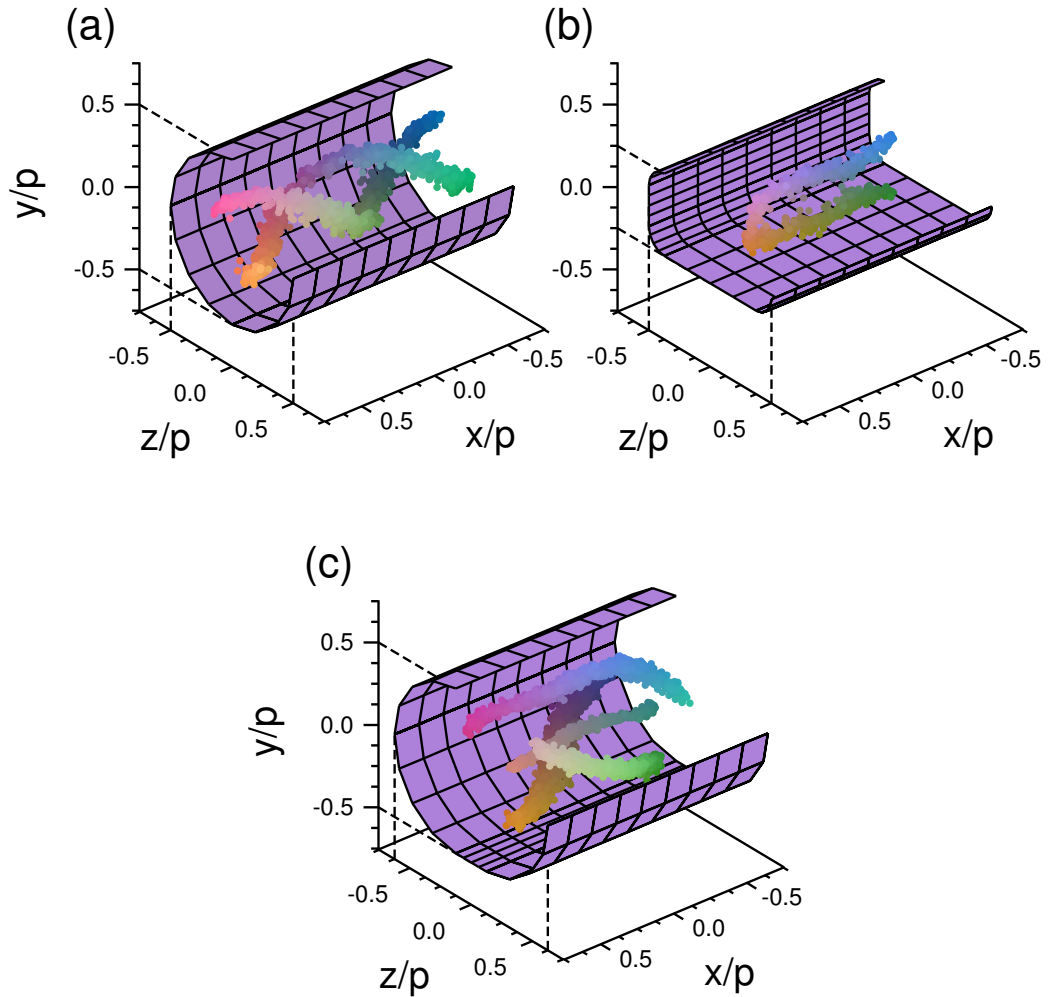


Figure 7.16. As Fig. 7.7, but for local planar anchoring of mesogens at the wall of a mesoscopic channel. (a) $s_y/p = s_z/p = 1.00$, $R/s_y = 0.50$, (b) $s_y/p = 0.50$, $s_z/p = 1.00$, $R/s_y = 0.25$, (c) $s_y/p = 1.00$, $s_z/p = 1.25$, $R/s_y = 0.50$.

conditions in Fig. 7.7(a) where ℓ is located in the vicinity of the walls. In the present case, however, ℓ has removed further apart from the wall.

FLAT CUBOID CHANNEL WITH ROUNDED CORNERS. Now we turn to a discussion of a flat channel (i.e., $s_y/s_z \leq 0.5$) whose shape is characterized by $s_y/p = 0.5$, $s_z/p = 1.0$, and $R/s_y = 0.25$. Under these geometrical conditions two double-twist helices can be accommodated next to each other. Plots of $\hat{n}(r')$ and $S(r')$ in Fig. 7.17 illustrate that the centers of the double-twist cylinders are located at $z/p = \pm 0.25$ and $y = 0$. Because of the channel size and shape as well as under the chosen anchoring conditions we observe no defects at the channel walls. However, at $z = 0$ the orientation of the mesogens competes with the anchoring at the top and bottom wall of the channel. Because of this mismatch two defects are observed evolving parallel to the line of vision as demonstrated by the plot of ℓ in Fig. 7.16(b).

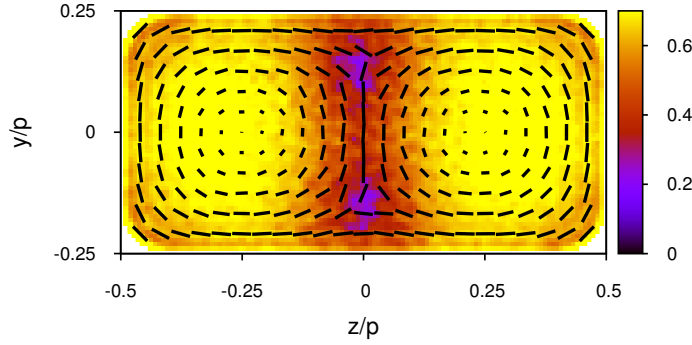


Figure 7.17. As Fig. 7.14, but for a flat cuboid channel with rounded corners characterized via $s_y/p = 0.50$, $s_z/p = 1.00$, and $R/s_y = 0.25$.

IRREGULAR CUBOID CHANNEL WITH ROUNDED CORNERS. The last case considered in this section is a channel characterized by an asymmetric extent of its shape in y - and z -directions realized by setting $s_y/p = 1.0$, $s_z/p = 1.25$, and $R/s_y = 0.5$. As shown in Fig. 7.18 the mesoscopic channel is large enough to accommodate three triangularly arranged double-twist cylinders. Consistent with ℓ , discussed for the irregular cuboid channel with rounded corners but homeotropic anchoring conditions in Fig. 7.13, we observe the formation of a topological defect between three double-twist cylinders at the center of the channel. As illustrated by the plot of ℓ in Fig. 7.16(c) this disclination line remains parallel with the channel axis throughout.

Furthermore, we notice three regions where $S(\mathbf{r}')$ is reduced. These regions arise because of competing orientations within two double-twist helices and the orientation at the channel wall. Hence, the defect structure shown in Fig. 7.16(c) consists of a straight disclination line parallel to \hat{e}_x wrapped by three additional disclination lines.

Notice that defect structures presented for an irregular cuboid channel with rounded corners with both homeotropic and circular planar anchoring conditions [see Fig. 7.11(c) and Fig. 7.16(c), respectively] have the same defect topology. They consist of a straight disclination line wrapped by three additional lines. However, in the present case (i.e., for circular planar surface anchoring) the three outer disclination lines are further removed from the channel walls whereas for homeotropic surface anchoring they are located in the vicinity of the walls.

We also emphasize that in the present case defects arise at the circumference of the double-twist cylinders whereas in the case of homeotropic anchoring conditions this occurs in the center of the double-twist cylinders. Finally, we note that the same structure has been observed in Fig. 10(a) of Ref. 151 but in a cylindrical channel.

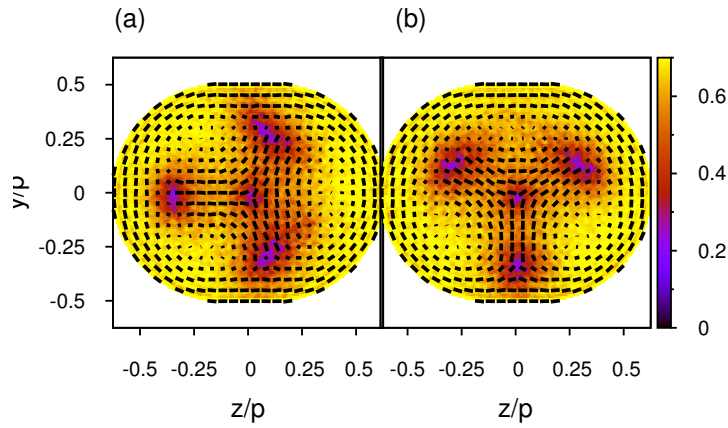


Figure 7.18. As Fig. 7.14, but for an irregular cuboid channel with rounded corners characterized via $s_y/p = 1.00$, $s_z/p = 1.25$, and $R/s_y = 0.50$.

7.3.3 Directional planar anchoring conditions

Finally, we consider unidirectional surface anchoring where the mesogens align with the channel axis [i.e., \hat{e}_x according to Eqn. (3.36)]. We begin the presentation with a defect structure which has been discussed for irregular cuboid channels with rounded corners with homeotropic and circular planar anchoring conditions displayed in Fig. 7.11(c) and Fig. 7.16(c), respectively.

SMALL CYLINDRICAL CHANNEL. We consider a cylindrical channel characterized by $s_y/p = s_z/p = 0.75$ and $R/s_y = 0.5$ and observe a single disclination line surrounded by three additional lines which form a triple helix along the symmetry axis of the channel [see Fig. 7.19(a)]. In the present case, the outer disclination lines are located at the channel walls [Fig. 7.19(a)], as found for homeotropic surface anchoring in Fig. 7.11(c). This is in contrast to circular planar anchoring conditions in Fig. 7.16(c) where these disclination lines are detached from the channel walls. It is also noteworthy that in the case of the directional planar surface anchoring this particular defect structure occurs only if the size of the channel in the y - and z -direction is equal (i.e., for cylindrical channels).

FLAT CHANNELS. Defect structures presented so far were disclination lines which evolve along the channel's axis either in a straight or helical fashion. However, as shown in Fig. 7.19(b) and (c) we also observe the formation of ring-like defects if the geometry of the channel is chosen to be flat (i.e., $s_y/s_z \leq 0.5$). This is realized by setting $s_y/p = 0.25$ or $s_y/p = 0.5$ whereas $s_z/p = 1.25$ and $R/s_y = 0.5$. In the flatter channel (i.e., for $s_y/p = 0.25$) disclination loops intertwine but do not intersect whereas in the wider channel (i.e., for $s_y/p = 0.5$) these loops are connected at certain tetrahedrally coordinated points at which pairs of disclination loops merge [see Fig. 7.19(b) and (c), respectively].

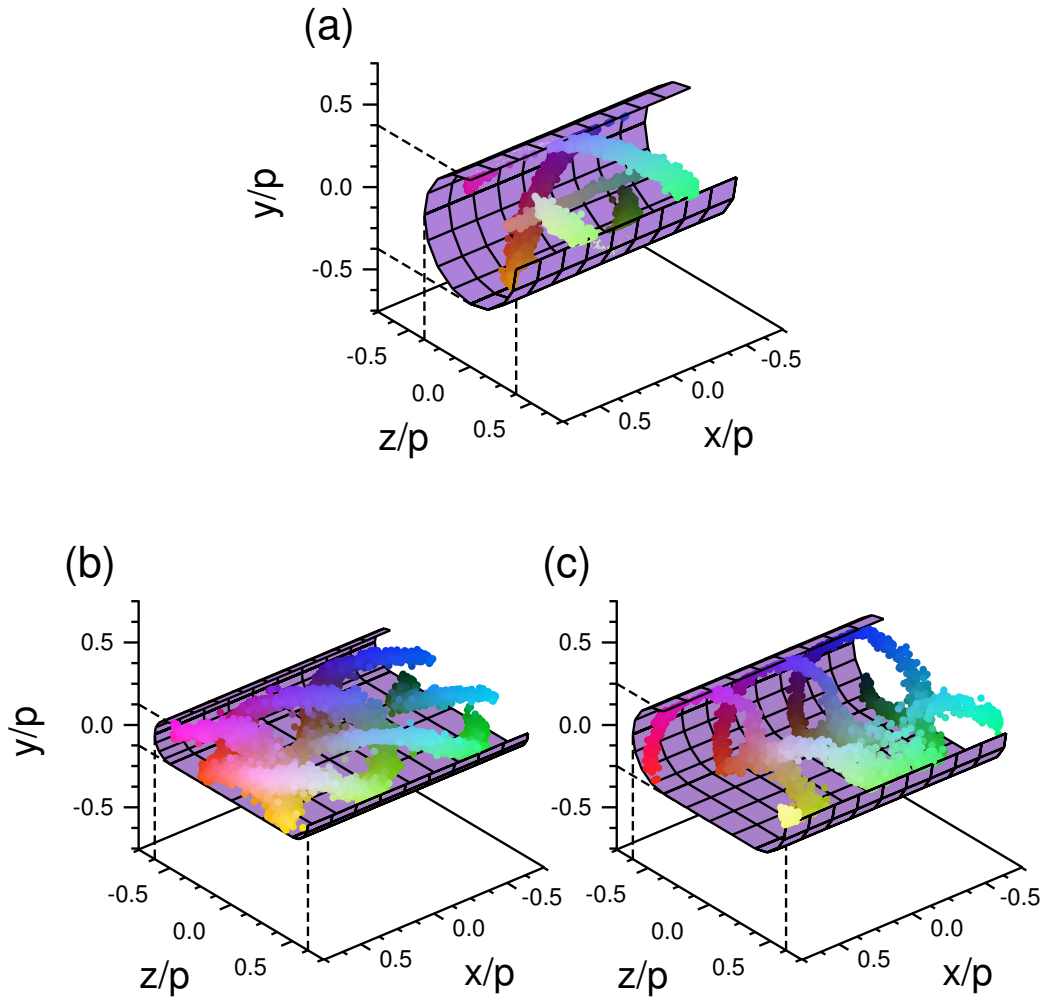


Figure 7.19. As Fig. 7.14, but for local directional anchoring of mesogens at the wall of a mesoscopic channel for a wall curvature of $R/s_y = 0.5$. (a) $s_y/p = s_z/p = 0.75$, (b) $s_y/p = 0.25$, $s_z/p = 1.25$, (c) $s_y/p = 0.5$, $s_z/p = 1.25$.

A detailed view of ℓ presented in Fig. 7.19(b) is shown in Fig. 7.20 where the local director, as well as the local nematic order parameter, is plotted to illustrate the circumstances leading to the formation of disclination loops. We observe the formation of a regular array of double-twist helices in the x - z plane at $y = 0$. As discussed earlier, among four double-twist cylinders the nematic order is perturbed and topological defects arise at $y = z = 0.0$ along the channels axis. Furthermore, at $y = 0$ and $z/p = \pm 0.5$ the orientational mismatch between two of the double-twist cylinders and the surface anchoring yields the formation of additional defects. These defect regions inside the x - z plane are very regular because of the well-ordered array of double-twist cylinders evolving along the y -direction until they reach the walls. Hence, disclination rings are bent with respect to the x - z plane at $y = 0$.

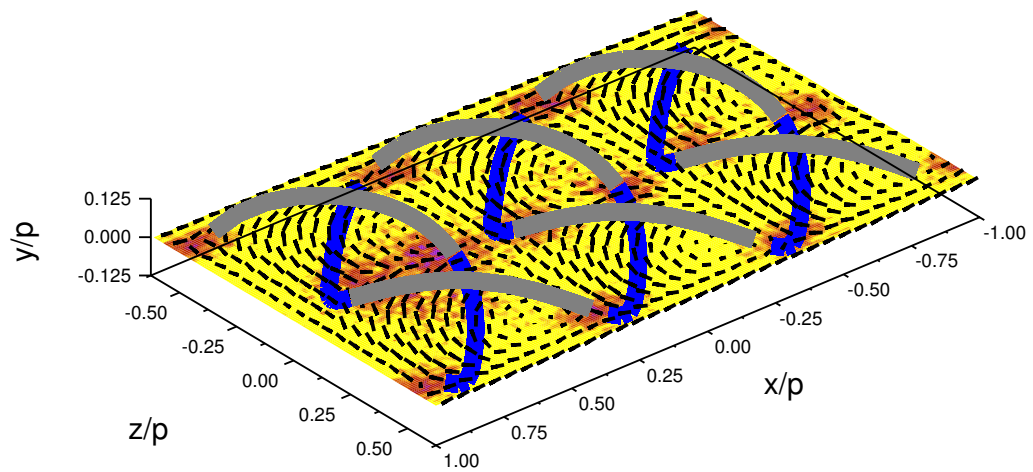


Figure 7.20. As Fig. 7.19(b), but for the local director field (dashes) and the local nematic order parameter. In addition, disclination rings are shown that are colored in gray if they lie above the x - z plane at $y = 0$ and are colored in blue otherwise.

Part IV

CONCLUSIONS AND OUTLOOK

CONCLUSIONS AND OUTLOOK

The subject of this work is the impact of curved surfaces on the liquid-crystalline order. In order to investigate this, we consider two different systems. The first system is composed of one or two colloidal particles that are dispersed in a liquid-crystalline carrier fluid. The second system consists of a mesoscopic channel which contains a chiral liquid crystal. Except for one special case [see Fig. 7.14(a)] the symmetry of colloids as well as of channels is not compatible with the symmetry of liquid-crystalline phases. Hence, perturbations arise and give rise for interesting phenomena such as the colloidal self-assembly or the broad variety of defect topologies found within the mesoscopic channel.

In order to investigate these phenomena, we perform Monte Carlo simulations carried out for a model liquid crystal. Because of the simplicity of the model potential (i.e., the isotropic core and small aspect ratio), it is possible to simulate systems consisting of up to 70×10^3 particles in a reasonable time. Large system sizes are necessary to investigate perturbations that arise due to the presence of a colloidal particle or to study periodic perturbations that arise inherently in blue phases on a length scale one or two orders of magnitude larger than the molecular one.

Furthermore, the computation of macroscopic quantities such as the tensor order parameter Q , Landau-de Gennes expansion coefficients A , B , and C , Frank's elastic constants K_1 , K_2 , and K_3 , or the surface energy W brings us in a position to compare our results with experimental findings as well as theoretical results based on a continuum approach. We emphasize that up to date and to the best of our knowledge there is no other molecule based description of A , B , and C than that introduced by us in Sec. 4.3.

8.1 COLLOIDAL DISPERSION

We begin by summarizing results that we obtained for colloidal particles dispersed in a liquid-crystalline host phase. More specifically, in Chapter 5 we investigate the self-assembly of a pair of colloids dispersed in a nematic host phase. We design our simulation cell by analogy with experimental setups. In fact, our system consists of two colloidal particles surrounded by N mesogens forming a nematic phase.

Inspired by the experimental setup we confine our system by two planar and structureless substrates to fix the global director \hat{n}_0 in space. The colloids are placed in the x - y plane equidistantly between the substrates. The separation of the substrates is chosen to be sufficiently large to avoid direct substrate effects on the structure of liquid crystalline order in the vicinity of the colloidal surface. Furthermore, we assume that on account of their size colloidal motion takes place on larger time scale.

Consequently, we fix the centers of mass of colloids in space. We vary only their relative arrangement in space (i.e., distance and the angle formed between \hat{n}_0 and the distance vector) in individual simulations.

It was also demonstrated experimentally first by Poulin and Weitz¹⁰ and later by Smalyukh *et al.*⁵⁰ and Zuhail *et al.*⁵⁷ that Boojum colloids (i.e., colloids with planar surface anchoring) self-assemble into chains tilted by an angle of 30° with respect to \hat{n}_0 . These authors mentioned that effective inter-colloidal interactions are mediated by perturbations of the liquid-crystalline phase. Thus, this particular angle of 30° arise due to minimizing the perturbations of the nematic host phase. This assumption is confirmed by Eskandari *et al.*⁵¹ within the framework of Landau-de Gennes theory.

The comparison of our results with those obtained experimentally^{50,57} and theoretically⁵¹ is carried out by linking the phenomenological Landau-de Gennes theory to our molecule-based approach (see [Chapter 4](#) and [Chapter 5](#)). Therefore, we first determine the phenomenological Landau-de Gennes expansion coefficients as follows. As an *ansatz*, we take a free energy which was obtained within the framework of classical density functional theory⁷⁷ and consists of two contributions, i.e., the orientational and anisotropic potential contribution. Expanding the orientational contribution of the free energy density as Taylor series immediately results in a similar form as the Landau-de Gennes free energy density. The anisotropic potential contribution drives the isotropic-nematic phase transition temperature which is, however, not captured adequately by the classical density functional theory. This is because an exact analytic expression for the pair correlation function is lacking and conventional approaches are valid for ideal systems or systems of low densities. The phase transition temperature may be determined by applying finite-size scaling theory with a high degree of accuracy. This theory utilizes that fact that in computer simulations one is always confronted with systems of finite size. This system-size dependence is then used to locate the exact phase transition temperature (see [Sec. 5.2](#) and [Sec. 6.1](#)).

Then, one only needs to determine the elastic constants to be in a position to calculate the Landau-de Gennes free energy from our MC data. Fortunately, the measurement of these constants in computer simulations is well known and was introduced by Allen and Frenkel.^{99,100} In their approach one considers fluctuations of the Fourier components $\tilde{Q}(k)$ of $Q(r)$ (see [Sec. 4.5](#)). In the limit of $|k| \rightarrow 0$ a linear relation exists which is used to determine all elastic constants (see [Fig. 6.5](#)).

Finally, we divide our system into a three-dimensional grid and compute the Landau-de Gennes free energy density [see [Eqn. \(4.6\)](#)] for different colloidal configurations. Therefore, for each spatial arrangement of the colloids, the local alignment tensor is computed as an ensemble average. Using the molecule based version of Landau-de Gennes expansion coefficients A , B , and C as well as Frank's elastic constants K_1 , K_2 , and K_3 we perform a volume integration of the free energy density in order to calculate the free energy associated with a specific colloidal configuration. This method allows us to quantify the perturbations of a nematic phase.

We mimic the experimental setup and consider^{10,50,57} a pair of colloids with planar anchoring conditions included in a nematic host phase that is confined between two

planar substrates. In a previous work,⁵⁹ we have demonstrated that a single colloid that anchors the mesogens in a planar fashion causes the formation of two Boojum defects in perfect agreement with experimental results.^{9,10} Hence, the model system is sufficiently realistic for our purpose.

We perform extensive MC simulations for various colloidal configurations and compute the Landau-de Gennes free energy associated with those configurations in order to obtain a free energy landscape (see Fig. 5.8). Using this landscape we immediately identify a global minimum of the free energy at 30° as predicted by experimental results^{10,50,57} and numerical calculations.⁵¹ Moreover, assuming pairwise additive interactions we use the free energy as a coarse-grained potential between a pair of colloids to investigate the colloidal self-assembly of multiple colloids performing implicit solvent simulations. Again, the results for high and low colloidal densities are in perfect agreement with experimental studies.⁵⁰

Apparently, colloidal self-assembly is driven by local perturbations of the global nematic order which arise because of the mismatch between the orientation mediated by the colloidal surface anchoring and \hat{n}_0 . Hence, by the replacement of Boojum colloids through Saturn ring colloids (i.e., colloids with homeotropic anchoring conditions) the perturbation of the nematic phase changes (see Fig. 5.1). Consequently, one expects that the colloidal self-assembly varies as well. In fact, Saturn ring colloids self-assemble into “zig-zag” chains perpendicular to \hat{n}_0 as demonstrated experimentally.^{10,92}

However, not only the colloidal surface anchoring but also elastic properties of the liquid crystal affects the self-assembly. Eskandari *et al.*⁵¹ demonstrated that for a certain choice of elastic constants (i.e., $K_1 = \frac{1}{2}K_2 = K_3$) Boojum colloids align parallel with \hat{n}_0 instead of forming chain tilted with respect to \hat{n}_0 . Because elastic properties are material specific one can either replace the liquid crystal or liquid crystalline-phase in order to vary the elasticity and eventually change the self-assembly.

Recent experiments by Zuhail *et al.*^{56–58} reveal that the replacement of the nematic by a smectic A phase has a crucial impact on the self-assembly. More specifically, the angle of 30° which is found for Boojum colloids decreases to 20° if the liquid crystal undergoes a nematic-smectic A phase transition. Hence, self-assembled colloidal quasi-crystals may be controlled by external stimuli such as thermodynamic conditions (e.g., temperature or pressure gradient) or electric/magnetic field that drive the phase transition.

In order to study the impact of temperature on colloidal inclusion in a smectic A phase and especially on perturbations caused by colloids with different anchoring conditions, we develop a novel potential to model the liquid-crystalline host phase. A careful study of equilibrium and non-equilibrium properties of that model reveals its realistic phase behavior, dynamics, and elasticity (see Sec. 6.1).

In fact, as the system is quenched the model exhibits an isotropic, nematic, and smectic A phase (see Fig. 6.1). The diffusion of the mesogens becomes anisotropic as the system is in the nematic or smectic A phase. In the nematic phase, the diffusion along the mesogens longer axes D_{\parallel} is enhanced with respect to the diffusion perpen-

pendicular to the mesogens axes D_{\perp} . In the smectic A phase, however, D_{\parallel} is smaller than D_{\perp} because of the one-dimensional solid-like structure of the smectic A phase (see Fig. 6.4). Diffusion in the nematic as well as smectic A phase is in perfect agreement with experimental systems.¹²¹ Elastic properties of our model are expressed in terms of three elastic constants (i.e., K_1 , K_2 , and K_3) referring to three characteristic deformations of a nematic liquid crystal, i.e., splay, twist, and bend, respectively. As for experimental systems (e.g., 8CB) we observe the divergence of two elastic constants (i.e., for K_2 and K_3) as the system approaches the nematic-smectic A phase transition (see Fig. 6.6).

After validating our carrier fluid is realistic enough, we include a colloidal particle in our system. Clearly, before investigating effective interactions based on nonlinear perturbations of the smectic A phase caused by a pair of colloids one needs to understand perturbations caused by a single colloid. Thus, we include a single colloidal particle at the origin of the simulation box, fix it in space, and confine it between two substrates as discussed before.

For a colloid that anchors the mesogens in a locally homeotropic fashion the well known Saturn ring defect arises if the mesogens are in the nematic phase. As the temperature is lowered the mesogens pass the nematic-smectic A phase transition and the ring defect shrinks but remains stable in the smectic A phase. On account of the strong surface anchoring, smectic layers are bent and a small region of lower density occur. In these regions, the orientation of the mesogens is undefined and results in the formation of a defect. This observation, however, is in contradiction with experimental observations where the ring defect vanishes.⁵⁸

To clarify the discrepancy between experiment and our results we decrease the anchoring strength by modifying the range of the mesogen-colloid potential [see Eqn. (3.19)]. The weaker surface anchoring is still strong in the nematic phase such that a Saturn ring defect is formed around the colloid. However, in the smectic A phase surface anchoring is too weak to bend the smectic layers. Consequently, the equidistant character of the layers is unperturbed and the formation of a ring defect is inhibited as predicted by experiments.⁵⁸

For a very strong homeotropic surface anchoring, we observe multiple concentric layers around the colloidal particle. This onion structure is known for sheared lyotropic liquid crystals and has recently been observed for the 8CB liquid crystal confined to a microscopic channel.¹³³ However, to the best of our knowledge, this is the first time that an onion structure is reported in the vicinity of a colloidal particle.

Considering a colloid with locally planar surface anchoring two point-like Boojum defects occur at the north and south pole of a colloid immersed in the nematic phase. As the temperature is decreased below the nematic-smectic A phase transition the limitation of our model becomes apparent. Because of the strong planar surface anchoring, the colloid perturbs layers which are not directly penetrated by it. However, to observe focal lines, which have been reported in experiments,⁵⁷ the layers located at much larger distances from the colloid have to follow the bending of the smectic layers in the vicinity of the colloid to preserve the equidistant layering. In our model,

however, the mesogens repel each other weakly if they are in the end-end configuration [see Fig. 3.1(d)] such that the preservation of equidistance is not strictly demanded by the interacting potential. For this reason, the equidistance is abrogated at the north and south pole and a low-density regime arises where, due to the orientational frustration of the mesogens, two Boojum defects arise.

The formation of equidistant layers in our system occurs because of the thermodynamic conditions. In order to improve the formation of equidistant layers we decrease the temperature, and additionally, we increase the anchoring strength by increasing the mesogen-colloid interaction range. In fact, we observe an elongation of the defect region as predicted from experiments.⁵⁷ However, the origin of the defects is different in our model. In experiments, a focal line is observed due to a discontinuous variation of the layer normal which automatically induces a mismatch between orientations of the mesogens located inside of this layer. Because of the equidistant stacking of the layers, this orientational mismatch is extended over a large distance. In our model, however, we observe an elongated low-density region without any positional or orientational order.

If surface anchoring is weakly planar, the colloid is not able to perturb the strong orientational order at the north and south pole. Hence, at the poles, the mesogens are perpendicularly oriented with respect to the colloidal surface. Because at the equator of the colloid surface anchoring is in good agreement with \hat{n}_0 , the mesogens align with their longer axes parallel to the surface. This gives rise to the formation of topological defects when the *effective* homeotropic surface anchoring changes to an *intrinsically* planar surface anchoring. The transition of the anchoring condition is analogous to that at the surface of a Janus colloid immersed in a nematic host phase where a surface ring is formed around the colloid.^{59,135} We observe the formation of two ring defects located at $\gamma_+ = 30^\circ$ and $\gamma_- = 150^\circ$ because of the transition from *effective* homeotropic to *intrinsically* planar and back to *effective* homeotropic if one goes from the north pole via the equator to the south pole.

After a discussion of perturbations caused by single colloids in a smectic A phase one consequently would turn in a discussion of effective interactions that arise between a pair of colloid. However, for reasons of time we limit ourselves to an outlook and a discussion of problems related to the extraction of effective interactions from perturbations of the smectic A phase. In principle, this could be evaluated by the method introduced in Chapter 5 for a pair of Boojum colloids dispersed in a nematic carrier fluid. However, for a smectic phase, this method has some problems.

1. Because of the larger colloidal size considered for the smectic A phase, the number of mesogens N is much larger, i.e. $50-70 \times 10^3$ and $16-20 \times 10^3$ for a single colloid included in a smectic A and nematic phase, respectively. Consequently, computation time increases drastically as one considers larger systems. To save computer time one may use massive parallelized molecular dynamics simulations on GPUs.⁸²

2. The contribution of the elastic deformation of the director field [see Eqn. (4.22)] has to be complemented by an additional term describing the layer compression.²¹ This term contains a new elastic constant which lacks a molecular interpretation.
3. The last and most serious problem concerns the free energy expansion at nematic-smectic A phase transition that is performed in the same fashion as for isotropic-nematic one [see Eqn. (4.6)]. Following de Gennes¹⁵⁷ one may cast the free energy of the smectic A phase as

$$f' = f_0^{\text{N}} + A'(T)\Lambda^2 + C'(T)\Lambda^4 \quad (8.1)$$

where A' and C' are expansion coefficient ($B' = 0$ because the nematic-smectic A phase transition is assumed to be continuous), Λ is the smectic A order parameter [see Eqn. (1.2)], and f_0^{N} is the free energy of the nematic phase. Beside the unknown coefficients A' and C' , f_0^{N} is the actual problem. All information about the orientational (i.e., nematic) order are given by f_0^{N} and could, in principle, be approximated by the Landau-de Gennes free energy [see Eqn. (4.6)]. However, Eqn. (4.6) is solely valid in vicinity of the isotropic-nematic phase transition (see Sec. 4.2). Hence, f_0^{N} remains undetermined.

Alternatively, one could determine the potential of mean force in order to investigate colloidal interactions. The potential of mean force is a measure of the effective difference in free energy between two different states as a function of several degrees of freedom, for instance, positions of the colloids. Using the potential of mean force within the framework of Monte Carlo simulations Kim *et al.*^{158,159} demonstrated the effectiveness of this method applied to systems consisting of a nematic phase that accommodates either two Saturn ring colloids or a single Saturn colloid in the vicinity of a substrate.

8.2 MESOSCOPIC CHANNELS

Finally, we turn to a discussion of defect structures exhibited in chiral blue phases confined to mesoscopic channels. Blue phases exhibit an inherent network of disclination lines. Because of the periodic and well-defined networks, blue phases are used as templates for colloidal and molecular self-assembly. The mechanism of this self-assembly is based on the attractive interactions between disclination lines with molecules and colloids.

Hence, the manipulation of defect networks is of crucial importance. This can be achieved, for instance, if the liquid crystal is confined to a channel. In Chapter 7, we discuss the impact of the channel's shape, size, and surface anchoring on the formation of defect structures. For blue phase II, we report defect structures which have been observed experimentally and theoretically within the framework of a continuum theory.^{37,144} Moreover, we report a host of novel defects. More specifically,

we observe the formation of helical ensembles of multiple disclinations, complex networks, and ring disclinations.

Recent experimental studies¹⁴² of chiral liquid crystals confined to nanochannels confirmed some defect topologies presented here. Unfortunately, on a length scale of 10nm, the experimental data are rather scarce if at all available. Hence, the method reported in this thesis may be used to analyze liquid-crystalline order locally. Comparison between experiments and computer simulations may be obtained via globally defined quantities. For example, measurements of optical retardation (i.e., the difference in time which light needs to travel in a direction along and perpendicular to the molecular axis) can be measured with a simple experimental setup. Optical retardation is proportional to the nematic order parameter^{141,142} which can be extracted from computer simulations. Hence, it is possible to link both computer simulation and experiments via the nematic order parameter in order to reveal local structures exhibited in a nanochannel.

Furthermore, our restriction to blue phase II may be lifted as demonstrated by Skutnik⁸⁸ who focused on blue phase I. Using the model system discussed in this thesis (see [Chapter 7](#)), Skutnik observed the formation of a blue phase I in the bulk for the first time in a computer simulation. Moreover, with this, he showed that the model potential used also in [Chapter 7](#) is capable of forming all chiral phases. He also studied the formation of defects which arise due to the presence of mesoscopic channel. Furthermore, recent studies^{139,160–162} of chiral phases confined to spherical geometries, i.e., droplets of bubbles reveal the broad interest in such systems. Again, because of the lack of molecular models, the model system discussed here is predestinated for further studies.

Part V

APPENDIX

BIBLIOGRAPHY

- [1] F. Reinitzer, *Monatsh. Chem.*, 1888, **9**, 421–441.
- [2] O. Lehmann, *Z. phys. Chem*, 1889, **4**, 462–472.
- [3] G. H. Heilmeyer and L. A. Zanoni, *Appl. Phys. Lett.*, 1968, **13**, 91–92.
- [4] G. H. Heilmeyer, L. A. Zanoni and L. A. Barton, *P. IEEE*, 1968, **56**, 1162–1171.
- [5] B. Bahadur and M. Tilton, *Liquid crystals: applications and uses*, World Scientific, Singapur, 3rd edn, 1992.
- [6] P. G. de Gennes, *The Physics of Liquid Crystals*, Oxford University Press, Oxford, 2nd edn, 2002.
- [7] S. Chandrasekhar and G. S. Ranganath, *Rep. Prog. Phys.*, 1990, **53**, 57.
- [8] V. Borshch, Y.-K. Kim, J. Xiang, M. Gao, A. Jákli, V. P. Panov, J. K. Vij, C. T. Imrie, M.-G. Tamba, G. H. Mehl *et al.*, *Nat. Commun.*, 2013, **4**, 1–8.
- [9] P. Poulin, H. Stark, T. C. Lubensky and D. A. Weitz, *Science*, 1997, **275**, 1770–1773.
- [10] P. Poulin and D. A. Weitz, *Phys. Rev. E*, 1998, **57**, 626.
- [11] A. Nych, U. Ognysta, M. Škarabot, M. Ravnik, S. Žumer and I. Muševič, *Nat. Commun.*, 2013, **4**, 1489.
- [12] I. Muševič, *Liq. Cryst.*, 2014, **41**, 418–429.
- [13] H. Kikuchi, M. Yokota, Y. Hisakado, H. Yang and T. Kajiyama, *Nat. Mat.*, 2002, **1**, 64–68.
- [14] J. Xiang and O. D. Lavrentovich, *Appl. Phys. Lett.*, 2013, **103**, 051112.
- [15] X. Wang, D. S. Miller, E. Bokusoglu, J. J. de Pablo and N. L. Abbott, *Nat. Mat.*, 2016, **15**, 106–112.
- [16] X. Wang, Y.-K. Kim, E. Bokusoglu, B. Zhang, D. S. Miller and N. L. Abbott, *Phys. Rev. Lett.*, 2016, **116**, 147801.
- [17] A. Sengupta, C. Bahr and S. Herminghaus, *Soft Matter*, 2013, **9**, 7251–7260.
- [18] W. Maier and A. Saupe, *Z. Naturforsch. A*, 1959, **14**, 882–889.
- [19] W. Maier and A. Saupe, *Z. Naturforsch. A*, 1960, **15**, 287–292.
- [20] N. V. Madhusudana and R. Pratibha, *Mol. Cryst. Liq. Cryst.*, 1982, **89**, 249–257.

- [21] P. M. Chaikin, *Principles of Condensed Matter Physics*, Cambridge University Press, Cambridge, Reprint edn, 2000.
- [22] D. Armitage and F. P. Price, *J. Chem. Phys.*, 1977, **66**, 3414–3417.
- [23] J. Thoen, *Phys. Rev. A*, 1988, **37**, 1754.
- [24] D. K. Yang and P. P. Crooker, *Phys. Rev. A*, 1987, **35**, 4419.
- [25] H. J. Coles and M. N. Pivnenko, *Nature*, 2005, **436**, 997–1000.
- [26] W. He, G. Pan, Z. Yang, D. Zhao, G. Niu, W. Huang, X. Yuan, J. Guo, H. Cao and H. Yang, *Adv. Mater.*, 2009, **21**, 2050–2053.
- [27] A. D. Ford, S. M. Morris and H. J. Coles, *Mater. Today*, 2006, **9**, 36–42.
- [28] R. M. Hornreich and S. Shtrikman, *J. Phys.-Paris*, 1980, **41**, 335–340.
- [29] R. M. Hornreich and S. Shtrikman, *Phys. Rev. A*, 1981, **24**, 635.
- [30] H. Kleinert and K. Maki, *Fortschr. Phys.*, 1981, **29**, 219–259.
- [31] H. Grebel, R. M. Hornreich and S. Shtrikman, *Phys. Rev. A*, 1983, **28**, 1114.
- [32] H. Grebel, R. M. Hornreich and S. Shtrikman, *Phys. Rev. A*, 1984, **30**, 3264.
- [33] J. P. Sethna, *Phys. Rev. Lett.*, 1983, **51**, 2198.
- [34] J. P. Sethna, D. C. Wright and N. D. Mermin, *Phys. Rev. Lett.*, 1983, **51**, 467.
- [35] S. Meiboom, J. P. Sethna, P. W. Anderson and W. F. Brinkman, *Phys. Rev. Lett.*, 1981, **46**, 1216.
- [36] S. Meiboom, M. Sammon and W. F. Brinkman, *Phys. Rev. A*, 1983, **27**, 438.
- [37] D. C. Wright and N. D. Mermin, *Phys. Rev. A*, 1985, **31**, 3498.
- [38] P. P. Crooker, *Liq. Cryst.*, 1989, **5**, 751–775.
- [39] M. Kléman and O. D. Laverntovich, *Soft matter physics: an introduction*, Springer Science & Business Media, Berlin Heidelberg, 2007.
- [40] S. Faetti and V. Palleschi, *Phys. Rev. A*, 1984, **30**, 3241.
- [41] J. A. Castellano, *Mol. Cryst. Liq. Cryst.*, 1983, **94**, 33–41.
- [42] G. P. Crawford and S. Zumer, *Liquid crystals in complex geometries: formed by polymer and porous networks*, CRC Press, Boca Raton, Fla, 1st edn, 1996.
- [43] S. V. Burylov, *J. Exp. Theo. Phys.*, 1997, **85**, 873–886.
- [44] G. De Luca and A. D. Rey, *J. Chem. Phys.*, 2007, **127**, 104902.
- [45] J.-i. Fukuda and S. Žumer, *Phys. Rev. Lett.*, 2010, **104**, 017801.

- [46] J.-i. Fukuda and S. Žumer, *Phys. Rev. Lett.*, 2011, **106**, 097801.
- [47] H. Stark, *Phys. Rep.*, 2001, **351**, 387–474.
- [48] I. Muševič, M. Škarabot, U. Tkalec, M. Ravnik and S. Žumer, *Science*, 2006, **313**, 954–958.
- [49] M. Škarabot, M. Ravnik, S. Žumer, U. Tkalec, I. Poberaj, D. Babič, N. Osterman and I. Muševič, *Phys. Rev. E*, 2008, **77**, 031705.
- [50] I. I. Smalyukh, O. D. Lavrentovich, A. Kuzmin, A. Kachynski and P. Prasad, *Phys. Rev. Lett.*, 2005, **95**, 157801.
- [51] Z. Eskandari, N. M. Silvestre and M. M. Telo da Gama, *Langmuir*, 2013, **29**, 10360–10367.
- [52] J. S. Lintuvuori, K. Stratford, M. E. Cates and D. Marenduzzo, *Phys. Rev. Lett.*, 2010, **105**, 178302.
- [53] J. S. Lintuvuori, D. Marenduzzo, K. Stratford and M. E. Cates, *J. Mat. Chem.*, 2010, **20**, 10547–10552.
- [54] V. S. R. Jampani, M. Škarabot, M. Ravnik, S. Čopar, S. Žumer and I. Muševič, *Phys. Rev. E*, 2011, **84**, 031703.
- [55] V. S. R. Jampani, M. Škarabot, S. Čopar, S. Žumer and I. Muševič, *Phys. Rev. Lett.*, 2013, **110**, 177801.
- [56] K. P. Zuhail, P. Sathyanarayana, D. Seč, S. Čopar, M. Škarabot, I. Muševič and S. Dhara, *Phys. Rev. E*, 2015, **91**, 030501.
- [57] K. P. Zuhail and S. Dhara, *Appl. Phys. Lett.*, 2015, **106**, 211901.
- [58] K. P. Zuhail, S. Čopar, I. Muševič and S. Dhara, *Phys. Rev. E*, 2015, **92**, 052501.
- [59] M. Melle, S. Schlotthauer, M. G. Mazza, S. H. L. Klapp and M. Schoen, *J. Chem. Phys.*, 2012, **136**, 194703.
- [60] G. Binnig, H. Rohrer, C. Gerber and E. Weibel, *Phys. Rev. Lett.*, 1982, **49**, 57.
- [61] W. Nolting, *Grundkurs Theoretische Physik 6: Statistische Physik*, Springer-Verlag, Berlin Heidelberg New York, 6th edn, 2007.
- [62] M. P. Allen and D. J. Tildesley, *Computer Simulation Of Liquids*, Clarendon Press, Oxford, Reprint edn, 2006.
- [63] D. A. McQuarrie, *Statistical Thermodynamics*, University Science Books, Sausalito, California, 2000th edn, 1974.
- [64] G. H. Findenegg and T. Hellweg, *Statistische Thermodynamik*, Springer, Berlin Heidelberg New York, 2nd edn, 2015.

- [65] F. Schwabl, *Statistische Mechanik*, Springer-Verlag, Berlin Heidelberg New York, 3rd edn, 2006.
- [66] K. E. Gubbins and C. G. Gray, *Theory of Molecular Fluids (International Series of Monographs on Chemistry)*, Oxford University Press, New York, 1st edn, 1984.
- [67] T. Gruhn and M. Schoen, *Phys. Rev. E*, 1997, **55**, 2861.
- [68] R. J. Baxter, *Exactly solved models in statistical mechanics*, Elsevier, Amsterdam, 1982.
- [69] D. Frenkel and B. Smit, *Understanding Molecular Simulation: From Algorithms to Applications (Computational Science)*, Academic Press, Amsterdam, Boston, 2nd edn, 2001.
- [70] M. Schoen and S. Klapp, *Nanoconfined fluids: Soft Matter between two and three dimensions*, John Wiley & Sons New York, New York, 2007, vol. 24.
- [71] D. P. Landau and K. Binder, *A Guide to Monte Carlo Simulations in Statistical Physics*, Cambridge University Press, Cambridge, 3rd edn, 2009.
- [72] R. Cools, *J. Comput. Appl. Math.*, 2002, **149**, 1–12.
- [73] N. Metropolis, A. W. Rosenbluth, M. N. Rosenbluth, A. H. Teller and E. Teller, *J. Chem. Phys.*, 1953, **21**, 1087–1092.
- [74] W. W. Wood, *Molecular Dynamics Simulations of Statistical Mechanics Systems*, 1986, 2–14.
- [75] I. R. McDonald, *Chem. Phys. Lett.*, 1969, **3**, 241–243.
- [76] P. N. Vorontsov-Velyaminov, A. M. Elyashevich, L. A. Morgenshtern and V. P. Chasovskikh, *High Temp. USSR*, 1970, **8**, 261–268.
- [77] S. Giura and M. Schoen, *Phys. Rev. E*, 2014, **90**, 022507.
- [78] W. B. Strett and D. J. Tildesley, *Proc. R. Soc. Lond. A.*, 1976, pp. 485–510.
- [79] A. J. Stone, *Mol. Phys.*, 1978, **36**, 241–256.
- [80] S. Hess and B. Su, *Z. Naturforsch. A*, 1999, **54**, 559–569.
- [81] M. Greschek and M. Schoen, *Phys. Rev. E*, 2011, **83**, 011704.
- [82] T. Stieger, M. Schoen and M. G. Mazza, *J. Chem. Phys.*, 2014, **140**, 054905.
- [83] T. Stieger, S. Püschel-Schlotthauer, M. Schoen and M. G. Mazza, *Mol. Phys.*, 2016, **114**, 259–275.
- [84] S. Püschel-Schlotthauer, T. Stieger, M. Melle, M. G. Mazza and M. Schoen, *Soft Matter*, 2016, **12**, 469–480.
- [85] H. Qi and T. Hegmann, *J. Mater. Chem.*, 2006, **16**, 4197–4205.

- [86] R. Memmer, H.-G. Kuball and A. Schönhofer, *Liq. Cryst.*, 1993, **15**, 345–360.
- [87] M. Melle, M. Theile, C. K. Hall and M. Schoen, *Int. J. Mol. Sci.*, 2013, **14**, 17584–17607.
- [88] R. A. Skutnik, *MSc thesis*, Technische Universität Berlin, Straße des 17. Juni 135, D-10623 Berlin, Germany, 2015.
- [89] L. D. Landau, *Zh. Eksp. Teor. Fiz.*, 1937, **11**, 19.
- [90] P. G. De Gennes, *Mol. Cryst. Liq. Cryst.*, 1971, **12**, 193–214.
- [91] E. C. Gartland Jr., P. Palffy-Muhoray and R. S. Varga, *Mol. Cryst. Liq. Cryst.*, 1991, **199**, 429–452.
- [92] M. Ravnik, M. Škarabot, S. Žumer, U. Tkalec, I. Poberaj, D. Babič, N. Osterman and I. Mušević, *Physi. Rev. Lett.*, 2007, **99**, 247801.
- [93] M. Ravnik, J.-i. Fukuda, J. M. Yeomans and S. Žumer, *Soft Matter*, 2011, **7**, 10144–10150.
- [94] R. Eppenga and D. Frenkel, *Mol. Phys.*, 1984, **52**, 1303–1334.
- [95] B. Gupta and P. Ilg, *Polymers*, 2013, **5**, 328–343.
- [96] G. M. Range and S. H. L. Klapp, *Phys. Rev. E*, 2004, **69**, 041201.
- [97] F. C. Frank, *Discuss. Faraday Soc.*, 1958, **25**, 19–28.
- [98] H. Mori, E. C. Gartland Jr., J. R. Kelly and P. J. Bos, *Jpn. J. Appl. Phys.*, 1999, **38**, 135.
- [99] M. P. Allen and D. Frenkel, *Phys. Rev. A*, 1988, **37**, 1813.
- [100] M. P. Allen and D. Frenkel, *Phys. Rev. A*, 1990, **42**, 3641.
- [101] P. Oswald and P. Pieranski, *Nematic and Cholesteric Liquid Crystals: Concepts and Physical Properties Illustrated by Experiments*, CRC Press, 1st edn, 2005.
- [102] H. G. Zachmann and A. Jüngel, *Mathematik für Chemiker*, Wiley-VCH, Weinheim, 6th edn, 2007.
- [103] M. P. Allen, M. A. Warren, M. R. Wilson, A. Sauron and W. Smith, *J. Chem. Phys.*, 1996, **105**, 2850–2858.
- [104] S. Püschel-Schlotthauer, V. Meiwes Turrión, T. Stieger, R. Grotjahn, C. K. Hall, M. G. Mazza and M. Schoen, *J. Chem. Phys.*, 2016, **145**, 164903.
- [105] I. Chuang, B. Yurke, R. Durrer and N. Turok, *Science*, 1991, **251**, 1336–1342.
- [106] D. Andrienko, G. Germano and M. P. Allen, *Phys. Rev. E*, 2001, **63**, 041701.
- [107] N. Schopohl and T. J. Sluckin, *Phys. Rev. Lett.*, 1987, **59**, 2582.

- [108] H.-R. Trebin, *Adv. Phys.*, 1982, **31**, 195–254.
- [109] T. C. Lubensky, D. Pettey, N. Currier and H. Stark, *Phys. Rev. E*, 1998, **57**, 610.
- [110] N. D. Mermin, *Phys. Today*, 1981, **34**, 46–53.
- [111] E. Penzenstadler and H.-R. Trebin, *J. Phys. France*, 1989, **50**, 1027–1040.
- [112] M. Greschek, M. Melle and M. Schoen, *Soft Matter*, 2010, **6**, 1898–1909.
- [113] D. J. Diestler, M. Schoen, J. E. Curry and J. H. Cushman, *J. Chem. Phys.*, 1994, **100**, 9140–9146.
- [114] K. Vollmayr, J. D. Reger, M. Scheucher and K. Binder, *Z. Phys. B: Condens. Matter*, 1993, **91**, 113–125.
- [115] M. Melle, S. Giura, S. Schlotthauer and M. Schoen, *J. Phys.: Condens. Matter*, 2011, **24**, 035103.
- [116] L. Senbetu and C.-W. Woo, *Mol. Cryst. Liq. Cryst.*, 1982, **84**, 101–124.
- [117] D. de las Heras, L. Mederos and E. Velasco, *Liq. Cryst.*, 2010, **37**, 45–56.
- [118] M. Tasinkevych, N. M. Silvestre and M. M. T. da Gama, *New J. Phys.*, 2012, **14**, 073030.
- [119] M. Melle, S. Schlotthauer, C. K. Hall, E. Diaz-Herrera and M. Schoen, *Soft matter*, 2014, **10**, 5489–5502.
- [120] J.-P. Hansen and I. R. McDonald, *Theory of Simple Liquids*, Academic Press, Amsterdam, Boston, 3rd edn, 2006.
- [121] M. Cifelli and C. Veracini, *Mol. Cryst. Liq. Cryst.*, 2013, **576**, 127–134.
- [122] H. Cang, J. Li and M. D. Fayer, *Chem. Phys. Lett.*, 2002, **366**, 82–87.
- [123] P. G. De Gennes, *Solid State Commun.*, 1972, **10**, 753–756.
- [124] L. Cheung, R. B. Meyer and H. Gruler, *Phys. Rev. Lett.*, 1973, **31**, 349.
- [125] L. Leger, *Phys. Lett. A*, 1973, **44**, 535–536.
- [126] M. Delaye, R. Ribotta and G. Durand, *Phys. Rev. Lett.*, 1973, **31**, 443.
- [127] A. De Vries, *Mol. Cryst. Liq. Cryst.*, 1970, **11**, 361–383.
- [128] T. Stieger, S. Püschel-Schlotthauer, M. Schoen and M. G. Mazza, *Mol. Phys.*, 2015, 1–17.
- [129] E. de Miguel, L. F. Rull, M. K. Chalam and K. E. Gubbins, *Mol. Phys.*, 1991, **74**, 405–424.
- [130] T. Kihara, *J. Phys. Soc. J.*, 1951, **6**, 289–296.

- [131] O. Diat, D. Roux and F. Nallet, *J. Phys. II*, 1993, **3**, 1427–1452.
- [132] D. Roux, F. Nallet and O. Diat, *Europhys. Lett.*, 1993, **24**, 53.
- [133] M. C. Choi, T. Pfohl, Z. Wen, Y. Li, M. W. Kim, J. N. Israelachvili and C. R. Safinya, *P. Natl. Acad. Sci. USA*, 2004, **101**, 17340–17344.
- [134] C. Blanc and M. Kleman, *Eur. Phys. J. E*, 2001, **4**, 241–251.
- [135] M. Conradi, M. Ravnik, M. Bele, M. Zorko, S. Žumer and I. Muševič, *Soft Matter*, 2009, **5**, 3905–3912.
- [136] A. Golemme, S. Žumer, D. W. Allender and J. W. Doane, *Phys. Rev. Lett.*, 1988, **61**, 2937.
- [137] O. D. Lavrentovich, *Liq. Cryst.*, 1998, **24**, 117–126.
- [138] J. Bezić and S. Žumer, *Liq. Cryst.*, 1992, **11**, 593–619.
- [139] D. Seč, T. Porenta, M. Ravnik and S. Žumer, *Soft Matter*, 2012, **8**, 11982–11988.
- [140] G. P. Crawford, D. W. Allender and J. W. Doane, *Phys. Rev. A*, 1992, **45**, 8693.
- [141] A. V. Kityk, M. Wolff, K. Knorr, D. Morineau, R. Lefort and P. Huber, *Phys. Rev. Lett.*, 2008, **101**, 187801.
- [142] S. Calus, M. Busch, A. V. Kityk, W. Piecek and P. Huber, *J. Phys. Chem. C*, 2016, **120**, 11727–11738.
- [143] A. V. Ryzhkova and I. Muševič, *Phys. Rev. E*, 2013, **87**, 032501.
- [144] M. Ravnik, G. P. Alexander, J. M. Yeomans and S. Žumer, *P. Natl. Acad. Sci. USA*, 2011, **108**, 5188–5192.
- [145] J.-i. Fukuda and S. Žumer, *Phys. Rev. E*, 2013, **87**, 042506.
- [146] R. Sahoo, O. Chojnowska, R. Dabrowski and S. Dhara, *Soft Matter*, 2016, **12**, 1324–1329.
- [147] O. Wiese, D. Marenduzzo and O. Henrich, *Soft Matter*, 2016, **12**, 9223–9237.
- [148] P. E. Cladis, A. E. White and W. F. Brinkman, *J. Phys.-Paris*, 1979, **40**, 325–335.
- [149] F. Lequeux and M. Kléman, *J. Phys.-Paris*, 1988, **49**, 845–855.
- [150] M. Ambrožič and S. Žumer, *Phys. Rev. E*, 1996, **54**, 5187.
- [151] J. Bezić and S. Žumer, *Liq. Cryst.*, 1993, **14**, 1695–1713.
- [152] K. S. Shing and S. T. Chung, *J. Phys. Chem.*, 1987, **91**, 1674–1681.
- [153] J. E. Adams and W. E. L. Haas, *Mol. Cryst. Liq. Cryst.*, 1971, **15**, 27–35.
- [154] H.-S. Kitzerow, B. Liu, F. Xu and P. P. Crooker, *Phys. Rev. E*, 1996, **54**, 568.

- [155] M. R. Wilson and D. J. Earl, *J. Mat. Chem.*, 2001, **11**, 2672–2677.
- [156] J. Aplinc, S. Morris and M. Ravnik, *Phys. Rev. Fluids*, 2016, **1**, 023303.
- [157] P. G. De Gennes, *Mol. Cryst. Liq. Cryst.*, 1973, **21**, 49–76.
- [158] E. B. Kim, R. Faller, Q. Yan, N. L. Abbott and J. J. de Pablo, *J. Chem. Phys.*, 2002, **117**, 7781–7787.
- [159] E. B. Kim, O. Guzmán, S. Grollau, N. L. Abbott and J. J. de Pablo, *J. Chem. Phys.*, 2004, **121**, 1949–1961.
- [160] Y. Li, J. J.-Y. Suen, E. Prince, E. M. Larin, A. Klinkova, H. Thérien-Aubin, S. Zhu, B. Yang, A. S. Helmy, O. D. Lavrentovich *et al.*, *Nat. Commun.*, 2016, **7**, 12520.
- [161] Y. Zhou, E. Bukusoglu, J. A. Martínez-González, M. Rahimi, T. F. Roberts, R. Zhang, X. Wang, N. L. Abbott and J. J. de Pablo, *ACS nano*, 2016, **10**, 6484–6490.
- [162] J. A. Martínez-González, Y. Zhou, M. Rahimi, E. Bukusoglu, N. L. Abbott and J. J. de Pablo, *P. Natl. A. Sci.*, 2015, **112**, 13195–13200.